Experimental Investigation of Gas Lift Technique in Viscous Fluids

Abubakr Ibrahim

Faculty of Engineering
University of Nottingham

This dissertation is submitted for the degree of
Doctor of Philosophy in Chemical Engineering

October 2017

To the memory of the person who dedicated his life until the very end to Multiphase flow, Prof. Barry Azzopardi, you shall forever be remembered ...

Declaration

I hereby declare that except where specific reference is made to the work of others, the contents of this dissertation are original and have not been submitted in whole or in part for consideration for any other degree or qualification in this, or any other university. This dissertation is my own work and contains nothing which is the outcome of work done in collaboration with others, except as specified in the text and Acknowledgements. This dissertation contains fewer than 65,000 words including appendices, bibliography, footnotes, tables and equations and has fewer than 150 figures.

Abubakr Ibrahim
October 2017

Acknowledgements

This work could have never been completed without the help and support of many individuals to whom I wish to convey my sincere appreciations. First, I would like to thank my supervisor, Dr. Buddhika Hewakandamby. Thank you for your constant support, inspiring mentorship, and practical guidance. I would also like to express my deepest sense of gratitude to my co-supervisor Prof. Barry J. Azzopardi, your boundless enthusiasm, knowledge and insight remain a constant inspiration. It has been a real privilege and a memorable experience to work with you.

My profound gratitude goes to Statoil, Norway especially Prof. Zhilin Yang for funding the project and for the thorough discussions and the uncanny engineering insight throughout the years. This project was funded under the auspicious of the Transient Multiphase Flow (TMF) consortium to all his participants a note of thanks is owed. The support of the Faculty of Engineering through the dean of engineering research excellence scholarship is greatly acknowledged.

I would like to thank my colleagues here at the Multiphase Flow research group, Nottingham. Thank you for creating an environment of joy, happiness and inspiration. I am ever so grateful for your support throughout the hard stages of my research. I have enjoyed your insightful discussions over coffee everyday and during the various meetings, and I am grateful for it. I would like to thank Dr.Shara Mohammed, Dr. Katerina Louizo, Dr. Josep Escrig, Dr. Rajab Omar, Dr. Mustafa Al-Bahadili, Dr. Yousof Alaufi, Dr. Vicky Lange, Dr. Komo Ebiundu and Dr. Joao Vasques.

My appreciation also extends to the technical staff of the faculty of Engineering at Nottingham University. Special note of thanks goes to Melvin Hemsley, thank you for transforming our plans into working things that produce results. I certainly wouldn't have made it through without the bubbly spirit you create in the labs, no matter how bad things get, you still manage to send me back with a smile. I am also thankful to Mick, Fred, Phil, Paul, Terry, Reg, Karl, Sean, Marion, Hannah, Dave and Dr. Katy McKenzie for the support they provided in the labs.

Special thanks go to my friends in Nottingham, Sid, Aziz, Salah, Mohamed, and all the rest- you know who you are. Your support, encouragement and camaraderie has made me a much better person. Lastly, but most of all I would like to acknowledge the support of my loving family. Words cannot express how grateful I am to have you. Your unconditional love and support made me persevere through the hardest of challenges. My mother, you are my heroine.

Abstract

Oil and gas often naturally flow to the surface driven by the high pressure of the reservoir. Over the time oil fields suffer a decline in production primarily caused by the decrease in the reservoir pressure coupled with the fact that fluids become thicker and more viscous. In addition, there are huge reserves of oil that have not been exploited because of the high drilling and pumping costs owing to the high viscosity and density of the oils within. The feasibility of drilling new wells or continuing production from 'dead' reservoirs depends to a great extent on the pumping cost. Pumping is achieved via several methods including gas-lift. It is applied by injecting gas to the base of the oil well which in turn reduces the weight of the oil column in the well riser. The decrease in pressure head results in an increased liquid flow.

The aim of this thesis is to study the dynamics of gas-liquid flows in vertical large diameter pipes, with particular emphasis on viscous fluids. The fundamental study to understand the underlying physical mechanisms underpinning the gas-liquid interactions when the viscosity is increased will thereafter be employed to investigate the performance of gas lift technique and explore avenues for optimisation. Ultimately resulting in improved modelling of the flow behaviour leading to an optimised design approach and a maximised oil productivity.

The aforementioned aim is achieved experimentally by simulating the flow behaviour in a 127 mm vertical pipe. The facility employed is capable of operating as a gas-lift facility and a fixed flow loop that is able to simulate the flow behaviour at controlled gas and liquid turbulence levels. The selection of simulant fluid is key in this work, the selected liquid has physical properties closer the petroleum oil. It is paramount to ensure that when the viscosity is increased, other relevant physical properties such as density and surface tension remain virtually constant. Therefore, silicone oils with four different viscosities were employed ; namely 4.0, 25.4, 51.1, 104.6 cP while varying the liquid superficial velocity from 0.07-0.86 m/s and the gas superficial velocity from 0.01-5.40 m/s, generating a matrix of 720 runs. Void fraction was measured using high spatial and temporal resolution measurement techniques: Electrical Capacitance

Tomography (ECT) and the Wire Mesh Sensor (WMS) at 5 different axial stations along the 10.12 m length of the test section.

First, a novel parametric study on the effect of viscosity in large diameter vertical pipes is presented; whereby the effect of viscosity on various two phase flow attributes is assessed and analysed both qualitatively and quantitatively. The results suggest that void fraction in general decreases with increasing viscosity. Also, the study reveals the presence of Taylor bubbles in the large diameter pipes at the high viscosities studied. Second, the performance of the state of the art models is assessed against the unique experimental data generated. Most models are found to grossly depart from the experimental data. In addition, new improved global models for various multiphase flow features are proposed. Thirdly, we discuss the issue of flow development and elucidate on how the entrance effect varies with increasing viscosity. That was achieved by employing three different injector nozzles for the four different viscosity fluids, producing 2160 experimental runs. The study suggests that the flow becomes independent of the injection method at 63 D axial distance from the injection point. Finally, an investigation of the performance of an actual large scale gas-lift pump is presented. The efficiency is observed to dramatically decrease with increasing liquid viscosity. The discussions extend onto assessing the performance of the state of the art models and proposing improved models based on conclusions drawn from the fundamental experimental study.

Quintessentially, the outcome of this research would help engineers and operators in the oil and gas industry to estimate, with greater accuracy, how much oil will they be getting for any specific gas input. Additionally, it provides improved estimation of pressure gradient and other global parameters that are essential for the design of wells and risers. The high resolution phase distribution information obtained in this work could serve as a benchmark data to test the performance of Computational Fluid Dynamics (CFD) codes developed for similar conditions against.

Table of contents

List of figures

List of tables

Chapter 1

Introduction

1.1 Importance

There are reports that oil wells have been drilled since before the 13th century [125]. Since then oil has been produced from underground reservoirs in colossal quantities (93.7 million barrels/day as per 2016) . Oil supplies about 33% of the global energy demand and the consumption increases steadily with the population growth and the rise of GDP per capita around the world [94]. Oil and gas often naturally flow to the surface driven by the high pressure of the reservoir. There are huge reserves of oil that have not been exploited because of the high drilling and pumping costs. Owing to the high viscosity and density of oils.

On the other hand, existing oil wells after years of production suffer a decline in production. This is primarily attributed to the decrease in reservoir pressure coupled with the fact that oils become thicker and more viscous over the years. This could be attributed to the tendency of fluids to arrange themselves in the reservoir according to their specific gravities; therefore lighter fluids escape earlier in the production life of the well. These changes are associated with many variations in both the chemical and compositional formation of the oil. Longer chain hydrocarbon compounds will begin to appear that essentially have higher viscosity and density.

The feasibility of drilling new wells or continuing production from 'dead' reservoirs depends to a great extent on the pumping cost. Pumping is achieved by several methods including gas-lift. Despite its low efficiency, gas-lift offers a huge advantage over other methods due to the flexibility it provides in controlling the production rate in concordance with the demand.

The design, operation, and implementation of gas-lift technique is hugely dependent on understanding the underpinning physical interactions of gas-liquid two phase flows. This thesis focuses on improving the understanding of two-phase flows in viscous fluids in general. Chiefly, the outcome of this research would help engineers and operators in the oil and gas industry to estimate, with greater accuracy, how much oil they will be getting for any specific gas input. Additionally, it provides improved estimation of pressure gradient and other global parameters that are essential for the design of wells and risers. Furthermore, it will also help operators and designers to avoid unfavourable operation conditions such as slugging. Besides, the high resolution phase distribution information obtained in this work could serve as a benchmark data to test the performance of Computational Fluid Dynamics (CFD) codes developed for similar conditions against.

1.2 Background

Oil production is affected by many interrelated factors. These include fluid properties, well diameter, reservoir conditions, and properties of the piping to the production facilities. Oil reservoirs are normally at high enough pressure to drive the fluids to naturally flow to the surface after the well has been drilled. However, with the ageing of the well the pressure of the reservoir decreases. In addition, the produced fluids become denser and more viscous. To make matters worse, the pressure drop in the well and piping configurations will increase owing to the corrosion and deposition of solid materials on the wall as well as many other mechanical reasons [175]. To salvage the situaion, four types of artificial lift techniques could be utilised to revive 'dead' oil wells. These can be categorised into mechanical pumping methods and gas-lift method. Mechanical pumping includes sub-surface rod pumping, submersible hydraulic and electric pumping, progressive cavity pumps, and plunger lift [95].

Gas-lifting is achieved by the injection of gas into the bottom of the well to decrease the effective density of the fluids in the well, accordingly decrease the gravitational pressure gradient without increasing much of the frictional pressure losses. This allows more fluids to be recovered. Gas-lift has two main advantages over the other methods: the absence of moving parts, and the ability to pump multiphase oils with solid particles in them [70]. Figure 1.1 explains the principle of gas lift together with basic equations to explain the gravitational pressure gradient change under the gas-lift condition.

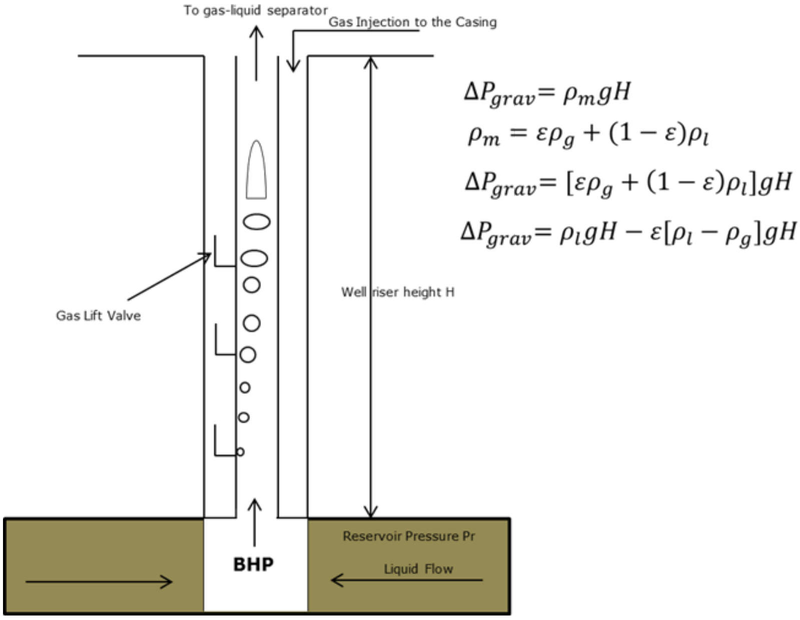

Fig. 1.1 A schematic of the principle of gas-lift technique.

The gas-lift efficiency is potentially dependent on many parameters including: gas injection rate, type and geometry of the gas injector which affects the bubble size and concentration, and essentially the flow regime. These inter-related parameters most likely pose a great influence on the bubble relative velocity, bubbles coalescence and break-up, time/space variation of void fraction and the flow pattern transition which ultimately affects the efficiency and the stability of the system [69].

The majority of the previous investigations on gas lift have been carried out in small pipe diameters (< 100 mm) and for considerably less viscous fluids (water, steam, air). This experimental study will be investigating the parameters affecting gas lifting technique for particularly high viscosity fluids in a 127 mm (5 inches) ID vertical pipe. Principally, this is a more realistic and a closer size to the typical range of oil well sizes ($\sim$5 - 20 inch) [44].

Effect of injector geometry on two phase flow is of great interest to the oil and gas industry. If the injection method appears to vary the two phase flow characteristics significantly, it can be employed to induce preferable two phase flow regimes and avoid rather unfavourable conditions, potentially saving a lot of costs. Additionally, the issue of flow development and entrance effect is crucial to consider when modelling two phase flows. A lot of the published experimental data and empirical models are based on measurements of flows that are not fully developed. Therefore, this thesis aims to fully investigate the issue of flow development and its evolution with increasing viscosity.

1.3 Aim and objectives

The aim of this thesis is to study the dynamics of viscous two-phase flows in vertical large diameter pipes. The fundamental study to understand the mechanisms that underpin viscous gas-liquid interactions will thereafter be employed to investigate the performance of gas lift technique and explore avenues of optimisation. Quintessentially leading to improved modelling of the flow behaviour resulting in improved design approach and maximised oil productivity.

The two-phase flow is influenced by many inter-related parameters, the investigations will tackle the variations as follows:

- Effect of viscosity on two-phase flow characteristics in vertical large diameter pipes
- Improved modelling of global two-phase flow parameters in viscous vertical large diameter pipes
- Effect of the gas injection geometry on vertical large diameter flows at elevated viscosities
- Effect of viscosity on gas-lift performance in vertical large diameter pipes.

1.4 Research method

The aforementioned objectives will be achieved experimentally by simulating the flow behaviour in a controlled laboratory environment. The facility should be capable of operating as a gas-lift facility (natural recirculation loop), whereby the liquid flow is solely controlled by the gas flow. Additionally, it should be able to simulate the flow behaviour at controlled gas and liquid turbulence levels serving as a fixed flow loop. This is needed to support the fundamental study necessary to understand the underlying mechanisms underpinning the gas-liquid interactions when the viscosity is increased.

The selection of the simulant fluid is key in this work. The selected fluid should have physical properties closer to that of petroleum oil. It is paramount to ensure that when the viscosity is increased that other relevant physical properties such as density and surface tension remain virtually constant. This is imperative to guarantee that the captured change of the two-phase characteristics is solely a viscosity effect and not influenced by other parameters that are not the focus of this work.

Access to advanced high spatial and temporal resolution sensing techniques of two-phase flows has revolutionised our understanding of two phase flows and provided a much clearer description of the evolution of the interface at different conditions. The captured information could thereafter be used to validate the models, qualitatively characterise the flow, and statistically treated to develop empirical models amongst many other avenues. In this study Electrical Capacitance Tomography (ECT) and the Wire Mesh Sensor (WMS) will be employed.

1.5 Structure of the thesis

This thesis will be structured as follows:

- Chapter 1: Introduction

  This chapter provides a background to the research work and highlight the research problem. It also shows the motivation behind the research and the expected impact of the research outcome. The general aim and objectives of the research are also explained in addition to a brief description of the methodology and the thesis structure.

- Chapter 2: Literature review

  In this chapter a broad introduction to two-phase flow in vertical pipes is presented. A brief description of the modelling approaches for two phase flow is also given. A review of the mathematical relations governing gas-lift are introduced with a particular focus on the effect of bubble size on the gas-lift efficiency and instability. Furthermore, the particular attributes of flow in large diameter pipes are given in addition to the flow regimes and their transition models.

- Chapter 3: Methodology

  In this chapter a detailed description of the experimental facility employed in this work is presented including the instrumentation and flow meters. The two void fraction measurement techniques employed in this work are also greatly expanded on. Additionally, the fluids characterisation is also presented.

- Chapter 4: Effect of viscosity on two-phase flow in a vertical large diameter pipe

This chapter presents the unique data collected on the effect of viscosity on two phase flow attributes. The chapter features the qualitative and quantitative assessment of the evolution of two-phase flow characteristics with increasing viscosity. This chapter also reports for the first time the observation and characterisation of Taylor bubbles in large diameter pipes at slightly elevated viscosities (51.1 and 104.6 cP).

- Chapter 5: Modelling of viscous flows in vertical large diameter pipes

  In this chapter an assessment of the performance of most popular phenomenological models of two phase flows in vertical pipes is presented. This includes drift flux models, pressure gradient, and structure frequency models. Two correlations are proposed for void fraction and frequency that are a function of both geometrical parameters and physical properties of the fluids.

- Chapter 6: Effect of injector geometry on two-phase flow in a vertical large diameter pipe at elevated viscosities

  In this chapter the influence of injector geometry on two-phase flow characteristics is discussed with particular emphasis on its evolution with increasing viscosity of the liquid. Moreover,the issue of flow development in vertical pipes is investigated with the increase of viscosity and the gas and liquid velocities.

- Chapter 7: Effect of viscosity on gas-lift performance in a vertical large diameter pipe

  In this chapter an assessment of the performance of gas-lift technique is presented. A report of the effect of viscosity on gas-lift curve, efficiency, and evolution of pressure gradient and void fraction is provided. Furthermore, an evaluation of the existing gas-lift models is elucidated together with suggestions of improved modelling.

- Chapter 8: Conclusions and recommendations for further work

  This chapter includes the conclusions from the research work presented in this thesis as well as recommendations for further expansion and improvement of the work.

Chapter 2

Literature review

2.1 Introduction

When gas and liquid flow in a conduit they pose a problem of multidimensional complexity. First the interface between the phases is infinitely deformable; i.e. bubbles can form in different shapes and sizes. Secondly, one of the two phases is compressible (the gas) whereby it expands and compresses depending on the change of the local pressure field. To be able to wholly model the phenomenon and predict exactly what would happen if gas and liquid of known proportions are injected into a pipe is therefore extremely challenging. To be able to analytically solve the evolution of the phases; the Navier-Stokes equations need to be solved in three dimensions and time. An analytical solution for those equations has not been achieved yet for single phase until now, however good numerical approximations are available (CFD modelling). Nevertheless, the problem is too complex whenever two phases are present; and computational models often fail to predict the behaviour due to lack of availability of closure models. Therefore, people often try to experimentally capture representative characteristics of these complex dynamics and formulate phenomenological models that can satisfactorily predict the 'steady state' attributes.

This chapter will give an introduction to multiphase flows with particular emphasis on flow in large diameter pipes. It also presents the different modelling approaches for flow regimes and their transitions as well as models for pressure gradient and void fraction. Moreover, the background of the gas-lift physics will be presented.

2.2 Two-phase flows

Multiphase flow is defined as the condition where two or more phases of the same material (steam and water) or different materials (water and oil) flow in a conduit. It can be gas-liquid, gas-solid, solid-liquid and liquid-liquid (immiscible liquids). Amongst all these multiphase combinations gas-liquid is considered the most complicated, this is because it combines the two issues of infinitely deformable interface between the two phases and the compressibility of the gas phase. It is commonly encountered in most of process engineering applications from oil and gas industry about which the subject of this thesis is concerned to power generation plants and different chemical industries. It is very ubiquitous in units like pipelines, heat exchangers, bubble columns, chemical reactors and phase separators. A schematic representation of multiphase flows encountered in an offshore oil production station is shown in Figure 2.1.

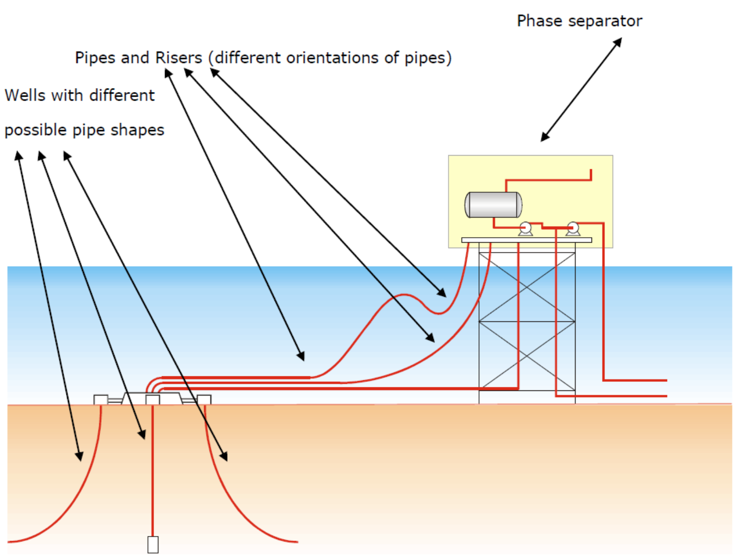

Fig. 2.1 Multiphase flow encountered in an offshore oil production facility [22].

2.2.1 Flow regimes

As gas and liquid flow in a conduit,because of the deformable interface between them, the phases arrange themselves in an infinite number of distributions. These distributions can be categorised into types of interfacial distributions that are termed flow regimes or flow patterns. Flow patterns for vertical upward flow in pipes can be classified into Bubbly flow, Slug, churn and annular flow as featured in Figure 2.2 [81]. Hewitt (2010) considers wispy-annular flow a separate regime while others consider it a sub-pattern of the annular flow.

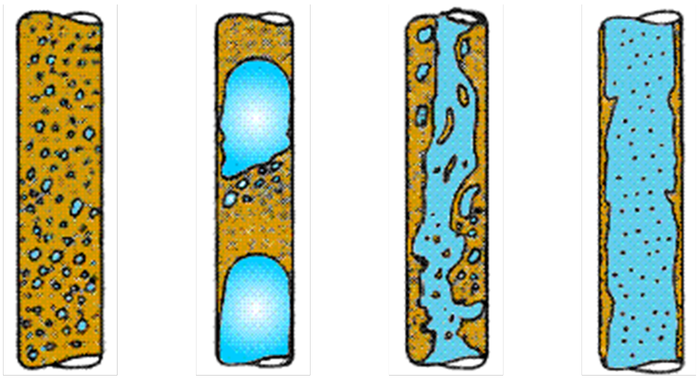

Fig. 2.2 Flow regimes for vertical upward flow. From the left bubbly, slug, churn, and annular flow [80].

Bubbly flow

It is characterised by a continuous liquid phase flow with gas bubbles dispersed in it. Bubbles may flow in a non-uniform motion where they sometimes cluster around the centre of the pipes and sometimes near the wall. Core-peaking and wall peaking bubbly flow are sometimes considered sub-patterns.

At low liquid velocities, bubble sizes are generally governed by the gas injector geometry or the heat transfer rate in the case of nucleate boiling. Usually the bubbles generated are irregular in shapes and sizes. Therefore some researchers cosider this regime discrete bubbly flow regime. On the other hand, at elevated liquid velocities, bubble size is dominated by the breakup generated by the liquid turbulence. This usually creates bubbles of virtually equal sizes. This regime is called dispersed bubbly flow [22].

Many other sub-patterns are proposed for bubbly flow. Kataoka et al (2010) classified bubbly flow according to the interaction of the bubbles-liquid interface into: separated bubble flow, interacting bubbles flow, churn-turbulent flow and clustered bubbly flow. A representation of those regimes is displayed in Figure2.3. Separated flow bubbles is self-explanatory, whereby a small number of bubbles flow in a pipe with limited interaction with each other. Interacting bubbles is when the bubbles density increases whereas they start interacting with each other through collision and wake traces. If bubbles density is further increased; bubbles coalesce and form big cap bubbles which form the churn-turbulent flow. These big bubbles then coalesce to form Taylor bubbles of the slug flow or churn flow gaseous structures in large diameter pipes [108].

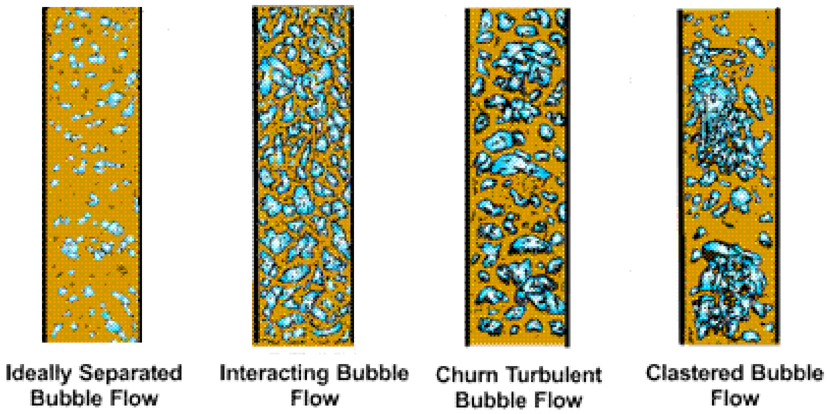

Fig. 2.3 Sub-patterns of bubble flow regime [108].

Slug flow

The main characteristic of the slug flow is the bullet shaped bubbles with equivalent diameter much bigger than that of the pipe surrounded by thin liquid film. These bubbles are first detected and characterised by Davies and Taylor (1950), therefore they are called Taylor bubbles [53]. The transition from bubbly flow happens when bubbles coalesce and form large bullet shaped bubbles that have an equivalent diameter bigger than that of the pipe. The bubbles are separated by liquid slugs that may contain dispersed bubbles. Cheng et al (1998) reported that this regime does not exist for large diameter pipes (>0.15 m), instead a direct transition to churn flow takes place [39].

The slug flow regime is also known for its inherent intermittent behaviour even at constant liquid and gas flow rates. This phenomenon makes the flow regime undesirable for many applications especially in oil and gas production whereas the momentum of liquid slugs may cause severe damages to the piping and separators as well as enhancing erosion of the piping. On the other hand, because of the high liquid velocities; this regime could be appealing for fluid transport purposes [57].

Churn flow

The primary characteristic of churn flow (Froth flow) is the oscillatory movement of the thick liquid film near the pipe wall that essentially has large waves. As the phases' velocities increase Taylor bubbles break, the slugs collapse forming unstable waves of liquid. This flow regime only appears in vertical or semi-vertical pipes because of the absence of gravity counter-action in horizontal flows, and it covers a wide range of liquid and gas velocities. In the lower range it takes place when the Taylor bubbles break-up with the gas flowing in the centre with intermittent bridging of the liquid to the cross-section of the pipe. The higher end however, can be treated as a semi-annular flow with alternating movement of the liquid film around the wall and very large waves on the film [22].

Because of the large fluctuations in void fraction and pressure drop, slug and churn flow are termed intermittent flows. Churn flow is one of the least understood of the flow regimes because of its over complexity. Many researchers consider it a 'chaotic' regime and others were very sceptical about even its existence. In churn flow the net flow of the liquid is normally in the direction of the gas movement although it could be zero or negative in some occasions [99]. There are three bounds for the churn flow, the lower bound of slug or bubble flow transition, the higher bound of churn-annular transition, and the maximum liquid velocity above which churn flow will not occur [98].

Annular flow

It is characterised by a thin liquid film flowing on the walls with a continuous gas flow in the core. Liquid droplets may present in the gas core as trapped droplets (mist). The transition to annular flow happens when the gas input is large enough that the interfacial gas shear stress will dominate over the gravitational forces of the liquid, which expels the liquid to the wall and form the film. The waves are generated on the interface between due to the shearing of the faster gas core on the film. The amplitude of the waves increases as the gas core velocity increases. At a certain range of high gas flow rates most of the liquid would be transported in the core as droplets which motivated some researchers to name this regime mist flow. The presence of the liquid film is a pre-requisite for the mist generation. Interchange between the film and entrained bubbles takes place, sometimes gas bubbles would be entrained in the film too. At high liquid flow rate, the liquid in the core is mostly transported in the form of wisps, this is known as wispy-annular flow [22]. The wispy annular flow is regarded as a separate flow regime by Hewitt and Taylor (1970) [81].

Flow regimes are characterised nowadays by different methods. Historically, the most popular approach is through visual observation of the flow aided by photographs if the experiments were conducted in transparent pipes. This is a very subjective process and very extensively influenced by personal judgement to the degree that Azzopardi (2010) [23] reported that some reputable laboratories used to cast votes of flow regime identification from team members in the 1960's. That was the case until Jones and Zuber (1975) [101] proposed the use of the shape of the probability density function (PDF) of void fraction time series to quantitatively characterise flow regimes. In their paper they published photographs of the flow accompanied by X-ray void fraction measurements together with the corresponding PDFs. The typical shapes corresponding to different regimes are shown in Figure 2.4 obtained from [48].

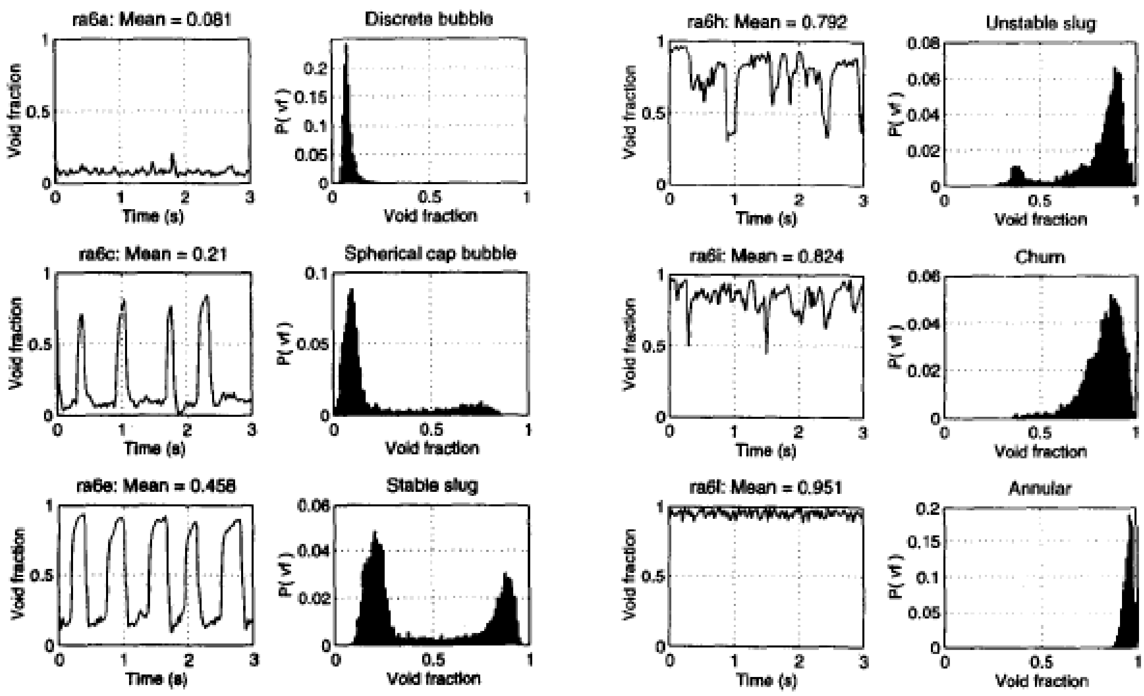

Fig. 2.4 Typical shapes of the probability density function (PDF) of void fraction time series for the different flow regimes obtained from [48]. This method was first experimentally proven by [101].

2.2.2 Gas-liquid flow modelling

Modelling multiphase flows is indispensable to establish an adequate design for the units in which such type of flow is encountered. There are some important design parameters that most of the models are concerned about; these include:

Pressure drop
Pressure gradient is one of the most important design parameters in most of the process engineering units. Evaluating pressure gradient is imperative for sizing different units, sizing pipelines, and determining pumping power as well as predicting flowrates.

Void fraction
Void fraction here is defined as the area fraction of cross-sectional area occupied by the gas phase. The significance of predicting void fraction can be realised in applications such as managing the inventory of a particular valuable phase such as in oil and gas industry and the very objective of this project of improving the recovery of oil in gas-lifted wells. It is also an essential pre-requisite for predicting the pressure gradient.

Heat and Mass transfer coefficients
It is very crucial in the design of heat transfer equipments such as heat exchangers, condensers, and reboilers. This is because the transfer rate greatly depends on the distribution of the phases. For mass transfer processes it is also important for example in the separation units of distillation and absorption, as well as chemical reactors; because phases distribution determines the interfacial area concentration available for heat, mass, and momentum transfer.

Flux limitations
It is essential to determine the limits of the flow system to maintain or avoid particular situations. For example the conditions where transition to a particular flow regime occurs that should be avoided. Also, knowledge of conditions like flow reversal and flooding in counter-current units and the minimum fluidisation velocity for fluidised bed is necessary for the design of most units handling multiphase flows.

Different approaches for two-phase flow modelling

Several approaches are adopted to model two-phase flows. The selection of the approach depends on the data availability and the degree of accuracy required. These methods include [80]:

Homogeneous flow approach
Where two phases are assumed to be travelling at the same velocity and the fluids are treated as one phase with representative properties.

Separated flow approach
The two fluids are regarded flowing separately at different velocities. The conservation equations are written accordingly.

Multi-fluids model
Conservation equations are derived separately for each phase whereby extra terms are included to accommodate the interaction between the phases.

Drift flux modelling
The fluid in this model is modelled in terms of a phase distribution parameter and a local velocity difference (drift velocity) parameter. The limitations of drift flux models are realised in the need for closure laws for the prediction of frictional pressure drop. The closure laws are often acquired from other models with assumptions that might not be consistent with the drift flux modelled void fraction.

Computational Fluid Dynamics models
It is accomplished by numerically solving the Navier-Stokes equations in one, two, or three dimensions.

2.3 Gas-lift

As introduced earlier, oil reservoirs pressure is normally high enough to push the fluids out to the processing facilities. However, with the aging of the wells the reservoir pressure decreases while the produced fluids become thicker and more viscous. Also, the pressure drop in the well configuration will increase because of the tubing resistance due to scaling and depositions and for many other mechanical reasons [175]. Four types of artificial lift techniques are employed for the pumping in 'dead' oil wells: mechanical pumping methods and gas-lift method. Mechanical pumping includes sub-surface rod pumping, submersible hydraulic, and electric pumping [95]. Gas lift is achieved by injecting gas to the bottom of the oil well which in turn decreases the weight of the fluids in the well allowing the recovery of more oil. Figure 2.5 shows a schematic representation of the different artificial lift methods. Gas lift has been practised since 1865 in Pennsylvania, United States [95].

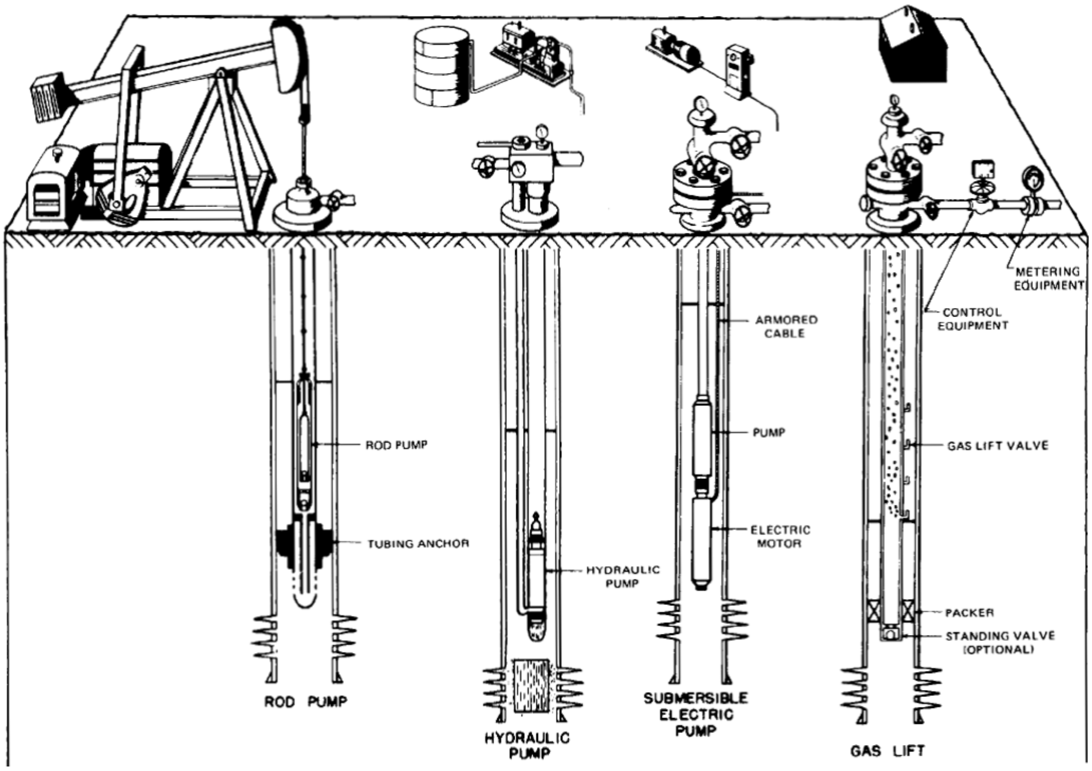

Fig. 2.5 Artificial lift methods [95].

Gas lifting can be categorised according to the operating strategy into continuous gas lift and intermittent gas lift. Continuous gas lift can be achieved by controlling the gas injection rate so that the production is kept at a stable rate. This normally takes place in high liquid production rates. However, if the reservoir pressure becomes very low and the production rate drops dramatically, intermittent gas lift is usually utilised. It is basically acheived by pushing the liquid out of the reservoir using intermittent injections of gas bubbles/structures into the riser. A very good understanding of the time taken to inject the gas bubble/structure and the production rate is important for a successful operation of the process [95].

Gas lift has the advantages of lower initial and operation cost compared to other artificial lift methods. Moreover, It has the distinctive advantage of flexibility in terms of controlling the oil production rate with the amount of the gas injected and the ability to lift multiphase oils that has solids [95]. However, major disadvantages include the potential higher cost arising from corrosive gases, low efficiency in wide well spacing, and very low pressure wells. Besides, the compressors installations may cost much higher than the pumps in some circumstances [95].

2.3.1 Gas-lift modelling

It is paramount to formulate models in order to predict oil production rate with respect to a given gas input in any gas-lifted well. Prediction of the flow rates necessitates accurate estimation of the pressure drop generated by the presence of the gas phase in the well tubing ($\triangle P_{Pipe}$). This should be linked to the pressure drop incurred as the fluids keep escaping the reservoir ($\triangle P_{Res}$). These coupled effects are usually modelled using two relationships:

Inflow performance Relationship (IPR)
The IPR relationship is used to relate the liquid flowrate leaving of the reservoir and the pressure drop associated with the flow. The model can be written based on Darcy's permeability law for fluids flowing through a porous media as:

$$Q_l = PI \triangle P_{Res} \tag{2.1}$$

Where Q_l is the liquid flowrate, PI is the productivity index for the well; It accounts for the permeability of reservoir and liquid's physical properties, and $\triangle P_{Res}$ is the reservoir pressure drop associated with the flow.

Tube Performance Curve (TPC)
The TPC relates the liquid flowrate to the pressure drop in the well tubing for a constant gas to liquid flow ratio. Tubing can be responsible for as much as 80% of the pressure losses in an operating well [144]. This pressure drop is caused by the gravitational, frictional, and the accelerational components which could be analysed using the general multiphase flow models to be described later on in this chapter.

Solving the two relationships (IPR & TPC) will generate potential operation conditions at a certain gas input (given the geometry of the well). Figure 2.6 shows a graph of the two relationships at a constant liquid to gas input ratio. The two curves cross at two points. The lower liquid rate point represents a non-stable operation condition at which if the liquid flow is perturbed negatively a higher pressure will be needed by the TPC than what the reservoir can provide (according to IPR), which is an unrealistic situation. At this condition the liquid flow may cease in the oil well. However, if the liquid flowrate is increased, a lower pressure than what the reservoir can provide will be needed and the liquid flow will continue to increase until it stabilises towards the second crossing point noted in Figure 2.6. This point represents the stable operating condition for the well, whereby friction stabilises the production rate [70].

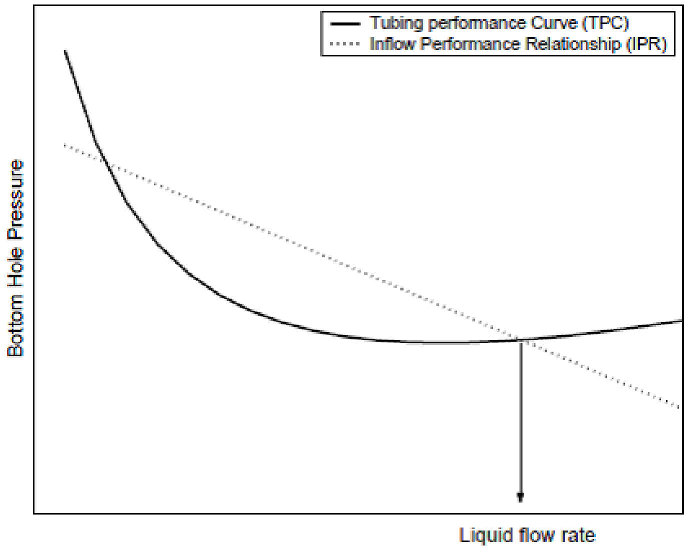

Fig. 2.6 A representation of the evolution of the flowing Bottom Hole Pressure (BHP) with the Tube Performance Curve (TPC) and Inflow Pipe Relationship (IPR) at constant gas/liquid ratio. The figure shows the unstable operating point (left) and the stable operating point (right) [70].

There are three approaches to predict liquid flowrate corresponding to a specific gas input. One approach is empirical whereby gas-lift experiments are performed and empirical correlations are generated by fitting the data. The second approach is analytical which involves performing energy balance investigating several conditions around the maximum efficiency. The most commonly used formula is Ingersoll-Rand equation. The third group of methods is a one dimensional two-phase flow modelling approach. It is based on developing representative mass and momentum balance equations for the system equations. Development of these models involves incorporating many simplifying approximations which limit the range of applicability of the proposed models. The simplifications include, neglecting the kinetic pressure drop and also the compressibility of the gas phase. Some of these models are published in [13, 68, 47, 179, 171]. Richardson and Higson (1962) developed a model to estimate the efficiency of gas-lift using an analytical approach [154]

$$\eta = \frac{Q_l h \rho_l g}{Q_g P_{atm} ln(\frac{BHP}{P_{atm}})} \tag{2.2}$$

Where η is the efficiency which is the ratio of the net lift work done on the liquid to the work spent on the isothermal compression of the gas. h is the tube height, Q_l and Q_g are the liquid and gas flowrates respectively and (BHP) is the Bottom Hole Pressure, P_{atm} is the atmospheric pressure [60].

Many investigators studied the influence of different parameters on the gas lift efficiency. These include, the effect of internal well diameter. It has been studied by [153] from 35 to 3mm diameter and [100] studied it for even smaller pipe diameters. The entrance effect of the fluid has been studied by [68]. Also, the effect of the gas injector has been extensively studied by [69, 128].

2.3.2 Gas-lift instability

Severe oscillations are observed in the wells in which gas lift is applied. This is because the increasing drop of the Bottom Hole Pressure (BHP) caused by the gas presence in the riser results in further more flow of the gas from the annulus to the well. The gas will continue flowing until most of the liquid is pushed out of the well. This will result in dramatic fall in the annulus pressure which will eventually cut the gas flow to the well. However, the liquid starts to accumulate in the bottom hole while the pressure in the annulus rises until it gets high enough to push the gas again through the injection valve to the well and a new cycle starts [1]. Figure 2.7 below shows a schematic representation of the well and annulus structure in gas lift technique.

2.3.3 Effect of bubble size on gas-lift efficiency

Bubble size was reported to greatly influence the gas-lift efficiency owing to three main effects according to Guet (2004) [69]. These effects can be summarised as follows:

- Bubble size influences the flow regime transition. Generally, flow regimes are categorised according to the bubble size. The bubble size was observed to

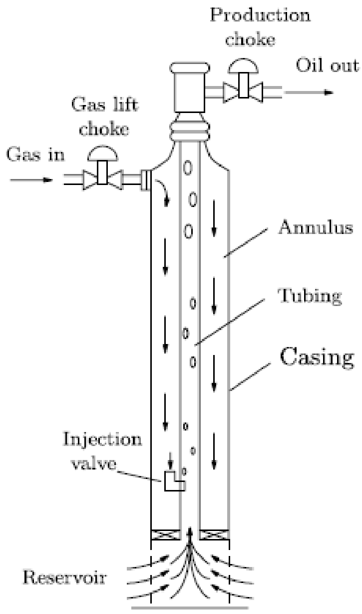

Fig. 2.7 Gas-lifted oil well showing the riser and the annulus [1].

influence the dynamics of bubbles movement and therefore influences bubbles tendency to coalesce to form a different regime or break-up depending on the turbulence conditions of the flow.

- Effect of bubble size on radial bubble distribution and radial velocity profiles. Bubble size affects the transverse migration of bubbles over the pipe cross-section.
- Effect of bubble size on relative gas liquid velocity. Bubbles of different sizes rise at different velocities. The bubble rise velocity is a direct function of the bubble diameter.

Van Geest (2000) studied the effect of air injectors on gas lift efficiency using three different fluids (water, glycerol-water, and ethanol-water). They compared a peripheral porous injector to a conical orifice injector. It was observed that liquid production increases when the porous injector is deployed to inject gas near the wall. Also, the transition from bubbly to slug flow was reported to occur further downstream the injection point when the porous injector is used [181]. Additionally, Guet (2004) studied experimentally the effect of the initial bubble concentration on gas lift efficiency in an air-water system. The investigations were carried out in a 72 mm diameter vertical pipe. It was reported that the smaller the bubble size, the higher the liquid production rate at constant gas injection flow. In other words, the efficiency of gas lift can be improved by introducing finer bubbles at the base of the well [69].

Forces acting on a single bubble

To understand how the viscosity would affect bubble dynamics and ultimately be able to model the global two phase flow parameters it is essential to know the forces acting on a bubble rising in liquid. There are four types of forces acting on the movement of a single bubble in a liquid continuum:

1. Buoyancy force (F_b): This could be represented in terms of the density difference between the fluids and the bubble characteristic volume as

$$F_b = \triangle \rho g \pi \frac{d^3}{6} \tag{2.3}$$

2. Drag Force (F_d): This force acts on the bubble surface against the direction of bubble movement. It could be written in terms of the drag coefficient (C_d) and the relative bubble velocity (u_r) as

$$F_d = -C_d \rho_l u_r \frac{\pi d^2}{4} \tag{2.4}$$

3. Lateral lift force (F_{LL}): This force drags the bubbles towards the wall. This force effect coupled with the oscillatory motions (dilation) of bubbles and the effect of bubble shape result in the lateral migration of bubbles. It could be expressed in terms of the lift coefficient (C_L) and relative bubble motion velocity (u_r) as

$$F_{LL} = -C_L \varepsilon_g \rho_l (u_l - u_g)(\triangledown u_l) \tag{2.5}$$

4. Wall shear stress forces (F_s): This force affects bubbles that flow closer to the pipe wall. The no-slip condition hinders liquid drainage between the bubble and the wall. The net effect will result in a force that expels the bubble away from the wall.

Effect of bubble size on flow pattern transition

Transition from bubbly to slug of churn flow is greatly affected by bubble size and essentially the gas injector. Guet et al (2004) investigated the transition from bubbly to slug flow in a 72 mm vertical upward flow using three different injectors. It is clear from

Figure 2.8 they produced that transition to slug flow took place at considerably higher gas superficial velocities when injectors that introduce finer bubbles are employed [69].

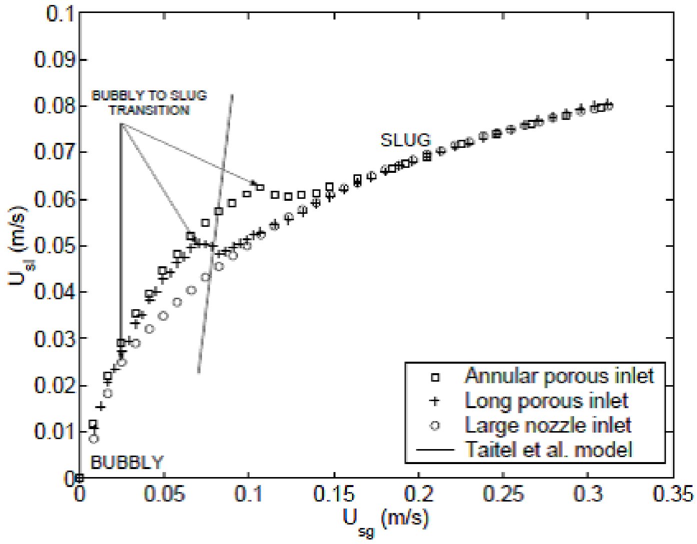

Fig. 2.8 Bubble to slug transition in gas lift using three different gas injectors as observed by [69].

Effect of bubble size on radial void fraction and velocity distributions

Many researchers have observed that bubble size greatly affects the bubbles radial profiles. Bubbles of small sizes tend to migrate towards the pipe wall, producing a wall peaking radial profile. Transition to core peaking occurs as the bubble size increases. Figure 2.9 shows a typical lateral void fraction distribution carried out by Serizawa (1975) [161] for air-water vertical upward flow system. It can be seen that the transition of void fraction peak from the wall to the core with increasing gas superficial velocity as per the legend. The void fraction lateral distribution is governed according to [108] by the following phenomena:

- Lateral lift force acting on a single bubble
- Non-uniformity of the turbulence effect in the pipe that imposes varying pressure field over the pipe cross-section
- A diffusion-like force caused by the void fraction concentration gradient
- Effect of eddies tramping of bubbles

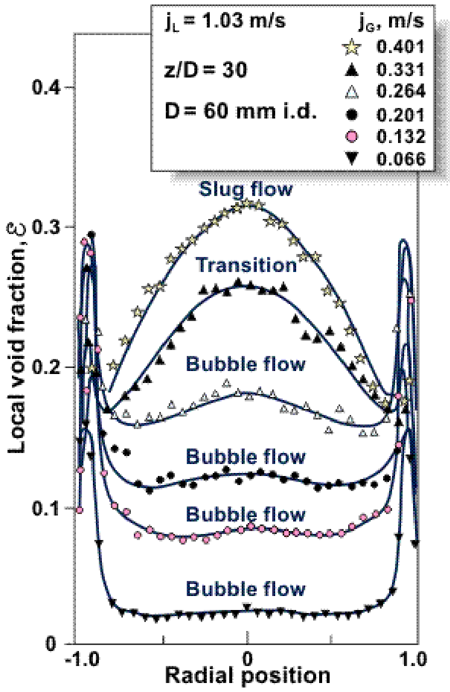

Fig. 2.9 Typical radial distribution of void raction in vertical upward liquid flow at constant gas superficial velocity and different liquid rates [161].

- Bubbles coalescence

The transverse migration of bubbles is not only affected by the bubble size, bubbles shape and orientation greatly affects radial distribution of void fraction [180, 118]. Tomiyama et al (2002) studied single bubbles motion in a linear shear field using a moving belt. They proved that bubble lateral lift force is a function of Reynolds (Re) and Eötvös (Eo) numbers. Accordingly, a model for lateral lift force was proposed in which C_L is correlated as a function of two dimensionless numbers. Bubbles of less than 1.3 mm diameter size were observed to be spherical in shape and travel upwards in rectilinear trajectories. Also these bubbles rising velocities were found to increase with their size. However, bubbles with size greater than 1.3 mm are usually ellipsoidal in shape and rise in wobbling, zig-zag or rectilinear trajectories, whereby their velocity depends on both the motion type and the size [22].

Effect of bubble size on gas-liquid relative velocity

It is clear that bubble velocity is very important in the understanding of interfacial forces such as the drag and lift forces. Bubbles of different sizes travel at different rising velocities. This however will affect the residence time of the gas bubbles in the gas lift riser, which in turn affects the average weight of the oil column that greatly influence the lift force [69]. Mendelson (1967) summarised the studies done on the rise velocities of bubbles of different sizes [124]. The bubble inviscid flow can be divided into surface tension dominated regime and buoyancy dominated regime. The transition occurs at Eo =1 around 0.7 mm bubble diameter. Figure 2.10 shows the data for bubble rise in pure water prepared by Haberman and Morton [72]. This curve is generally better explained when it is divided into regions. Bubbles in region 1 (d_e<0.35 mm) are essentially spherical in shape and follow the Stokes law. Region 2 bubbles (0.35mm>d_e<0.7 mm) their terminal velocity is limited by the viscous forces too but they exhibit internal recirculation that limits the shear stress acting on the interface. Therefore, their velocities are higher than what is predicted by stokes law. Region 3 bubbles (0.7 mm>d_e>3 mm) are non-spherical in shape whereby they rise in swirling or zigzag paths. The velocity is affected by the modification of drag forces due to the zigzag flow as depicted in equation 2.6.

$$V_\infty = 1.35\sqrt{\frac{\sigma}{d_e\rho}} \tag{2.6}$$

Region 4 bubbles (d_e>3 mm) are nearly cap spherical shape whereby their terminal velocity can be predicted by equation 2.7 below.

$$V_\infty = 1.02\sqrt{gd_e} \tag{2.7}$$

However, very viscous fluids do not exhibit similar behaviour. Mendelson (1967) used the wave equation to predict the rise velocity of large bubbles depending on the analogy between the waves and the interfacial disturbances. The results were confirmed with Haberman and Morton's data [124]. They proposed the following expression (equation 2.8) for the terminal velocity.

$$V_\infty = c = \sqrt{\frac{\sigma}{d_e\rho} + gd_e} \tag{2.8}$$

2.4 Flow characteristics in large diameter pipes

According to Ohnuki and Akimoto (2000), flow in large diameter pipes should be the starting point for modelling two phase flows because of the lack of geometry restrictions (i.e. wall effect) and ultimate dependency of the flow on the physics of interfacial

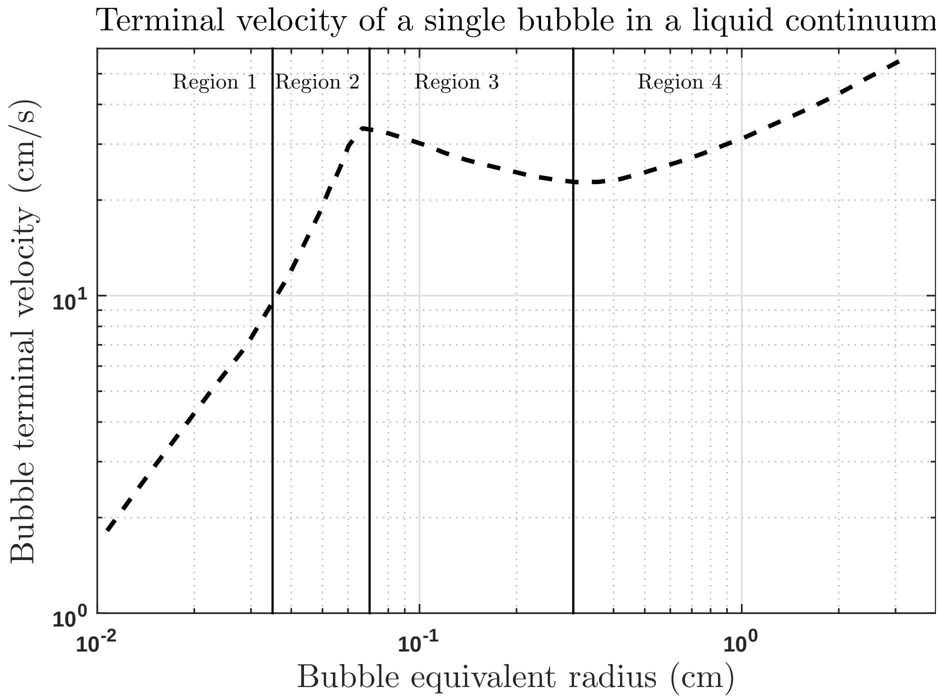

Fig. 2.10 Bubble terminal velocities as function of the bubble size in low viscosity liquids[124].

interactions between the phases [135]. Flow in large diameter pipes has these following distinct characteristics as described by [135] and [157]:

- Large stable Taylor bubbles cannot be formed because of interfacial instabilities and difference in radial void fraction profile as per the available literature. Prasser et al (2001) referred that to the absence of the wall confining effect that present in small diameter pipes [147]. Shen et al (2015) attributes it to the collisions of turbulent eddies generated by large cap bubbles and the shearing-off and interfacial instability of the cap bubbles which increases the break-up probability of large bubbles of size larger than the pipe diameter [164]

- At low U_{ls} wall peaking of void fraction is observed in small diameter pipes whilst core peak is formed in large diameter pipes with eddies filling the pipe cross-section

- Large bubbles are developed in churn bubbly flow in large diameter pipes with core peak radial void fraction distribution. There are also large differences in gas-liquid interactions that result in formation of stagnation regions near the wall with a negative or zero liquid velocity

- At the same bubble size the wall peaking phenonmenon is smaller or even lacking in large diameter pipe in comparison to small diameter pipes. Also, when cap bubbles grow to a maximum diameter, above which they cannot maintain their shape because of the Taylor instability. This maximum bubble size is expressed as a dimensionless diameter given by [107] and [37] as 30 to 52 as below

$$D^* = \frac{D_p}{\sqrt{\frac{\sigma}{g\Delta\rho}}} \tag{2.9}$$

- Enhanced bubble induced turbulence is critical in large diameter pipes because of the large density of large bubbles, which leads to the increase in bubble break-up rate and therefore higher void fraction at the same flow conditions compared to smaller diameter pipes. The simultaneous occurrence of the bubble induced turbulence and the wall-shear induced turbulence results in vigorous local flow swirling [164]

- The effect of inlet geometry and inlet conditions is more prevalent in large diameter pipes as reported by [84, 85]. In large diameter pipes, the effect of diameter on Taylor bubble size and therefore gas velocity (because of buoyancy influence) is insignificant because of the non-existence of slug flow.

2.4.1 Flow regimes in large diameter pipes

Flow patterns are usually presented on two dimensional maps of gas and liquid superficial velocity coordinates, the boundaries are often very different from one work to another and rather subject to personal judgement. Flow patterns transitions depend on the flow velocities, pipe geometry, and fluid properties [173].

Hewitt and Hall-Taylor (1970) divided flow distributions in vertical pipes in general into the four main known flow regimes (bubbly, slug, churn and, annular flow). As detailed earlier, the characteristics of flow in large diameter pipes are considerably different to those in small diameter pipes [81]. Shen et al (2014) proposed the following classification of regimes for large diameter pipes [165]:

- Undistributed bubbly flow/dispersed bubbly flow
  It is characterised by small spherical bubbles flowing upward in almost straight vertical trajectories. This regime is similar to separated bubbly flow in small diameter pipes.

- Agitated bubbly flow
  It is characterised by large eddies including clusters of bubbles filling the pipe cross-section moving randomly. Frequent downward flow of the bubble clusters is observed in this regime.

- Churn-bubbly flow
  It is characterised by significant mixing and prevalent coalescence and break-up of bubbles. This region has been sub-categorised for large diameter pipes by Shen et al. (2014) into:

  – Developing cap-bubbly flow: characterised by incipience of appearance of growing middle and large cap bubbles that move faster upward among small bubbles, they agitate the flow and cause local turbulence and secondary flow.
  – Developed cap-bubbly flow: characterised by appearance of intermittent, dominant cap bubbles with diameter size close to, or bigger than the pipe diameter.

- Churn-slug flow
  When bubble coalescence dominates, large intermittent irregular-shaped structures are formed in the flow whilst smaller bubbles get trapped in the liquid film between the big structures and the wall.

- Developed churn flow
  It is characterised by a froth of small bubbles and cap size bubbles/structures with large unstable bubbles that coalesce and break-up very frequently.

2.4.2 Flow regimes transitions

It is important to first understand the mechanisms by which these transitions take place. Some of the popular transition mechanisms proposed by various investigators in the literature are detailed in this section.

Bubble to slug transition

Transition from dispersed bubbly flow to slug flow is dependent on the competition between the bubble coalescence because of increasing density of bubbles with increasing gas input and the break-up mechanism induced by the turbulence in the liquid phase.

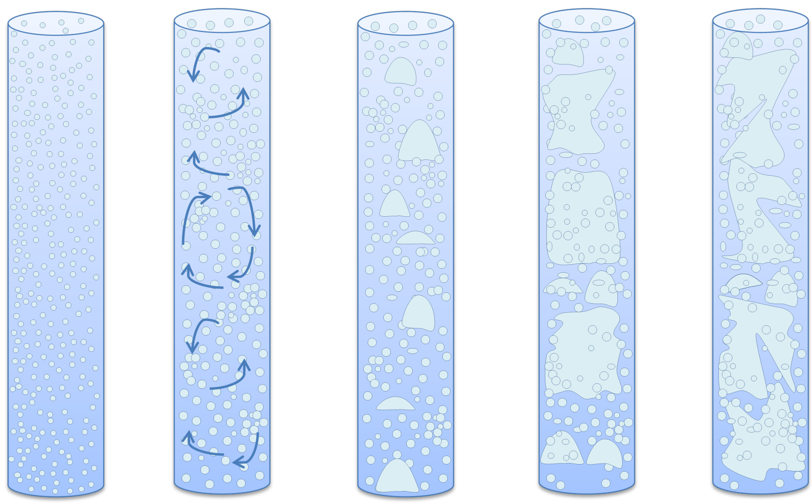

Fig. 2.11 Flow regimes in large diameter pipes featuring (a) undistributed bubbly flow (b) Agitated bubbly flow (c) Churn bubbly flow (d) Slug churn flow and (e) Froth churn flow.

According to Taitel et al (1980) [173] small bubbles of less than 1.5 mm behave like solid particles and rise in rectilinear trajectories. Bigger bubbles however rise in random zigzag paths. Much more bigger bubbles also appear, they are called cap bubbles refering to their cap-like tip similar to that of Taylor bubbles. They have an equivalent diameter less than or equal to that of the pipe. If the bubble equivalent diameter grows larger than the pipe diameter it can then be called Taylor bubble. Bubble flow transitions to slug is experimentally proved to take place around void fraction values 0.2-0.3 [173].

Radovcich and Moissis (1962) [152] proposed a theoretical method for calculating the probability of bubbles' coalescence and calculating the frequency of coalescence as illustrated in Figure 2.12. They were able to predict the time required for bubbles to coalesce and form a Taylor bubble from the frequency of collisions and successful coalescence amongst the collisions as in the equation below.

$$t = f\frac{0.206}{P}\frac{D_b}{c}\frac{(1+f)^2}{f}\left(\frac{D_p}{D_b}\right)^3\left[\langle\frac{0.74}{\varepsilon}\rangle^{\frac{1}{3}}-1\right]^5 \tag{2.10}$$

Where f is the frequency, D_b is the bubble diameter and D_p is the pipe diameter, P is the fraction of successful coalescence amongst the collisions, c is the characteristic bubble velocity in $\left(\frac{ft}{s}\right)$.

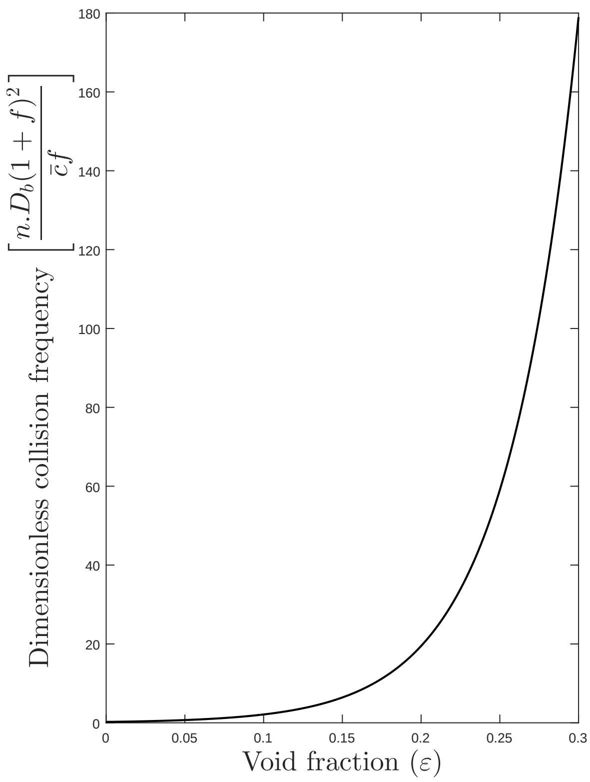

Fig. 2.12 Frequency of bubbles collisions and the corresponding void fraction relationship as proposed by Radovcich and Moissis (1962) [152].

Taitel et al (1980) however proposed a model based on the maximum number of spherical bubbles a cubic lattice can fit. This registers a maximum void fraction of 0.52. They proposed a threshold void fraction below which bubbles can have enough space to randomly move without sharp increase in the coalescence rate which is half their radius that corresponds to 0.25 void fraction. The liquid phase average velocity can be defined as: gas velocity – bubble rise velocity; because bubble rise velocity is relative to the liquid velocity [173].

$$\frac{U_{ls}}{1-\varepsilon} = \frac{U_{gs}}{\varepsilon} - U_o \tag{2.11}$$

If the equation of Harmanthy (1960) [74] for large bubble rise velocity below is used;

$$U_o = 1.53\left(\frac{g(\rho_l - \rho_g)\sigma}{\rho_l^2}\right)^{\frac{1}{4}} \tag{2.12}$$

The following transition equation is produced

$$U_{ls} = 3U_{gs} - 1.15\left(\frac{g(\rho_l - \rho_g)\sigma}{\rho_l^2}\right)^{\frac{1}{4}} \tag{2.13}$$

Hinze (1955) [88] proposed a model for the maximum dispersion size of stable bubbles based on the competition between the surface tension forces and the turbulent fluctuations forces as

$$d_{max} = 1.14\left(\frac{\sigma}{\rho_l}\right)^{\frac{3}{5}}(E_d)^{\frac{-2}{5}} \tag{2.14}$$

where (E_d) is the energy dissipation rate per unit mass. Brodkey (1967) [36] gave the critical bubble size that can remain spherical and not agglomerate nor coalesce with other bubbles as

$$d_{crit} = \left[\frac{0.4\sigma}{g(\rho_l - \rho_g)}\right)^{\frac{1}{2}} \tag{2.15}$$

Neglecting the slip velocity, the equation for the turbulent induced dispersion (U_{gs}, U_{ls}) above which transition to slug flow never occurs has been proposed by Taitel et al (1980) as follows

$$U_{ls} + U_{gs} = 4\left[\frac{D^{0.429}(\frac{\sigma}{\rho})^{0.029}}{v_l^{0.072}}\left(\frac{g(\rho_l - \rho_g)\sigma}{\rho_l^2}\right)^{0.446}\right] \tag{2.16}$$

The above equation neglects the effect of void variation on coalescence and break-up bubble sizes.

Slug to churn transition

- Wake effect mechanism

  This transition mechanism was proposed by Mishima and Ishii (1984)[126] and Chen and Brill (1997) [38]. The transition occurs when the Taylor bubbles get closer to each other and the wake of the leading Taylor bubble touches the nose of the following one. This results, because of the strong wake effect, in breakage of the liquid slug and creation of large liquid structures. Transition was predicted to occur when the average void fraction is equal or larger than the average void fraction in the Taylor bubble.

- Flooding Mechanism

  It was proposed by Nicklin et al (1962)[133] where they predicted that the transition occurs when flooding takes place in the liquid film enveloping the Taylor bubble. This situation happens when the velocities of the Taylor bubble and the surrounding liquid film satisfy flooding conditions. Then the liquid film will eventually breakdown and start falling counter-currently to the gas and essentially the flow direction. Hewitt and Hall-Taylor (1970) [81] explained the experimental procedure proposed by [133] for determining the transition point as follows:

  1. Carry a separate experiment for calculating the flooding flowrates (conditions that make a liquid film flow reverse in a vertical pipe)
  2. Get instantaneous measurements of the void fraction by incrementally increasing the gas flowrate and then calculate the instantaneous flows from the following expressions

$$Q_g = U_{TB} A \varepsilon \tag{2.17}$$

$$Q_l = (Q_g + Ql) - U_{TB} A \varepsilon \tag{2.18}$$

  Hewitt et al (1964) [82] showed the flooding gas flow decreases with the increasing length of the pipe. Taylor bubbles are shorter for long pipes which leads to under prediction of the flooding velocity for shorter pipes as is the case for Nicklin and Davidson method. A semi-empirical equation was proposed by Hewitt and Wallis (1963) [83] to predict the flooding gas and liquid flow rates. The equation is

$$U_{gs}^{*} = U_{gs}\left[\frac{\rho_g}{gD(\rho_l - \rho_g)}\right]^{\frac{1}{2}} \tag{2.19}$$

$$U_{ls}^{*} = U_{ls}\left[\frac{\rho_l}{gD(\rho_l - \rho_g)}\right]^{\frac{1}{2}} \tag{2.20}$$

The transition is predicted to take place when the constant C reaches a critical value (C=0.88 or C=1) from the relationship below

$$C = \sqrt{U_{ls}^{*}} + \sqrt{U_{gs}^{*}} \tag{2.21}$$

The correlation above was validated in a 0.75 and 1.25 inch pipes. Wallis (1969) [183] extended the above correlation to accommodate the effect of viscosity, Aziz and Govier (1972) [21] reported that the correlation has been tested for viscosities ranging from 1-3000cP.

$$C = m\sqrt{U_{ls}^{*}} + \sqrt{U_{gs}^{*}} \tag{2.22}$$

Where C and m are functions of a number called dimensionless inverse viscosity number (N_{μ_l}) defined as

$$N_{\mu_l} = \frac{[gD^3(\rho_l - \rho_g)\rho_l]^{\frac{1}{2}}}{\mu_l} \tag{2.23}$$

$$m = 10, N_{\mu_l} > 250 \tag{2.24}$$

$$m = 69N_{\mu_l}^{-0.35}, 18 < N_{\mu_l} > 250 \tag{2.25}$$

$$m = 25, N_{\mu_l} < 18 \tag{2.26}$$

$$C = 0.345\left[1-\exp\left(\frac{-0.01N_{\mu_l}}{0.345}\right)\right]\left[[1-\exp\left(\frac{3.37Eo}{m}\right)\right] \tag{2.27}$$

McQuillan and Whalley (1985) [122] employed the above approach to calculate flooding velocities based on the liquid film superficial velocity U_{lf} and the Taylor bubble superficial velocity U_{TBs} as follows

$$U^*_{gs} = U_{TBs}\left(\frac{\rho_g}{gD(\rho_l-\rho_g)}\right)^{\frac{1}{2}} \tag{2.28}$$

$$U^*_{ls} = U_{fs}\left(\frac{\rho_l}{gD(\rho_l-\rho_g)}\right)^{\frac{1}{2}} \tag{2.29}$$

That was based on the assumption that the Taylor bubble is long enough to satisfy the Nusselts film thickness relationship which is given by the following expression.

$$\delta_N = [\frac{3U_{fs}\mu_l D}{4g\rho_l}]^{\frac{1}{3}} \tag{2.30}$$

The film superficial velocity can be calculated from the following relationship

$$U_{fs} = U_{TB} - (U_{ls} + U_{gs}) \tag{2.31}$$

- Entrance Effect Mechanism

  Taitel et al (1980) [173] suggested that entrance zone in a slug flow riser is churn and justified the assumption based on the falling liquid slug as two consecutive unstable Taylor bubbles coalesce. Taylor bubble velocity was predicted by [133] as

$$U_g = 1.2U_l + 0.35\sqrt{gD} \tag{2.32}$$

Where 1.2 U_l is the centreline liquid velocity and the second term is the Taylor bubble velocity in a stagnant liquid continuum. The length of stable slug flow is fairly constant, minimum stable slug length ($\frac{L}{D}$) is 8 up to 16 D in air water system. Taitel et al (1980) [173] suggested equation 2.33 for predicting the entry length (EL) to create a stable slug in which they assumed the observed flow regime is churn based on the turbulence distribution around the Taylor bubble; considering the film as falling two dimensional jet.

$$\frac{l_E}{D} = 40.6(\frac{U_m}{\sqrt{gD}} + 0.22) \tag{2.33}$$

- Bubble Coalescence mechanism

  Brauner and Barnea (1986) [34] suggested that transition occurs when the void fraction in the liquid slug increases. This will mean an increase in the number of entrained bubbles in the liquid slug. As the gas superficial velocity increases the number of bubbles increase and therefore the rate of coalescence increases too. When the void fraction rises over a critical value, the liquid slug becomes unstable the then breaks to form large bridge that gets lifted by the subsequent Taylor bubble. The trailing bubble as a result will become narrower and distorted. The critical void fraction is predicted by Brauner and Barnea to be 0.52. Which is the same value as Taitel et al. (1980) [173] suggested for the transition to slug flow. A model was proposed to relate the mixture velocity boundary to the incurring void fraction based on the competition between the interfacial forces and the turbulent forces as follows

$$2\left[\frac{0.4\sigma}{(\rho_l-\rho_g)g}\right]^{\frac{1}{2}}(\frac{\rho_l}{\sigma})^{\frac{3}{5}}\left[\frac{2}{D}C_l(\frac{D}{v_l})^{-n}\right]^{\frac{2}{5}} \times U_m^{\frac{2(3-n)}{5}} = 0.725 + 4.15\varepsilon^{0.5} \tag{2.34}$$

  Where the C_L and n are the Blasius correlation for friction factor (C_L=0.046 and n=0.2).

  The equation 4.2 above is drawn in Figure 2.13 for a 1.25 cm pipe for air-water system. It can be observed that at the transition boundary between the dispersed liquid and the slug flow, if U_{gs} is increased, the level of turbulence in the dispersed bubbly flow cannot accommodate more gas. Therefore, large gas bubbles are formed. However, the level of turbulence and the void fraction within the liquid slug remains at the same level of the dispersed bubbly flow at the transition boundary at a constant $U_m (U_m = U_{slug})$.

Transition to annular flow

Annular flow transition occurs when the gas velocity (U_g) is high enough to carry the largest stable droplet upward. This can be calculated using Hinzes (1955) [88] stable

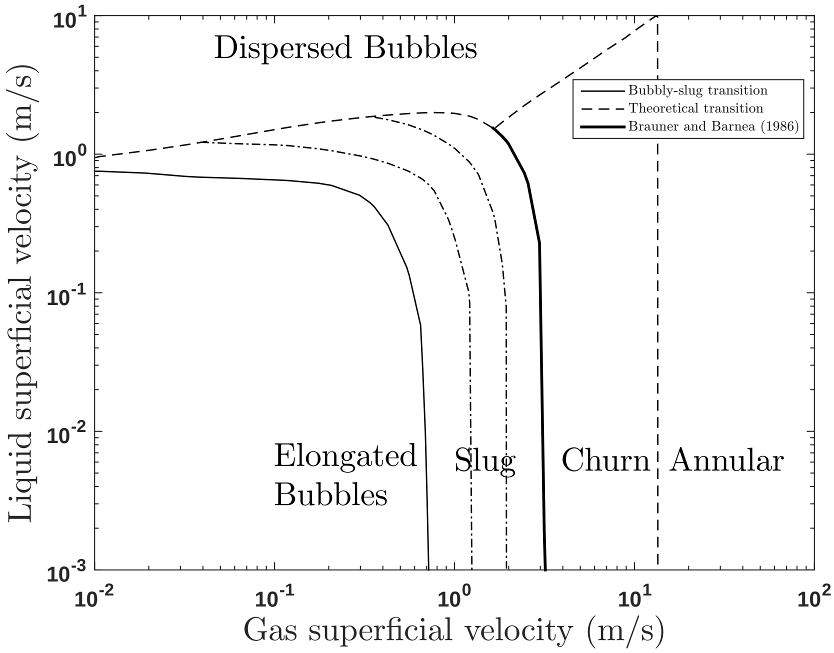

Fig. 2.13 Flow regime map, showing locus of constant void fraction in liquid slugs, and the slug-churn transition boundary proposed by Brauner and Barnea (1986) [34] for a 1.25 cm pipe using air-water.

droplet equation and the balance between gravity and drag forces around the bubble as in equation 2.35.

$$U_g = \left(\frac{4k}{3C_d}\right)^{\frac{1}{4}} \left[\frac{g(\rho_l - \rho_g)\sigma}{\rho_l^2}\right]^{\frac{1}{4}} \tag{2.35}$$

Where k is the critical Weber number, which is estimated to be in the range of (20-30) at the transition according to [173].

2.5 Pressure drop

Pressure drop, according to the momentum conservation equation, is formulated of three components; the gravitational, frictional, and accelerational pressure gradients as denoted in equation 2.36. Several approaches are used to predict this paramount two-phase flow design parameter. These approaches will be briefly discussed in this section.

$$\left(\frac{dp}{dz}\right)_T = \left(\frac{dp}{dz}\right)_G + \left(\frac{dp}{dz}\right)_F + \left(\frac{dp}{dz}\right)_A \tag{2.36}$$

2.5.1 The homogeneous flow model

The homogeneous flow approach is based on assuming perfect mixing of the two-phases (i.e fluids are travelling at equal velocity and have uniform characteristics). The behaviour of the two-phase flow will be modelled using representative physical properties of the homogeneous mixture. This is the simplest approach because it does not necessitate the evaluation of void fraction to predict the pressure drop, whereas void fraction is evaluated from the mass fraction of the two-phases as in equation 2.37. The homogeneous two phase pressure gradient can be expressed by equation 2.38 [22].

$$\rho_{TP} = \frac{\rho_g \rho_l}{x\rho_l + (1-x)\rho_g} \tag{2.37}$$

$$-\left(\frac{dp}{dz}\right) = (g\rho_{TP}\sin\beta) + \left(\frac{\overline{\tau}P}{S}\right) + \frac{d}{dz}\left(\frac{\dot{m}^2}{\rho_{TP}}\right) \tag{2.38}$$

The frictional pressure gradient is predicted by using a two-phase friction factor (f_{TP}) obtained from the Reynolds number (equation 2.39) employing the homogeneous two-phase density (equation 2.37), the total volumetric flux ($\dot{m}$), and the homogeneous two-phase kinematic viscosity. The friction factor is then evaluated using any suitable empirical equation like the Colebrook-White equation. The two-phase kinematic viscosity is often expressed by the form of equation 2.40, however many other expressions are used, mostly empirical correlations. The homogeneous model is found to depart grossly from experimental data, adjusting the viscosity terms does not result in much improvement of the model [81].

$$Re_{TP} = \frac{\dot{m}D}{\eta_{TP}} \tag{2.39}$$

$$\frac{1}{\eta_{TP}} = \frac{x}{\eta_G} + \frac{1-x}{\eta_l} \tag{2.40}$$

This modelling approach produces acceptably accurate results when compared against experimental data for homogeneous dispersed flows ($\pm 25\%$)[35]. The homogeneous flow model is often used as a reference case in oil and gas industry for its simplicity. The model predictability improves dramatically at higher pressures (where gas density is higher) and higher flowrates [136]. One of the most widely used correlations of this approach is the one by Beggs and Brill (1973) [31].

2.5.2 The separated flow model

Initially, it was developed to avoid the assumption of equal liquid and gas velocity. It is formulated as a simple, area or time-averaged one dimensional model with no interfacial interactions considered. The approach assumes isothermal condition for the gas and liquid [22]. Most of the models derived using this approach are empirical or semi-empirical models. This is because of the absence of interfacial momemtum transport formulation between the phases [113]. The overall pressure drop can be be written as equation 2.41 corresponding to the three respective components of pressure gradient expressed in equation 2.36.

$$-\left(\frac{dp}{dz}\right) = ([\varepsilon_g \rho_g + (1-\varepsilon_g)\rho_l] g \sin\beta) + \left(\frac{\overline{\tau} P}{S}\right) + \frac{d}{dz}\left(\dot{m}^2\left[\frac{x_g^2}{\varepsilon_g \rho_g} + \frac{(1-x_g)^2}{(1-\varepsilon_g)\rho_l}\right]\right) \tag{2.41}$$

The separated flow model incorporates three main assumptions to simplify the momentum and energy equation. These include that the liquid and the gas flow separately in the pipe, each occupying an area proportional to their void fraction at that axial location. The second assumption is that the local density of either phase is considered constant over the entire pipe. This is considered inadequate especially where velocity profile differs dramatically in the cross-section of the pipe. The third assumption is that the wall shear stress is regarded equal irrespective of the radial location of the interface [81].

The frictional pressure gradient is evaluated as the ratio of two-phase pressure gradient to the frictional pressure drop if only the liquid is flowing in the pipe, only the gas is flowing, or to the frictional losses if total flow is regarded as a liquid or as a gas. The most popular correlations of this approach are the ones by Lockhart and Martinelli (1949) [116] and Friedel (1979) [61]. Friedel correlation proved to be the most accurate correlation available in the literature for the prediction of overall pressure drop. However, it becomes less accurate at low gas to liquid density ratio [22]. Better prediction of pressure gradient can be achieved using phenomenological models that are often flow regime dependent.

2.6 The drift flux model

It was first proposed by Zuber and Findlay (1965) [193] where the velocity of gas phase is expressed as a function of the mixture velocity and the drift velocity. The model was proposed taking into consideration the effect of non-uniformity of flow by introducing a distribution parameter (C_o). Also, it considers the slip velocity between the two phases by introducing a weighted mean drift velocity (V_{dg}) as shown in the equation below.

$$v_g = C_o(U_{ms}) + \frac{(\varepsilon V_{dg})}{(\varepsilon)} \tag{2.42}$$

Where

$$C_o = \frac{\langle \varepsilon U_{ms} \rangle}{\langle \varepsilon \rangle \langle U_{ms} \rangle} \tag{2.43}$$

The closest model to the current drift-flux model is introduced by Nicklin et al (1962) [133] that was introduced for slug flow. The distribution parameter (Co) was introduced as 1.2 because Taylor bubble travel faster at the centre of the pipe and the drift velocity as the bubble rise velocity. Zuber and Findlay (1965) proposed the following expression for the calculation of the distribution parameter in circular ducts assuming axially symmetric profile of void fraction distribution.

$$\frac{U_{ms}}{(U_{ms})_{centre}} = 1 - \left(\frac{r}{R}\right)^m \tag{2.44}$$

And the void fraction follows the same function, they concluded $C_o = 1$ for uniform distribution $C_o > 1$ for higher void concentration at the centre $C_o < 1$ for lower void concentration in the centre However the drift velocity is dependent on momentum transfer between the two phases which follows a dependence on the stress fields in both phases and the geometry of the interface. This means a dependency on the void concentration profile and therefore the flow-regime. Therefore, drift velocity is expressed in regime dependent formula. Zuber and Findlay (1965) suggested the following expression if the flow is little affected by void concentration as in turbulent bubbly flows

$$\frac{\langle \varepsilon V_{dg} \rangle}{\langle \varepsilon \rangle} = \frac{1}{\langle \varepsilon \rangle A} \int_A \mathrm{v}_{\mathrm{terminal}} (1-\varepsilon)^{\mathrm{k}} \varepsilon \, \mathrm{d}A \tag{2.45}$$

And for the slug flow the drift velocity is calculated by

$$\frac{\langle \varepsilon V_{dg} \rangle}{\langle \varepsilon \rangle} = 0.35[\frac{g(\rho_l - \rho_g)D}{\rho_l}]^{\frac{1}{2}} \tag{2.46}$$

And for churn flow it is expressed as

$$\frac{\langle \varepsilon V_{dg} \rangle}{\langle \varepsilon \rangle} = 1.53[\frac{g(\rho_l - \rho_g)\sigma}{\rho_l^2}]^{\frac{1}{4}} \tag{2.47}$$

Many drift flux correlations were presented in the literature for the drift velocity and the phase distribution parameter for different flow conditions and regimes. An overview of the correlations for large diameter pipes and their application range is shown in the table below adapted from Shen et al (2014) [165].

1. **Ishii (1977)** [96]

C_o	V_{dg}	Notes
$1.2-0.2\sqrt{\frac{\rho_g}{\rho_l}}$	$\sqrt{2}(\frac{\sigma g \triangle \rho}{\rho_l^2})^{\frac{1}{4}}(1-\langle\varepsilon\rangle)^{1.75}$	Bubbly flow, Negligible shear gradient effect
$1.2-0.2\sqrt{\frac{\rho_g}{\rho_l}}$	$0.35(\frac{\sigma g \triangle \rho}{\rho_l^2})^{\frac{1}{2}}$	Slug flow
$1.2-0.2\sqrt{\frac{\rho_g}{\rho_l}}$	$\sqrt{2}(\frac{\sigma g \triangle \rho}{\rho_l^2})^{\frac{1}{4}}$	Churn Flow
$1+\frac{(1-\langle\varepsilon\rangle)}{\langle\varepsilon\rangle+4\sqrt{\frac{\rho g}{\rho_l}}}$	$\frac{1-\langle\varepsilon\rangle}{\langle\varepsilon\rangle+4\sqrt{\frac{\rho_g}{\rho_l}}}\left[\langle V_{gs}\rangle+\sqrt{\frac{\triangle\rho g D(1-\langle\varepsilon\rangle)}{0.015\rho_l}}\right]$	Annular Flow

2. **Hills (1976)** [87]

C_o	V_{dg}	Notes
$\frac{1.35}{U_m^{0.07}}$	0.24	$U_{ls} > 0.3m/s$ Fully developed
$1 or \frac{1}{1-\langle\varepsilon\rangle}$	$(1-\langle\varepsilon\rangle(0.24+4\langle\varepsilon\rangle^{1.72} or (0.24+4\langle\varepsilon\rangle^{1.72})-\frac{U_{gs}}{(1-\langle\varepsilon\rangle)}$ $(0.24+4\langle\varepsilon\rangle^{1.72})-\frac{U_{gs}}{(1-\langle\varepsilon\rangle)}$	$U_{ls} < 0.3m/s$ Fully developed, (150mm ID)

3. **Shipley (1984)** [166]

C_o	V_{dg}	Notes
1.2	$0.24+0.35[\frac{U_{gs}}{U_m}]^2(gD\langle\varepsilon\rangle)^{\frac{1}{2}}$	Experiments in 457mm

4. **Clark and Flemmer (1985)** [45]

C_o	V_{dg}	Notes
$0.935(1+142\langle\varepsilon\rangle)$	$1.53(\frac{\sigma g}{\rho_l})^{\frac{1}{4}}$, =0.25 for air/w	Experiments in 100mm

5. **Clark and Flemmer (1986)** [46]

C_o	V_{dg}	Notes
$0.93(\frac{U_{ls}}{U_m}) + 1.95(\frac{U_{ls}}{U_m})$	$0.25m/s$	Experiments in 100mm

6. **Murase et al (1986)** [130]

C_o	V_{dg}
$\left[1.2 - 0.2\sqrt{\frac{\rho_g}{\rho_l}}\right]\left[1 - e^{-18<\varepsilon>}\right]$ for $\varepsilon \leq \varepsilon_c$	$7.1D_h^{\frac{1}{8}}\left[1 - \left\{1.2 - 0.2\sqrt{\frac{\rho_g}{\rho_l}}\right\}\left(1 - e^{-18\langle\varepsilon\rangle}\right)\langle\varepsilon\rangle\right]\langle\varepsilon\rangle^{0.6}$ for $\varepsilon \leq 0.33$
$1 + 0.2\left(1 - \sqrt{\frac{\rho_g}{\rho_l}}\right)\left[1 - \left(\frac{\langle\varepsilon\rangle - \langle\varepsilon_c\rangle}{1 - \langle\varepsilon\varepsilon_c\rangle}\right)^2\right]$ for $\varepsilon > \varepsilon_c$	$16.4D_h^{\frac{1}{8}}\left[1 - \left\{1.2 - 0.2\sqrt{\frac{\rho_g}{\rho_l}}\right\}\left(1 - e^{-18\langle\varepsilon\rangle}\right)\langle\varepsilon\rangle\right]\left[(-ln(1 - \langle\varepsilon\rangle^{1.45})\right]$ for $0.33 < \varepsilon \leq \varepsilon_c$
$\varepsilon_c = 0.588 - 1.817\sqrt{\frac{\rho_g}{\rho_l}} + 2\frac{\rho_g}{\rho_l} - 3.344\left(\frac{\rho_g}{\rho_l}\right)^{\frac{3}{2}}$	$16.4D_h^{\frac{1}{8}}\left[1 - \left\{1.2 + 0.2\left(1 - \sqrt{\frac{\rho_g}{\rho_l}}\right)\right\}\left[1 - \left(\frac{\rho_g}{\rho_l}\right)^2\right]\langle\varepsilon\rangle\right]\left[-ln\left(1 - \langle\varepsilon\rangle^{1.45}\right)\right]$ for $\varepsilon > \varepsilon_c$

7. **Hirao et al (1986)** [89]

C_o	V_{dg}
$1.2 - 0.2\sqrt{\frac{\rho_g}{\rho_l}}$	$0.52\left(\frac{\sigma g \Delta\rho}{\rho_l}\right)^{\frac{1}{2}}$

8. **kataoka and Ishii (1987)** [107]

C_o	V_{dg}
$1.2-0.2\sqrt{\frac{\rho_g}{\rho_l}}$	$0.0019D_h^{*0.809}\left(\frac{\rho_g}{\rho_l}\right)^{-0.157}N_{\mu l}^{-0.562}\left(\frac{\sigma g\Delta\rho}{\rho_l^2}\right)^{\frac{1}{4}}$ for $N_{\mu l}\leq 0.00225$ and $D_h^*\leq 30$
	$0.03\left(\frac{\rho_g}{\rho_l}\right)^{-0.157}N_{\mu l}^{-0.562}\left(\frac{\sigma g\Delta\rho}{\rho_l^2}\right)^{\frac{1}{4}}$ for $N_{\mu l}\leq 0.00225$ and $D_h^*\geq 30$
	$0.92\left(\frac{\rho_g}{\rho_l}\right)^{-0.157}\left(\frac{\sigma g\Delta\rho}{\rho_l^2}\right)^{\frac{1}{4}}$ for $N_{\mu l}>0.00225$
	$N_{\mu l}=\frac{\mu_l}{\left(\rho_l\sigma\sqrt{\frac{\sigma}{g\Delta\rho}}\right)^{\frac{1}{2}}}$

9. **Ishii and Hibiki (2003)** [85]

C_o	V_{dg}	Notes
$exp\left\{0.475\left(\frac{U_{gs}^*}{U_m^*}\right)^{1.69}\right\}\left(1-\sqrt{\frac{\rho_g}{\rho_l}}\right)+\sqrt{\frac{\rho_g}{\rho_l}}$	$V_{dg}^*=V_{dg/I}^*e^{-1.39U_{gs}^*}+V_{dg/K}^*e^{1-1.39U_{gs}^*}$	Bubbly, $\langle\varepsilon\rangle<0.3$,$0\leq\frac{U_{gs}^*}{U_m^*}\leq 0.9$
$\left(-2.88\left(\frac{U_{gs}^*}{U_m^*}\right)+4.08\right)\left(1-\sqrt{\frac{\rho_g}{\rho_l}}\right)+\sqrt{\frac{\rho_g}{\rho_l}}$	$V_{dg}^*=V_{dg/I}^*e^{-1.39U_{gs}^*}+V_{dg/K}^*e^{1-1.39U_{gs}^*}$	Bubbly, $\langle\varepsilon\rangle<0.3$,$0.9\leq\frac{U_{gs}^*}{U_m^*}\leq 1$
$1.2e^{\left\{0.11(U_m^*)^{2.22}\right\}}\left(1-\sqrt{\frac{\rho_g}{\rho_l}}\right)+\sqrt{\frac{\rho_g}{\rho_l}}$	$V_{dg}^*=V_{dg/Kataoka}^*$	Cap-bubbly, $\langle\varepsilon\rangle<0.3$,$0\leq U_m^*\leq 1.8$
$\left[0.6e^{\left\{-1.2U_m^*-1.8\right\}}+1.2\right]\left(1-\sqrt{\frac{\rho_g}{\rho_l}}\right)+\sqrt{\frac{\rho_g}{\rho_l}}$	$V_{dg}^*=V_{dg/Kataoka}^*$	Cap-bubbly, $\langle\varepsilon\rangle<0.3$,$U_m^*\geq 1.8$

10. **Ishii and Hibiki (2003b)** [86]

C_o	V_{dg}	Notes
$C_o = \dfrac{L}{(K_o + (1-K_o)\langle\varepsilon\rangle^r)}$	$V_{dg} = C_g V_{dg}^o$	Bubbly flow
$L = \dfrac{1 - e^{-\frac{4P_{crit}^2}{P(P_{crit}-P)}\langle\varepsilon\rangle}}{1 - e^{\frac{4P_{crit}^2}{P(P_{crit}-P)}}}$	$C_g = (1-\langle\varepsilon\rangle)^{B1}$	$\langle\varepsilon\rangle < 0.3$
$K_o = B_1 + (1-B_1)\Big(\dfrac{\rho_g}{\rho_l}\Big)^{\frac{1}{4}}$	$V_{dg}^o = 1.41\Big(\dfrac{\sigma g \Delta\rho}{\rho_l^2}\Big)^{\frac{1}{4}} C_2 C_3 C_4$	$0 \leq \dfrac{U_{gs}^*}{U_m^*} \leq 0.9$
$r = \Big[1 + 1.57\dfrac{\rho_g}{\rho_l}\Big](1-B_1)$	$C_2 = \begin{cases} 1 & \text{if } C_5 \geq 1 \\ \dfrac{1}{1 - exp\big(\frac{-C_5}{1-C_5}\big)} & \text{if } C_5 < 1 \end{cases}$	
$B_1 = min\Big[0.8 \text{ or } A_1\Big]$	$C_3 = max\begin{cases} 0.5 \\ 2exp\Big[\dfrac{-Re_l}{60000}\Big] \end{cases}$	
$A_1 = \dfrac{1}{1 + exp\big[\frac{-Re}{60000}\big]}$	$C_4 = \begin{cases} 1 & \text{if } \Big(\dfrac{D_2}{D_h}\Big)^{0.6} \geq 1 \\ \dfrac{1}{1 - exp\Bigg(\frac{-\big(\frac{D_2}{D_h}\big)^{0.6}}{1-\big(\frac{D_2}{D_h}\big)^{0.6}}\Bigg)} & \text{if } \Big(\dfrac{D_2}{D_h}\Big)^{0.6} < 1 \end{cases}$	
	$C_5 = \sqrt{\dfrac{150}{\frac{\rho_g}{\rho_l}}}$	

Chapter 3

Methodology

3.1 Introduction

This chapter will describe the experimental facility used in the study. It will also include detailed information about the different void fraction measurement techniques used in this work. Moreover, it will provide a brief description of the instrumentations used as well as fluids characterisation.

3.2 Statoil gas-Lift facility

A U-tube rig is used to generate the results of this thesis, it comprises of a riser section of a 127 mm diameter of and a reservoir section of 300 mm diameter. Most of the pipes are made of transparent Acrylic segments to allow for visual observation of the flow. The total height of the rig is 10.12 m. A schematic of the rig is shown in Figure 3.1. The apparatus is equipped with two parallel channels at the bottom that connect the two columns. One is a straight pipe that enables operating the facility as a natural recirculation loop. The second is equipped with an inline positive displacement pump to allow running the apparatus as a fixed flow loop with controlled liquid and gas flows. The reason the downcomer column is designed to be this large is to first improve bubbles escape in the gas-lift mode and also reduce static pressure perturbations generated by the falling liquid slugs in the gas-lift arrangement. Moreover, such large size will hold larger volumes of liquid and therefore increase residence time of fluid, leading to improved bubble removal in the recycled liquid stream.

Progressive cavity pump is used at the base of the U-tube to positively induce liquid flow in the fixed flow setting. The pump is of type NEMO NM053BY01L06B, which is acquired with an inverter that allows controlling the liquid flow by changing the motor frequency in the range of (5-90 Hz). The pump can handle fluids with nominal viscosities up to 300 cP, achieving a maximum volumetric flow of 670 l/min (0.88 m/s).

Gas (i.e. air) is injected at the bottom of the column from the laboratory high pressure air mains. Three different geometries are used for gas injection (Figure 3.3). The gas flowrate is measured by a thermal mass flowmeter with an integrated controller and the liquid flow is measured using an ultrasonic flowmeter for the passive-lifting line and an oval gear flowmeter for the pump line. Gas temperature and pressure are measured just before the injection point using a pressure transducer and a thermocouple. Pressure at the base of the riser column is also measured by another transducer. The liquid temperature is monitored before and near the base of the riser column where mixing takes place. Differential pressure gradient is measured at various locations along the riser column using a differential pressure sensor connected to various pressure taps at different stations on the pipe wall along the height of the test section.

Void fraction is measured at five axial positions using two Electrical Capacitance Tomography (ECT) devices. The two ECT sensors employed; each has two planes. One is mounted at about 15D from the injection point and the other is fitted just below the WMS at about 62D from the injection point. A 32x32 capacitance Wire Mesh Sensor (WMS) devise is placed at the end of the riser (about 63D from injection) to minimise the intrusiveness effect on the flow. The positioning of these sensors downstream the pipe was chosen according to the recommendation from flow development study of Lucas et al (2005)[117]. Figure 3.2 below shows a 3D diagram of the facility featuring the location of the void fraction measurement devices.

Three different geometries for gas injection are selected, to vary both the initial bubble size and the lateral location in the pipe cross-section where the gas is introduced. Figure 3.3 shows the dimensions of the gas injectors used in the study. The first injector is a concentric pipe with a 25.4 mm ID to introduce the gas concurrently to the liquid flow at the core of the pipe. The second geometry is a perforated PVC pipe of 36 mm ID perforated in the order of 16 rows each has 40 circular holes of diameter 1 mm. This injector is chosen to introduce the gas as smaller bubbles in a perpendicular direction to that of the liquid flow. The third injector is a conical copper cap placed on top of a 36 mm concentric pipe. The cone is capped from the top and has chamfered edges to avoid adhesion of the generated gas bubbles on the surface of the cone and therefore ensure that small enough bubbles are generated. The conical injector introduces the

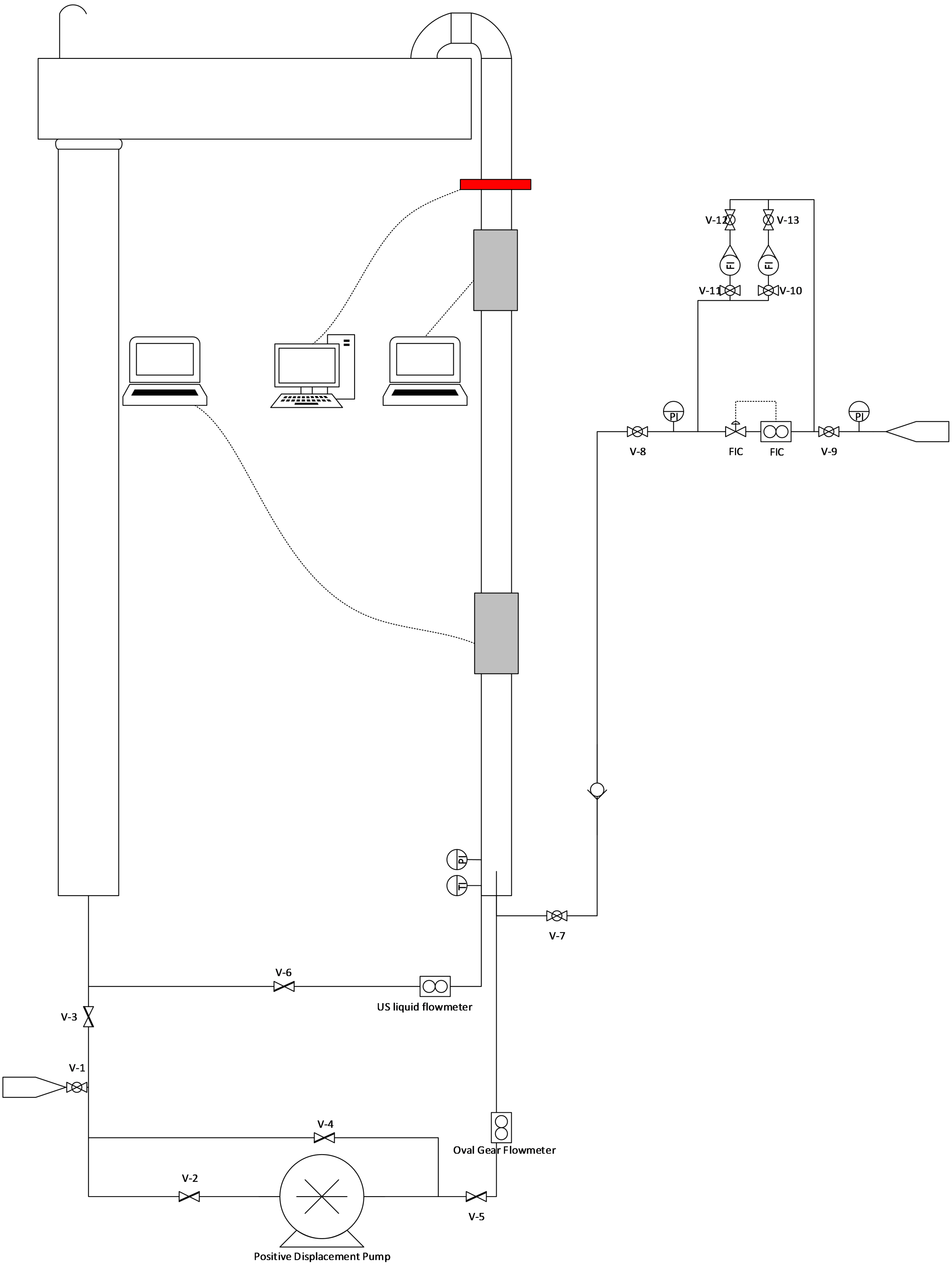

Fig. 3.1 A schematic diagram of the Statoil gas-lift facility.

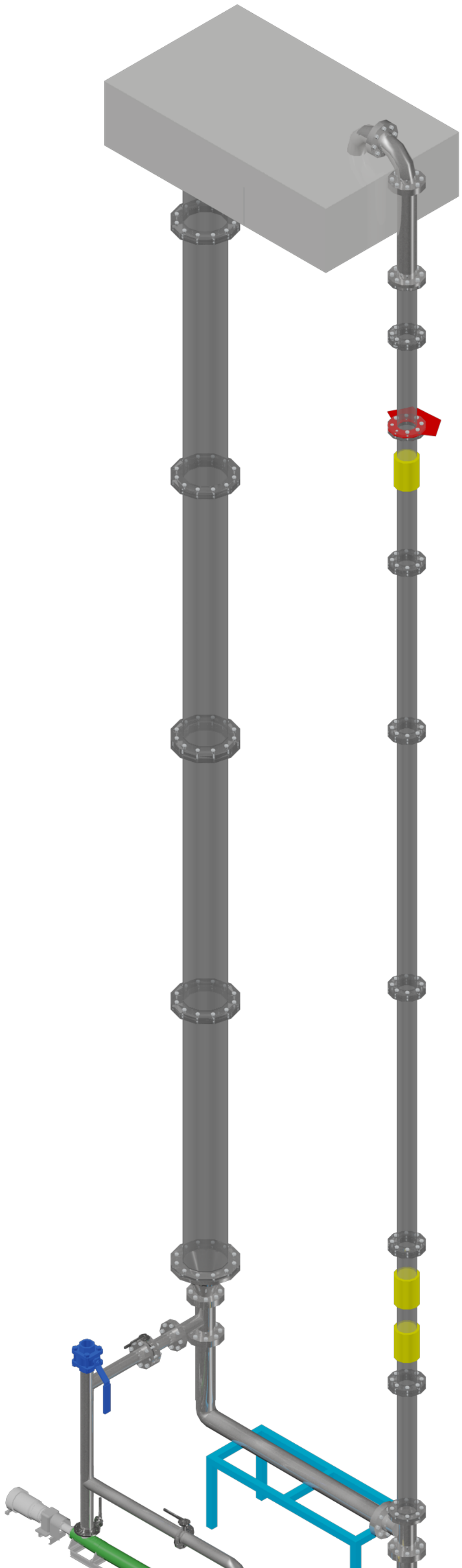

Fig. 3.2 A 3D model of the Statoil gas-lift apparatus featuring location of ECT sensors (yellow) and WMS (in red).

gas near the wall of the pipe at a direction nearly opposite to that of the flowing liquid creating more turbulence at the inlet.

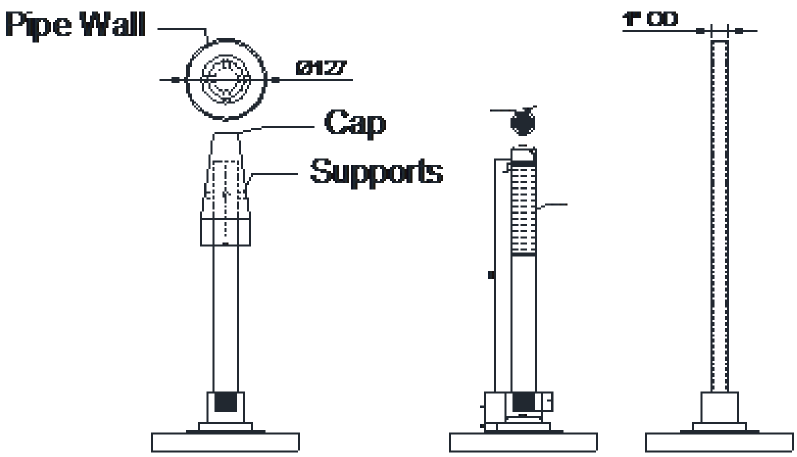

Fig. 3.3 Geometries of the injectors used in this study showing cap injector (left), perforated injector (middle) and concentric tube injector (right).

3.2.1 Flow measurements

Liquid and gas flowrates are measured using different techniques. Gas flow is measured using a thermal mass flowmeter with an integrated controller, the liquid is measured using an ultrasonic liquid flowmeter and an oval gear flowmeter each fitted on one of the two parallel channels explained earlier.

Gas flow

Air is used as the gas phase in the experiments of this study. The flowrate is measured by a thermal mass flowmeter and controller supplied by Bronkhorst (Model F-203AV-1M0-ABD-99-V). The flowmeter uses two probes to measure the gas flow. The first probe is heated whilst the other measures the gas temperature gained by the convective heat transfer from the first heated probe. With the knowledge of the distance between the probes, temperature difference, the gas properties the gas flow rate can be measured using a formula in the form of equation 3.1 below.

$$Q_h = K^{'}(1 + Kq_n^m)\Delta T \tag{3.1}$$

where Q_h is the supplied heat, q_m is the mass flowrate, and ΔT is the measured temperature difference. The terms $K, K^{'}$ are heat transfer related constants to account for the transfer rate and surface area [30]. The flowmeter accuracy was reported by the manufacturer to be ±0.5% of Reading (RD) plus ±0.1% of Full Scale (FS) (At calibration conditions). It operates in the range of 0-1670 l/min.

The high inertia of the probe to adapt to an immediate change of temperature in the surrounding air makes the flowmeters response quite slow. However, if the power needed to keep constant temperature at the first probe is used to calculate the velocity the response becomes much faster. The flowmeter calibration is included in Appendix A.

Liquid flowrate

Ultrasonic liquid flowmeter

The FLEXUS 7404 ultrasonic flowmeter is installed on the apparatus to measure the liquid flowrate in the natural recirculation loop configuration. This particular genre is selected firstly; because it is a non-intrusive flowmeter. It is a clamp-on version that goes outside of the pipe. The second reason is that it is a more suitable flowmeter to capture the transient behaviour of the flow and the turbulence effect compared to the second monst economically viable option (magnetic flowmeter) [30].

The flowmeter is clamped on the pipe walls in a horizontal position. The transducers are arranged to form two beams reflective arrangement as shown in Figure 3.4 below. A summary of the meter specifications is shown in Table 3.1.

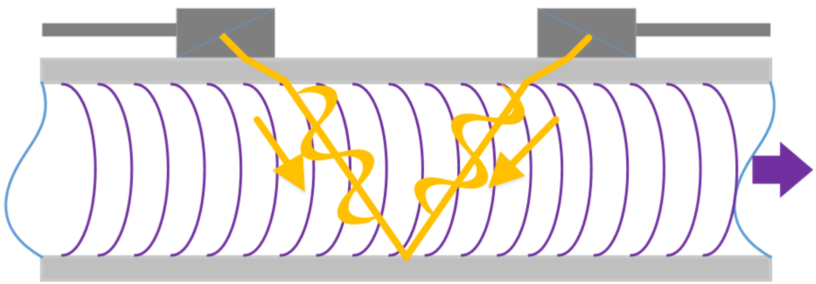

Fig. 3.4 Two beam installation of the wrap around ultrasonic flowmeter (adapted from FLEXIM).

Clamp on ultrasonic flowmeters measuring approach is built on the transit time principle. Foretunately, the time of flight measurement principle is the most accurate of the ultrasonic methods. Flow pulsation often causes fluid flattening in the pipes which results in gross measurement errors owing to incorrect measurement of the diametric ultrasonic beam. Nonetheless, magnetic and ultrasonic flowmeters are less affected by the pulsation of the fluid compared to other types of flowmeters [30].

Table 3.1 Specifications of the ultrasonic liquid flowmeter.

Property	Value
Flow range (l/min)	7.6-19000
Low cut-off (l/min)	7.6
Mounting position from nearest fitting	8.9D
Accuracy	5%

For more details about the ultrasonic flowmeter measurement principle refer to Appendix A.

Oval gear flowmeter

Oval gear flowmeter supplied by Kobold is installed on the rig for the measurement of liquid flowrate in the forced flow loop line (model No. DON-145FB4Z) driven by the pump. The flowmeter is selected for its suitability to measure flowrates of high viscosity liquid flowrates. The flowmeter has two oval gears that rotate when a known volume of liquid passes through. Pulses corresponding to the number of rotations are generated by embedded magnets in the gears. It measures in the range of (35-750 l/min), producing a linear analogue signal of (4-20 mA) corresponding to the flowrate. More information about the calibration is provided in Appendix A.

3.2.2 Pressure measurements

Local pressure measurements

The gas injection and the riser base pressures are measured by flush mounted diaphragm pressure transmitters from IMPRESS Sensors. The transmitter has a sensitive diaphragm that gets displaced according to the amount of pressure imposed on it. The transducer changes the mechanical signal into a digital signal representative of the pressure (0-5 V). Both sensors were calibrated in house as well as by the manufacturer.

Differential pressure measurements

The differential pressure is measured by a capacitive diaphragm differential pressure transmitter from Kobold (PAD-DEE5S2NS00). The cell is equipped with a small sensor that measures the capacitance between the diaphragm and a metal plate implemented in the senor and correlates it to the measured pressure. The same aim could be accomplished using two different pressure transducers for each end and subtract the pressures. This however will propagate the inherent error associated with each of the instruments and increases measurement uncertainty [127]. That in addition to the uncertainty associated with signal delay. The DP cell measures in the range (0-1.86 bar). The accuracy provided by the manufacturer as 0.075% of the full calibration span. The DP cell is connected to two pressure taps along the length of the test section located at 2.03 m and 7.11 m from the base of the column. It must be noted that the DP cell performance was validated against single phase flow (liquid) measurements.

3.2.3 Temperature measurements

Liquid and gas temperatures are constantly monitored using type K thermocouples located at various locations around the rig. A thermocouple for the gas line, another at the base of the test section, and a third at the base of the reservoir (300 mm) column. The thermocouples are calibrated for the range from $(0 - 100^oC)$ using icy and boiling water to achieve both temperatures and the output signal was analysed accordingly. Temperature measurement is captured using an NI9211 module.

3.2.4 Data acquisition system

All measurements are synchronously acquired using a hardware system provided by National Instruments (NI) and programmed by LabVIEW. A program was written to configure the acquisition the signals from the various instrumentations in the rig when a triggering signal arrives initiated from the WMS electronic box. All the instruments are chosen to give a current or voltage output that could be instantaneously logged using the data acquisition device compactDAQ from National Instruments. The chassis number (NI-cDAQ-9178) is employed with two modules: NI-9205 module for voltage inputs and NI-9211 for thermocouple inputs. An external triggering system is designed to receive the starting signal from the WMS box in order to initiate the measurements in all the instruments. It also triggers the measurements in the two other ECT devices. A description of the program is included in the Appendix A.

3.3 Void fraction measurement Techniques

Void fraction information is acquired using two different techniques; Electrical Capacitance Tomography (ECT) and the Wire Mesh Sensor (WMS). This section will introduce these two measurement techniques in detail, their measurement principles, background mathematical operations, limitations, and the uncertainty associated with the measurements produced.

3.3.1 Electrical Capacitance Tomography (ECT)

It is a non-intrusive measurement technique that allows discriminating the phases/materials distribution of two dielectric materials inside a pipe or a vessel by sensing electrical capacitance which depends on the permittivity. That is accomplished by installing a number of electrodes (usually 8 or 12) around the pipe periphery which output electrical voltage and then capture the signals in all other electrodes. A number of independent capacitance measurement (M) equals to n(n-1)/2 will be recorded; where n is the number of electrodes. Image reconstruction algorithms are then employed to provide permittivity distribution of the pipe cross-section and hence generate a material or phase distribution. The results are displayed as frames of images of the pipe cross-section and values for the materials/phases concentration. If two ECT sensor planes are used the structure velocity can be measured using cross-correlation principle.

The selection of the electrodes number is a balance between the capacitance measurements uncertainty and the number of independent measurements. The greater the number of independent capacitance measurements the clearer representation of the system is obtained. However, the more electrodes in the system the less sensing area and more significant capacitance measurement error [189].

The TFL R5000 ECT sensor comprises of four main parts, the sensor electrodes that are placed around the pipe circumference, the data acquisition and processing box and a computer to display the data with the aid of ECT32v3 software or Matlab. Figure 3.5 below shows an image of the components of the ECT sensor.

The permittivity distribution relationship to capacitance can be expressed by the following equation

$$C = -\frac{1}{V} \int \int_{\Gamma} \epsilon(x, y) \bigtriangledown \phi(x, y) d\Gamma \tag{3.2}$$

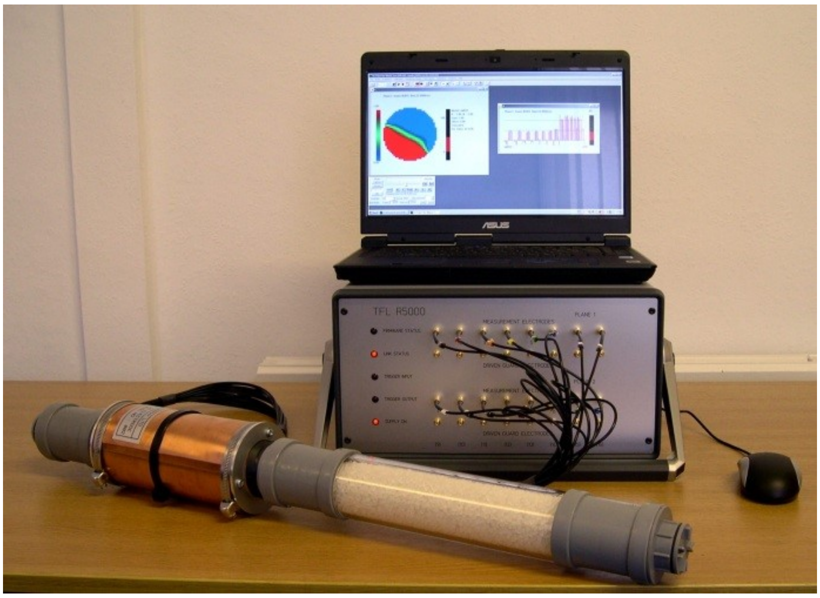

Fig. 3.5 Electrical Capacitance Tomography (ECT) sensor components (courtesy of PTL).

Where C is the capacitance, $\epsilon(x, y)$ is the permittivity distribution and $\phi(x, y)$ is the voltage field distribution and Γ is the electrode surface area. This equation is ill-posed because the change in permittivity distribution is very sensitive to a small change in the capacitance values; which maximises errors from the noise. In addition, there are much lesser independent number of measurements (28 for 8 electrodes) for the number of output values needed(32×32 pixels).

There are three major challenges with the image reconstruction in the ECT system [189]. First issue is the inherent non-linearity of the capacitance and permittivity relationship and the associated deformation of the electrical field by the sensed materials themselves.

Secondly, there are limited independent measurements which underdetermine the certainty of the permittivity distribution (i.e the number of pixels N is much larger than the number of capacitance readings M). Thirdly, is the inverse problem. Regularisation techniques are used to solve the inverse problem which involves imposing some constrains to generate expected values for the permittivity distribution (g) from the normalised capacitance matrix (λ). The solution of the inverse problem can be expressed as

$$g = \lambda S^{-1} \tag{3.3}$$

However the sensitivity (S) matrix is never invertible. That is because there is no enough information to uniquely determine the solution. In geometrical terms the sensitivity matrix has zero eigenvalues that makes the inversion non-existent.

3.3.2 The Wire Mesh Sensor (WMS)

There are two versions of the wire mesh sensor (WMS); conductivity WMS and capacitance WMS (CapWMS). The conductivity measurement is applicable only in the presence of at least one continuous conductive phase (exclusively used for steam, water systems). It was originally developed by Prasser et al (1998) [146]. On the other hand, the capacitance WMS was developed by Da Silva et al (2007) [51] to accommodate measurement of multiphase systems with dialectic materials. The WMS provides high spatial and temporal resolution information of the phase distribution in the pipe cross-section. It discriminates between phases based on the permittivity difference between them. It is available in different sizes, the one employed in this study comprises of two planes of 32 stainless steel wires distributed equally across the pipe cross-section. The wires are only 0.25 mm in diameter, they are spaced by 3.85 mm distance from each other. The two planes are oriented perpendicular to each other and positioned about 2.8 mm apart.

The sensor measures the permittivity of the material in between the crossing points of the sensor. That is achieved by frequently sending multiplexed sinusoidal voltage signals from the emitting electrodes and measuring the current in the receiving electrodes in the second wire plane [146]. It has the ability to provide a spatial resolution of up to 4 mm and temporal resolution of up to 10000 frames per second [51]. However, the 32×32 resolution for 127 mm diameter size is about 4 mm whereby 820 pixels will be obtained per frame [162]. A photograph of the wire mesh sensor is shown in the Figure 3.6 below.

The electronics are arranged in a way at which the cross-talk between the electrodes is suppressed whereby only the signal from the activated cross point is received. That was achieved by designing the transmitter outputs and receivers inputs at substantially lower impedance compared to the fluid to be sensed. This will guarantee the best possible spatial resolution to be achieved [146].

The most important feature of the wire mesh sensor is that it does not require image reconstruction algorithms; it is based on direct high speed sensing of the phases based of the local spatial permittivity measurements; which is an exact representation of the permittivity distribution in the pipe cross-section.

Fig. 3.6 The Wire Mesh Sensor mounted on a bar for calibration.

Electronic build of the WMS

The capacitance (C) measured at the crossing points of the electrode wires is directly proportional to the relative permittivity ϵ_r of the material in between the two planes according to equation 3.4

$$C = \epsilon_r \epsilon_o k_g \tag{3.4}$$

Where ϵ_o is the vacuum permittivity and k_g is a geometry factor. If the crossing points are approximated as square plate capacitors of length equal to wires spacing (l) with the material in between the two plates the shape factor can be approximated by $k_g = \frac{l^2}{d^2}$ and d is the distance between the two planes. The electronics must be able to detect very small capacitance values in the order of femtofarads to be able to discriminate phases with low relative permittivity values.

The electrodes are activated by an AC voltage signals, however unlike the conductance WMS where the current is converted into a DC signal, the CapWMS receives the current and treats it in an excitation AC scheme. The receiving electrodes measure the current from the excitation electrodes that are connected to an amplifier that converts the currents into voltages, which are in turn converted to DC signals through a logarithmic detector (V_{log}). The DC signals are then transformed to a digital format and sent to the computer for storage and visualisation. Figure 3.7 below shows the different electronic components of the capacitance WMS.

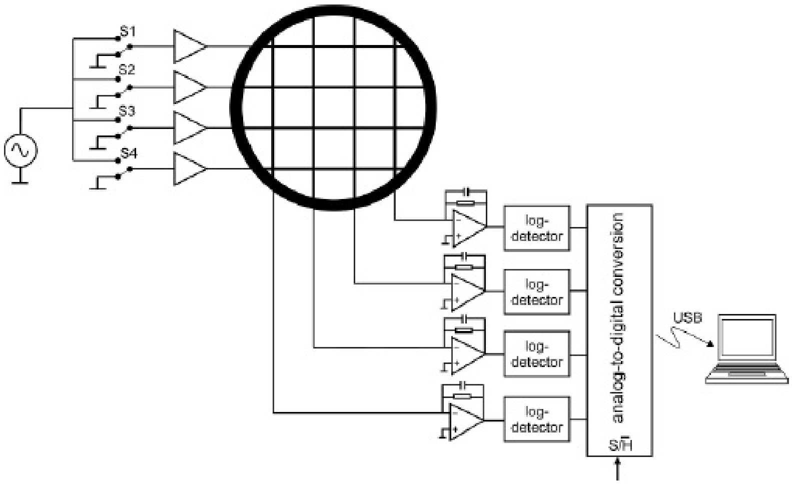

Fig. 3.7 A schematic representation of a 4×4 CapWMS electronic circuitry from [51].

The raw data is stored in the form of two dimensional matrix with the values of measured voltages over the cross-section. The raw data is then further processed to calculate the permittivity distribution in the cross-section via equation 3.5 below

$$C = \frac{V_b e^{\frac{v_{log}}{V_o}}}{|V_i|} C_f \tag{3.5}$$

Where C is the change in capacitance, V_a, V_b are constants determined experimentally, C_f is the feedback network capacitance, V_o is the voltage output and V_{log} is the log detector output.

Calibration procedure

Due to the differences in the characteristics of the sensors electrical elements; the measurements will vary in each crossing point. This can be mitigated through the application of calibration routine for the sensor measurements. The sensor will first be fully covered with the low permittivity material and a matrix will be obtained and averaged in all the crossing points to obtain V^L, then it is filled with the high permittivity material and another matrix is obtained and averaged to get V^H. For each measured voltage matrix V_o the corresponding local void fractions $\alpha(i,j,k)$ is related according to equation 3.6 below

$$\alpha(i,j,k) = \frac{V_o(i,j,k) - V^L(i,j)}{V^H(i,j) - V^L(i,j)} \tag{3.6}$$

Where i,j are the crossing point indices, k is the temporal notation. This relationship in equation 3.6 is a linear simplification as the sensing cross-points are considered as parallel plate capacitors. Da Silva et al (2007) calculated the sensor uncertainty based on the uncertainty of voltage measurements as a maximal value of $\pm 0.52\%$ [51].However, the overall uncertainty of the sensor is reported to be less than 10% [168].

To find the appropriate settings for the gain and offset values for calibration the pipe needs to be inclined by 45 degrees, to cover half of the WMS section in the liquid and the other half will be filled with air. Trial and error for gain and offset values to set the voltage bars minimum to 10% the maximum of 90% for full liquid. These are set to prevent saturation of the electrodes. Otherwise the pipe will need to be filled and emptied several times to calibrate [162].

Droplets of liquid remain on the wires should be cleaned by compressed air in open systems. Calibration should be at least repeated twice for every set of measurements for WMS. This is because the permittivity varies with temperature [162].

Visualisation of the WMS results

- Spatio-temporal images of phase distribution

  WMS produced three dimensional matrix of (32 x 32 x (time x frequency)). Each pixel is an independent measurement of void fraction in the pipe cross-section. The time dimension of the matrix is resolved into an equivalent spatial length of the pipe by the knowledge of pitch size and the structure velocity calculated by cross-correlating time series of void fraction obtained from the neighbouring ECT sensor in addition to the acquisition frequency. The images are produced by selecting the middle frame of the cross-section and resolving it over equivalent axial distance. Figure 3.8 below shows an example of the produced results.

- Three-dimensional contours of gas-liquid interface

  These projections are obtained using ray-tracing algorithms in which illumination of parallel light is assumed and then light intensity is calculated in the direction of the virtual observer [52]. An example image obtained using the framework software supplied by HZDR is shown in Figure 3.9.

- Time series of cross-sectionally averaged void fraction

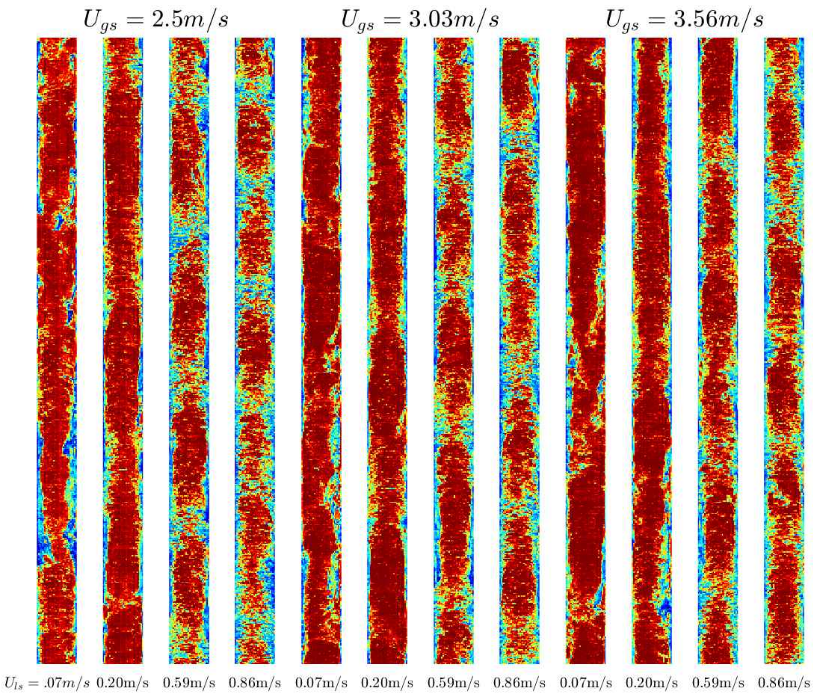

Fig. 3.8 Spatio-temporal images generated by the WMS.

Fig. 3.9 3D contours of the gas-liquid interface obtained from the WMS data [26].

Time series of void fraction measurements by averaging the void fraction in space. Cross-sectionally averaged and temporal averaged void fraction can also be calculated by taking the time average of time series.

Bubble sizes can be measured by integrating the local void fraction of the area occupied by the bubble. Single bubbles can be described in terms of shape and orientation by 3D image-processing algorithms[147]. Three plane WMS could be used for bubble velocity measurements using the cross-correlation technique.

The minimal bubble size that WMS can measure is determined by the spacing between the electrode wires. For the current arrangement in the 32×32 sensor, the smallest bubble can be detected is 4 mm in size [162].

Intrusiveness of the WMS

The WMS wires are made of uncoated stainless steel of 0.25 mm diameter which occupy about 2-3% of the pipe cross-section. This will result in a very small pressure drop. Higher resolution of the WMS can be obtained by employing more wires in the sensor. This however will intensify the obstruction of the flow by the sensor [162].

Prasser et al (2001) [147] investigated the intrusive effects of the WMS by detecting single bubbles flowing through the mesh using high speed camera. It is found that the mesh causes significant fragmentation of bubbles as they cross the sensor wires. However, the captured image would still represent the distribution of bubbles before fragmentation had taken place. Also, as the size of fragmented bubbles increase the effectiveness of coalescence become more significant and the initial bubble shape would be restored. The intrusive effect also includes deceleration of bubbles induced by the pressure drop in the sensor planes [147].

Hardware set-up of the WMS

The CapWMS box has four receivers ports and four excitation electrodes ports too. This box enables the acquisition of data from two sensors or a three plane sensor. The sensor should be connected to the appropriate ports in the box as shown in Figure 3.10 below. The box is connected to the computer via a specially configured Ethernet cable (cross-over) using a dedicated IP address.

CapWMS data acquisition and saving takes place in two consecutive stages which increases the risk of data loss, it is also a time consuming process. The CapWMS employed in this study cannot be externally triggered, but it can generate a triggering

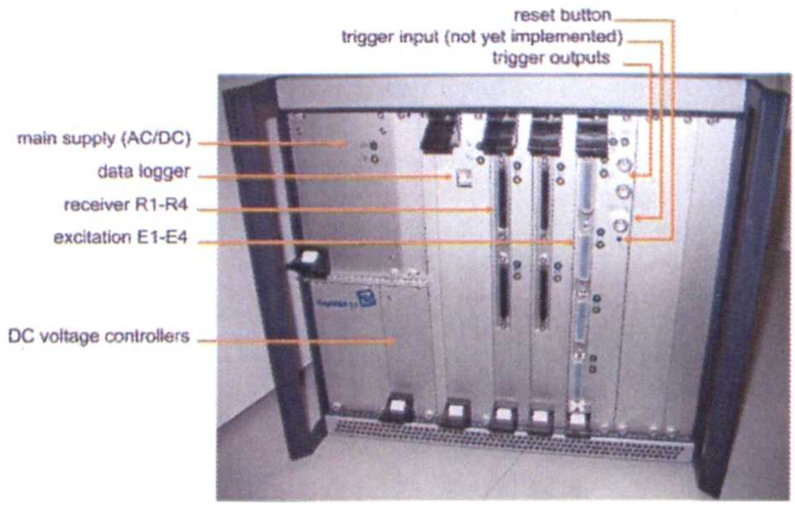

Fig. 3.10 CapWMS data acquisition and processing unit[162].

signal for the ECT and the NI device to acquire the readings simultaneously [26]. The triggering function is controlled by the CapWMS software interface.

3.4 Fluids characterisation

The fluids used are air for the gas phase from the laboratory high pressure lines (100 psi). Typical air density is 1.204 kg/m^3 and kinematic viscosity is 0.0015 mm^2/s at the normal conditions. Polydimethyleseloxane (PDMS) Silicone oils of varying viscosities have been used.Table 3.2 below shows the physical properties measured in the fluids characterisation lab. It must be noted that throughout the experimental campaign, the temperature variation is kept below $\pm 2^oC$. The lab tests indicates that the corresponding variations in density, viscosity, and surface tension relating to temperature change are very minimal and can therefore be neglected.

Table 3.2 Measured physical properties of liquids used in this thesis.

Fluid Name	Density $\left(\frac{kg}{m^3}\right)$	Dynamic Viscosity $\left(cP\right)$	Surface tension (mN/m)
5 cSt silicone oil	915	4.04	19.32
25 cSt silicone oil	921	25.35	19.53
50 cSt silicone oil	924	51.10	19.90
100 cSt silicone oil	925	104.58	19.98

3.5 Data management plan

The data presented in this thesis is jointly owned by The University of Nottingham and the Transient Multiphase Flow (TMF) consortium. The time averaged void fraction and pressure gradient information will be made available for all the future publications from this work after approval by the consortium. Regarding 3D transient void fraction data from the WMS, it can be made available via the online repository of The University of Nottingham subject to the approval of the consortium.

Chapter 4

Effect of viscosity on two phase flow in a vertical large diameter pipe

4.1 Introduction

High viscosity hydrocarbons have gained more attention owing to the increasing energy demand around the world and depletion of lighter reserves. When gas and liquid are introduced into a pipe, both phases arrange themselves in very random structures, as a result of interaction of very complex dynamic forces. These forces are heavily dependent on the physical properties of the fluids being handled.

Little is known about two-phase flow characteristics in large diameter vertical pipes. Even less is known about the effect of viscosity on these characteristics. Limited number of investigations have been carried out to try to understand this effect. Regrettably, most of these investigations are either carried out using water solutions where surface tension changes dramatically with the change of viscosity (i.e. concentration of the solute). Or that the experiments are conducted in smaller diameter pipes, where the characteristics are remarkably different than larger diameters to the extent that one flow regime (slug flow) is considered non-existent in large diameter pipes (D>100 mm) [135]. Therefore most of published parametric studies are not conclusive and hence the confusion amongst the scientific community about the actual effect of viscosity on two phase flows. Some studies suggest that viscosity increase results in a decrease of void fraction [187, 103, 63], other group argued the opposite [172, 79], and a third group reported both negative and positive influence on void fraction [32, 143, 182, 151, 137].

Therefore, a solid experimental understanding of these effects on flow characteristics is essential; for the improvement of modelling and establishment of closure laws for commercial simulation packages. Moreover, the data generated extends to serve as a benchmark data for the validation of computational codes, improvement of mechanistic and phenomenological models, optimising performance and design of facilities, and safe operation.

4.1.1 Background and review

Two phase flows in vertical pipes has been extensively investigated both theoretically and experimentally. However, most of these investigations were focused on low viscosity flows. A lot of the earliest studies of viscous flow were focused on horizontal flows [119, 185, 174, 17, 131]. Until very recently more studies were published on horizontal flows [66, 120, 109, 29, 58]. Very limited work was published on viscous flow in vertical pipes.

Fukano and Furukawa (1998) studied the effect of viscosity on interfacial shear stress and pressure drop in annular flow in a 26 mm pipe . They found that average film thickness increases with increasing viscosity. It was also found that with increasing viscosity interfacial friction factor increases. Correlations were proposed for prediction of film thickness and frictional pressur drop [62]. Furukawa and Fukano (2001) studied viscosities in the range of (1-17 cP) in a 19.2 mm pipe. They observed that as viscosity increases, both lengths of large bubbles and that of the liquid slugs decrease. The study confirmed the increase of film thickness with viscosity reported by [62]. It was also observed that as viscosity rises, the size of entrained bubbles in liquid film and slug decreases but their concentration increases. The study also reported that the interface becomes more stable and less wavy with increasing viscosity. However, the opposite was observed for annular flow regime. As viscosity increases, more liquid gets transported through the liquid film, as opposed to large waves on the interface at lower viscosities. It was also reported that large bubbles develop faster as viscosity increases. On the transition of flow regimes, it was reported that transition from bubbly to slug flow move towards lower gas superficial velocity as viscosity increases, however transition from churn to annular flow shifts to higher gas superficial velocity [63].

McNeil and Stuart (2003) investigated flow characteristics for five viscous oils ranging from (1-550 cP) in a 26.12 mm pipe. They developed a new correlation for the estimation of interfacial friction factor. However, in contradiction to what was observed by [63], it was found that interfacial friction factor decreases with increasing viscosity [121]. Da Hlaing et al (2007) studies pressure drop using two viscosity fluids (1-4.5 cP) in a 19 mm pipe. Higher pressure gradient was registered as viscosity increases due to higher wall shear stress in agreement with the results of [121]. Also trasnsition from bubble to slug flow was observed to shift towards higher gas superficial velocity as viscosity increases whereas transition to churn and annular flows was found not to be much affected [50].

Schmidt et al (2008) carried out 87 runs on viscous flow in a 54.5 mm pipe using both water and water-polyvinylpyrodine solution covering viscosities ranging from (1-6880 cP). Average void fraction was reported to decrease with increasing viscosity. the study proposed a modified drift flux correlation for void fraction in higher viscosities and another based on slip ratio. Radial distribution of void fraction was approximated assuming symmetry in the pipe. Core peaking of void fraction was observed, core peaking was reported to be more pronounced with increasing gas superficial velocity [159]. Szalinski et al (2010) studied viscous flow a 67 mm pipe using water and 5 cP silicone oil. The study showed that void fraction increases with increasing viscosity. Bubble size distribution (BSD) obtained from the WMS suggested that coalescence rate decreases with viscosity, therefore smaller bubbles were observed at higher viscosity. The BSD also revealed that small diameter bubbles peak shifts towards bigger size with increasing viscosity [172]. However, difference in characteristics between the two viscosities might not be solely a viscosity effect, because the surface tension for water is 3.6 times that of silicone oil.

Alamu (2010) studied viscous flow in a 5 mm vertical pipe employing water and water-glycerol solutions featuring viscosities of (1, 10, and 12 cP). Their study concluded that viscosity increase lowers average void fraction and increases frequency and velocity of gas structures. They also observed that transition boundaries shift towards lower gas superficial velocity with increasing viscosity. They proposed a drift flux model to predict the structure velocity [11]. Hewakandamby et al (2014) investigated viscous flow in a large diameter pipe using water and glycerol solution covering viscosities in the range of (1-16.2 cP). The study showed that average void fraction increases with increasing viscosity. It was also reported that the liquid film becomes thinner as the viscosity increases contrary to what was observed by [62]. The WMS results also revealed that in churn flow larger entrained liquid structures in the gas core are formed as viscosity increases [79].

Alruhaimani (2015) studies viscous flow in a long 50.8 mm pipe using Lubsoil (DN-50) employing quick closing valves and capacitive wire sensors. The oil viscosity was changed from (586-127 cP) by varying the temperature of the oil using an integrated heater on the rig. Some of the findings were later published in [10]. The study came in agreement with [62, 63] regarding decrease of slug length and increase of pressure drop with increasing viscosity. The slug-churn and churn-annular transitions were reported to shift towards lower gas superficial velocity as viscosity increases [14].

Vieira et al (2015) carried out experimental study on annular viscous flow in a 67 mm pipe, using water-methyl cellulose solution covering viscosities in the range of (1-40 cP). The study reported increase of void fraction as viscosity is increased from 1 to 10 cP then void fraction was reported to exhibit a significant decrease as viscosity increases to 40 cP. Also, structure frequency was found to be higher at higher viscosities [182]. Parsi et al (2015) studied similar range of viscosities in a similar facility in the churn flow region. The study showed that average void fraction first increases, then decreases with the increase of viscosity. The frequency of liquid slugs was reported to decrease with viscosity. Characteristic slug shape of void fraction PDF was recorded, however no Taylor bubbles were observed. Increase in viscosity was reported to increase liquid slug frequency, however huge waves' frequency was found to decrease [143].

Table 4.1 below shows a summary of the studies published on viscous flow in vertical pipes.

Table 4.1 Summary of previous investigations on viscous two-phase flows in vertical pipes

Reference	Liquid Type	Liquid Viscosity (cP)	Liquid Density (kg/m3)	Liquid Surface Tension(N/m)	Gas Type	Gas Density (kg/m3)	Pipe Diameter(mm)	Velocities (m/s)	Measured Values	Notes
Fukano & Furukawa (1998) [62]	Water	0.85	998	0.072	Air	-	26.0	$U_{gs} = 10 - 50$	Void fraction	Atmospheric pressure
	45wt% Glycerol-water	3.8	1113	0.065		-		$U_{ls} = 0.04 - 0.3$	High speed images	
	53wt% Glycerol-water	6.4	1149	0.062					Film thickness	
	60wt% Glycerol-water	10.0	1159	0.066					Interfacial friction factor	
Furukawa & Fukano (2001) [63]	Water	1	1000	0.072	Air	-	19.2	$U_{gs} = 0.05 - 40.0$	Time-spatial map	Pressure 0.15MPa
	53wt% Glycerol-water	6.4	1125	0.065				$U_{ls} = 0.1 - 1.0$	Still photographs	
	72wt% Glycerol-water	17.2	1172	0.062						
McNeil & Stuart (2003) [121]	Water	1	1000	0.072	Air	-	26.12	$U_{gs} = 22 - 120$	Void fraction	$U_{ls} = 0.2 - 4.2$
	Glycerol-water	50	1190	-		-		$U_{gs} = 22 - 100$	Pressure drop	
	Glycerol-water	200	1235	-				$U_{gs} = 17 - 96$	Interfacial friction factor	
	Glycerol-water	550	1260	-				$U_{gs} = 12 - 110$		
Da Hlaing et al (2007) [50]	Water	0.85	1000	-	Air	-	19.0	$U_{gs} = 0.0021 - 58.7$	Pressure drop	Pressure = 1bar
	50vol% Glycerol-water	4.5	1121	-		-		$U_{ls} = 0 - 0.1053$	Flow imaging	
Schmidt et al (2008) [159]	Water	1.0	997	-	Nitrogen	-	54.5	$U_{gs} = 0 - 30$	Void fraction	87 runs
	water and Polyvinylpyrolidone	900-6880	1054.3-1094.3	-		-		$U_{ls} = 0.005 - 3.4$	Radial void distribution	Gamma densitometry
Szalinski et al (2010) [172]	Water	1.0	1000	0.072	Air	-	67.0	$U_{gs} = 0.05 - 5.7$	Void fraction	Bubble size distribution
	Silicone oil	5.25	900	0.02		-		$U_{ls} = 0.2 - 0.7$	Radial void distribution	WMS
Hewakandamby et al (2014) [79]	Water	1	998	0.068	Air	2.35	127.0	$U_{gs} = 3.26 - 17.46$	Void fraction	WMS
	Glycerol-water	12.2	1152	0.064				$U_{ls} = 0.03 - 0.24$	Diametrical void distribution	
	Glycerol-water	16.2	1166	0.061						
Alruhaimani (2015) [14]	Water	-	-	-	Air	-	50.8	$U_{gs} = 0.5 - 5.0$	Void fraction	Temp changed to change μ
Al-Sarkhi et al (2016) [10]	DN-50 oil	127-586	884.4 @25^oC	0.036 @19.8^oC		-		$U_{ls} = 0.05 - 0.70$	Pressure drop	from $21 - 49^oC$
Vieira et al (2015) [182]	Water	1	-	-	Air	76	76.0	$U_{gs} = 10 - 40$	Void fraction	WMS
	Water-Carboxy Methyl Cellulose (CMC)	10	-	-				$U_{ls} = 0.005 - 0.1$	Structure velocity	
	Water-Carboxy Methyl Cellulose (CMC)	40	-	-						
Parsi et al (2015) [143]	Water	1	-	-	Air	76	76.2	$U_{gs} = 10 - 27$	Void fraction	WMS
	Water-Carboxy Methyl Cellulose (CMC)	10	-	-				$U_{ls} = 0.46 - 0.76$	Structure velocity	
	Water-Carboxy Methyl Cellulose (CMC)	40	-	-						

4.1.2 Objectives

The studies mentioned in the earlier section demonstrate the contradictory findings on the effect of viscosity on the two phase flow characteristics. These contradictions can be attributed to two main aspects, one major problem is the negligence of the effect of surface tension. As many of the aforementioned works managed to successfully vary viscosity within a wide range, surface tension did change dramatically and therefore the parametric study cannot be conclusive to whether the change happened due to viscosity or surface tension or density change. The second attribute can be referred to the high dependency of multiphase characteristics on geometrical parameters. In the instance of flow in vertical pipes, it is mainly the pipe diameter. It is evident that flow characteristics are highly dependent on diameter [27, 135, 163, 149, 77]. Therefore, mechanistic and phenomenological models deduced for small diameter pipes cannot be easily extrapolated to conditions in large diameter flows without sacrificing much accuracy. In some instances the physical characteristics are entirely different and may lead to catastrophic decisions if small diameter models are used.

None of the studies reviewed in the previous section was conducted in a large diameter pipe (D>100 mm) except the one by [79]. However, their experiments did not cover a large range of viscosities. In addition, due to the fact that surface tension of water is more than 360% that of petroleum oils, the characteristics could be remarkably deviant to conditions in oil and gas industry. This chapter will therefore present a novel parametric study on the effect of viscosity in a vertical large diameter pipe. In this chapter experiments conducted in a 127 mm ID, 10.12 m vertical pipe will be presented using Polydimethylsiloxane (PDMS) silicone oil of varying viscosities and air. Four different viscosities were studied, namely 4.04, 25.35, 51.10, and 104.58 cP. The significance of these experiments lies in the fact that that only the viscosity is varied while the other physical properties of the liquid remained virtually constant. The influence of viscosity on flow characteristics will be presented in terms of:

- Transient effect on void fraction and pressure drop
- Time-averaged effect on radial and axial void fraction evolution
- Influence on pressure drop
- Effect on structures, their shapes,3D reconstruction of phase distribution
- Frequency and velocity of structures, comparison with high speed flow
- Flow regimes (moving boundaries as f(D, μ, etc) and transitions)
- Bubble size distribution.

4.2 Results and discussions

4.2.1 Experimental matrix

180 runs were obtained for each viscosity in the range of gas superficial velocity (U_{gs}) of 0.01-5.40 m/s, and liquid superficial velocity (U_{ls}) in the range of 0.07-0.86 m/s. The experimental matrix is shown in Figure 4.1 plotted on the flow regime map of Taitel et al (1980) [173]. A total of 720 experimental runs are reported in this chapter.

4.2.2 Effect of viscosity on the dynamic behaviour of void fraction

Transient behaviour of two phase flows may not be very useful for design purposes, however it is of very critical importance for validation of CFD models and control/operation of facilities where two-phase flows are encountered. This section discusses the effect of viscosity on the transient behaviour of both void fraction and pressure drop.

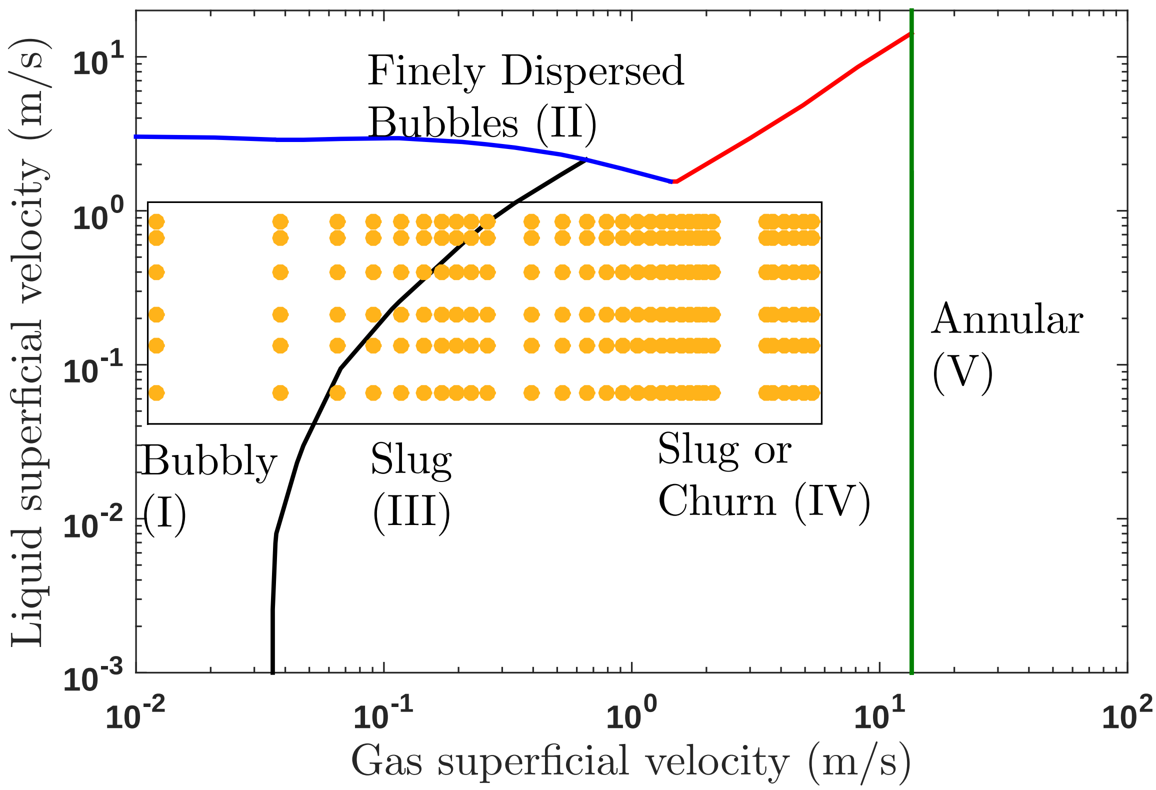

Fig. 4.1 Experimental matrix plotted in the flow regime map of Taitel et al. (1980) [173].

Effect on cross-sectionally averaged void fraction time series

Time series of void fraction often gives a very clear indication of the incurring flow regime in the pipe. It will also be used later for calculating the frequency and lengths of the flow structures. In this section the shape of time series upstream and downstream of the test section will be discussed. The discussion will be focussed on how the shape of the time series evolves with the change of gas and liquid momentum and also the viscosity. The issue of flow development will be discussed by comparing the time series upstream and downstream the pipe. Moreover, from the shapes of void fraction time series this section will also reveal how flow development is affected by liquid viscosity.

Figure 4.2 shows void fraction time series obtained at 15D axial position from the injection point for 8 different gas superficial velocities at a constant liquid superficial velocity (U_{ls}=0.21 m/s. The Figure shows the time series for the four viscosities. The general trend of increasing average void fraction with increasing gas input can be observed. It can also be observed that at higher viscosity in the low gas superficial velocity range, the peaks of time series become very well defined (i.e. the difference between the peak and average void fraction becomes bigger). This suggests that gas bubbles trapped in the liquid bulk are smaller in size and/or concentration whilst the gas structures are bigger. Furukawa and Fukano (2001) reported smaller bubble size and higher concentration at higher viscosity [63]. However this difference seems to decrease with increasing gas superficial velocity although at the highest gas superficial velocity (4.93 m/s) this higher difference can still be observed. A similar behaviour was observed in the published time series by [182] for 40 cP water-glycerol solution, it was explained as transition to slug flow had occurred. However, since this behaviour seems consistent in all the regimes/velocities covered here, it can be referred to the fact that higher viscosities stabilises large gas structures and the interface, resulting in formation of larger gas structures and less entrained bubbles in the liquid bulk. Which could also be linked to the previous reports that higher viscosity shifts breakup-coalescence balance towards enhanced coalescence and therefore larger gas structures and less presence of smaller bubbles in the liquid bulk, in concordance with the works of [103, 172].

One more information to be extracted from the time series is that the void fraction in liquid bulk is always lower at higher viscosity. On the other side, void fraction seems to be higher in gas structures only at the lower range of gas superficial velocities (0.01-0.66 m/s), it remains virtually the same at the higher range of gas velocities. This suggests that the gas-structures/bubbles grow to a certain size until they occupy the cross-section of the pipe then any increase in gas input will contribute to the growth of the gas structures lengthwise rather than in width. The influence of gas input increase on liquid film around these structures becomes almost negligible.

The peaks at the lower range of gas superficial velocities (0.01-0.66 m/s) could be representative of either cap-bubbles or large zig-zag bubbles that are produced in the flow in the undistributed bubbly regime. These bubbles rise in swirling trajectories and create a lot of smaller bubbles in their wakes. Eye observation during experiments showed that these bubbles also introduce a lot of gas-induced turbulence that breaks down bigger/medium size bubbles in their wakes, unless they become distantly spaced at higher viscosities. High speed imaging could provide more information about the behaviour of bubbles in this regime. It is observable that the size of these bubbles/gas-structures increases with increasing gas superficial velocity. Also, it can be noted that the peaks are regular and more defined at higher viscosity, they become inconspicuous and random as the viscosity decreases.

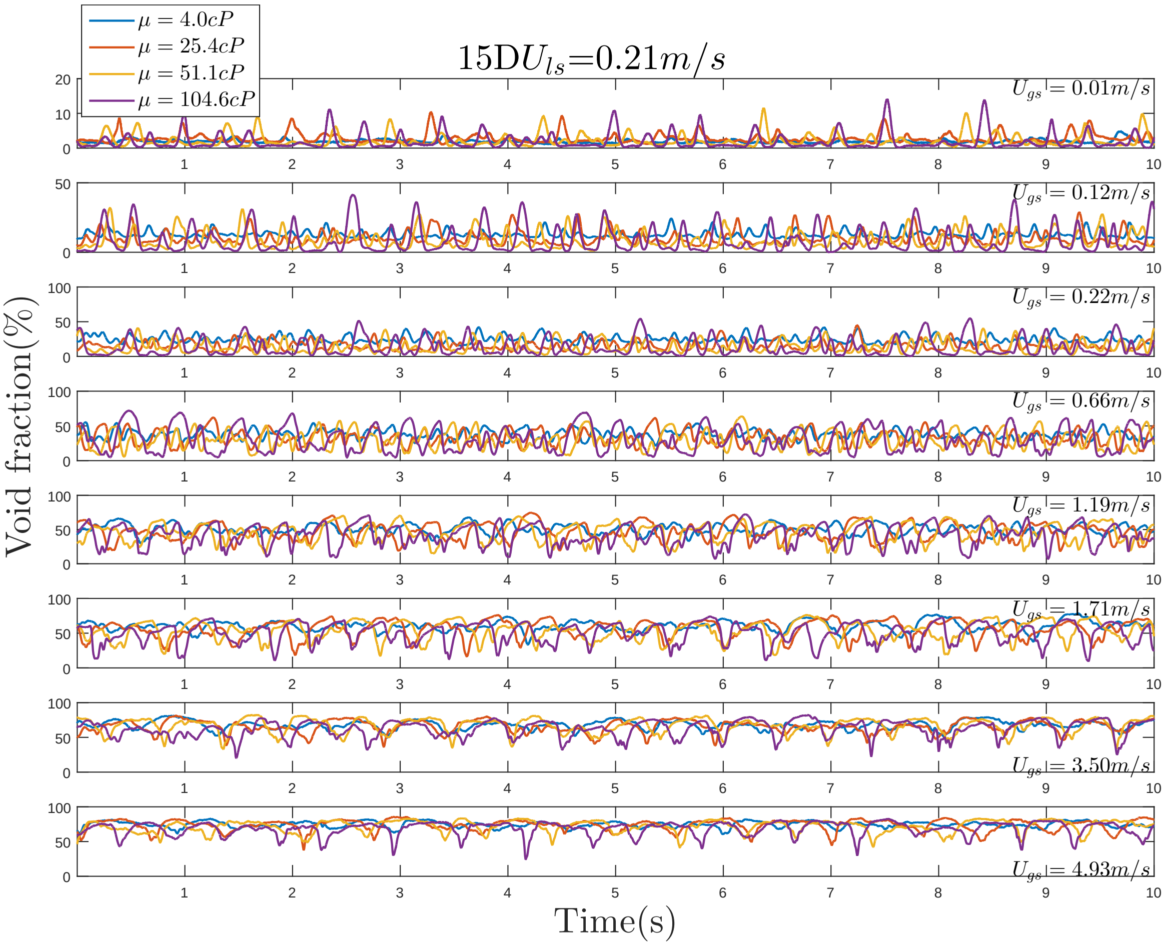

Fig. 4.2 Void fraction time series obtained at 15D axial distance from the injection point plotted for the four viscosities (4.0, 25.4, 51.1, 104.6 cP) at $U_{ls} = 0.21\,m/s$ for 8 gas superficial velocities.

It is hard to judge the frequency of structures from Figure 4.2 especially for lower liquid superficial velocities. This is because in bubbly flow region the time series frequency is representative of smaller bubbles that have higher frequency. Also for lower viscosities the peaks are very obscure and hard to identify. But generally the number of peaks seems to increase slightly with increasing viscosity. For instance, frequency of troughs for U_{gs}=4.93 m/s registers 1.9 Hz for 104.6 cP viscosity while it is 1.6 Hz for 4.0 cP. This will be discussed in detail in the frequency section of this chapter.

Figure 4.3 and 4.4 show the effect of increasing liquid superficial velocity on the shape of void fraction time series at 4.0 cP and 104.6 cP respectively. It can be clearly seen that average void fraction decreases with increasing liquid superficial velocity. It can also be seen that the frequency of peaks increases with increasing liquid superficial velocity. This suggests that increase in liquid turbulence enhances bubble break-up producing smaller bubbles that register higher frequency. It is also observable that the effect becomes less pronounced at higher gas superficial velocities.

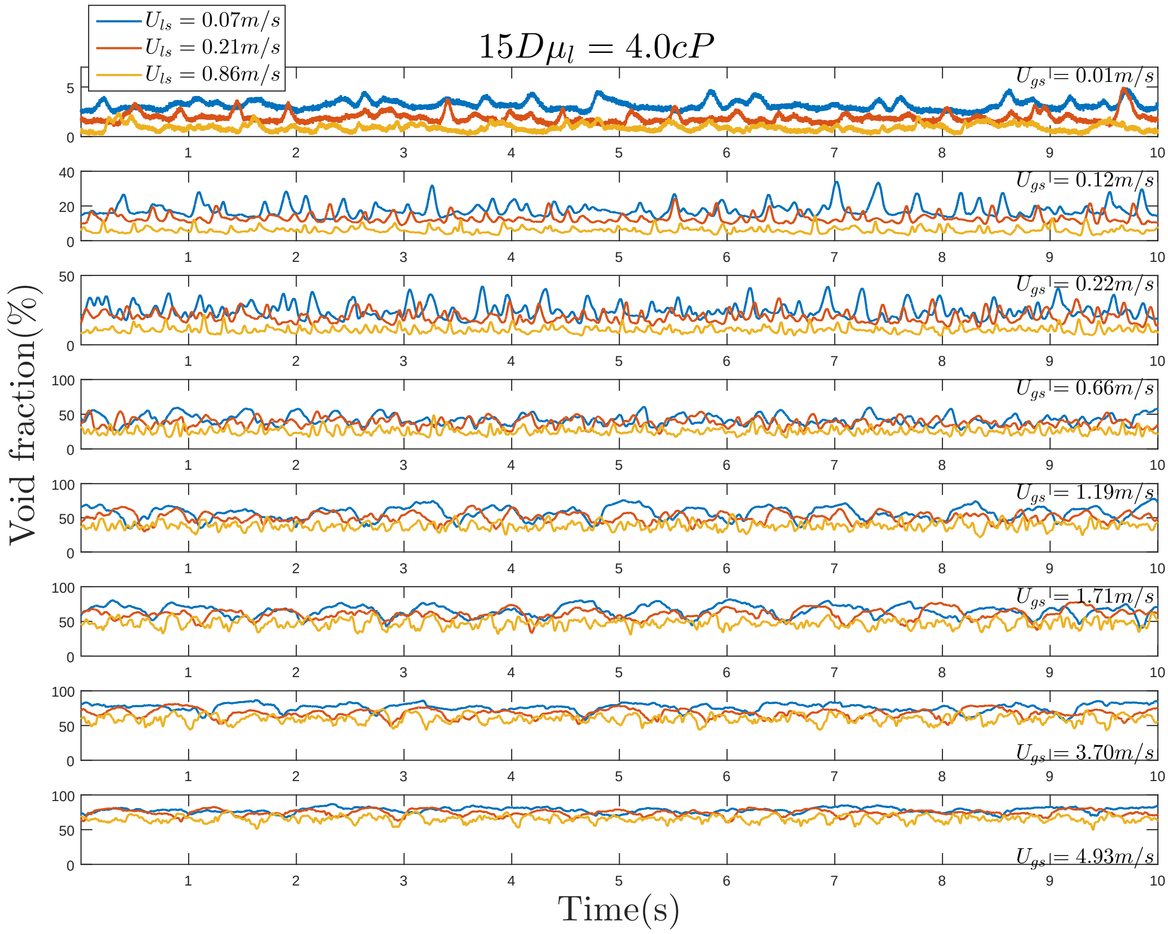

Fig. 4.3 Effect of increase in liquid turbulence on time series of void fraction at 15D axial position for 4.0 cP oil.

Looking at effect at different viscosities, it can be seen that the change in liquid flow has a more pronounced effect at higher viscosities. Looking at Figure 4.4, at lower gas superficial velocities (0.01-0.22 m/s) the effect of increased liquid flow seems to affect the peak heights (i.e. bubble/gas-structure size) and has negligible effect on the liquid bulk average void fraction. At higher gas superficial velocities increasing liquid flow seems to mainly produce smaller gas-structures with higher frequency.

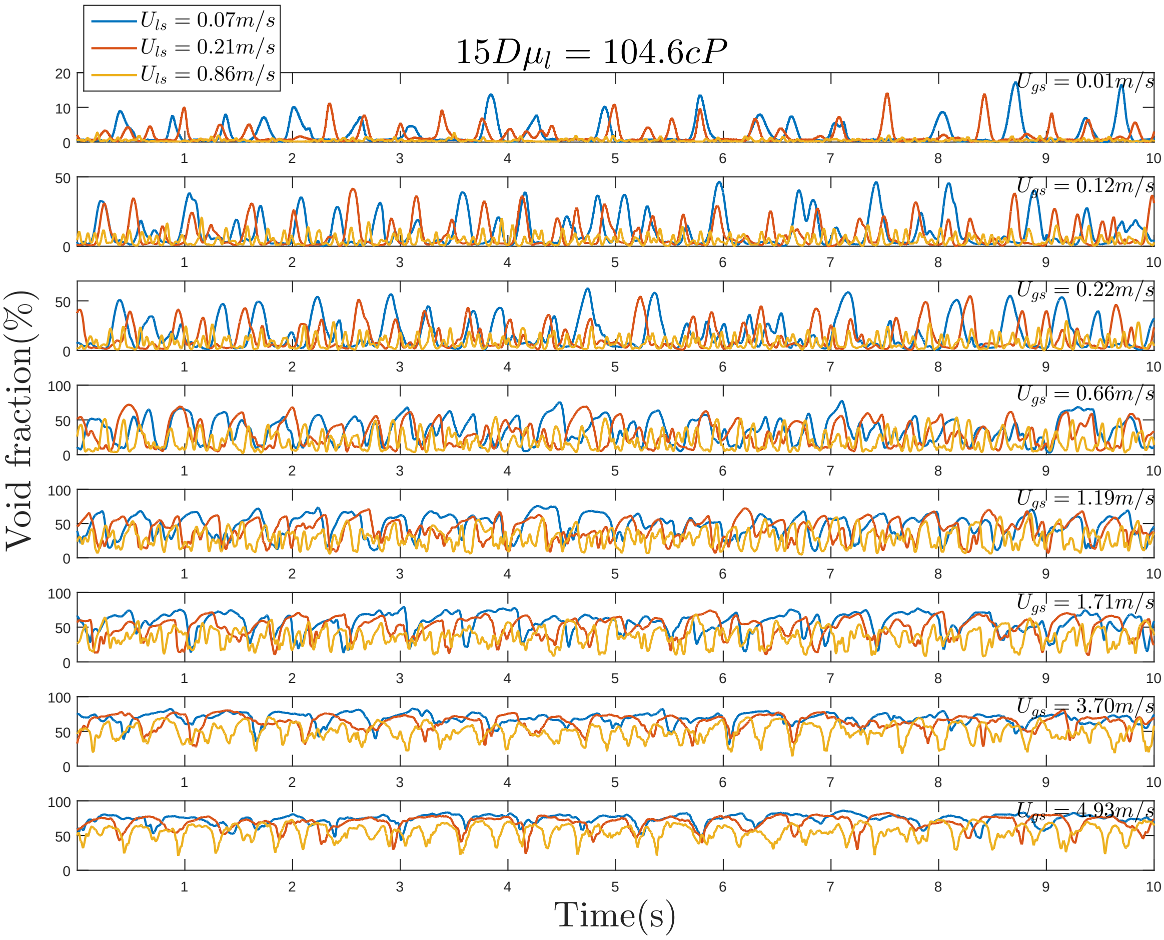

Fig. 4.4 Effect of increase in liquid turbulence on time series of void fraction at 15D axial position for 104.6 cP oil.

Figure 4.5 presents the effect of axial position on void fraction time series. The Figure shows time series obtained at 15D in blue and 62D axial distances from the injection point for 104.6 cP oil. First feature to be observed is the significant decrease in the number of peaks as the fluids rise in the test section. Which can be attributed to the increased coalescence of bubbles as they expand and have more contact time while rising. Average void fraction does not seem to change much, although it increases slightly downstream the pipe due to gas expansion owing to the lower static pressure downstream. These differences in frequency become smaller at higher gas superficial velocities. This can be attributed to the fact that slug flow develops faster and therefore it is very unlikely that two "Taylor bubbles" would coalesce as opposed to large number of smaller bubbles in bubbly flow that coalesce more rapidly in the wake of each other at lower gas superficial velocities.

Similar behaviour is registered for flow at lower viscosities and different liquid superficial velocities to the ones in Figure 4.5. It will be later revealed whether the frequency decrease due to coalescence or expansion is affected by change of liquid viscosity as it cannot be conclusively deduced from the shapes of the time series presented here.

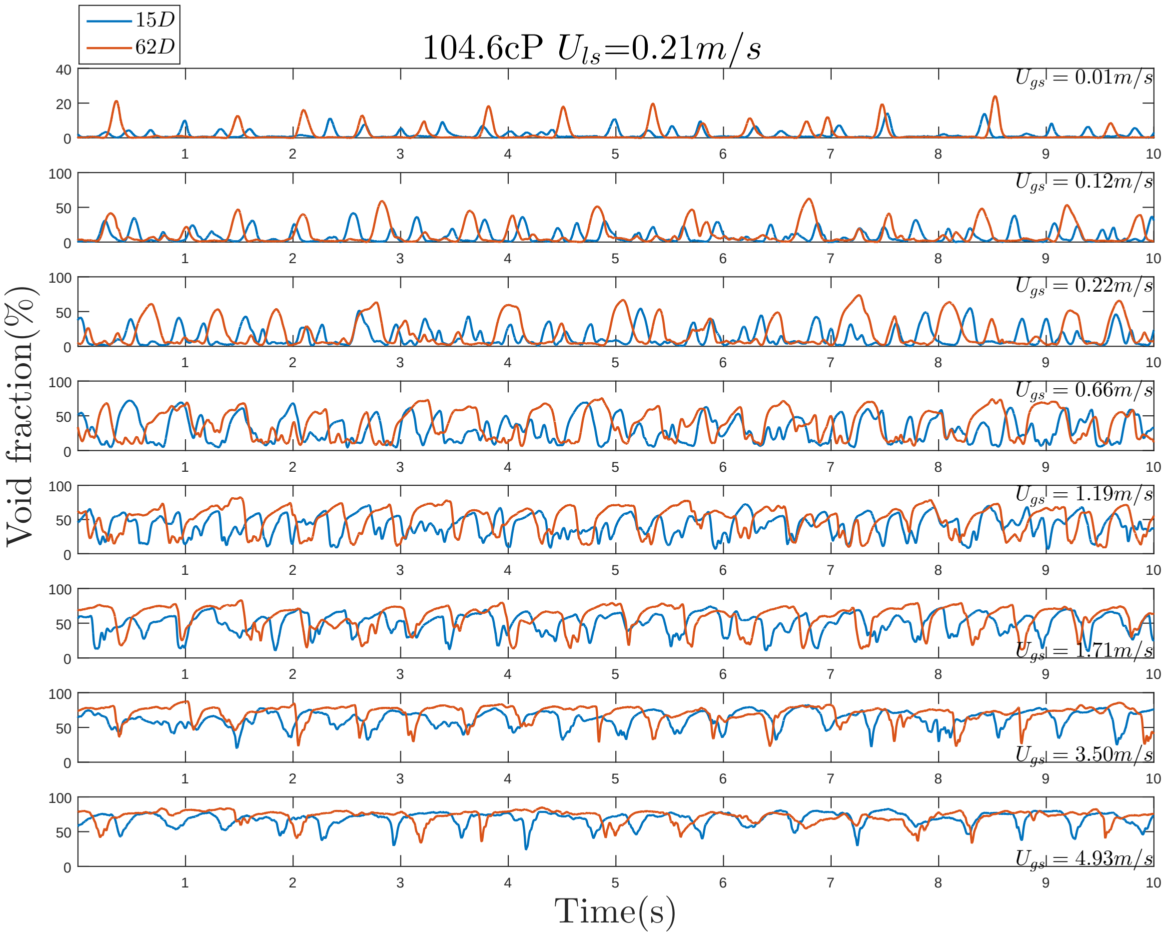

Fig. 4.5 Void fraction time series for 8 different gas superficial velocities plotted at U_{ls}=0.21 m/s for 104.6 cP oil. The figure shows effect of axial position and flow development on the shape of void fraction time series.

The temporal behaviour of the differential pressure signal was found to be mirroring that of void fraction; this is an indication that the flow is gravity dominated whereby the gravitational pressure gradient is responsible for most of the pressure drop. For brevity, the pressure drop time series is not included here.

4.2.3 Effect of viscosity on time averaged axial void fraction

Figure 4.6 and Figure 4.7 show the development of time averaged axial void fraction with gas superficial velocity for 4.0 and 104.6 cP oils respectively. Before discussing the effect of viscosity the figures reflect the general trend of void fraction evolution with increasing gas superficial velocity. It can be seen that void fraction exhibits a parabolic relationship with increasing gas superficial velocity regardless of the viscosity. The Figures demonstrate that the influence of increase in gas input is very high at low gas superficial velocities and decreases gradually with increasing gas input. Moreover it can be seen that the full curve shifts towards lower void fraction with increasing liquid superficial velocity. The behaviour is consistent in all the four studied viscosities, only two extreme viscosity curves are shown here for brevity. The first part of the relationship, up to $U_{gs} = 2.1\, m/s$ can be accurately modelled by a cubic polynomial relationship. The higher range of gas superficial velocities $U_{gs} = 2.1 - 5.6\, m/s$ almost follows a linear trend. This change in behaviour may be linked to change in flow regime, most likely a transition to churn-annular regime where any increase in gas input travels through the gas core and contributes mainly to reducing the liquid film thickness; which has a smaller impact on void fraction. The anomaly observed at $U_{ls} = 0.21 m/s$ is potentially a result of some fluctuation in the gas flowmeter.

At higher viscosities void fraction almost exhibits a similar behaviour (Figure 4.7). Two main distinctions can be spotted out, first is that the void fraction generally exhibits a large drop compared to the case at the lower viscosity. The second discrepancy is regarding the shape of the profile, the "linear" relationship of void fraction with gas superficial velocity noted at higher bound of gas velocities seems less reflected at the higher viscosity. This might be because the flow regime did not develop to the churn-annular regime and form a gas core that causes the linear trend observed for lower viscosity cases. However this cannot be confirmed without examining the spatio-temporal images of flow from the WMS that will be discussed in later sections of this chapter.

Figure 4.7 shows that at low liquid superficial velocities, namely 0.07, 0.13, and 0.21 m/s there is a local bump in the profile. Comparing with Figure 4.6 this is not observed at the lower viscosity. However, it is observed in all the higher viscosities studied (25.4, 51.6, and 104.6 cP). The bump becomes more profound with increasing

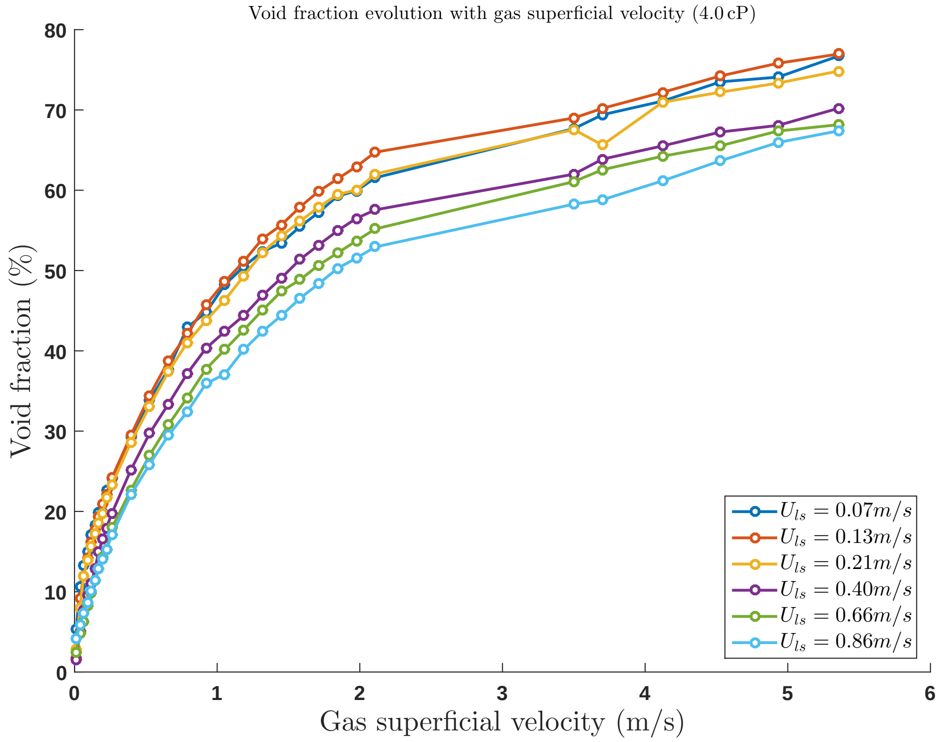

Fig. 4.6 Evolution of average void fraction with gas superficial velocity at 15D axial distance measured using 4.0 cP viscosity oil.

viscosity. This could be associated with transition of flow regime from bubbly to slug flow regime reported before by [69] (refer to Figure 2.7 in Chapter 2). The other likely explanation is a reflection of transition from homogeneous to non-homogeneous bubbly flow regime reported before in [156]. The graphs show that the bump disappears at higher liquid superficial velocities. This might be because at higher liquid turbulence the break-up/coalescence is more dominated by liquid dynamics rather than the gas as it is the case at lower liquid velocities. The anomaly observed at $U_{ls} = 0.07m/s$ is potentially a result of some fluctuations in the gas flowmeter.

Figure 4.8 shows void fraction profiles against gas superficial velocity for the four viscosities studied plotted at a constant liquid superficial velocity in each sub-figure for three different velocities, namely 0.07, 0.21 and 0.86 m/s. It can be clearly noted that lower void fraction is registered as viscosity is increased for the same liquid and gas superficial velocities, as plainly evident by the profiles. Moreover, the discrepancy between the different viscosity profiles seems to lessen with increasing liquid superficial velocity. Which suggests that viscosity effect on void fraction is less significant at higher liquid turbulence level. One more observation to be drawn is that profiles generated

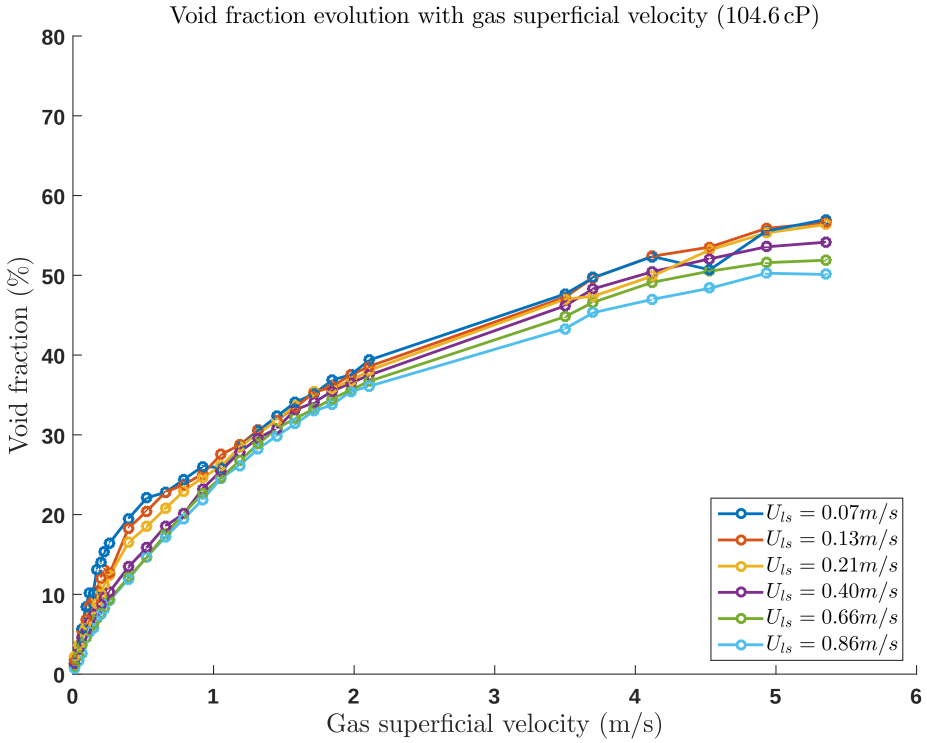

Fig. 4.7 Evolution of average void fraction with gas superficial velocity at 15D axial distance measured using 104.6 cP viscosity oil.

by different viscosities do not cross, but at very low gas superficial velocities. They almost overlap in the case of 25.4 and 51.1 cP viscosities especially at higher liquid superficial velocities.

The crossing of void fraction profiles at low superficial gas velocities is presented in Figure 4.9. It infers that void fraction can increase with increasing viscosity to a certain threshold and then it decreases, a similar observation can be found in [137, 151]. This could be a manifestation of what has been described as the "dual effect of viscosity" where smaller bubbles are generated at lower viscosities in the bubbly flow regime resulting in a higher void fraction. On the other side, higher viscosity encourages formation of stable bigger bubbles and therefore lower void fraction is registered at the same gas input [32]. This might be better explained by considering the effect of increased drag force on the bubbles at higher viscosity, where initially drag effect is more significant on the bubbles due to the high ratio of surface area to volume, with increasing gas superficial velocity and accordingly increasing average bubble size, the drag effect on the bubbles lessens and void fraction eventually falls. The decrease on drag effect can be adhered to two different attributes; first is the decreased average

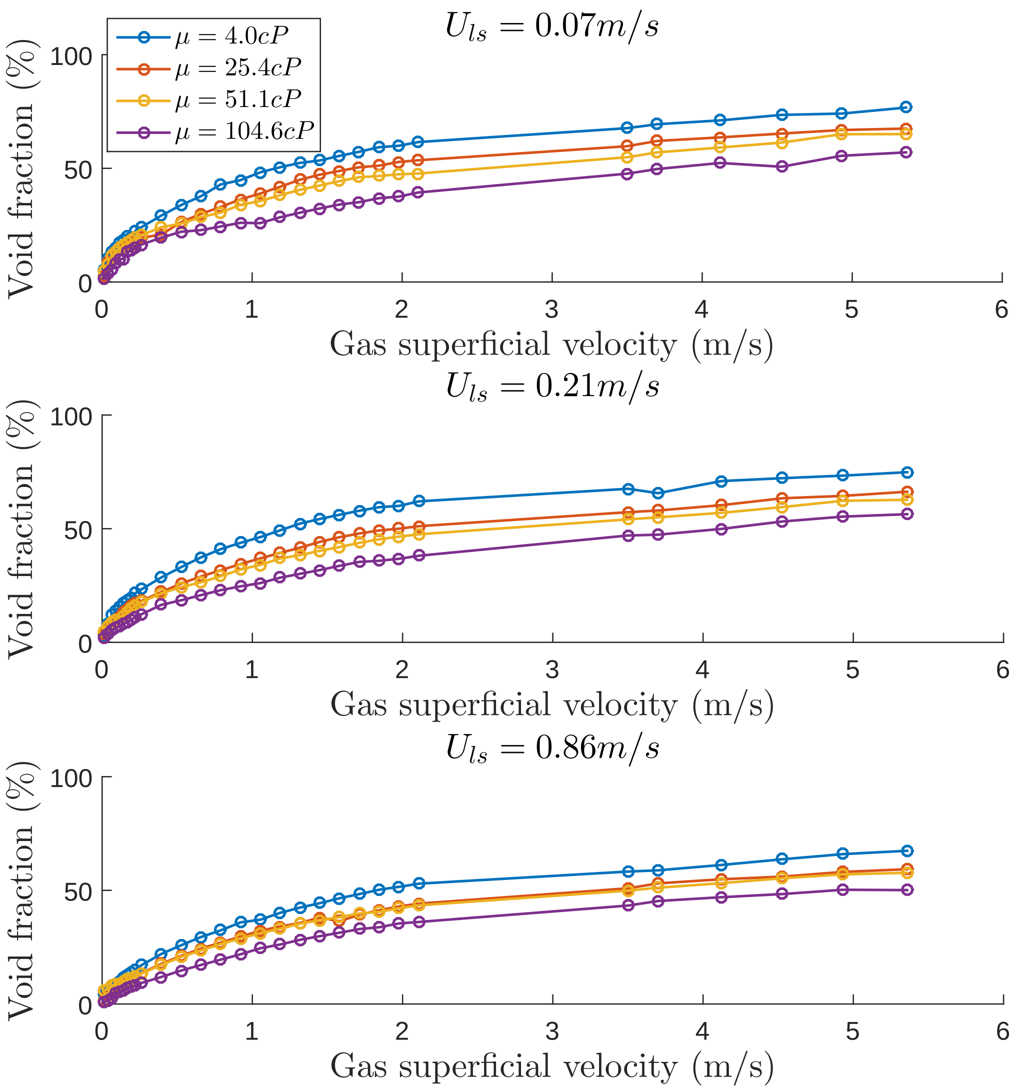

Fig. 4.8 Evolution of average void fraction with gas superficial velocity at the four viscosities studied at three liquid superficial velocities ($U_{ls} = 0.07, 0.21, 0.68\,m/s$). The Figure shows how increase in liquid superficial velocity limits variation of void fraction as viscosity increases.

bubble surface area ratio to volume and therefore more dominant buoyancy force. The second attribute is the decreased effective viscosity of the liquid bulk due to the entrapment of fine bubbles into it producing a cloudy milkish medium. However, this phenomenon is probably limited by a certain threshold of viscosity difference, above which it is not observed, hence the non-crossing of the profiles at 4.0 cP and the ones at 104.6 cP in Figure 4.9.

Figure 4.10a and 4.10b show void fraction evolution with increasing viscosity at liquid superficial velocities of 0.07 and 0.86 m/s respectively. The figures show in clearer representation the decrease of void fraction with increasing viscosity with the exception of conditions at lower gas superficial velocities ($U_{gs} = 0.01 - 0.22\, m/s$). These anomalies could correspond to the dual effect of viscosity as discussed earlier in this section.

The relationship can be judged to be nearly linear with increasing negative slope with increasing gas superficial velocity. When comparing the profiles at different liquid superficial velocity, the profiles seem to maintain a similar trend.

To better understand how the effect of viscosity on void fraction varies with changing gas and liquid superficial velocities Figure 4.11a and 4.11b are generated. These graphs were produced by obtaining the first order partial derivatives $\left(\frac{d\epsilon_g}{d\mu}\right)$ for the relationship of viscosity and void fraction obtained in Figure 4.10. The Figure4.11a shows the rate of change of void fraction with viscosity $\left(\frac{d\epsilon_g}{d\mu}\right)$ expressed as $\left(\frac{\%}{cP}\right)$ against gas superficial velocity. Figure 4.11b shows the rate of change against liquid superficial velocity. These figures reflect quantitative values for how the effect of viscosity on void fraction varies with gas and liquid superficial velocities. Care must be taken when studying these graphs because the y-axis is a negative scale, although the relationship shows a negative slope in Figure 4.11a, it is a positive correlation with gas superficial velocity. On the contrary, Figure 4.11b shows a positive dependency on liquid superficial velocity, therefore it is a negative correlation.

It is observable from Figure 4.11a how viscosity affects void fraction negatively in almost all the studied matrix. It is evident that the influence is less pronounced at lower gas superficial velocity, and increases exponentially with increasing gas superficial velocity reaching a maxima around $U_{gs} = 2.0\, m/s$ above which it starts decreasing and nearly plateaus around the higher bound of gas superficial velocity range. These relationships suggest that viscosity impact on void fraction has a positive dependency on gas input. This positive dependency is exponential and reaches a maximum above which it decreases and plateaus. The maximum does seem to be independent of liquid

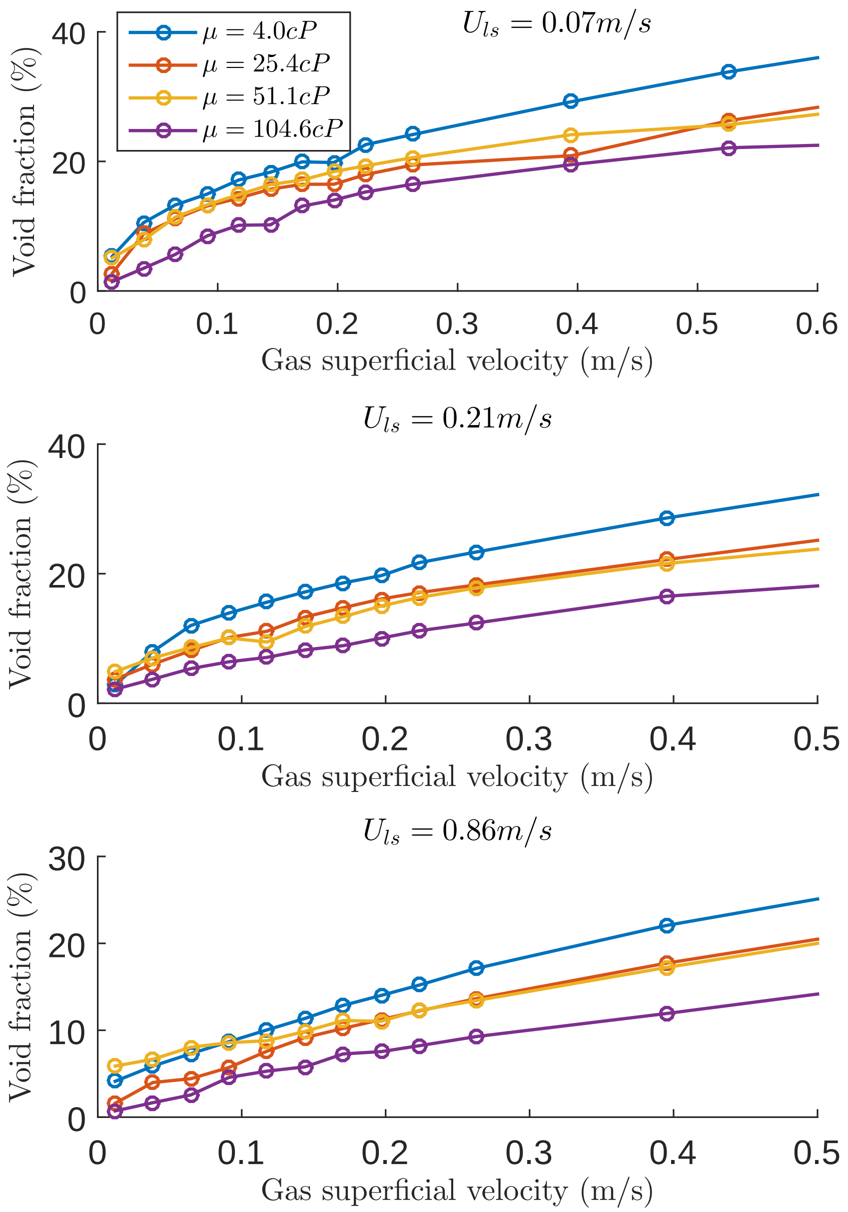

Fig. 4.9 Evolution of average void fraction with gas superficial velocity at the four viscosities studied at three liquid superficial velocities ($U_{ls} = 0.07, 0.21, 0.68\, m/s$). The Figure shows crossing of void fraction profiles produced by different viscosities.

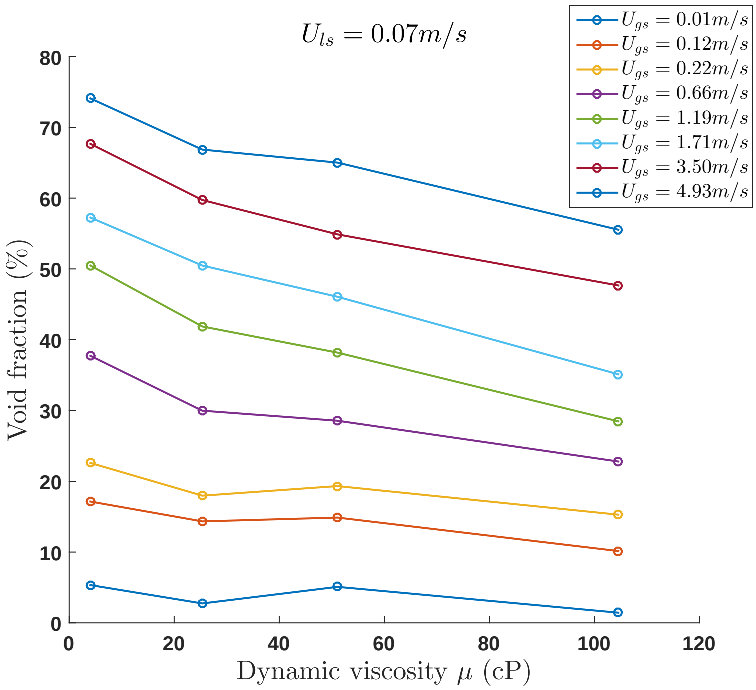

(a)

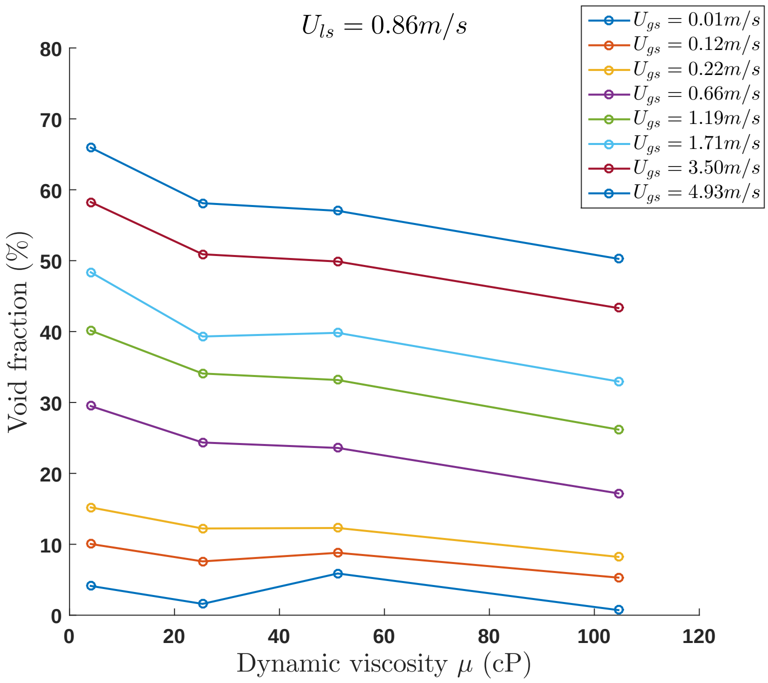

(b)

Fig. 4.10 (a) Void fraction plotted against viscosity for a selection of gas superficial velocities. (a) shows plots at lower liquid superficial velocity of (0.07 m/s). (b) shows void fraction change at higher liquid superficial velocity (0.86 m/s).

superficial velocity. This behaviour might indicate that viscosity has a small effect on void fraction in bubbly flow regime and much more pronounced effect in slug and churn flow regimes, then the effect becomes independent of both liquid and gas superficial velocities at higher gas superficial velocities.

Figure 4.11b shows how the rate of change of void fraction with viscosity changes with liquid superficial velocity for a selection of gas superficial velocities. The figure reveals that increase in liquid superficial velocity lessens the viscosity effect on void fraction especially at higher gas superficial velocity. In other words, if increase in viscosity resulted in 10% change in void fraction at a lower liquid superficial velocity, if the same increment in viscosity is applied at a higher liquid superficial velocity; the resultant change in void fraction will most likely to be less than the 10% given that the gas input is maintained constant. Moreover, Figure 4.11b shows that liquid superficial velocity does not have an appreciable impact on viscosity effect on void fraction at lower gas superficial velocities.

From the discussion above it can be deducted that Figures 4.11a and 4.11b indicate a competition between liquid and gas superficial velocity in influencing viscosity impact on void fraction. It appears that at lower liquid superficial velocity, increase in gas superficial velocity results in a greater deviation in void fraction (Figure 4.11a). On the other hand, at higher gas superficial velocity, increase in liquid superficial velocity has a more dramatic impact on the effect of viscosity on void fraction.

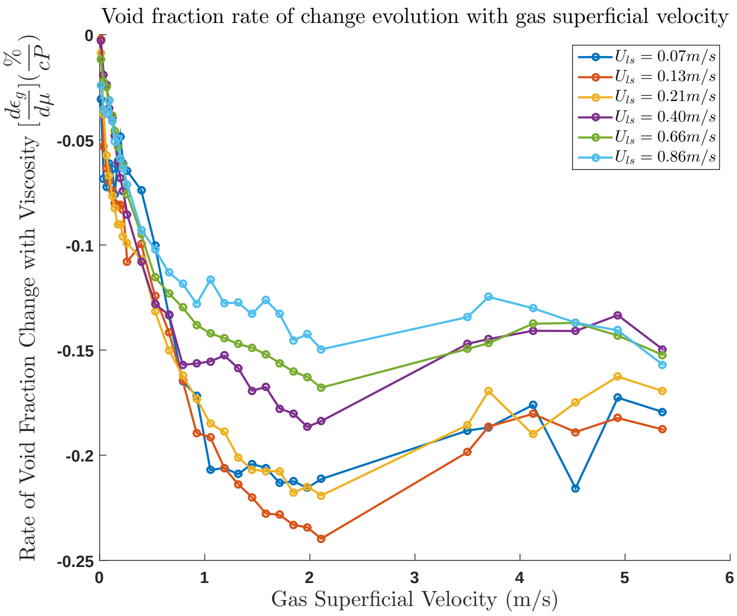

(a)

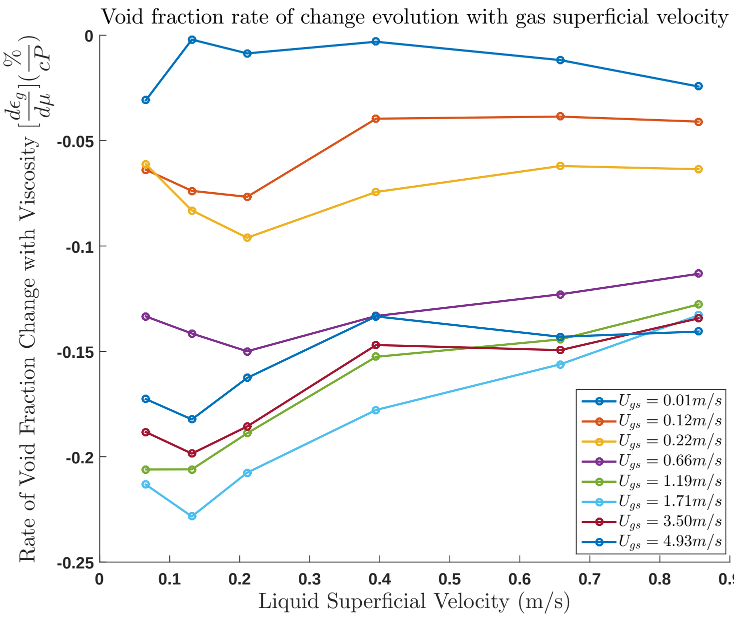

(b)

Fig. 4.11 Rate of change of void fraction with viscosity expressed as $\left(\frac{\%}{cP}\right)$ plotted against (a) gas superficial velocity (m/s) and (b) liquid superficial velocity(m/s). The points are generated by fitting a linear relationship to the viscosity (μ) vs gas superficial velocity relationships shown earlier in Figure 4.10a and 4.10b.

4.2.4 Effect of viscosity on radial distribution of void fraction

Not many researchers have investigated the effect of viscosity on radial distribution of void fraction. Schmidt et al (2008) proposed fitting a power law relationship to the radial profiles assuming axisymmetry of the profiles around the pipe centre (as depicted in equation 4.1). This is a reasonable assumption given that forces are expected to be equal in the two sides of the vertical pipe. They reported a stronger core peaking with increaing gas superficial velocity [159]. Szalinski et al (2010) however observed flattening of higher viscosity profile (silicone oil) at low gas velocities compared to lower viscosity fluid (water). They also added that the void fraction profile for the slug flow region appears much flatter for the higher viscosity fluid [172]. However, this observation might again not be a viscosity effect more that a surface tension effect due to the fact that higher viscosity increases film thickness and therefore the time-averaged radial void fraction profile is expected to be more parabolic.

Abolore (2013) studied variation of radial void fraction profile in the wake of a stationary Taylor bubble emplolying two different viscosities, namely 42 cP and 152 cP. They reported a lower average void fraction at higher viscosity in agreement with what observed in this study. In addition, they observed that viscosity has insignificant effect on radial distribution of void fraction at low gas superficial velocity [2]. Rabha et al (2014) studies radial distribution of viscous fluids and slurries in a bubble column setting using ultra-fast X-ray tomography. The data presented showed no significant variation in the shape of radial profile when viscosity is ever slightly increased from 1.29 cP to 2.15 cP, however enhanced coalescence was observed when comparing the pure fluids with the seeded ones [151].

$$\epsilon_g = \epsilon_{max} \left[1 - \left(\frac{r}{R} \right)^n \right] \tag{4.1}$$

Figure 4.12 shows radial void fraction distribution obtained for the four studied viscosities at the lowest liquid superficial velocity ($U_{ls} = 0.07\,m/s$) and three gas selected gas superficial velocities ($U_{gs} = 0.01, 1.58, 5.36\,m/s$). First observation to be noted is the average lower void fraction with increasing viscosity in most cases, except at the very low gas superficial velocity. The behaviour is maintained in both the pipe core and near the wall. It is also observable that wall peaking is exhibited by the lowest viscosity fluid at the lowest gas velocity. At the same liquid and gas velocity higher viscosities exhibited core peaking. Ohnuki and Akimoto (2000) suggested that wall peaking is likely not to be observed in large diameter pipes owing to the higher turbulence dispersion forces near the wall pushing bubbles away [135]. However, wall peaking was observed in a 127 mm pipe using air-water medium at low gas velocities by [162]. It is also noted that the shapes of the profiles produced by different viscosities are different at lower gas superficial velocity. The profiles grow more resemblant and closer to each other with increasing gas velocity. In addition, the difference in void fraction between the core and the wall enlarge with increasing gas velocity, as profiles become more parabolic.

Figure 4.12 shows that at $U_{gs} = 0.01\, m/s$ the void fraction profile exhibited by the 51.1 cP fluid features a shifted core-peaking. This can potentially be a measurement uncertainty since the number of pixels (void fraction measurements) being used to calculate the average radial void fraction is very small near the core. Therefore if any error in any of these pixels increases the uncertainty in the calculated value. In other words, due to the small number of population being sampled, the uncertainty associated with the mean presented in the figure is higher.

At the higher gas superficial velocity, the profiles become more flat in the vicinity of the core owing to the formation of the continuous gas core upon transition to churn/annular flow. It can also be seen that the profiles drop sharply near the wall representing the liquid film with trapped bubbles within. The profiles shown at $U_{gs} = 5.36\, m/s$ feature a strong indication of the film thickness variation with viscosity. As can be seen, the point where profile becomes more steep near the wall (the film interface) migrates away from the wall towards the core with increasing viscosity. This commends what other researchers reported before on the increase of film thickness of viscosity [63, 62, 121]. One more observation to be realised is that discrepancies between void fraction profiles of different viscosities are more pronounced near the wall as opposed to the core as manifested in Figure 4.12 .

To look with more thorough into the evolution of the effect of viscosity on radial profile of void fraction with variation of gas and liquid superficial velocities, Figure 4.13 and Figure 4.14 are presented comparing profiles of the highest and lowest viscosities studied (4.0 and 104.6 cP). Since the collected matrix is quite large, for brevity only profiles of velocities where appreciable change of behaviour is observed are included. Figure 4.13 shows radial distribution at the lower bound of gas superficial velocity, for each viscosity three profiles are presented; each correspond to a different liquid superficial velocity. First observable feature is the wall peaking for lower viscosity and its complete absence in the case of highest viscosity. Another notable feature is that at higher viscosity, profiles are arranged in an ascending order of liquid superficial

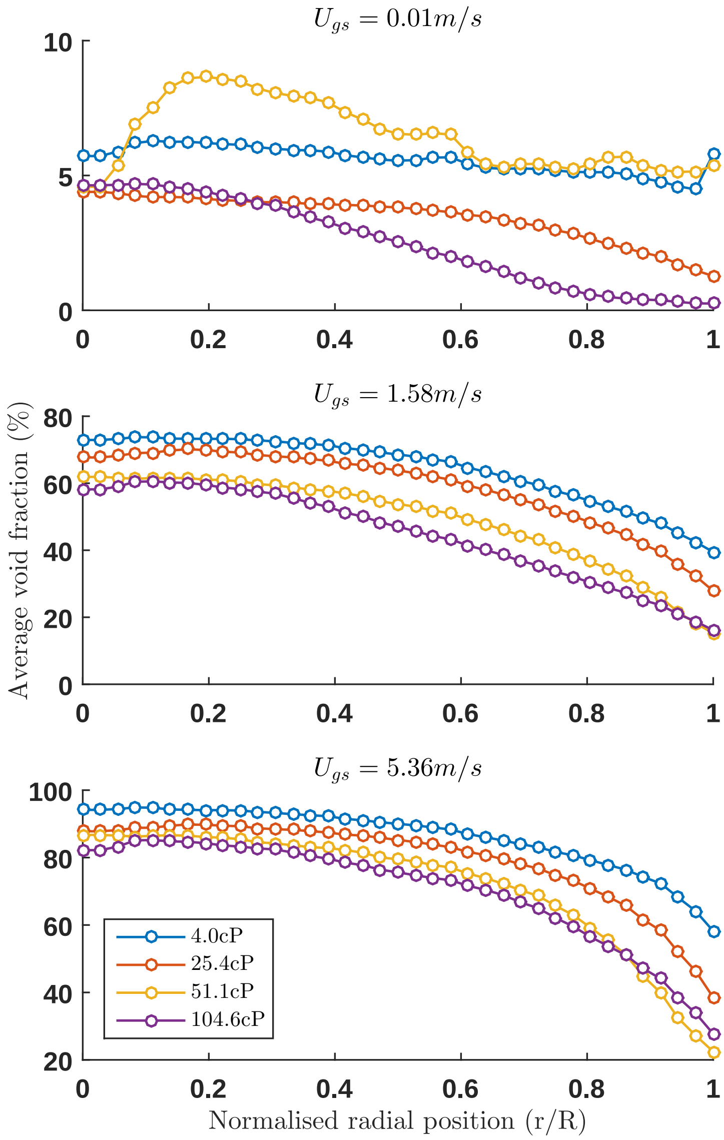

Fig. 4.12 Effect of viscosity on radial distribution of void fraction for the four studied viscosities at three different gas superficial velocity at $U_{ls} = 0.07\,m/s$.

velocity where higher void fraction is registered at lower liquid superficial velocity and it decreases with increasing liquid velocity. This conduct is not violated by the higher viscosity for all the gas velocities studied. On the other hand, for lower viscosity profile, it is evident that highest liquid superficial velocity profile feature higher void fraction profile compared to the lower liquid velocity profile, it then migrates downwards gradually with increasing gas superficial velocity until it rests lower than other lower liquid flow profiles. This might be attributed to the incurring flow regime, where increased liquid velocity enhances bubbles' break-up resulting in smaller, more dispersed bubbles marking higher void fraction.

Moreover, Figure 4.13 shows higher void fraction discrepancies between the different liquid flow profiles of 4.0 cP compared to the higher viscosity profiles (104.6 cP), which suggests that the effect of liquid superficial velocity on void fraction is more significant at lower viscosities in the range of velocities presented in the figure. Additionally, the discrepancies between profiles generated at the same viscosity and different liquid flows seem to be higher near the core compared to the wall, indicating that conditions in the pipe core are more affected by the liquid superficial velocity compared to the pipe wall. This is understandable owing to the viscous effect, resulting in a decreased velocity profile near the wall.

Figure 4.14 shows similar profiles to the ones in Figure 4.13 but at higher gas velocities extending to the highest gas superficial velocity studied (5.36 m/s). The shapes of profiles do not seem to change much with increasing gas superficial velocity, however as indicated earlier it becomes more flat near the core as the flow regime is approaching annular flow. Profile-crossing can be observed near the core between higher and lower viscosity profiles, with increasing gas velocity, void fraction of lower viscosity rises above that of higher viscosity. Another notable feature is the profile crossing of lines generated by same viscosity at different liquid flows. This phenomenon is more significant and repetitive at higher viscosity (around 70% non-dimensional radial distance).

From the discussion presented earlier, it is clearly evident that radial distribution of void fraction is hugely dependent on superficial velocities of both phases as well as the viscosity of the liquid phase. Therefore, a lot of the models proposed in literature to model void distribution and hence velocity distribution are expected to fail predicting profiles presented in this study as they are deduced a function of only gas and liquid superficial velocities (see Schmidt et al (2008) [159]).

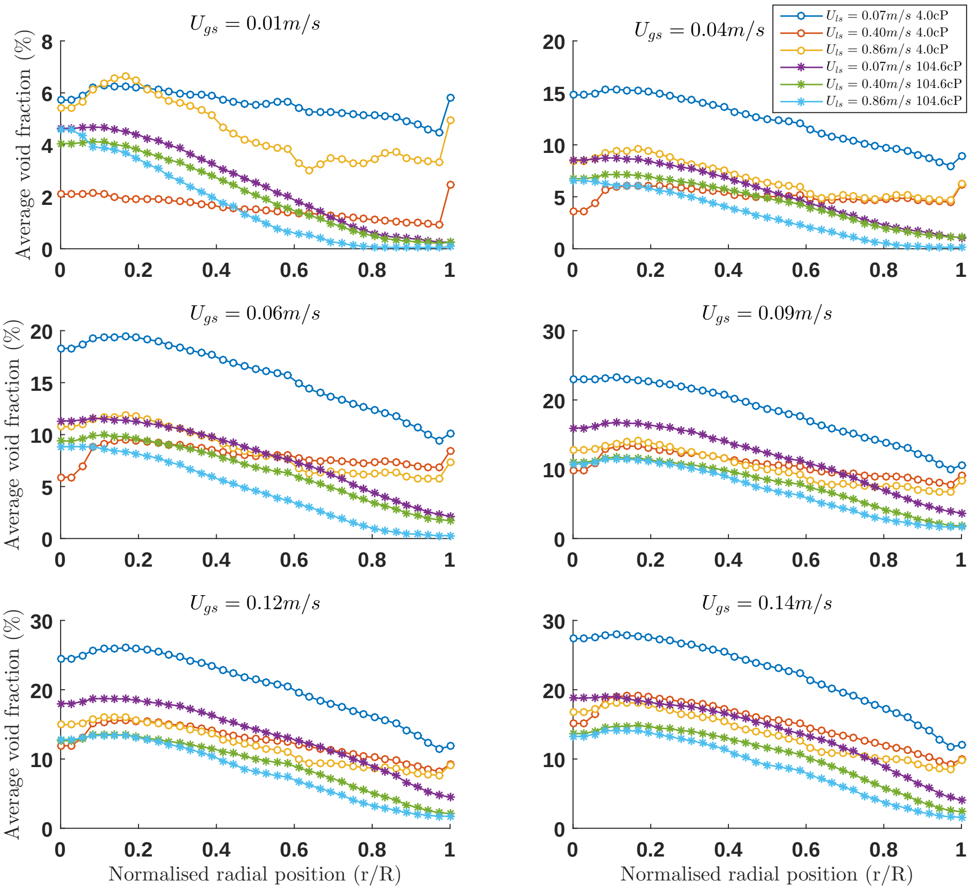

Fig. 4.13 Evolution of radial distribution of void fraction with gas superficial velocity for the lowest and highest viscosity studied (4.0 cP and 104.6 cP). The figure covers the lower bound of gas superficial velocity $U_{gs} = 0.01 - 0.14\,m/s$.

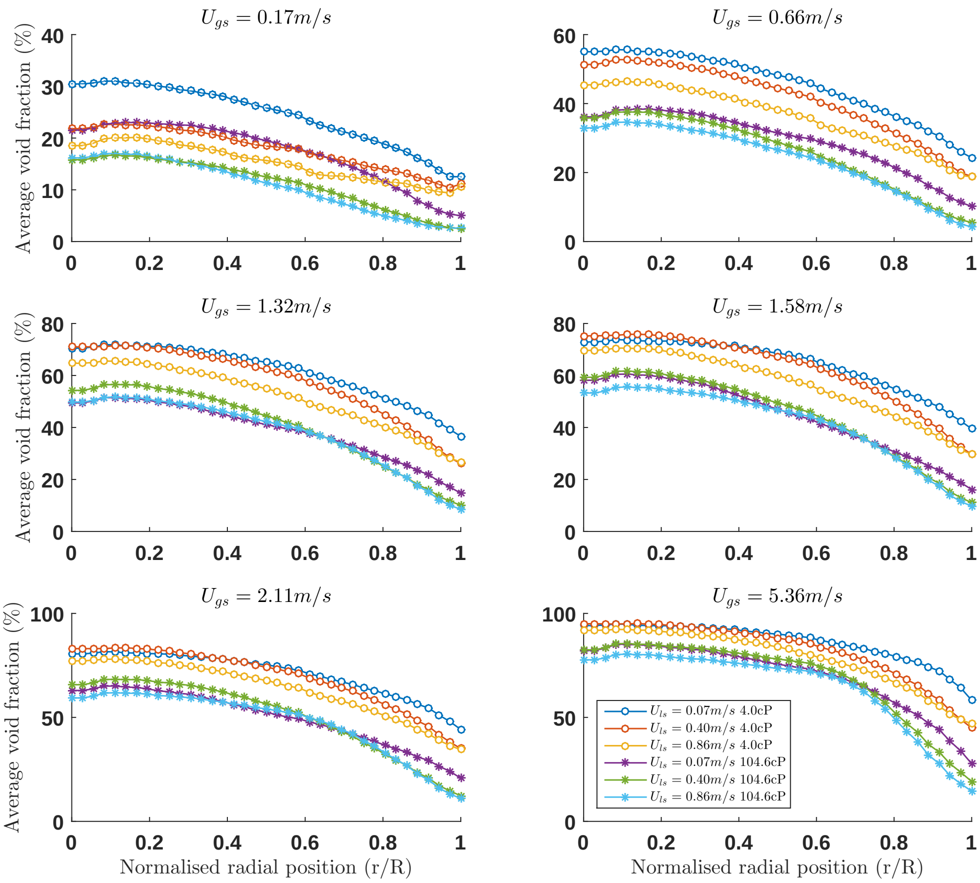

Fig. 4.14 Evolution of radial distribution of void fraction with gas superficial velocity for the lowest and highest viscosity studied (4.0 cP and 104.6 cP)for the bound of gas superficial velocity $U_{gs} = 0.17 - 5.36\, m/s$.

4.2.5 Effect of viscosity on pressure drop

Viscosity effect on pressure drop has received a slightly higher attention compared to other aspects of vicsous multiphase flow considering its imperative significance on the design of multiphase installations and the direct dependency of frictional pressure gradient on viscosity. It is expected that increase in viscosity would increase pressure drop owing to the higher interfacial friction factor. Fukano and Furukawa (1998) proposed a correlation to estimate frictional pressure gradient for high viscosity annular flow based on the film thickness estimation and momentum balance [62]. McNeil and Stuart (2003) investigated extrapolating momentum flux models into predicting pressure drop in higher viscosity mediums. They found that models performed poorly at higher viscosities, however Chisolm's (1967) model [41] showed a slightly better prediction, whereas Friedel's (1979) [61] correlation was found to overpredict pressure gradient progressively with increasing viscosity. Their data also reflected that the method of Chisholm (1973) [42] gradually underpredicts pressure gradient with increasing viscosity. They recommended using flow regime phenomenological models for prediction of pressure gradient where they presented a correlation to predict interfacial friction factor as a function of vicosity and Froude number [121].

Da Hlaing et al (2007) experimentally studied viscous flow pressure drop in a small vertical tube (19 mm); using water-glycerol to formulate two viscosities (0.85 cP and 4.5 cP). It was noted that higher viscosity produces less perturbations in the pressure signal [50]. Abolore (2013) studies viscous pressure gradient in a similar pipe diameter to the one in the current study (127 mm) using a 35 cP oil. They obtained a smooth profile for the pressure gradient against gas superficial velocity, where attenuations in the profile marking flow regimes' transition were not observed. They also studied the effect of gas-density (by elevating the rig pressure from 4.5 to 7.9 bar) where a slightly lower pressure gradient was observed at the higher pressure [2].

Alsarkhi et al (2016) studied viscous flow pressure gradient in vertical pipes where they reported positive frictional pressure gradient in the slug flow region. They attributed the phenomenon to the competition between wall shear stress in the slug region and the Taylor bubble region where backward liquid film flow occurs and therefore positive frictional pressure gradient is generated. They proposed a criterion to detect change in frictional pressure drop sign based on comparison between the mixture velocity and the predicted film velocity obtained from a model they introduced [10].

Figure 4.15 shows the pressure gradient for all the considered viscosities in relation to the gas superficial velocities at three liquid superficial velocities, namely 0.07, 0.40, and 0.86 m/s. It is clear that the overall pressure drop decreases with increasing gas superficial velocity in a smooth decaying exponential relationship. This is because in this range of velocities gravitational pressure gradient is dominant, therefore the decrease in two phase density because of increasing gas velocity is reflected in the overall pressure drop. It is also observed that the rate of drop of pressure gradient with increasing gas velocity decreases in concordance with the behaviour of void fraction with increasing gas input. At the higher bound of gas velocity it can be seen that the profile nearly plateaus, and that because of the increasing significance of frictional pressure gradient due to higher momentum of the gas and liquid coupled with decreasing effect of gas velocity on void fraction when the regime transitions to near annular flow conditions.
Looking at the effect of viscosity on the profiles' shape, it is notable that higher viscosity lines feature higher pressure gradient in conformity with the deduced viscosity impact on void fraction in earlier sections. Expectedly, with increasing liquid superficial velocity, higher pressure gradient is registered for the liquids with identical viscosity. In effect, viscosity influence on average pressure drop can be viewed analogous to the effect of increasing liquid superficial velocity.

Non-dimensional pressure gradient plotted against non-dimensionalised gas superficial velocity together with the trends observed by Owen (1986) are shown in Figure 4.16. The pressure drop is non-dimensionalised with reference to the single phase pressure gradient according to equation 4.2. The gas superficial velocity is presented in a form of Froude number as depicted in equation 4.3. As can be seen in Figure 4.16 the current data fall in the lower range of non-dimensional gas velocity falling into the slug flow region of Owen's data. Although the gas velocity could not be increased to higher values to investigate transitional attenuations on pressure curve, yet it was demonstrated in earlier sections that the flow has transitioned beyond churn flow regime. The absence of trend changes marking regime transitions can be attributed to the vast difference in pipe diameter. Owen's (1986) experiments were conducted in a 31.8 mm pipe whilst current data is generated in a 127 mm riser.

$$dP_{ND} = \left[\frac{\frac{dP}{dz} - \rho_g g}{(\rho_l - \rho_g) g} \right] \tag{4.2}$$

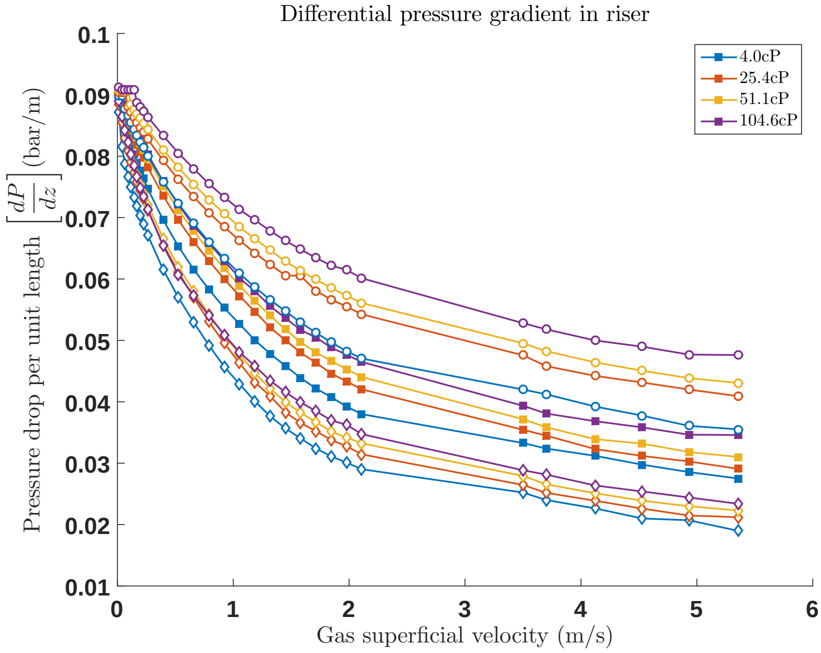

Fig. 4.15 Overall pressure gradient for the four viscosities studied against gas superficial velocity, diamond marked points correspond to $U_{ls} = 0.07\,m/s$, square markers stand for $U_{ls} = 0.40\,m/s$ and the circles represent $U_{ls} = 0.86\,m/s$. The lines are colour-coded to the corresponding viscosities as per the legend.

$$U^*_{gs} = \left[\frac{U_{gs}\rho_g^{0.5}}{\sqrt{gD(\rho_l - \rho_g)}} \right] \tag{4.3}$$

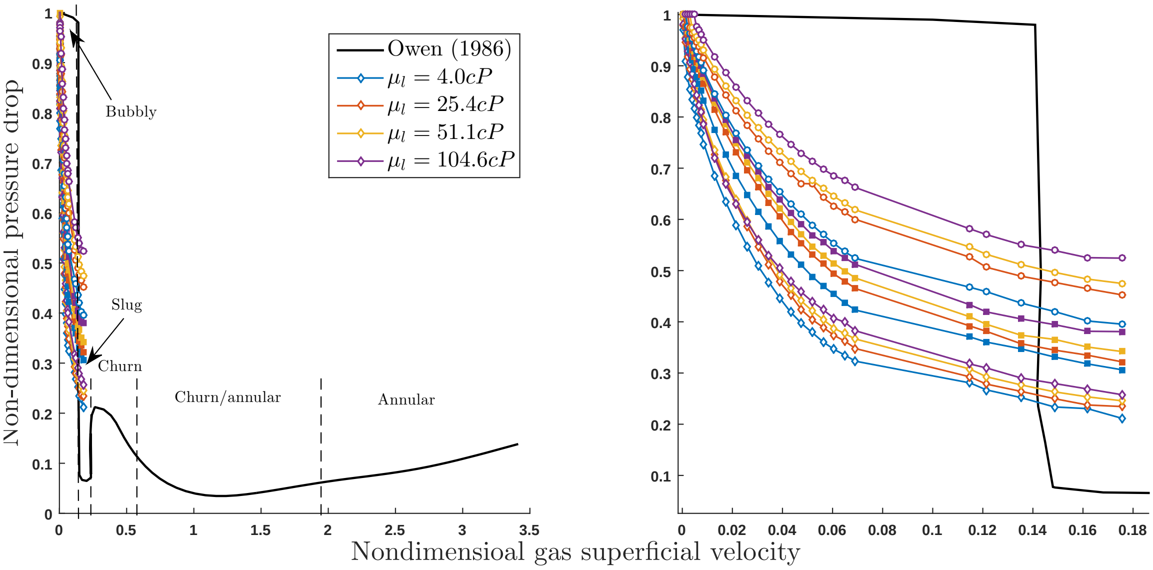

Fig. 4.16 Non-dimensional pressure gradient plotted against non-dimensionalised gas superficial velocity compared to the work of Owen (1986) [142], diamond marked point correspond to $U_{ls} = 0.07\, m/s$, square markers stand for $U_{ls} = 0.40\, m/s$ and the circles represent $U_{ls} = 0.86\, m/s$. Owen's (1986) data is for $U_{ls} = 0.0053\, m/s$ using water ($\mu_l \simeq 1.0\, cP$).

4.2.6 Effect of viscosity on transition of flow regimes

One of the most developed methods to characterise flow regimes is by plotting the probability distribution function of void fraction time series. The method was first proposed by [101], where time series of cross-sectionally averaged void fraction for different flow regimes were found to produce a unique Probability Density Function (PDF) footprint. The characteristic shapes of PDFs for different flow regimes were shown earlier in Chapter 2 (see Figure 2.4).

The information given in this section will show the shapes of the PDFs for all the studied range of flows and viscosities. It will help to address the issue of flow development as the PDFs will be compared both upstream and downstream the test section. Figure 4.17 below shows PDFs obtained at 62D axial distance from the injection point for all the viscosities studied. A clear distinction in the shape of the PDFs can be spotted between the profiles generated using different viscosity oils. Looking at the general characteristics of all viscosities combined with variation of liquid and gas superficial velocities, it can be seen that almost all the characteristic shapes of flow regimes are registered. It can be observed that at the lowest gas superficial velocity the

PDF have a single peak at void fraction less than 20% indicating bubbly flow. As gas superficial velocity is increased, the peak shifts towards higher void fraction, in some cases creating a tail at higher void fraction reflecting the formation of cap-bubbles. As the gas velocity is further increased, another peak starts growing at at higher void fraction (often >50%) representing "Taylor bubbles" or large gas structures, whilst the other peak at lower void fraction represents liquid slug void fraction. with increasing gas superficial velocity the peak shifts towards higher void fraction, the other peak at lower void fraction diminished gradually. This shape represents churn flow, a single wide peak at higher void fraction. At the highest bound of gas velocity, the peak becomes narrower and shifts towards very high void fraction (<70%) representing near annular flow regime.

Very clear distinctions can be spotted between the different viscosity PDF shapes. The differences seem to lessen at higher gas superficial velocities (namely above 2.11 m/s). At the lower bound of gas superficial velocity ($U_{gs} = 0.01, 0.12\,m/s$) the profiles generated by all viscosities feature bubbly flow regime. However, it is clear that as viscosity increases the PDF shape seems to create a tail spreading to higher values of void fraction. Given that in most of the cases the overall average void fraction is lower at higher viscosity as excessively discussed earlier in section 4.2.3; this observation suggests that larger structures (i.e. bubbles in this case) are formed as viscosity is increased registering instances with higher void fraction in the time series, hence the tail on the PDF. Moreover, it can be noted that higher viscosity profiles peak at lower void fraction, implying that in bubbly flow with increasing viscosity the void fraction distribution shifts to a more of a sluggish/undistributed phenomenon, where smaller bubbles are trapped in the liquid bulk whilst bigger bubbles are formed creating the observed tail on the PDF shape. Another scenario that could also be happening is that as viscosity increases larger bubbles are generated in the liquid bulk but in smaller concentration, this was observed by [151].

In the range of gas superficial velocity between 0.40 and 2.11 m/s, the difference in PDF shape becomes more dramatic. In cases of higher viscosities, the PDF registers two distinct peaks, indicating slug flow, whilst the lower viscosity profile has only one peak indicating churn flow. The two peaks become more distinct and defined at higher viscosities. It should be noted here that slug flow was reported not to exist in pipes larger than 100 mm in diameter [135, 158, 163]. however, the current PDF shapes indicate otherwise. Nevertheless, complete characterisation of the flow regime cannot be established without the aid of he spatio-temporal images from the WMS in addition to the high speed imaging of the flow. Observing the PDFs that have two peaks it can be seen that consistently the peak at lower void fraction shifts towards lower void fraction with increasing viscosity, suggesting that there is less gas trapped in the liquid bulk when viscosity is increased. On the other hand the higher void fraction peak does not seem to appreciably vary with viscosity.

On the effect of gas velocity on variation of PDF shape with viscosity, it can be seen that the variation in PDF shape between different viscosities is more significant at low gas superficial velocities, almost similar PDF shapes are produced at higher gas superficial velocities ($U_{gs} \geq 2.11\, m/s$). Increase in liquid superficial velocity on the other hand seems to increase the region of slug flow regime or intermittent behaviour in general as the number of PDFs with two peaks increases with liquid superficial velocity.

One general observation to be drawn is that the difference in shape of PDFs between the 4.0 cP and the other three viscosities is very significant. However, no substantial difference can be spotted between the shapes of the three higher viscosities.

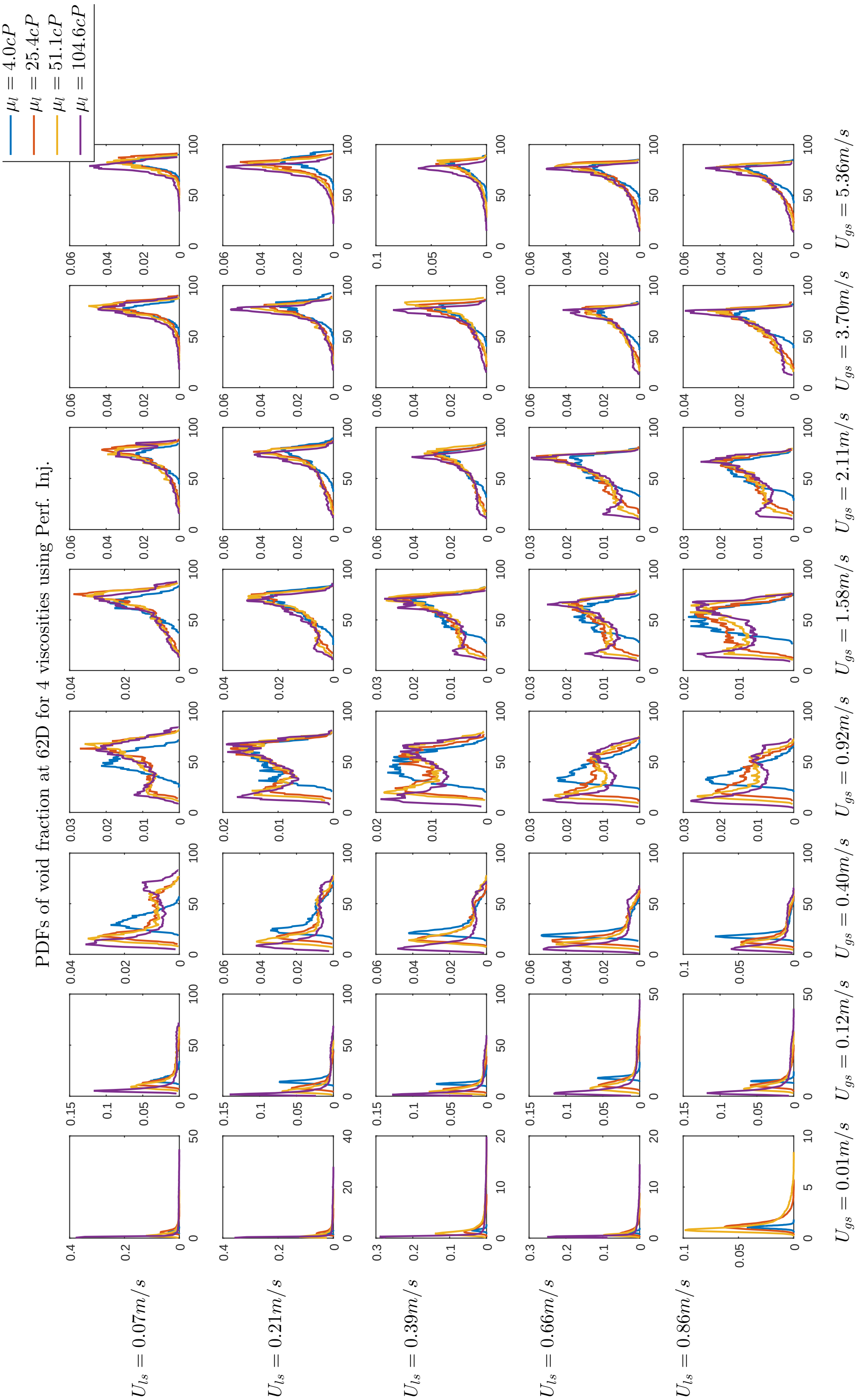

Fig. 4.17 Probability density function (PDF) of void fraction time series plotted for the four viscosities studied for a selection of liquid and gas superficial velocities obtained at 62 axial distance from the injection point.

Figure 4.18 shows PDF of cross-sectionally averaged void fraction obtained upstream the pipe at 15D axial distance from the injection point. This is obtained to try to assess how viscosity affects flow development, which will be reflected on the variation of PDF shape, hence the resultant flow regime, upstream and downstream the pipe. First observation to be made is that the slug flow regime is not observed near the injection point in all the velocities. Which suggests that the slugs are not developed yet; therefore mostly single peaks are generated indicating bubbly-churn flow regime. This could be analogous to the entrance effect theory about churn-slug flow proposed by Taitel et al (1980) [173]. It is also observable that the void fraction variance increases with increasing viscosity. Which suggests that close to the injection point as viscosity is increased, the generated gas structures become diverse in size and concentration. In other words flow becomes less homogeneous with increasing liquid viscosity. This observation applies also to the condition further downstream the pipe as shown in Figure 4.17. When comparing difference between profiles upstream and downstream the pipe (comparing Figure 4.17 with 4.18) it is observable that the profiles maintain their shapes in the bubbly flow region ($U_{gs} \leq 0.40\, m/s$). Same applies to conditions at higher gas superficial velocity ($U_{gs} \geq 3.70\, m/s$). Contrarily, at intermediate range of gas superficial velocity ($0.40\, m/s \geq U_{gs} \leq 3.70\, m/s$) where slug flow is observed, PDFs shape is observed to significantly change with axial position with increasing viscosity.

It is also observable that the variation in shapes of PDFs of different viscosities is more pronounced upstream the pipe whilst they tend to collapse into one line downstream the pipe. This behaviour must be related to the flow development and the coalescence-break-up equilibrium.

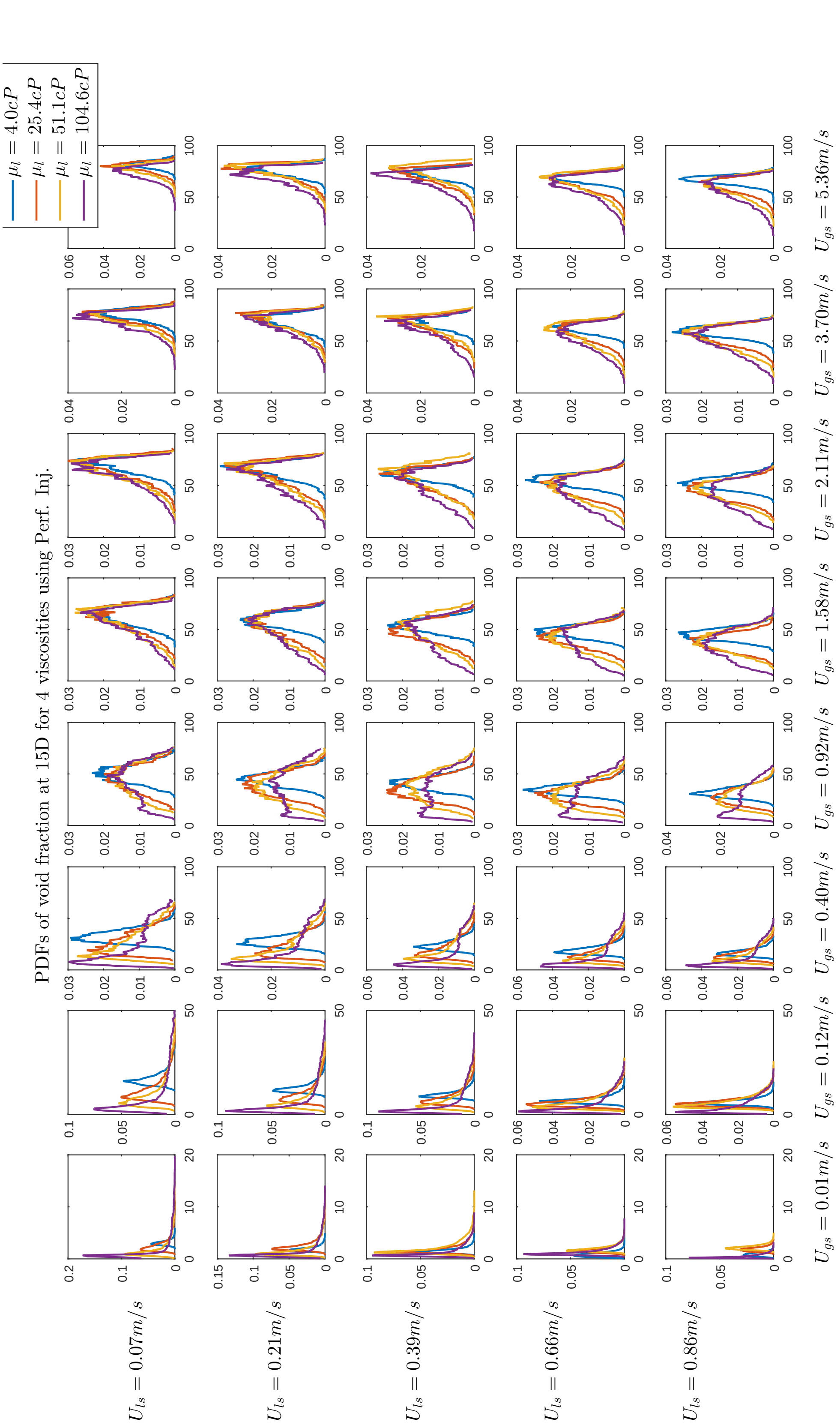

Fig. 4.18 PDFs of void fraction time series plotted for a selection of liquid and gas superficial velocities at 15D axial distance from the injection point for the four viscosities studied.

4.2.7 Effect of viscosity on two-phase flow structures

WMS produced three dimensional matrix of (32 x 32 x (time x frequency)) pixels. Each pixel is an independent measurement of void fraction in the pipe cross-section. The time dimension of the matrix is resolved into an equivalent spatial length of the pipe (L_E) by the knowledge of pitch size (P_s) and the structure velocity (U_g) calculated by cross-correlating time series of void fraction obtained from the neighbouring ECT sensor. The scaling is achieved using the equation 4.4 below, where f is the acquisition frequency and t is the time scale. The images are produced by selecting the middle frame of the cross-section and resolving it over equivalent axial distance.

$$L_E = t \times U_g \times P_s \times f \tag{4.4}$$

Figure 4.19 shows the effect of viscosity on the shapes of gas structures at the lowest liquid superficial velocity ($U_{ls} = 0.07\,m/s$) the top row features 4.0 cP images, followed by 25.4 cP, then 51.1 cP and the bottom row represents the 104.6 cP images. The flow regimes presented range from dispersed bubbly flow up to annular flow where gas core continuum can be clearly observed. Looking at the effect of viscosity on the resultant flow regimes, first notable observation is that as viscosity increases, distributed/homogeneous bubbly flow regime seems to disappear, as clearly evident at 104.6 cP, the featured flow regime is undistributed bubbly flow at the lowest gas superficial velocity. This comes in agreement with the observation made in earlier sections regarding decrease of void fraction with increasing viscosity. The images suggest that increase in viscosity improves coalescence of bubbles, therefore larger bubbles are observed. The figure also suggests that, gas entrainment in the liquid decreases with increasing viscosity. This is evident by the decrease of the greenish shade on the images with increasing viscosity, the colour that represents foamy mix of oil and gas structures.

Looking at the slug flow region of the images, it is observable that slugs become more stable with increasing viscosity. The stability comes from the decrease of gas entrainment rate in the liquid slugs and also in the liquid film surrounding the bubbles. Eye observation and high speed videography information indicates that only very small bubbles are trapped in the liquid forming a milky mixture, while most of the gas is contained in the gas-structure. The images of 104.6 cP oil in Figure 4.19 depicts very clearly the existence of Taylor bubbles in the pipe at this viscosity. This provides a first ever report of the existence of Taylor bubbles in a large diameter pipe at this range of viscosities. The characteristic shape of the Taylor bubble was not only captured by the WMS spatio-temporal images, high speed images also show clearly the shape of the bubble as can be seen in Figure 4.20d and Figure 4.21. Figure 4.19 also shows, in concordance with what has been previously reported in the literature, the increase of the slug unit length with increasing viscosity. An attribute that can be linked to the effect of viscosity on enhancing bubble coalescence.

Moreover, time resolved videos of images similar to those displayed in Figure 4.19 were generated to alow observation of flow for a prolonged period of time; to establish a more rigorous characterisation of the flow regime, before judging the regime transition boundaries. The videos and images of Figure 4.19 suggest that bubble-slug transition shifts to lower gas superficial velocity with increasing viscosity. Which can again be attributed to the enhanced coalescene induced by the viscosity increase. On the contrary, the slug-churn transition seems to shift to higher gas superficial velocity; which suggests that slugs become harder to break with increasing viscosity due to the low gas entrainment in the liquid slug and the higher stability of the interface. The churn-froth flow to churn-annular flow regime shifts towards higher gas superficial velocity as viscosity increases. At 104.6 cP churn-annular flow was not observed, instead very long gas structures followed by frothy liquid structures were dominating the flow at the higher bound of gas superficial velocity. At the higher bound of gas superficial velocity, it can be seen that viscosity increase produces thicker liquid film, this observation was made by several researchers including Furukawa and Fukano (2001) [63].

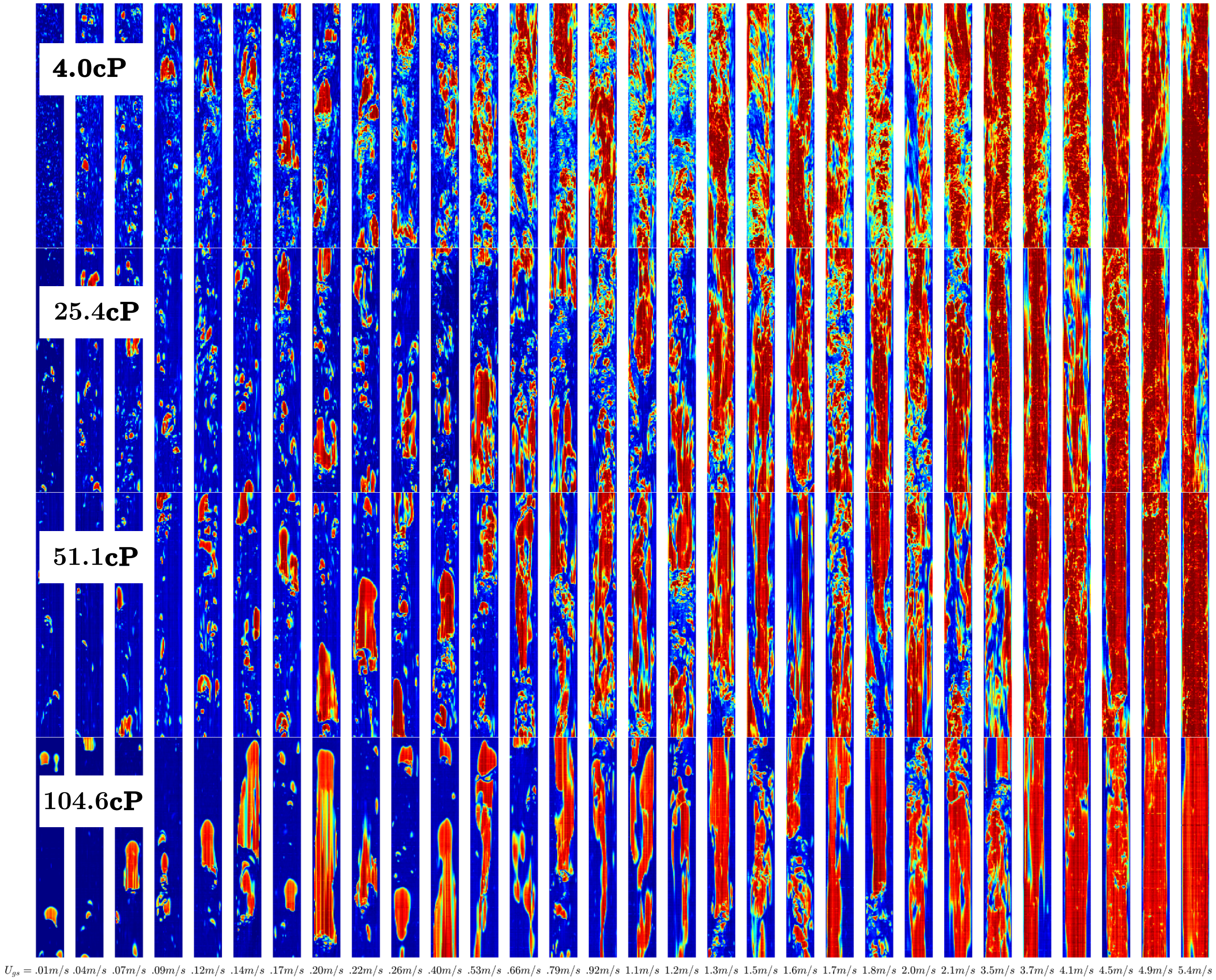

Fig. 4.19 Spatio-temporal images of void fraction distribution for the four viscosity mediums obtained at the $U_{ls} = 0.07\,m/s$. Top row is lowest viscosity (4.0 cP), bottom row is the highest (104.6 cP). The y-axis represents the equivalent spatial distance based on the fluids translational velocity.

Figure 4.20 and Figure 4.21 show captured frames from the high speed imaging experiments, arranged for the four viscosities studied, where 4.0 cP viscosity on the left increasing to the highest viscosity studied (104.6 cP) on the right at constant liquid superficial velocity ($U_{ls} = 0.07\,m/s$). Figure 4.20 covers gas superficial velocity in the range of (0.01-0.09 m/s), while Figure 4.21 covers higher gas superficial velocities from 0.12 to 0.22 m/s. Still photographs from higher velocities are not included due to the increased presence of more bubbles in the liquid film masking gas structures, making it very hard to identify their shapes. However, such videos can be useful in validating the frequency and lengths estimation of liquid slugs.

Figure 4.20 shows how flow regime changes from homogeneous/distributed bubbly flow regime at the lower 4.0 cP, where bubbles of almost uniform shape rise in almost rectilinear trajectories are observed, to a non-homogeneous regime where bigger bubbles are observed near the pipe core and they grow gradually with increasing viscosity. At 104.6 cP cap-shaped bubble can be clearly observed with high concentration of daughter bubbles in its wake. Generally, it can be seen that bigger bubbles grow in size with increasing gas superficial velocity. However, the opposite is observed in general for the smaller bubbles dispersed in the liquid film. As evident from the images in Figure 4.20 smaller bubbles become smaller with increasing gas superficial velocity, a phenomenon that can be attributed to the increase in gas-induced turbulence created by the higher shearing by the bigger bubbles. The figure shows that these bubbles become much smaller in size but higher in density with increasing viscosity as can be also clearly observed in Figure 4.21, although the presence of these smaller bubbles happens at higher gas superficial velocity with increasing viscosity.

Figure 4.21 shows that the interface is persistently more stable at higher viscosity with increasing gas superficial velocity. The Figure features larger bubbles at higher viscosity with more clear boundaries and more regular shape, where lower viscosities feature very deformed and frothy behaviour. At $U_{ls} = 0.22\,m/s$ Taylor bubbles observed at higher viscosities grow longer than the axial length of the recording field, yet the images reflect the uniformity of the shape of the Taylor bubble. One more information to be noted from Figure 4.20 and Figure 4.21 is that gas structures seem to move away from the wall towards the core with increasing viscosity. This comes in agreement will what was observed earlier regarding the evolution of the radial profile of void fraction with viscosity and the observation of McNeil and Stuart (2003) [121].

Figure 4.22 shows spatio-temporal images for the four studied viscosities at higher liquid superficial velocity ($U_{ls} = 0.40\,m/s$). It is notable that the bubbly flow region

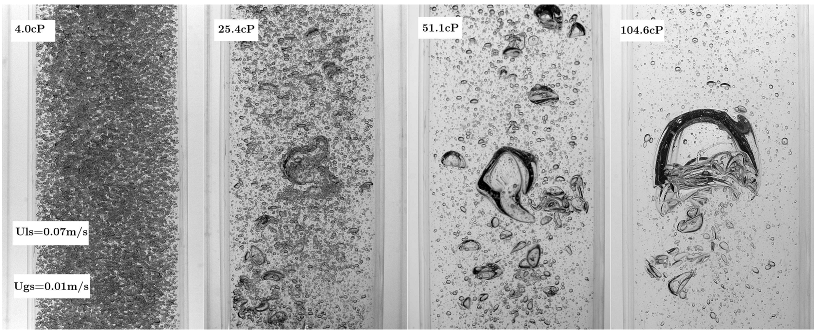

(a)

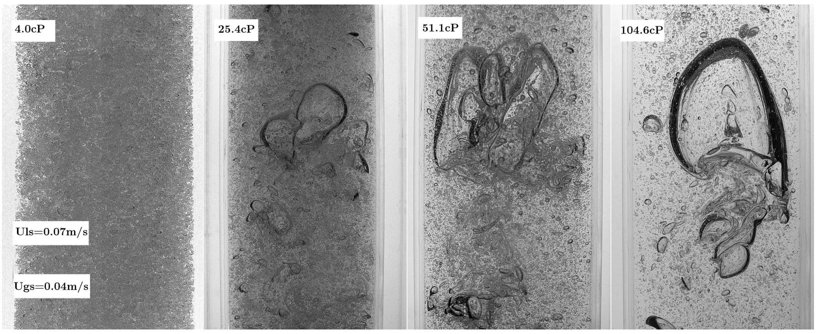

(b)

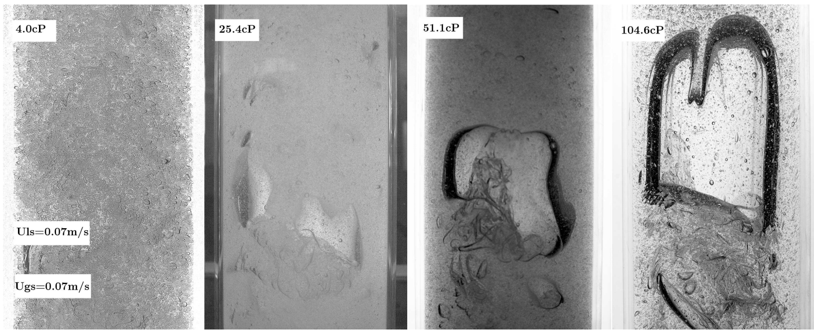

(c)

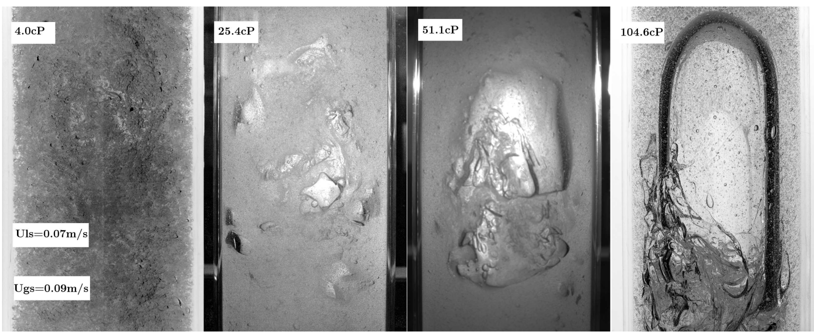

(d)

Fig. 4.20 Images of gas structures captured for the four viscosities at constant liquid superficial velocity ($U_{ls} = 0.07\,m/s$) arranged in ascending viscosity order from left (4.0 cP) to right (104.6 cP). (a) represents $U_{gs} = 0.01\,m/s$ (b) represents $U_{gs} = 0.04\,m/s$ (c) represents $U_{gs} = 0.07\,m/s$ and (d) represents $U_{gs} = 0.09\,m/s$. The figure shows the decreasing frothiness of the flow with increasing viscosity and the distinctively large difference in the shape of structures with increasing viscosity. (d) shows observation of Taylor bubble in a large diameter pipe for the first time in this range of viscosities.

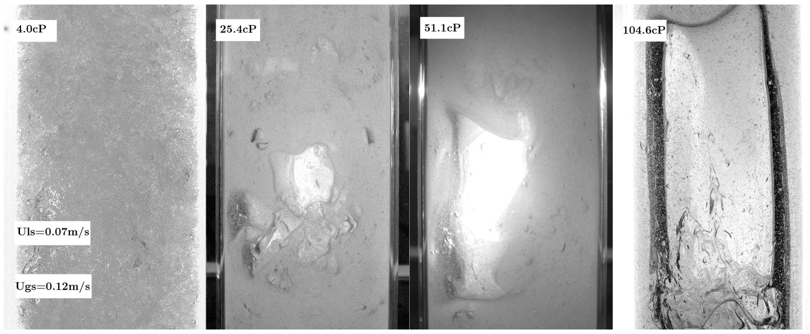

(a)

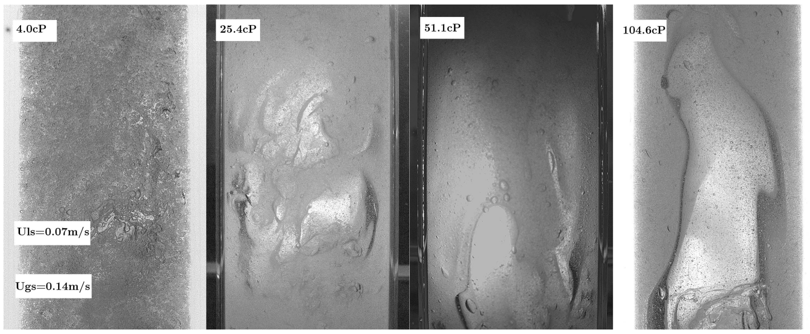

(b)

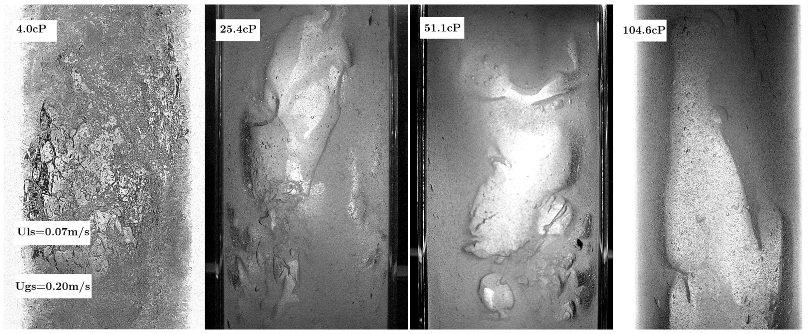

(c)

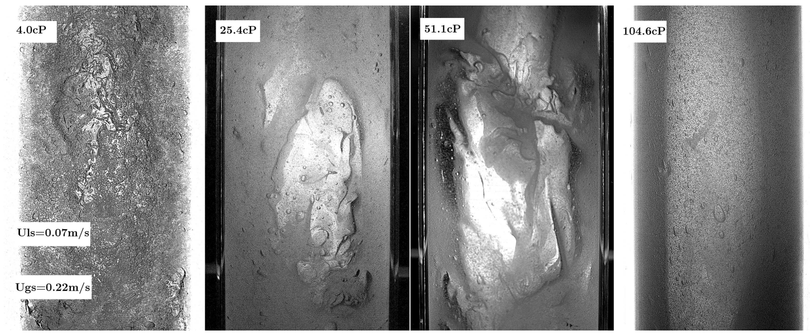

(d)

Fig. 4.21 Images of gas structures captured for the four viscosities at constant liquid superficial velocity ($U_{ls} = 0.07\,m/s$) arranged in ascending viscosity order from left (4.0 cP) to right (104.6 cP). (a) represents $U_{gs} = 0.12\,m/s$ (b) represents $U_{gs} = 0.14\,m/s$ (c) represents $U_{gs} = 0.20\,m/s$ and (d) represents $U_{gs} = 0.22\,m/s$. The figure shows the decreasing frothiness of the flow with increasing viscosity and the distinctively large difference in the shape of structures with increasing viscosity. (a) shows observation of Taylor bubble in a large diameter pipe for the first time in this range of viscosities.

shifts towards higher gas superficial velocity for all viscosities owing to the increased liquid turbulence effect; enhancing bubbles break-up. The Figure also expectedly indicates shifting of churn-annular transition to higher gas superficial velocity. In agreement with the observation of Figure 4.21, the Figure shows expansion of the slug flow region with increasing liquid viscosity and improved coalescence with increasing viscosity.

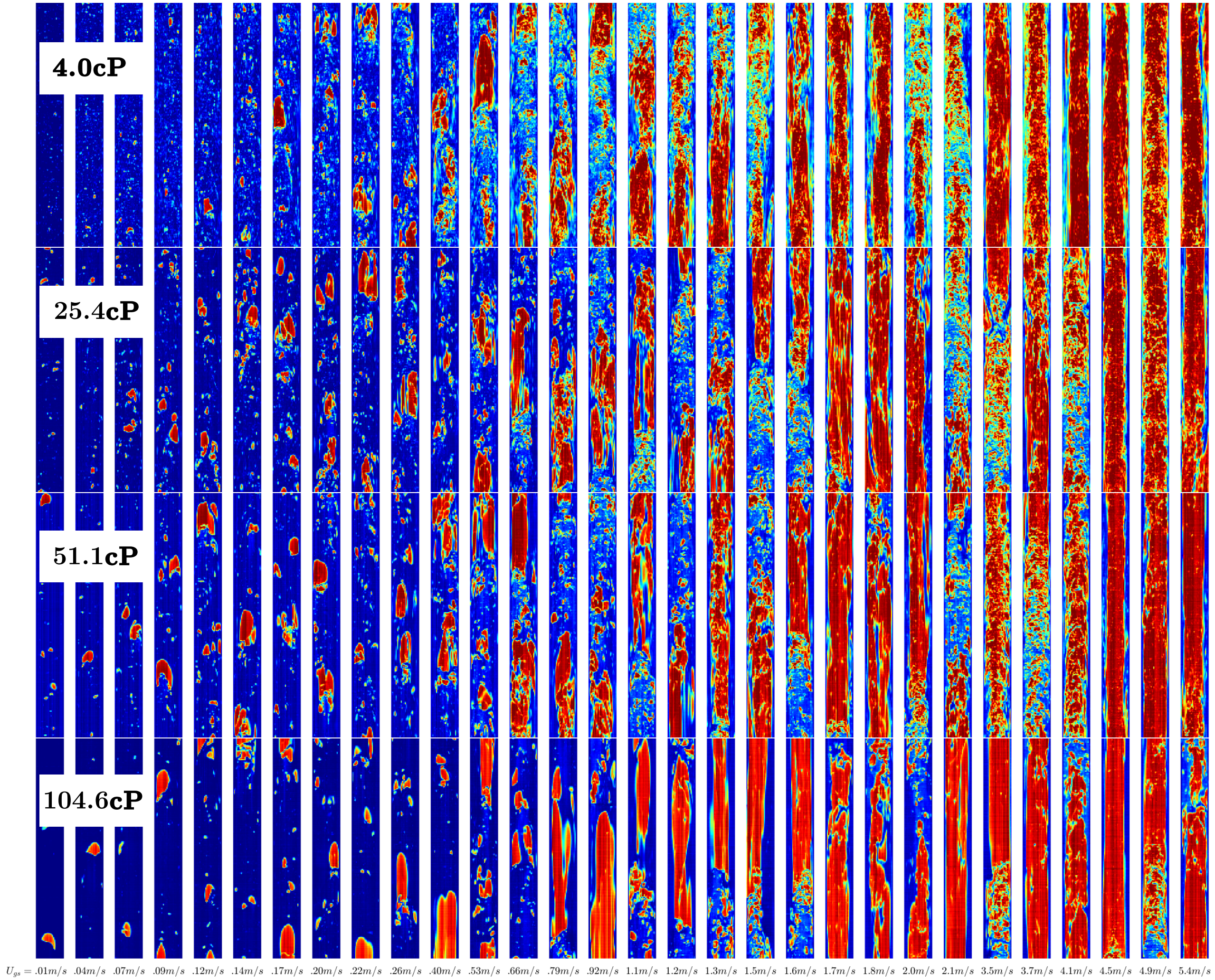

Fig. 4.22 Spatio-temporal images of void fraction distribution for the four viscosity mediums obtained at the $U_{ls} = 0.40\,m/s$. The y-axis represents the equivalent spatial distance based on the fluids translational velocity.

Figure 4.23 shows the spatio temporal images at the higher bound of liquid superficial velocity ($U_{ls} = 0.86\,m/s$). The figure provides more information about the shape of structures and incurring flow regime when liquid superficial velocity is increased more than ten folds the initial velocity. Expectedly, the figure indicates that bubbles become more disperse with increasing liquid superficial velocity. In addition transition boundaries from bubbly to slug flow shift towards higher gas superficial velocity in all the viscosities. Churn-annular flow is only observed at the higher bound of gas superficial velocity for the 4.0 cP oil,the corresponding images for the rest of the higher viscosities feature slug-churn flow regime. Another notable feature from the Figure is that transition boundaries seem to differ less between the different viscosities as the liquid superficial velocity is increased. That in addition to featuring a similar shape of structures between the different viscosities. This could be attributed to the increasing dominance of the liquid turbulence on coalescence-break-up rates.

Figure 4.23 shows that the shape of Taylor bubbles become slightly distorted and more irregular with increasing liquid superficial velocity. The Taylor bubbles seem to lose that bullet-shaped head and instead display agglomerated gas structures with a deformed tip at the pipe core. This is an attribute of the increasing liquid turbulence, intensifying bubble break-up and destabilising the interface. This observation can be further verified looking at the high speed images obtained for the same liquid superficial velocity ($U_{ls} = 0.86\,m/s$) at the low bound of gas superficial velocity ($U_{gs} = 0.01 - 0.09\,m/s$) shown in Figure 4.24. The Figure shows how bubbles maintain their dispersed distribution at the lowest viscosity, while they coalesce and grow bigger with increasing viscosity. Compared to the case of lower liquid superficial velocity presented in Figure 4.21, it can be seen that the size of gas structures/bubbles is significantly smaller at the same viscosity and gas superficial velocity. Looking at the change in the size of bigger bubbles/gas structures between different viscosities, it can be seen, compared to the case at lower liquid superficial velocity, that the difference in size does not seem to be as significant. Moreover, the density of smaller bubbles dispersed in the liquid bulk evidently seems to decrease with increasing viscosity. These observations come in conformity with the spatio-temporal images shown in Figure 4.23. Also in agreement with the conditions at lower liquid superficial velocity, it seems that at this lower range of gas superficial velocity, increasing liquid superficial velocity does not seem to significantly distort the cap-shaped tip of the gas structures at the highest viscosity.

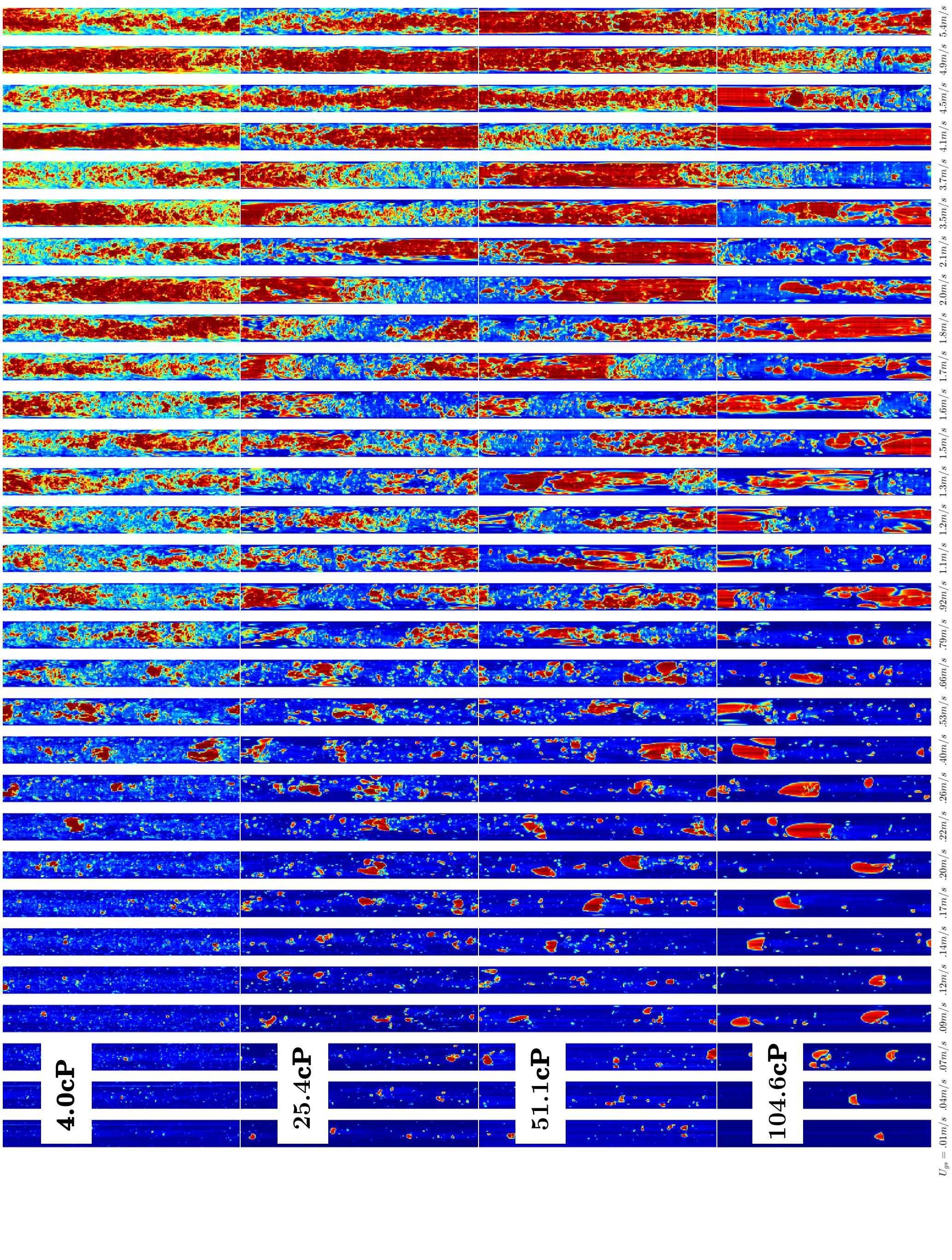

Fig. 4.23 Spatio-temporal images of void fraction distribution for the four viscosity mediums obtained at the $U_{ls} = 0.86m/s$. The y-axis represent the equivalent spatial distance based on the fluids translational velocity.

To investigate further into the effect of liquid superficial velocity on shapes on gas structures Figure 4.25 is presented. It shows images for a higher range of gas superficial velocity similar to the ones in Figure 4.20, but at higher liquid superficial velocity ($U_{ls}- = 0.86\,m/s$). In coherence with the observations stemmed from Figure 4.24 the images show that the size of both small bubbles dispersed in the liquid bulk and the bigger gas structures seem to increase with increasing viscosity. With increasing gas superficial velocity, especially at higher viscosity, the Taylor bubbles/gas structures seem to deviate slightly from the core of the pipe, instead becoming rather elongated showing a more pointy tip and a thinner width along the body of the bubble as evident in Figure 4.25c and 4.25d. Comparing to images in Figure 4.20 it can be seen that, other than the substantially smaller size of bigger bubbles, the density of smaller bubbles in the liquid bulk is much smaller at higher liquid superficial velocity while their size is visibly bigger. This might suggest that the increased liquid turbulence works mostly towards breaking down bigger bubbles possibly upto a certain gas superficial velocity above which bubble induced turbulence enhance breaking smaller bubbles creating the milky liquid bulk observed at higher gas superficial velocities.

Figure 4.26 shows the variation of transition boundaries with changing viscosity plotted in the flow regime map of Taitel et al (1980) for all the viscosities studied [173]. The incurring flow regime was characterised using a combination of techniques; looking at videos of the spatio-temporal images from the WMS, the high speed imaging videos collected downstream the test section, and the shape of the PDF of void fraction time series. As can be seen the flow regime boundaries deviate significantly from the Taitel's (1980) map even at the lowest viscosity studied. That can be referred to the significant variation of behaviour in large diameter pipes due to the reduced wall effect as extensively discussed in [135]. The second attribute is the liquid's physical properties that are remarkably deviant than water, from which most of the experimental regime maps are constructed.

Figure 4.26 shows that transition boundaries from bubbly to slug flow, slug-churn, and churn-annular transition boundaries for the all viscosities except for Figure 4.26d where annular flow regime was not observed in all the runs. As can be seen with increasing liquid viscosity the bubbly-slug transition boundary shift to lower gas superficial velocity. On the other hand, slug-churn and churn-annular transition boundaries shift to higher gas superficial velocity with increasing viscosity. This suggests that with increased liquid viscosity the probability of having slug flows in pipelines is very likely and therefore it might require considerable adjustment to the

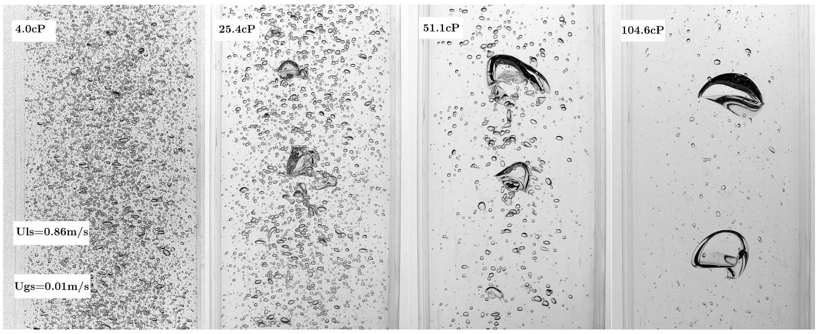

(a)

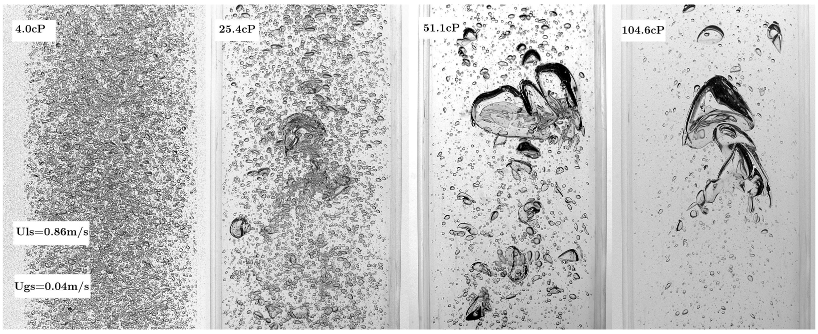

(b)

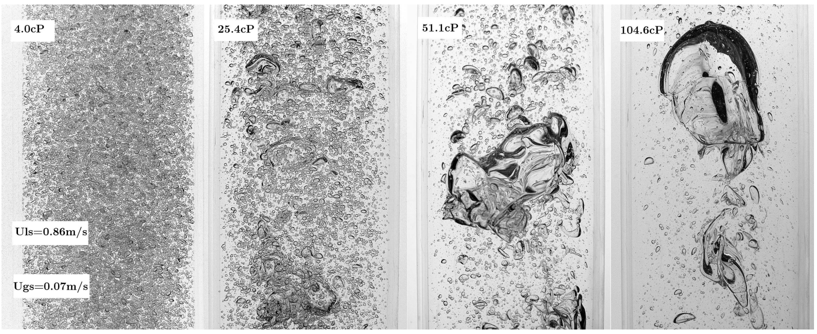

(c)

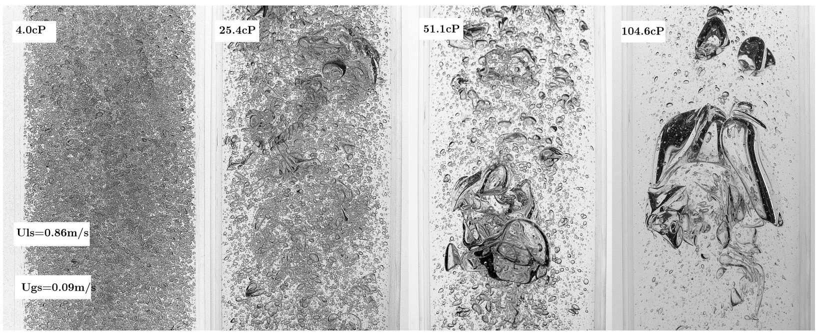

(d)

Fig. 4.24 Images of gas structures captured for the four viscosities at constant liquid superficial velocity ($U_{ls} = 0.86\,m/s$) arranged in ascending viscosity order from left (4.0 cP) to right (104.6 cP). (a) represents $U_{gs} = 0.01\,m/s$ (b) represents $U_{gs} = 0.04\,m/s$ (c) represents $U_{gs} = 0.07\,m/s$ and (d) represents $U_{gs} = 0.09\,m/s$. The figure shows the decreasing frothiness of the flow with increasing viscosity and the distinctively large difference in the shape of structures with increasing viscosity.

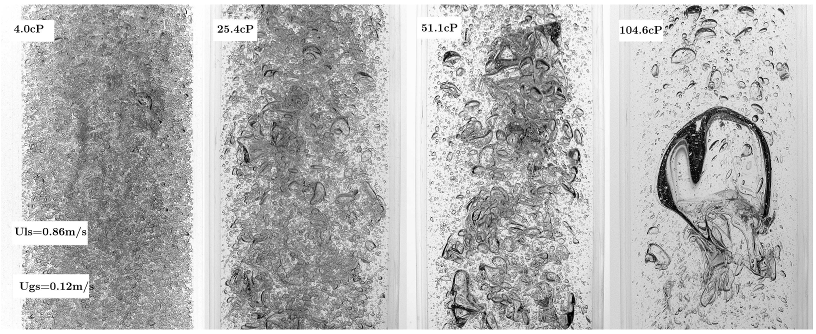

(a)

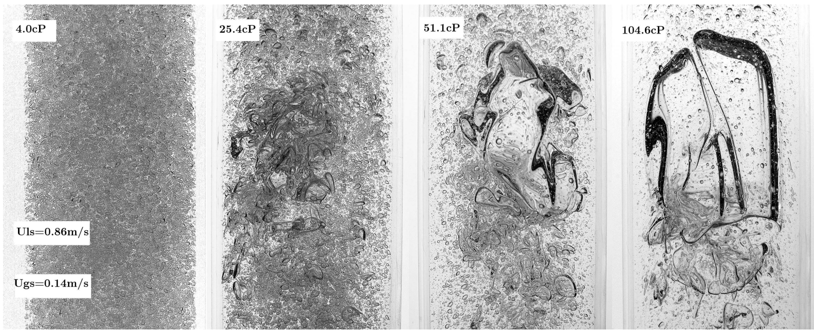

(b)

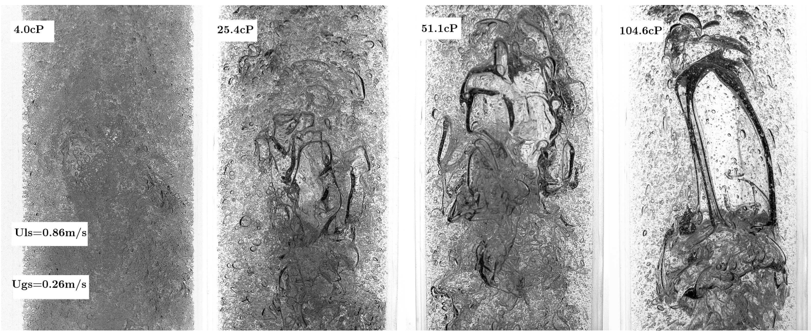

(c)

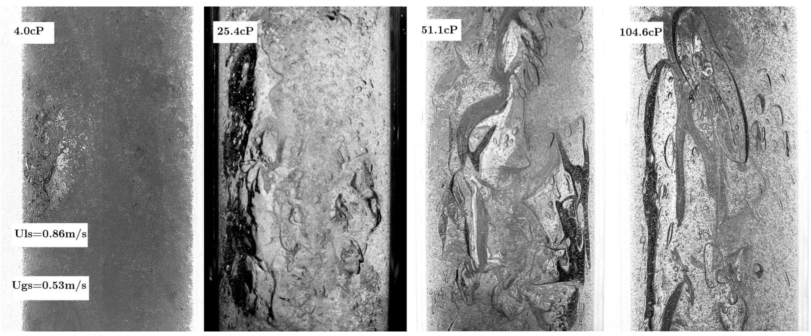

(d)

Fig. 4.25 Images of gas structures captured for the four viscosities at constant liquid superficial velocity ($U_{ls} = 0.86\,m/s$) arranged in ascending viscosity order from left (4.0 cP) to right (104.6 cP). (a) represents $U_{gs} = 0.12\,m/s$ (b) represents $U_{gs} = 0.14\,m/s$ (c) represents $U_{gs} = 0.26\,m/s$ and (d) represents $U_{gs} = 0.53\,m/s$. The figure shows the decreasing frothiness of the flow with increasing viscosity and the distinctively large difference in the shape of structures with increasing viscosity.

velocities to be avoided. Moreover, it can be seen that transition boundaries become more steeper with increasing viscosity, suggesting that liquid superficial velocity has a more significant effect on the regime transition. Meaning that at higher viscosity if liquid superficial velocity is increased ever slightly, it will require much more increase in gas flow to achieve a regime transition compared to the amount of gas boost needed for a lower viscosity liquid.

It can be noted that at 104.6 cP the bubbly-slug transition boundary overlapped with that of Taitel, which implies that with increasing viscosity the behaviour in large diameter pipes becomes more resemblant to that in small diameter pipes, mainly due to the increased confining effect of the wall with increasing viscosity. This observation on the effect of visocisty on flow regime transition is consisent with that of Furukawa and Fukano (2001) [63]. Alruhaimani et al (2016) reported different findings where they observed no change in bubbly-slug and slug-churn transition boundaries with increasing viscosity and a shift towards lower gas superficial velocity with increasing viscosity [9]. Such behaviour might be the case for the viscosities they considered (127-586 cP) which are higher than viscosities investigated in this study. It is intriguing to find out if the behaviour at higher viscosities will follow their observation.

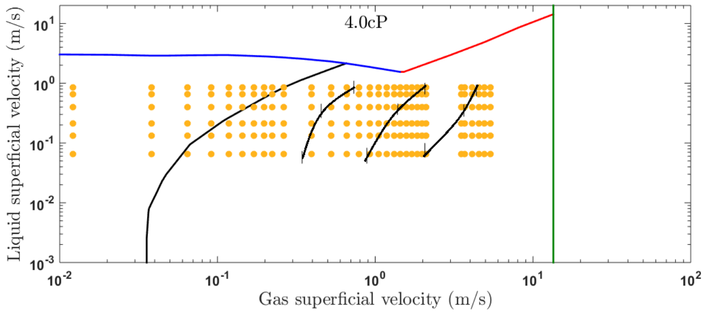

(a)

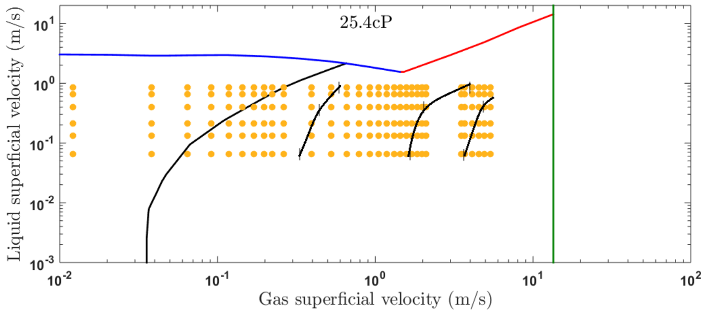

(b)

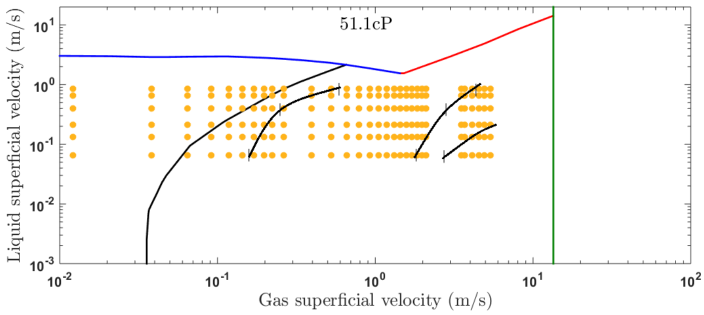

(c)

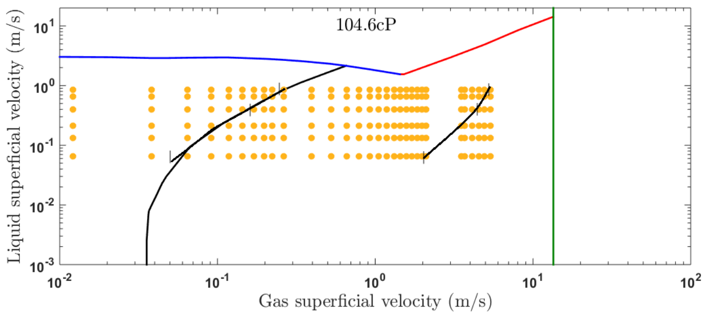

(d)

Fig. 4.26 Variation of flow regime boundaries with increasing viscosity, plotted in the flow regime map of Taitel et al (1980). (a) for 4.0 cP, (b) for 25.4 cP, (c) for 51.1 cP and (d) for 104.6 cP viscosities. The Figure illustrates the shifting of transition boundary from bubbly to slug flow towards lower gas superficial velocity with increasing viscosity. Slug-Churn and churn-annular transition boundaries however shift towards higher gas superficial velocity as viscosity rises.

4.2.8 Effect of viscosity on the velocity and frequency of structures

Gas structure velocity is calculated by means of cross-correlating the cross-sectionally averaged void fraction time series acquired by the two closely located planes of the ECT sensor. In the case of current experiments, structure velocity was calculated at both upstream and downstream the test section. This information gives added insight into the flow development and an indication of change of structures' shapes and sizes as they rise in the test section.

As indicated from the results discussed earlier, increase in viscosity generally results in a drop of void fraction. However, at lower gas superficial velocity, it was observed that void fraction exhibits an increase initially with increase of viscosity then eventually decreases. From the inversely proportional relationship of void fraction and average gas velocity $U_g = \frac{Ugs}{\epsilon_g}$ it is expected that the structure velocity will increase in general with increasing viscosity. This can be referred to the increase of bubble size due to the stabilisation effect of viscosity with increasing viscosity and therefore increase in their average rise velocity.

Previous works in the literature have reported decrease of structure velocity with viscosity, and it was mainly attributed to the increase in drag force due to viscosity effect that reduces the drift velocity of the bubbles altogether with the liquid adjacent to the pipe wall [103, 32]. However the data and model proposed by Schmidt et al (2008) demonstrate a positive proportionality between viscosity and slip ratio (hence gas structure velocity) [159].

Figure 4.27a shows the evolution of structure velocity with gas superficial velocity for the lowest (4.0 cP) and highest viscosity (104.6 cP) studied in this work measured at 15D axial distance from injection point. To better visualise the difference in structure velocity between the two viscosities Figure 4.27b shows the two quantities plotted against each other. Figure 4.27 shows that at low gas superficial velocity, the velocity profile at low viscosity seems to decrease slightly, then increase or equate with the lower viscosity profile to decrease again as gas superficial velocity is increased. However, at lower gas superficial velocity, the profiles seem to follow a different trend especially at higher liquid superficial velocity, where higher viscosity structure velocity becomes higher than that of the lower viscosity. This is most likely a reflection of the transition from homogeneous bubbly flow regime to the non-homogeneous or undistributed flow regime that has been exhaustively reported in bubble column systems [156, 32, 137].

It has been reported that increase in viscosity stabilises the dispersed bubbly regime (homogeneous regime), that might explain why the same behaviour is not exhibited by the 4.0 cP viscosity profile. The reason why this behaviour is only observed at higher liquid superficial velocity is seemingly because higher liquid velocity shifts coalescence-break-up towards more break-up rate. Therefore increase in gas flow contributes mainly towards increasing concentration of small bubbles that remain virtually at same size, hence the plateau in structure velocity profile whilst the bump in void fraction profile (see Figure 4.7).

At intermediate gas superficial velocity range($U_{gs} = 1.5 - 2.5\,m/s$) it is observed that the profile takes another turn almost for all liquid superficial velocities where structure velocity becomes higher for higher viscosity. That might be attributed to transition to undistributed/cap-bubbly flow regime where larger and more stable bubbles are formed at higher viscosity that rise in a considerably larger velocity compared to situation at lower viscosity. It could also correspond to the slug flow regime that higher viscosity creates longer "Taylor bubbles" according to [103]. The profile changes sign again at higher gas superficial velocity where lower structure velocity is registered at higher viscosity. This might correspond to condition where the flow regime has transitioned to annular flow and the structure velocity captured correspond to huge waves or wisps on the liquid film that will probably travel slower at higher viscosity due to the higher drag force near the wall although the liquid film is reported to become thicker at higher viscosity [62, 103].

Figure 4.28 shows the structure velocity calculated downstream the test section at 62D axial distance from the injection point. It seems that the previous changes of trend observed near the injection point nearly diminish as the fluids rise in the test section where structures have more time to develop. The difference in structure velocity between the low viscosity and the higher viscosity seems to diminish at lower gas superficial velocity where no appreciable difference can be spotted. However, the higher viscosity profile becomes markedly lower at higher gas superficial velocity, which is most likely reflecting higher velocity structures on the liquid film at annular and near annular flow conditions.

A similar behaviour to Figure 4.28 is observed when comparing structure velocity profiles of 51.1 cP and 25.4 cP viscosities against 4.0 cP viscosity. Viscosity does not seem to affect structure velocity considerably at lower gas superficial velocity, as gas velocity is increased, structure velocity of higher viscosity becomes appreciably lower than that of lower viscosity. The only anomaly to that is when comparing the

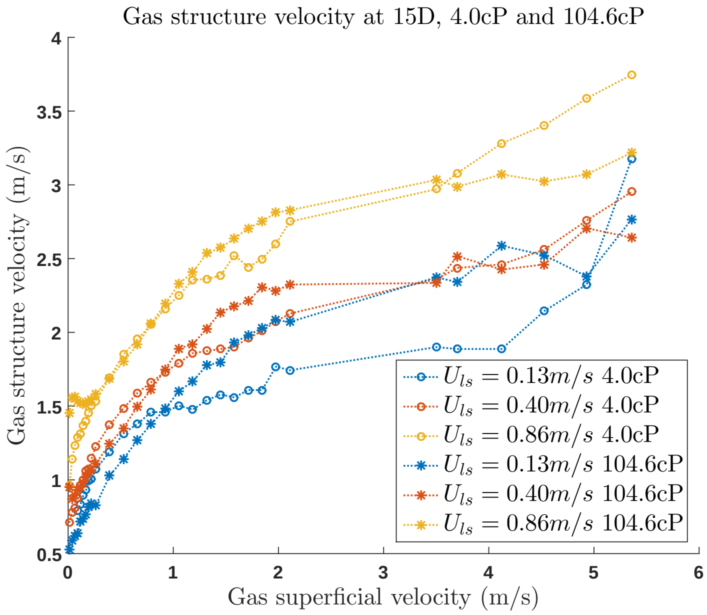

(a)

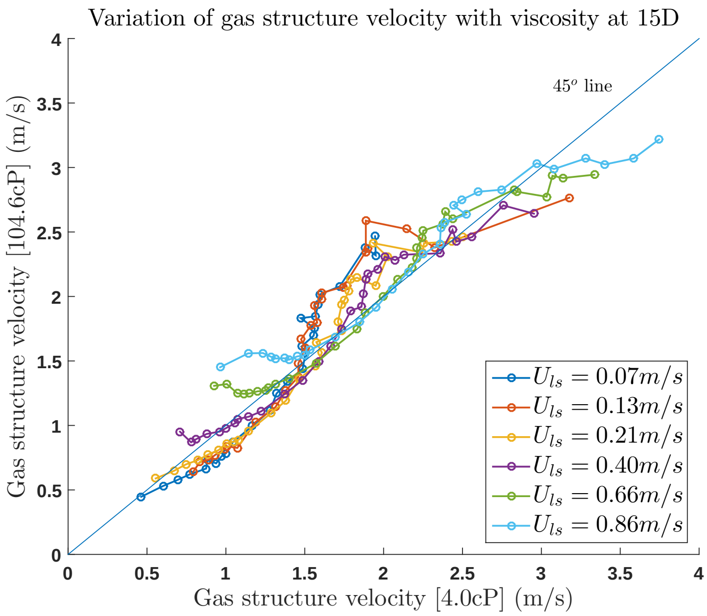

(b)

Fig. 4.27 (a)Variation of structure velocity calculated via cross-correlation of void fraction time series at 15D axial distance from the injection point with gas superficial velocity open circles (o) represent 4.0 cP viscosity and the asterisk (*) represent 104.6 cP viscosity. (b) Gas structure velocity calculated at 4.0 cP plotted against structure velocity of 104.6 cP.

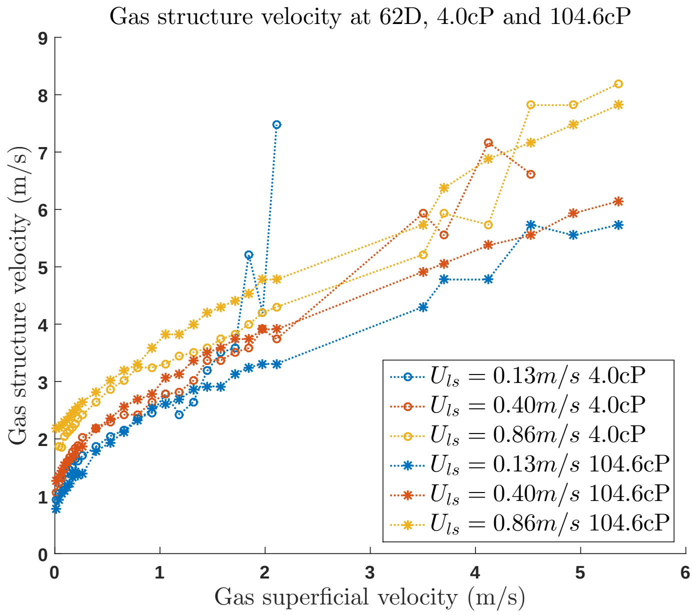

(a)

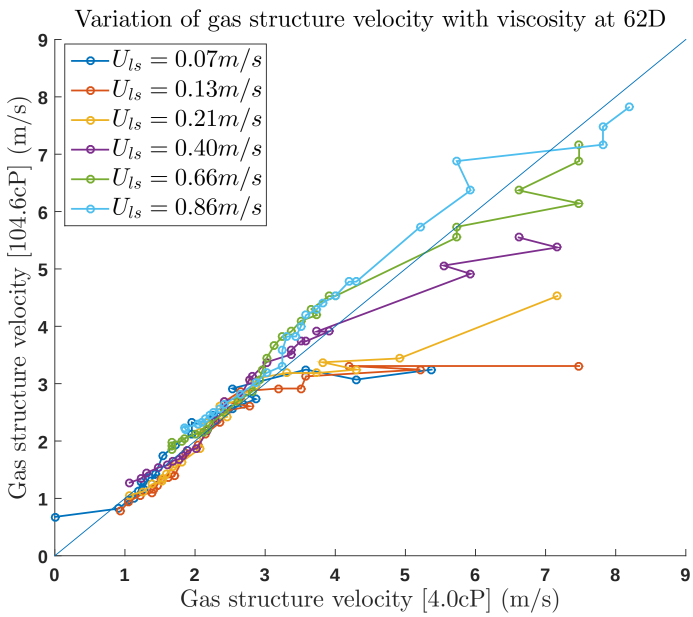

(b)

Fig. 4.28 (a)Variation of structure velocity calculated via cross-correlation of void fraction time series at 62D axial distance from the injection point with gas superficial velocity open circles (o) represent 4.0 cP viscosity and the asterisk (*) represent 104.6 cP viscosity. (b) Gas structure velocity calculated at 4.0 cP plotted against structure velocity of 104.6 cP.

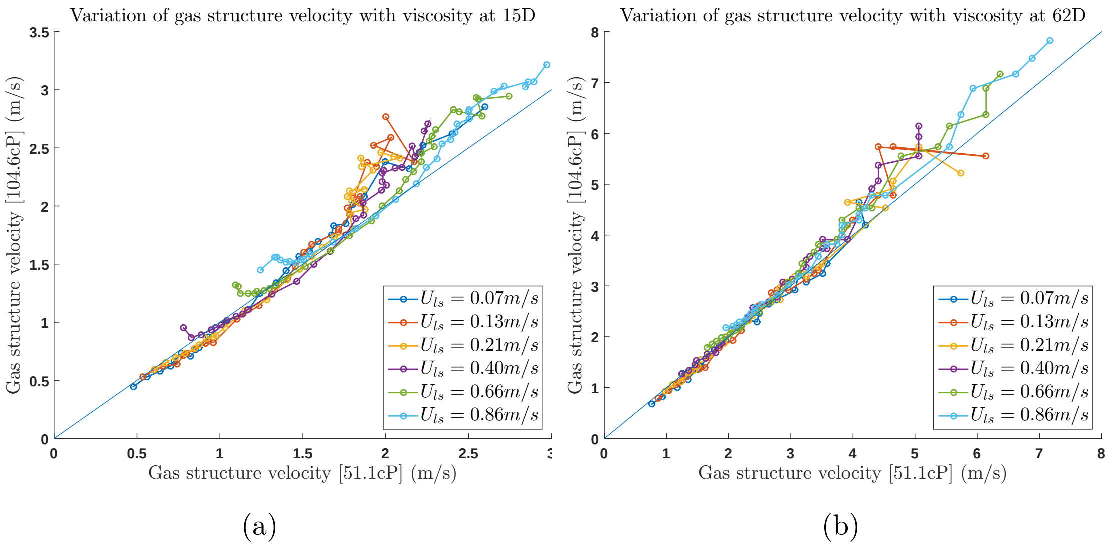

Fig. 4.29 Structure velocity profile of 51.1 cP plotted against that of 104.6 cP (a) upstream the test section (15D axial distance) and (b) downstream the test section (62D axial distance from injection). The Figure shows average increase in structure velocity with increasing viscosity.

profile of 51.1 cP against the 104.6 cP where higher structure velocity on average is registered for the higher viscosity fluid (104.6 cP) both upstream and downstream the test section as depicted in Figure 4.29. The decrease in structure velocity with viscosity can be attributed to increased drag force on the interface. Besagni et al (2017) calculated swarm velocity in a large diameter bubble column by means of video tracking bubbles near the wall for different viscosities ranging from 0.89 cP to 7.9 cP. The results indicated both decrease and increase of swarm velocity with viscosity. However, the swarm velocity might not be particularly representative of all bubbles since it only considers bubbles near the wall [32]. Kajero et al (2012) [103] observed the decrease of structure velocity with increasing viscosity in bubble column setting, but in a considerably lower range of gas superficial velocity. Alruhaimani (2015) [15] observed a slight increase in the structure velocity with increasing viscosity. The linear fittings produced from their data showed an increase in drag coefficient(C_o) with increasing viscosity, and a decrease in drift velocity (V_d). This observation is to some extent analogous with the current study in the lower range of gas superficial velocity, however, the superficial velocity they studied was limited by a smaller range.

To investigate the effect of axial distance on flow development and structure velocity, the profiles upstream and downstream of the test section are compared as depicted in Figure 4.30. It is observed that the structure velocity exhibits a behaviour that can be

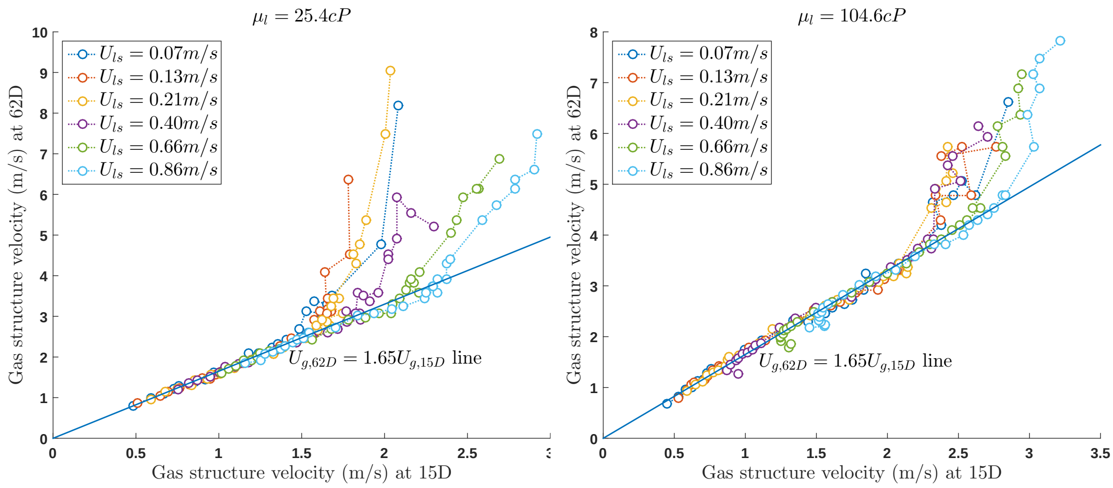

(a) (b)

Fig. 4.30 Two regimes of variation of structure velocity with axial position. The Figure shows structure velocity at 62D plotted against that at 15D for (a) 25.4 cP viscosity and (b) 104.6 cP viscosity. The figure features the relationship where the velocity downstream the test section increases by about 65% for a certain range of velocities irrespective of viscosity or liquid superficial velocity.

categorised into two different regimes. First regime, is at lower range of gas superficial velocity, where structure velocity was found to increase by a constant factor of about 65% for all the viscosities studied when structures rise from 15D to 62D axial distance irrespective of the liquid superficial velocity. Above a certain gas superficial velocity value (the second regime), the structure velocity increases by a value much higher than 65% downstream the test section. The rate of increase in structure velocity is directly proportional to the liquid superficial velocity as can be seen from the slopes on Figure 4.30. The dependency on liquid superficial velocity is seen to decrease with increasing viscosity, where transition of regime is observed to be independent of liquid superficial velocity at 104.6 cP. This can be attributed partly to what was discussed earlier in section 4.2.3 where viscosity effect on void fraction was observed to decrease with increasing viscosity, at higher gas and liquid superficial velocity the viscosity effect on void fraction becomes almost independent of both gas and liquid input (see Figure 4.10 and Figure 4.11).

Effect of viscosity on frequency has been studied with greater focus in horizontal flows and particularly for slug flow regime where prediction of slugs frequency is of huge significance for two-phase flow installations [65, 59, 29]. However, a limited number of studies have investigated the effect of viscosity on frequency for vertical flows [143, 172, 182, 2]. In horizontal flows it has been reported that viscosity rise results in an increase in the frequency of slugs and a decrease in their length according to [29, 65]. A similar behaviour was reported for vertical flows by [15, 172], while [143] reported an increase in slugs frequency but a decrease in that of huge waves with increasing viscosity. The increase in frequency with viscosity is analogous to the decrease in void fraction with viscosity. As discussed earlier, reduced void fraction necessitates formation of larger gas structures with higher rise velocity, therefore a higher passing frequency is expected.

Figure 4.31 shows the evolution of frequency with gas superficial velocity for all liquid superficial velocities studied both upstream and downstream the test section. Quintessentially, the data presented in Figure 4.31 suggests that increase in viscosity results in a slight increase of the characteristic frequency of gas structures. This comes in agreement with the previous reports in both vertical and horizontal flows [15, 172, 29, 65]. However, at lower gas superficial velocity the situation seems to differ where lower frequency is registered for the higher viscosity fluid. Szalinski et al (2010) reported a smaller frequency for higher viscosity in bubble column setting at low gas superficial velocity ($U_{gs} < 0.4\, m/s$) which could be comparable to the case at hand to some extent [172]. The behaviour at low liquid superficial velocity can be attributed to the increase of coalescence rate with increasing viscosity and therefore lower frequency bigger bubbles are formed. The profiles seem to undergo an inversion point as gas superficial velocity is increased. This inversion point might correspond to flow regime change from cap-bubbly to slug flow. The inversion point appears to move towards lower gas superficial velocity with increasing liquid velocity.

It is also observable that effect of viscosity on frequency lessens with increasing liquid superficial velocity where all profiles almost collapse into a single line. This comes in concordance with what observed in earlier sections on the decrease of viscosity effect on void fraction with increasing liquid velocity. One might argue that it is an illusion due to change of scale on the y-axis, yet the relative change of frequency is minimal and the statement should still hold. Figure 4.34 shows the relationship with greater calrity. On a general note the results confirm the known observation that frequency increases with liquid velocity and decreases with increasing gas superficial velocity [163, 2, 172]. A plausible explanation for this is the growth of gas structures length with increasing gas velocity and therefore decrease in their passing frequency. Moreover, a slight increase in frequency can be observed at the higher bound of gas superficial velocity and lower liquid superficial velocity. The rise in frequency might be linked to the transition to froth-annular flow where most liquid is transported through huge waves in the liquid film that travel faster with the increase of the velocity of the shearing gas core. A similar observation was reported by Sharaf et al (2016) and others [163, 143, 182].

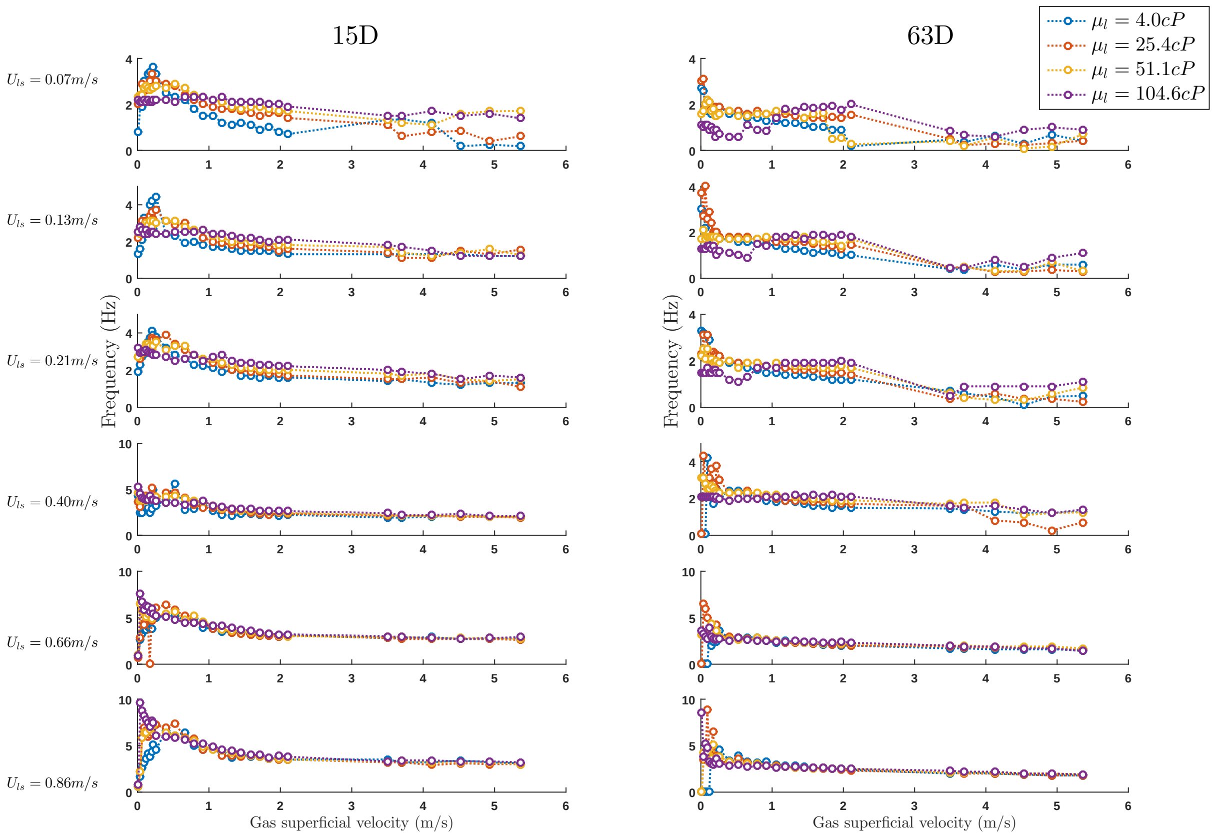

Fig. 4.31 Frequency evolution with gas superficial velocity upstream and downstream the test section at various liquid superficial velocities for the four viscosities studied.

Figure 4.32 shows frequencies of higher viscosity plotted against frequencies obtained for the lowest viscosity studied (4.0 cP). The figure shows that most of the data points fall within ±20% although it is observable that most points fall above the 45^o line. This strongly suggests that viscosity does increase frequency, however the effect can be described as insignificant. The aforementioned statement might not apply to all flow regimes. It is expected that these effects vary with flow regimes as can be stemmed from Figure 4.31 where considerably deviant regions can be spotted between the different viscosity profiles.

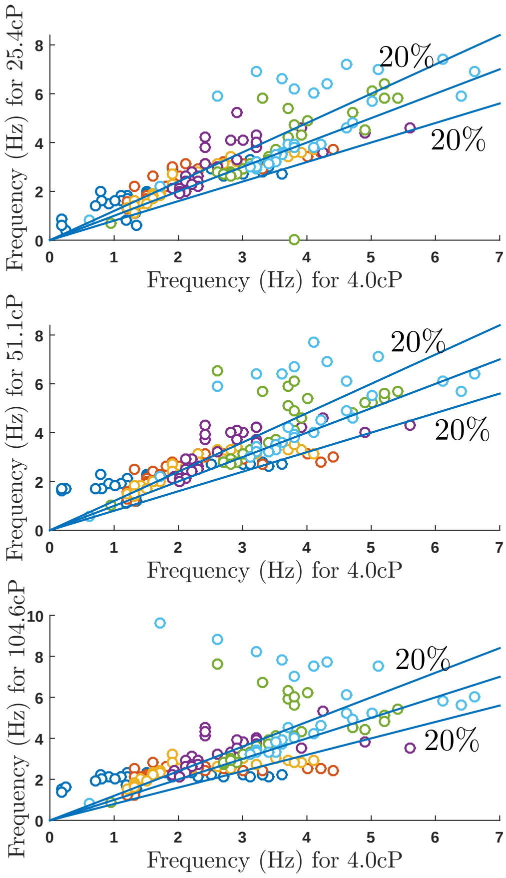

Fig. 4.32 Higher viscosities frequency plotted against lowest viscosity studied (4.0 cP). A slight increase in frequency with increasing viscosity is notable despite the few outliers.

When comparing profiles upstream and downstream the test section Figure 4.33 shows that frequency exhibits a dramatic decrease with increasing axial distance. Figure 4.33 suggests that an average drop by about 40% is achieved when structures rise from 15D to 63D axial distance from the injection point. This is most likely a development effect where gas structures get more time to coalesce and develop as they rise in the test section. As demonstrated from the time series analysis, the flow is not considered developed at 15D axial distance, however above 50D axial distance it is suggested that the flow becomes developed. It can also be observed that the variation of frequency with axial position does not seem to differ with the viscosities studied, it remains virtually constant around 40%.

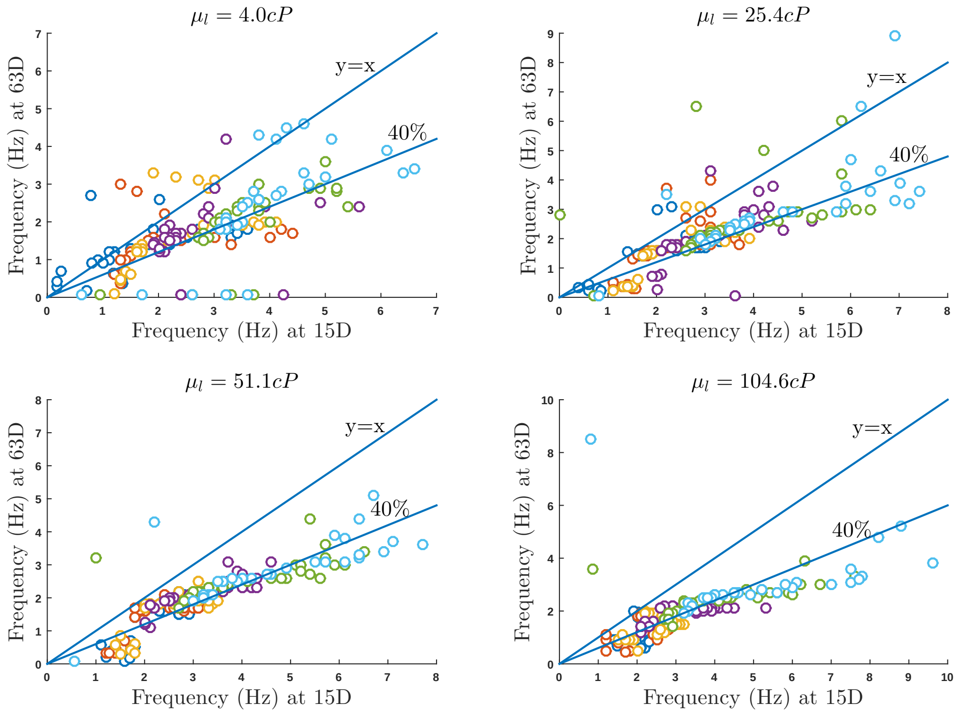

Fig. 4.33 Variation of the structures' characteristic frequency with axial position for the four studied viscosities. An average decrease in frequency by about 40% is observed owing to flow development.

Figure 4.34 illustrates the relationship of liquid superficial velocity with frequency and how it changes with variation of gas superficial velocity. The black lines provide and indication for the disparity of the data. The middle line represents mean linear fit for the frequencies of all the viscosities, the other two lines represent the 20% deviation boundaries. The linear increase of structure frequency with liquid superficial velocity is plainly evident on the figure. In addition, the profiles show a higher frequency for the higher viscosity fluid on average, in conformity with the relations in Figure 4.31 and 4.32. It is also clear that different viscosity lines comes closer at higher liquid superficial velocity (except at lower gas velocity range); which suggests that viscosity effect on flow lessens at high liquid turbulence level. An observation that has been drawn in multiple occasions in this chapter from different two-phase flow characteristics.

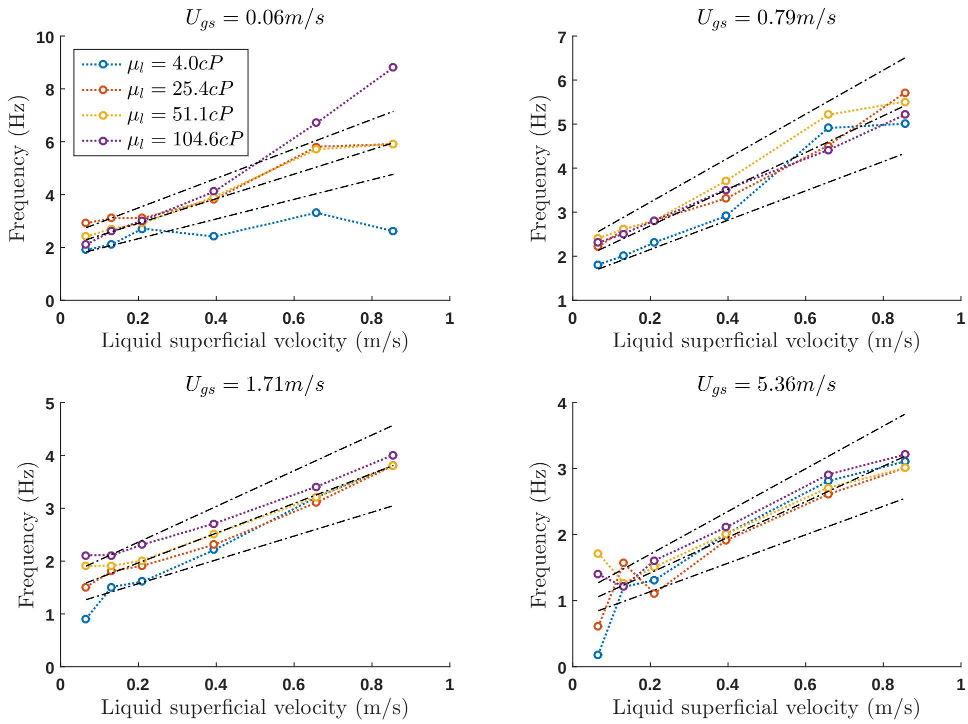

Fig. 4.34 Effect of liquid superficial velocity on structures characteristic frequency plotted for all viscosities studied. The black lines represent the best fit line for the mean of the frequency values at the corresponding liquid and gas velocity and the ±20% deviation lines.

4.2.9 Effect of viscosity on bubble size distribution

Bubble size distribution is calculated using Prasser's (2001) filling algorithm from the WMS data. More information about the algorithm can be found in [147]. Care must be taken when discussing these results, due to the limited spatial resolution of the WMS (∽2.0mm); smaller bubbles will not be represented, especially at higher viscosities where the dispersed bubbles in the liquid bulk appear to be much smaller. However, these bubbles are counted for in the cross-sectional measurements.

Rabha et al (2014) studied the effect of viscosity on bubble size distribution in a large diameter bubble column, investigating viscosities in the range 1.33-1149 cP. They observed a decrease in bubble size with increasing viscosity up to 8.95 cP, above which bubble size increases as viscosity is raised. They also observed an increase in the bubble size with increasing gas superficial velocity [151].

Figure 4.35 shows the bubble size distribution for a selection of gas and liquid superficial velocities across the studied range for the four viscosities. At higher gas superficial velocity where churn-annular flow is observed, bubble size distribution was not calculated. The distribution is expressed in terms of % of contribution by each cluster of bubbles of a certain average equivalent diameter to the overall volumetric void fraction (%/mm) plotted against volume equivalent bubble diameter in (mm). At lower gas superficial velocity it can be clearly seen that increasing viscosity dramatically increases the bubble size and shifts the distribution away from the homogeneous phase, with bubbles of proportionate sizes featuring a sharp peak distribution. Bubbles seem to grow and become more diverse in size with increasing viscosity. This is evident from the change in the shape of the bubble size distribution becoming more flattened, spreading across a wider range of bubble sizes with increasing viscosity.

Increasing gas superficial velocity generates bigger bubbles creating a bimodal distribution with a second peak at larger bubble diameter. The bigger bubble diameter represents the average diameter of gas structures; be it cap-bubbles, Taylor bubbles, or large gas structures. Although the bimodal shape is produced by all the viscosities, yet it can be clearly seen that the bigger peak extends to a larger bubble diameter with increasing viscosity.

Furthermore, it can also be observed from Figure 4.35 that the smaller diameter peak (bubbles dispersed in liquid) is always shorter for the higher viscosity fluid, which suggests that frothiness of flow decreases with increased viscosity. In other words, concentration of smaller bubbles trapped in the liquid bulk decreases with increasing viscosity, although their sizes exhibit a slight increase with increasing viscosity. At the higher bound of gas superficial velocity it is observed that larger gas structures are formed by the lower viscosity fluids, which suggests that shorter gas structures are formed by higher viscosity which suggests that increasing viscosity initially increases bubble size, above a certain value the effect reverses. This comes in agreement with the slug-churn transition observation reached in earlier sections, where transition boundary was observed to shift towards higher gas superficial velocity with increasing viscosity.

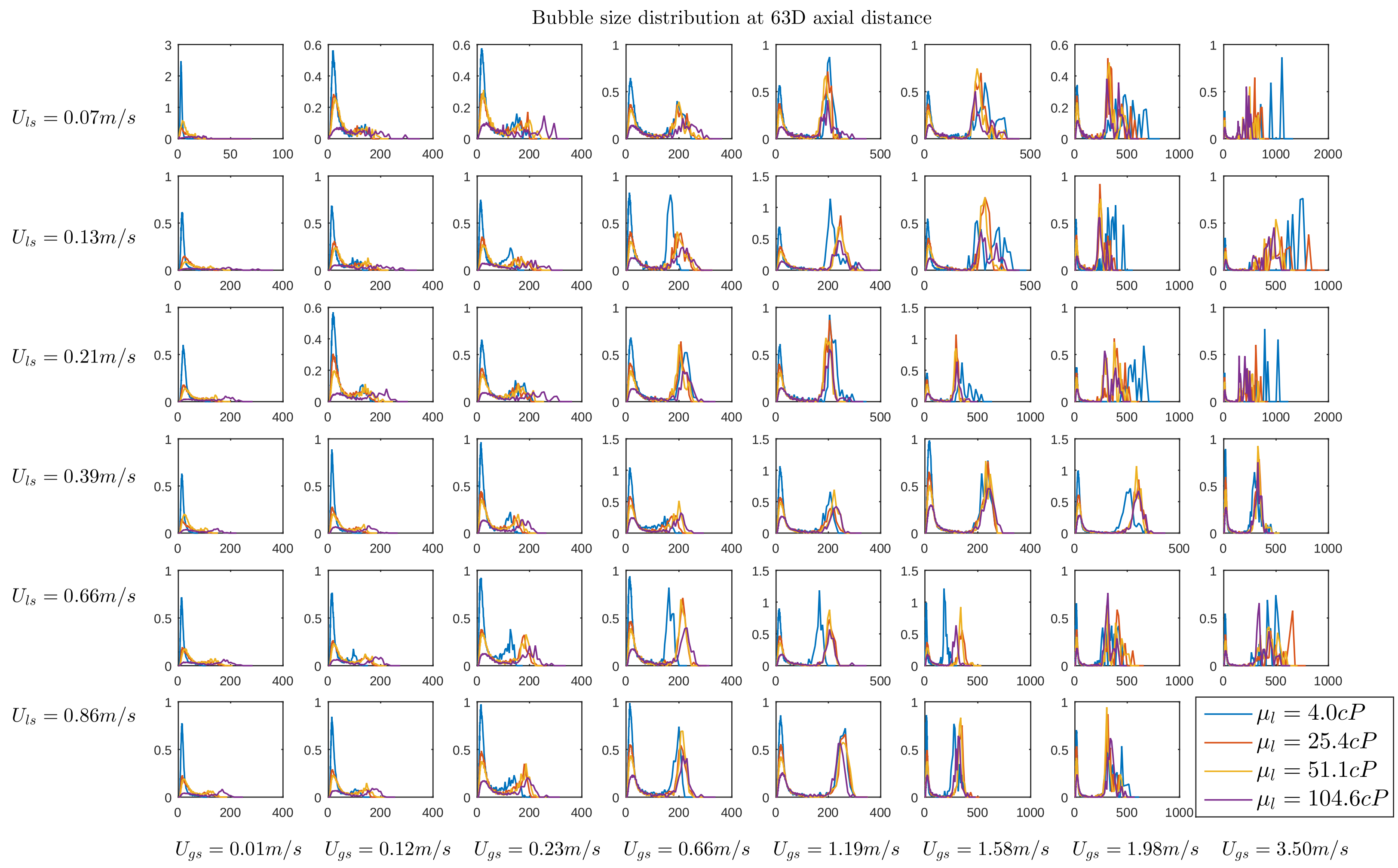

Fig. 4.35 Bubble size distribution computed using Prasser's algorithm for the studied matrix of gas and liquid superficial velocities expressed as % contribution to the volumetric void fraction by each class of bubbles $[\frac{\Delta\epsilon}{\Delta d_B}](\%/mm)$ (y-axis) plotted against volume equivalent diameter in the x-axis in (mm).

To further demonstrate the effect of viscosity on bubble size, Figure 4.36 is shown. The figure shows average bubble size profiles produced by the four different viscosity fluids at equal gas and liquid superficial velocities. The average bubble diameter is calculated from equation 4.5 below. As can be seen higher viscosity produces bigger bubbles consistently throughout the studied experimental matrix. This provides further consolidation to the enhancing effect of viscosity on bubbles coalescence deduced from the many other attributes of two phase flows discussed in this chapter.

$$d_{B,average} = \frac{\sum\left(\frac{\Delta\epsilon}{\Delta d_B}\right).d_B}{\sum\left(\frac{\Delta\epsilon}{\Delta d_B}\right)} \tag{4.5}$$

Figure 4.36 also shows that increase in gas superficial velocity increases bubble size almost linearly. The difference in bubble sizes produced by different viscosities seems smaller at lower gas superficial velocity. At lower liquid superficial velocity a slight decrease in bubble size with increasing gas superficial velocity is observed. The decrease becomes steeper and more pronounced with increasing viscosity. This is synonymous to the behaviour of structure velocity profiles obtained in Figure 4.27, where bigger bubbles that has faster terminal velocity are formed, with increasing gas input bubble induced turbulence enhances bubbles' breakup and dramatically reduces the bubble size, before it rises back up again due to the formation of very small bubbles in the liquid bulk that reduces its effective viscosity. Due to the higher drag in the higher viscosity fluids, the bubble-induced turbulence is more significant at higher viscosity fluids and therefore was not observed at lower viscosities.

Figure 4.37 allows the study of liquid superficial velocity effect on bubble distribution. It is expected that increasing liquid turbulence enhances bubbles' break-up and therefore smaller bubbles are generated. This behaviour is observed at the lower range of liquid superficial velocities, where a sharp decrease in bubble size is observed with increasing liquid input, however at higher velocity (specifically above 0.40 m/s) the bubble size remains constant or even increase with increasing liquid input. It is also observable from Figure 4.37 that at lower gas superficial velocity, an increase in bubble size is observed with increasing liquid flow, this might be referred to the effect of bubble induced turbulence where the increase of liquid input decreases the number of bubbles and therefore hiders the break-up induced by faster bubbles creating eddies in their wakes. However, above a certain gas input this effect becomes negligible due to the high concentration of bubbles.

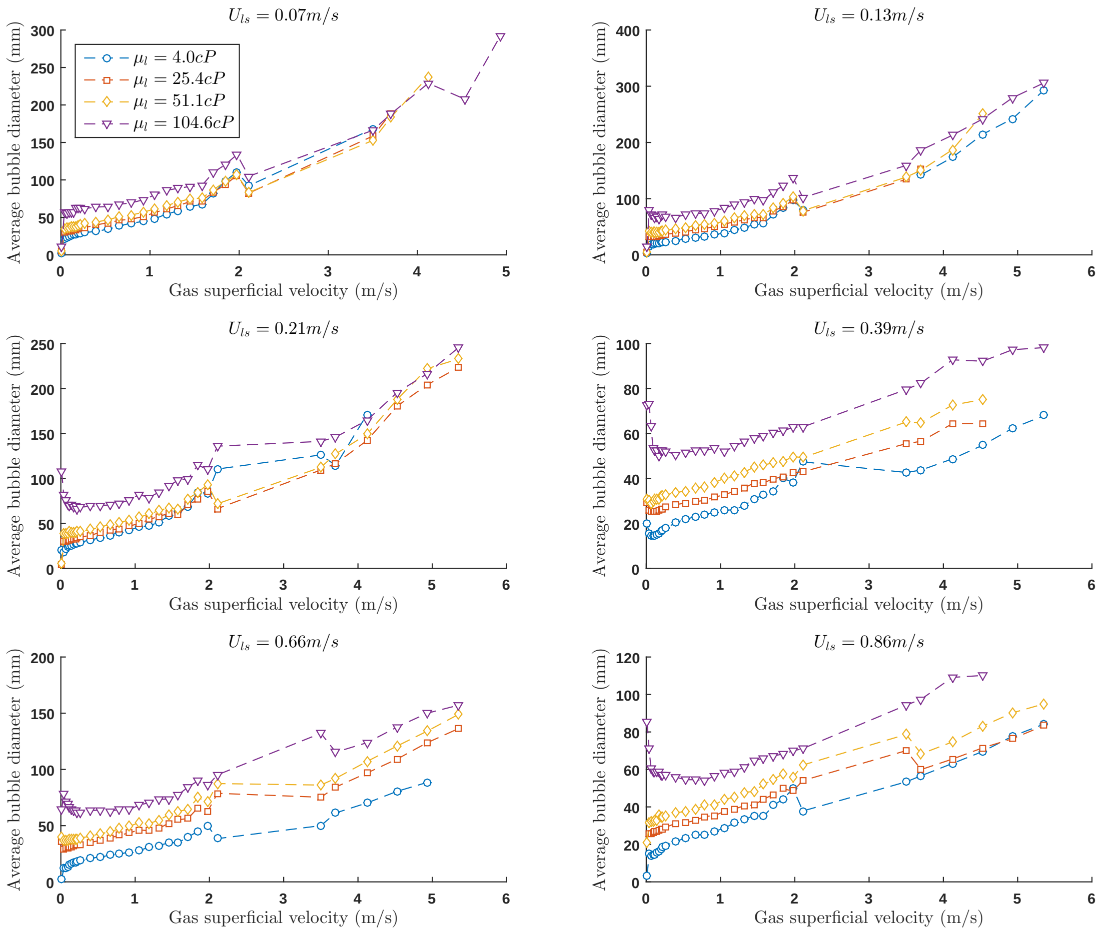

Fig. 4.36 Average bubble diameter calculated for all the viscosities at 6 different liquid superficial velocities. The figure shows how higher viscosity produces bigger bubbles consistently throughout the studied range of velocities.

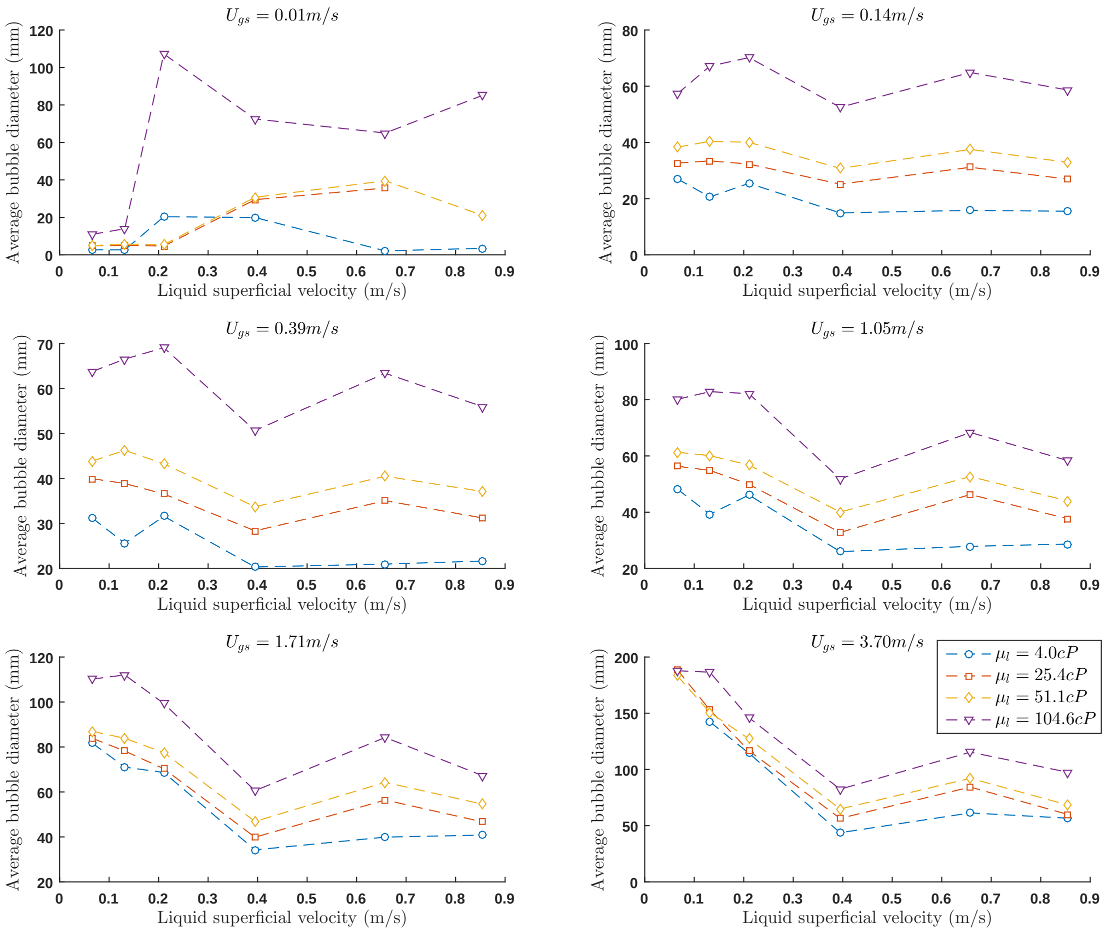

Fig. 4.37 Effect of liquid superficial velocity on average bubble diameter obtained at 6 different gas superficial velocities. A general decrease in size is observed with increasing liquid velocity.

4.3 Conclusions

Time series of cross-sectionally averaged void fraction suggests that increase in viscosity enables formation of large and stable gas structures. That was stipulated from the large, distinct peaks observed at higher viscosities. Generally speaking, average void fraction was found to decrease with increasing viscosity. This was attributed to the viscosity effect on shifting the coalescence/break-up equilibrium towards higher coalescence. The "dual effect of viscosity" was observed in the data where profiles at higher viscosity register higher void fraction at low gas superficial velocity and eventually fall below that of lower viscosity.

Void fraction was found to vary in a parabolic relationship with increasing gas superficial velocity. The behaviour was found coherent in all viscosities, albeit the decrease in overall void fraction with increasing viscosity. A change in the shape of void fraction-gas superficial velocity profile is observed at lower gas superficial velocity, it is found to become more pronounced with increasing viscosity. It is suspected that it marks transition from cap-bubbly to slug flow regime. Analysis of the variation of the effect of viscosity on void fraction with change in gas and liquid superficial velocity reveals that increase in liquid superficial velocity lessens the viscosity impact on void fraction. However, at lower liquid superficial velocities, increase in gas superficial velocity has a greater impact on the effect of viscosity on void fraction.

Radial distribution of void fraction revealed a shift from wall peaking to core peaking at lower gas superficial velocity at lower viscosity. However, no wall peaking is observed at higher viscosity. Large diversions of the shape of profiles are observed at lower gas superficial velocity, they grow more resembling with increasing gas superficial velocity. The radial profiles indicate that liquid film becomes thicker with increasing liquid viscosity near annular flow regime. The shape of radial profiles was found to be hugely dependent on the liquid viscosity. Pressure gradient was found to increase with increasing liquid viscosity, it relates to gas superficial velocity with a decaying exponential relationship analogous to the effect of gas superficial velocity on void fraction. The pressure gradient in the studied range of velocities was found to be gravity dominated. The profiles generated are found to be smooth with no changing trends marking regime transitions observed.

PDFs of void fraction time series coupled with spatio-temporal images of void fraction distribution indicate the existence of bubbly, slug, churn and churn-annular flow regimes. PDF shapes reveal that increase in viscosity results in generation of larger gas structures in the bubbly flow region. Slug flow regime was observed in the mediums with higher viscosities, confirmed by both PDF shape with distinct two peaks observed together with the spatio-temporal images from the WMS. The slug flow region seems to increase with increasing liquid superficial velocity. Comparing PDF shapes upstream and downstream the pipe suggests that flow develops faster at lower viscosities, it needs a longer distance as viscosity increases. Spatio-temporal images indicate that gas entrainment (foaminess) in the liquid bulk decreases with increasing viscosity. Also larger bubbles are observed with increasing viscosity. This might be attributed to the stable interface and stabilisation effect introduced by the increase in viscosity. Thicker liquid film in annular flow region is also shown by the images.

The effect of viscosity on structure velocity is found to be highly dependent on liquid and gas superficial velocities. Generally, structure velocity was found to increase with increasing liquid viscosity, although some anomalies were registered especially at lower gas superficial velocities. The increase is mainly referred to the increase in coalescence of bubbles, and therefore higher rise velocity. Increase in viscosity results in a slight increase of the characteristic frequency of gas structures. It was also found that the effect of viscosity on frequency lessens with increasing liquid superficial velocity. It was also found that frequency drops by about 40% as structures rise from upstream the test section to the downstream. Increase in liquid superficial velocity was found to increase the structure frequency monotonically.

Bubble size distribution revealed that increasing viscosity results in formation of bigger bubbles in almost all the studied cases, in concordance with the void fraction behaviour. It was also found that increasing gas superficial velocity increases bubble size in a semi-linear fashion. A sharp decrease in bubble size with increasing liquid superficial velocity is observed at lower liquid superficial velocities, with increasing liquid flow bubble size becomes almost insensitive to the increase in liquid input.

Chapter 5

Modelling of viscous flows in vertical large diameter pipes

5.1 Introduction

It has been demonstrated in Chapter 4 that the two-phase characteristics remarkably differ with increasing liquid viscosity. It has also been reflected that data for viscous flows in vertical large diameter pipes is almost non-existent. It is therefore expected that the state of the art closure models - which are predominantly empirical - available in the literature will fail to predict the two-phase characteristics in this case since the behaviour has not been reported before.

5.1.1 Objectives

This chapter aims to test existing models' performance against the newly acquired unique data for viscous flows in a vertical large diameter pipe. A viscosity dependent drift-flux model will be proposed based on the experimental results presented in Chapter 4. The performance of the existing theoretical, empirical and phenomenological models will be tested against the data. The following aspects will be discussed

- Evolution of drag coefficient and drift velocity with viscosity
- Performance of void fraction models at high viscosities
- Performance of pressure gradient models at high viscosities
- Prediction of structure frequency at high viscosities

5.2 Results and discussions

5.2.1 Overall void fraction prediction

One of the most widely used approaches to predict void fraction has been the drift flux approach that was first introduced by Zuber and Findlay (1965) [193]. Albeit its simplicity the drift flux approach proved to be one of the most accurate models to predict two-phase flow behaviour. A brief review of the available correlations and their range of applicability has been provided in Chapter 2.

To calculate the drift velocity (V_d) and the distribution coefficient (C_o) of the experimental data, the average gas velocity $\left(U_g = \frac{U_{gs}}{\varepsilon_g}\right)$ is plotted against mixture superficial velocity ($U_m = U_{ls} + U_{gs}$) for all the viscosities studied as shown in Figure 5.1. The void fraction employed to estimate the average gas velocity is measured at 62 D axial distance from the injection point using the ECT sensor. It can be seen that all the gas velocities collapsed into a single line that can be fitted to a linear relationship of the sort of equation 5.1. The corresponding drift velocities and distribution coefficients are gathered together with more values obtained from the experiments of Omebere (2006) [138] using air-water in a 5 mm vertical pipe and the Naphtha-Nitrogen experiments in a 189 mm pipe.

$$U_g = \frac{U_{gs}}{\varepsilon_g} = C_o \times U_{ms} + V_d \tag{5.1}$$

To look at the effect of viscosity on the evolution of velocity distribution coefficient and drift velocity, it has been decided to plot the values against the non-dimensional viscosity number (N_μ), or what is termed buoyancy Reynolds number in some literature given by equation 5.2. To include the effect of surface tension, it was decided to correlate the drift velocity model coefficients against the product of the non-dimensional viscosity number and Morton number given by equation 5.3. Figure 5.2 shows the experimental relationship of the distribution coefficient and drift velocity to the product of Morton number and the buoyancy Reynolds number. The relationship has been fitted to power-law formula given in equation 5.4 for the distribution coefficient and equation 5.5 for the drift velocity.

$$N_\mu = \frac{\sqrt{gd^3(\rho_l - \rho_g)\rho_l}}{\mu_l} \tag{5.2}$$

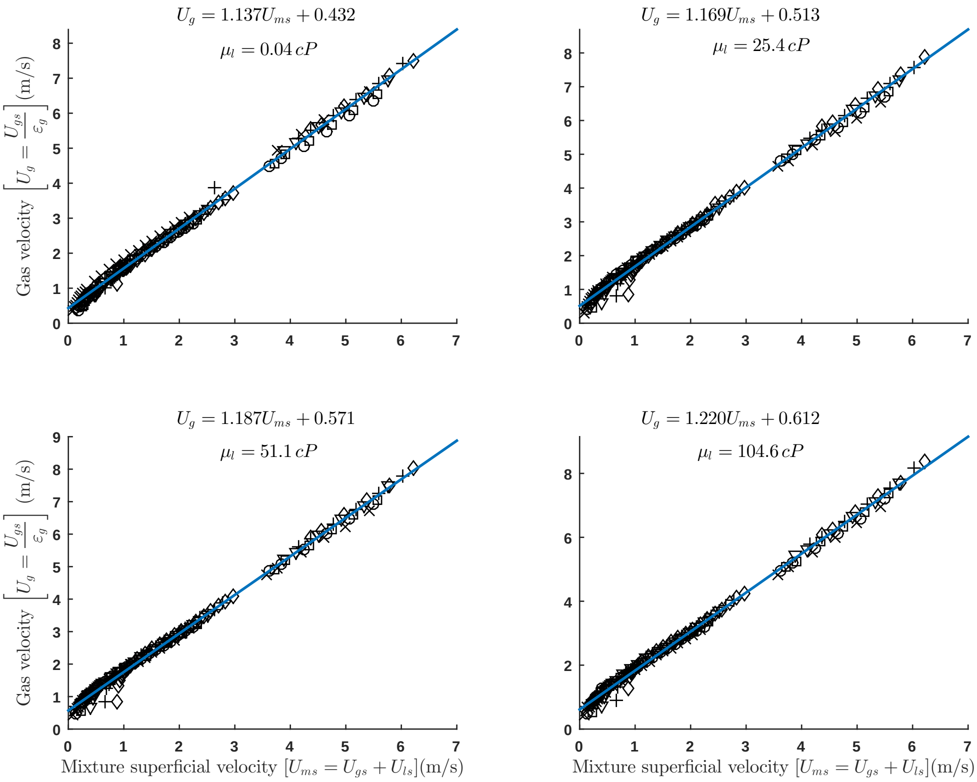

Fig. 5.1 Experimental gas velocity plotted against mixture superficial velocity for the four viscosities studied.

$$N_{Mo} = \frac{g\mu_l^4(\rho_l - \rho_g)}{\rho_l^2\sigma_l^3} \tag{5.3}$$

$$C_o = 0.038 \times (N_\mu N_{Mo})^{0.249} + 1.089 \tag{5.4}$$

$$V_d = [0.2061 \times (N_\mu N_{Mo})^{0.127} + 0.172]\sqrt{gD} \tag{5.5}$$

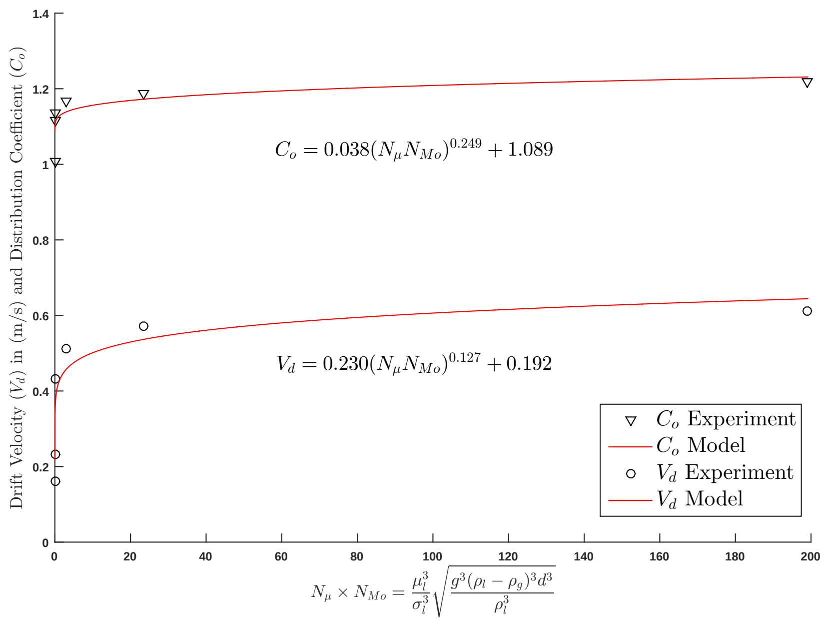

Fig. 5.2 Correlation of velocity distribution coefficient (C_o) and the drift velocity (V_d) with the product of non-dimensional viscosity number (N_μ) and Morton number (N_{Mo}). The figure shows the power relationship for both quantities with the non-dimensional number evolution.

The proposed correlation performance against the experimental data of this campaign is shown in Figure 5.3. It can be seen that most the void fraction for most of the data is predicted with ± 10% deviation. A slightly larger deviation is observed at the lowest liquid superficial velocity ($U_{ls} = 0.07m/s$). Figure 5.3 also suggests that the predictability improves slightly with increasing liquid viscosity.

The newly proposed correlation's void fraction was plotted against the data of Omebere et al (2008) [139] in a 189 mm vertical pipe and that of Abolore (2013) [2]. This data is particularly selected to investigate whether the correlation would perform satisfactorily at the extreme conditions of this data. The data of Omebere (2008) [139] is obtained in a 189 mm pipe using Naphtha (0.325 cP) and Nitrogen at 90 bar, whilst

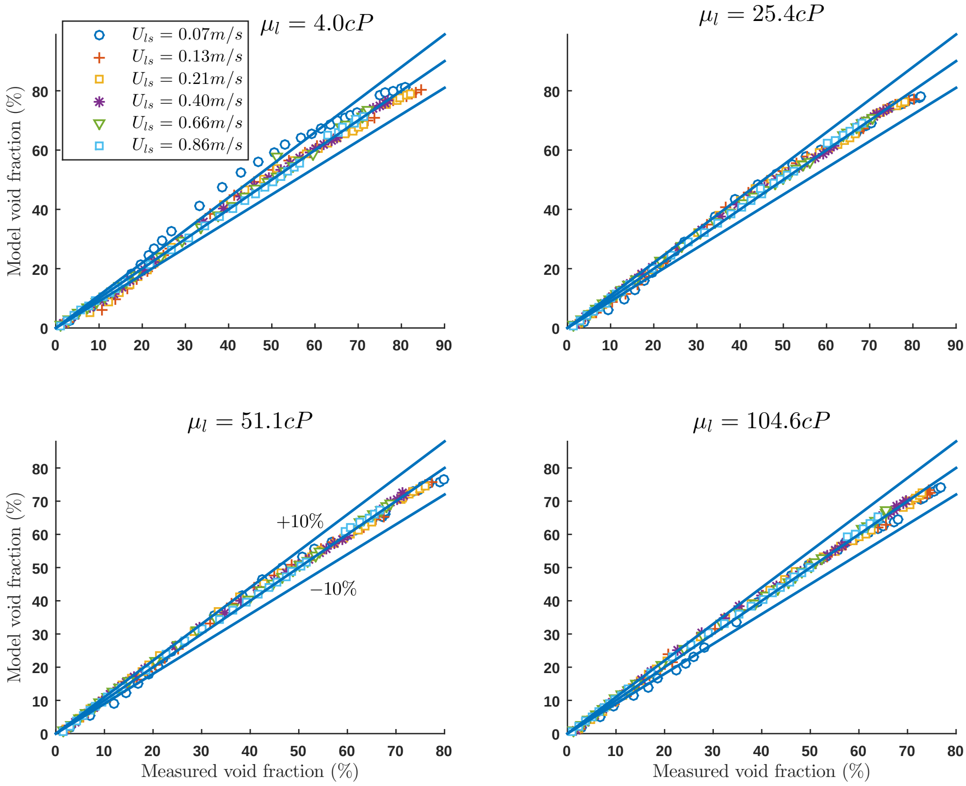

Fig. 5.3 Performance of the newly formed drift flux correlation in predicting void fraction of the current experimental data across all viscosities.

that of Abolore (2013) [2] is measured using SF_6 and a 35 cP oil in a 127 mm pipe at 7.9 bar. In both cases the gas to liquid density ratio is much higher than the data used to formulate the correlation. It can be seen that the model reproduces most of the data within ± 20% as shown in Figure 5.4. The correlation seems to perform better with the increase of both gas and liquid superficial velocities as well and the liquid viscosity. It is also observable that the correlation seems to mostly under-predict the experimental data in Figure 5.4. This can be attributed to the large difference in gas/liquid density ratio, whereby void fraction is expected to be higher at higher gas to liquid density ratio due to higher turbulence at equal gas flow rate.

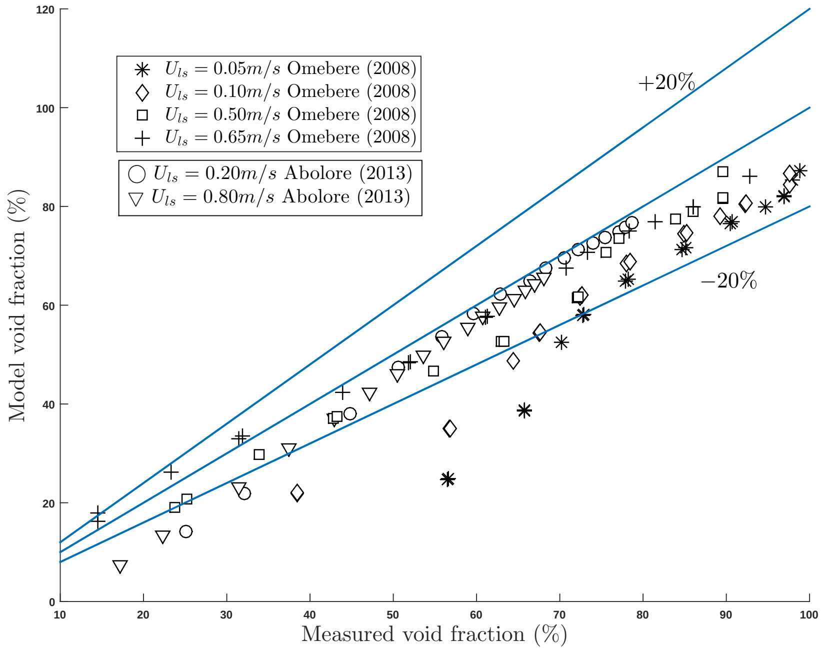

Fig. 5.4 Performance of the newly formed drift flux correlation in predicting void fraction of the experimental data of Omebere et al (2008) [139] in a 189 mm vertical pipe using Naphtha and Nitrogen and Abolore (2013) [2] in a 127 mm vertical pipe using a 35 cP oil and SF_6. Both experimental values were obtained in pressurised rigs, at 90 and 7.9 bar respectively.

Figure 5.5 shows the average percentage error and the absolute percentage error in of the proposed correlation in predicting experimental void fraction in comparison with popular correlations from various approaches. It can be seen that the proposed correlation's performance is much superior compared to the other methods featuring average percentage error of 3.2% and absolute percentage error of 7.3%. The error seems to decrease dramatically with increasing liquid viscosity. The performance of the correlation is yet to be tested against other correlations available in the literature and a broader range of experimental data with different diameters and physical properties of fluids.

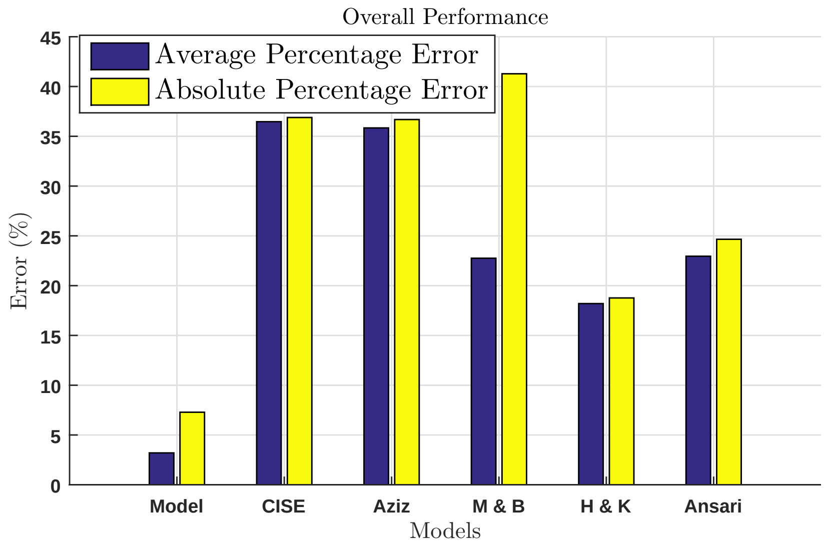

Fig. 5.5 Average percentage error and Absolute percentage error of selected correlations and the proposed correlation in predicting experimental void fraction. The correlations included are the Premolie et al (1971) denoted as (ICSE), Aziz et al (1972) [21], Mukherjee and Brill (1973) (M & B), Kabir and Hasan (1990) [102] (H & K), and Ansari et al (1994) [18].

5.2.2 Performance of pressure gradient models at high viscosities

It has been demonstrated in chapter 4 that two-phase flow characteristics differ dramatically with liquid viscosity. It is expected that increasing liquid viscosity increases the interfacial friction factor and therefore positively increases frictional losses. Moreover, it has been manifested that viscosity has an even greater influence on the distribution of the two-phases and therefore void fraction. This is expected to impact on both the frictional and the gravitational components of the pressure gradient.

McNeil and Stuart (2003) measured pressure gradient in annular flow region in a 26.12 mm vertical pipe studying viscosities in the range of 1-550 cP. They presented frictional pressure losses in terms of two phase multiplier and interfacial friction factor. They reported that Friedel's (1979) correlation [61] progressively over-predicts frictional losses with increasing viscosity whilst Chilsolm's method [41] for the Lockhart and Martinelli (1949) correlation grossly under-predicts frictional losses with increasing viscosity [121]. When presenting frictional pressure losses in terms of interfacial friction factor, they found that the correlation of Fukano et al (1998) [62] increasingly under-predicting the friction factor with increasing viscosity. They also studied the model of Ambrosini et al (1991) [16] where a much closer prediction of friction factor was obtained however slightly over-predicting the experimental results. They proposed a correlation to predict inrterfacial friction factor based on liquid film thickness Froude number [121].

Omebere (2006) studied pressure drop in a 189 mm vertical pipe at very high pressures (20 and 90 bar) using Nitrogen-Naphtha while measuring void fraction at 5 axial locations using multiple gamma densitometers. The pressure gradient was measured at 3 axial positions using diffential pressure sensors. Their study reported the decrease of total pressure gradient with increasing gas superficial velocity which was attributed to the decrease in two phase density. The study also investigated the predictability of serveral void fraction and pressure gradient models. They found the correlation of Beggs and Brill [31] consistenetly over-predicting pressure gradient, whilst Friedel and CISE consistently underpredicting the experimental results. The correlation of Hagedon and Brown (1965) [73] and the homogeneous model performed the best amongst the studied models [138].

Da Hlaing et al (2007) measured two-phase pressure gradient in a 19 mm vertical pipe using water and glycerol-water solution featuring viscosities of 0.85 and 4.48 cP investigating bubbly and slug flow regimes. They found that the correlation of Nicklin et al (1962) [133] is more suitable for predicting bubbly flow and slug pressure drops while the one by Wallis (1969) [183] predicts pressure gradient with a reasonable accuracy in annular flow [50]. Zangana (2011) studied at Nottingham total pressure drop in a 127 mm vertical pipe using air-water fluids while measuring the wall shear-stress. Their study revealed that wall shear stress decrease with increasing gas superficial velocity in the the churn-annular flow region whilst the profile exhibits a minima for smaller diameter pipes, no minima was observed in their experimental results. They also tested the performance of several pressure gradient models, where the model of Chisolm (1976) produced closer values, the model of Friedel (1979) considerably under-predicted experimental results, whilst Beggs and Brill (1973) significantly over-predicted the measured pressure gradient [191].

Abolore (2013) investigated pressure gradient in an equal pipe diameter to this study (127 mm) using a 35 cP oil by mixing Exxsol D80 and Nexbase 3080 and Sulphur Hexafluoride (SF6) gas in a pressurised rig at the SINTEF laboratory. They measured diferential pressure using a DP cell connected between 16D and 61D from the injection while measuring the void fraction using an ECT and a WMS at 43D and 51D axial distance from the injection respectively. The study showed a systematic decrease of total pressure gradient with increasing gas superficial velocity which was attributed to the decrease in liquid hold-up with increasing gas input [2].

Alruhaimani (2015) studied pressure gradient at high viscosities in a 50.8 mm vertical pipe investigating viscosities in the range of (127-586 cP). They reported that total pressure gradient increases with increasing viscosity in most of their experimental runs. Which was owed to the increase in frictional losses induced by the viscosity increase. However, at low liquid and gas superficial velocities ($U_{ls} < 0.3\,m/s$ and $U_{gs} < 2.0\,m/s$) the opposite was observed which was referred to the existence of a positive frictional pressure drop at higher viscosities [14]. This positive frictional pressure gradient was published in [10] where a criterion for detecting positive frictional losses in slug flow was proposed based on the wall shear stress competition between the Taylor bubble region and the liquid slug. It was suggested that if the liquid film velocity is smaller than the mixture superficial velocity, a positive frictional pressure gradient will occur [10].

Investigation of frictional pressure gradient of the experimental data of the current campaign

If the accelerational pressure gradient can be approximated from the void fraction measurements at 15D and 62D axial positions assuming constant gas density using the following separated flow formulae

$$-\left(\frac{dp}{dz}\right)_A = \frac{d}{dz}\left(\dot{m}^2\left[\frac{x_g^2}{\varepsilon_g\rho_g} + \frac{(1-x_g)^2}{(1-\varepsilon_g)\rho_l}\right]\right) \tag{5.6}$$

and the gravitational pressure gradient from the average two phase density evaluated from the two axial measurements of void fraction at (15D and 62D) using

$$-\left(\frac{dp}{dz}\right)_G = ([\varepsilon_g\rho_g + (1-\varepsilon_g)\rho_l]g\sin\beta) \tag{5.7}$$

the frictional pressure gradient can be approximated from the total pressure gradient by subtracting the gravitational and accelerational pressure components in the form of

$$\left(\frac{dp}{dz}\right)_F = \left(\frac{dp}{dz}\right)_T - \left(\frac{dp}{dz}\right)_G - \left(\frac{dp}{dz}\right)_A \tag{5.8}$$

The calculated accelerational pressure drop per unit length can be seen in Figure 5.6. It is clear that the accelerational pressure drop is very insignificant and only relevant at very low gas superficial velocities where bubbles accelerate considerably as they grow in size, and therefore can be neglected.

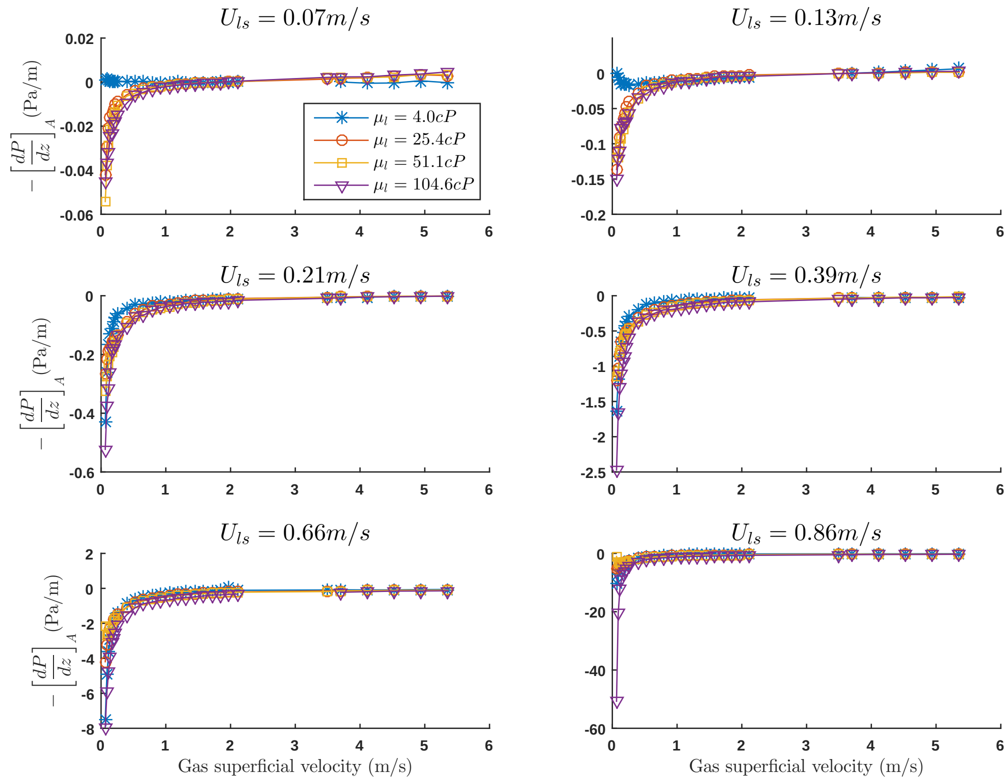

Fig. 5.6 Accelerational pressure gradient approximated from the measured void fraction at 15 and 62D axial locations using equation 5.6. The figure shows the variation for all the studied liquid superficial velocities and all the viscosities.

The experimental frictional pressure gradient approximated by equation 5.8 is plotted for all the viscosities in Figure 5.7. The void fraction selected to estimate gravitational pressure gradient is measured at 62 D axial distance using the ECT sensor. It can be seen that the trend and the values obtained at low liquid superficial velocities are quite uncommon and might seem counter-intuitive because the frictional losses are expected to increase with increasing gas superficial velocity which is the contrary to the trend reflected in Figure 5.7. On the other hand, a positive frictional pressure gradient is registered at low liquid superficial velocities and high gas superficial velocities. This behaviour reverses as liquid superficial velocity increases above 0.21 m/s.

This might appear as a violation of the conservation of energy equation. However, quite a number of researchers have detected the positive frictional pressure gradient in vertical pipes [40, 186, 10, 15, 115, 177, 8, 114, 170, 67]. One might argue that the resultant approximation of the frictional losses carries a lot of uncertainties especially the one associated with the void fraction measurement. It should be noted that the void fraction was measured at three axial locations using two different measurement techniques. Also these experiments were repeated three times and the same behaviour is reproduced.

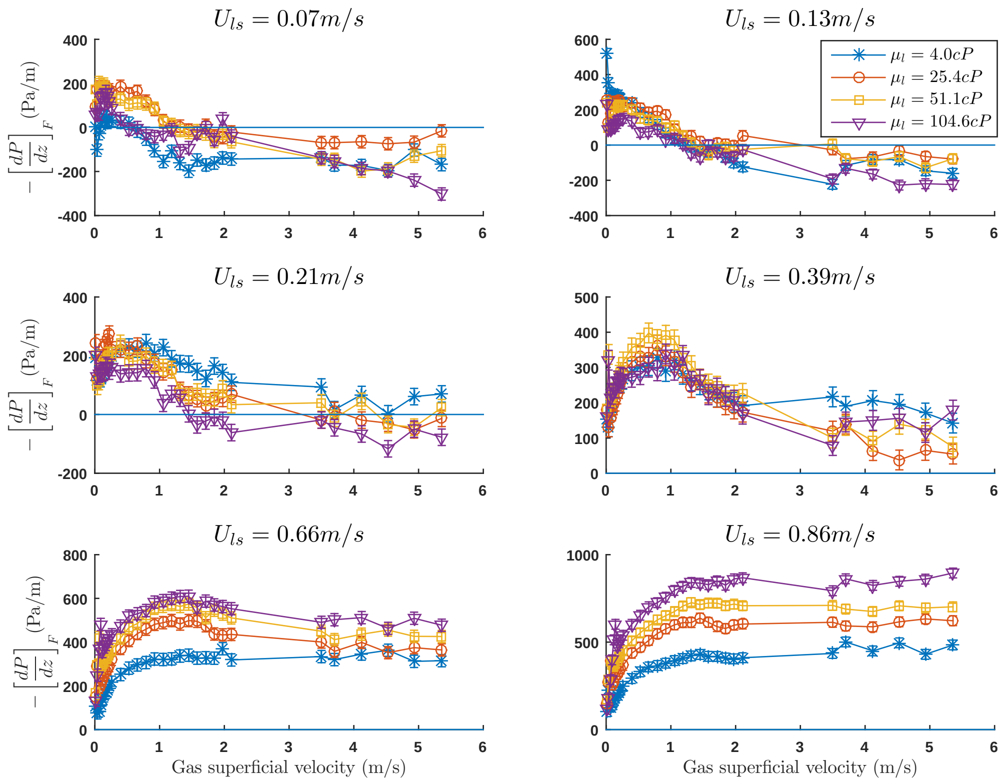

Fig. 5.7 Experimental frictional pressure gradient approximated from the time and axially averaged two-phase density using equation 5.8. The figure shows the variation for all the studied liquid superficial velocities and all the viscosities.

The issue of positive frictional pressure gradient has been reported by many researchers [186, 10, 15, 115, 177, 8, 114, 170, 67]. The occurrence of positive frictional pressure gradient is attributed to the average instantaneous wall shear stress. While in unidirectional upward flow only negative frictional pressure gradient is expected because the wall shear stress is always positive working against the direction of flow. However, in two-phase flows, especially at low liquid superficial velocities, considerable back flow of the liquid film occurs as larger bubbles and gas structures travel upwards the pipe. The instantaneous circumferentially-averaged wall shear stress can be either positive of negative (with respect to the direction of flow) depending on the direction of the film movement. The time-average of that circumferentially-averaged wall shear stress will determine if the frictional pressure drop is positive or negative. One of the earliest observations of this phenomenon is the measurements of wall shear-stress presented by Whalley and McQuillan (1985) [186]. Where the averaged wall shear-stress was clearly negative in the slug flow region. Some of the recent reports on this are the works of Liu (2014) [115] and Al-Sarkhi et al (2016) [10]. Liu (2014) [115] attributed the negative frictional energy loss to the existence of a buoyancy-like term that is induced by slippage, gravity and inclination angle together with the frictional pressure drop term. This hypothesis was challenged by Al-Sarkhi et al (2016) arguing that even the downward film flow would irreversibly dissipate energy in terms of heat and would not compensate for the positive energy loss . Al-Sarkhi et al (2016) proposed that the positive frictional pressure gradient in slug flow is the result of the competition of two opposing actions; the downward falling film around the Taylor bubble and the upward moving liquid slug [10].

Investigation of frictional pressure gradient from experiments generated by other authors

The experimental values obtained in this campaign are compared to other experimental pressure gradient results obtained for large diameter pipes. Figure 5.8 shows current frictional pressure gradient obtained in a 127 mm vertical pipe by Abolore (2013) [2] using SF_6 and a 35 cP oil at elevated pressures (4.5 and 7.8 bar). The pressure gradient results obtained at both pressures are quite close. Figure 5.8 shows the frictional pressure gradient calculated from the total pressure gradient and void fraction data published in [2]. The figure shows frictional pressure gradient data obtained at two liquid superficial velocities, namely 0.20 m/s and 0.80 m/s from [2] and the profiles at similar liquid superficial velocities at the two comparable liquid viscosities, namely 25.4 and 51.1 cP. It can be seen that the trend obtained in both cases show a huge resemblance with the existence of positive frictional pressure gradient at low liquid superficial velocity and moderately high gas superficial velocities. The considerably higher drop in frictional pressure gradient exhibited by Abolore's (2013) data is most likely a density ratio issue, where a much higher backward liquid film flow is needed to sustain the rising momentum of the 28 times denser gas travelling upward compared to the current set of data.

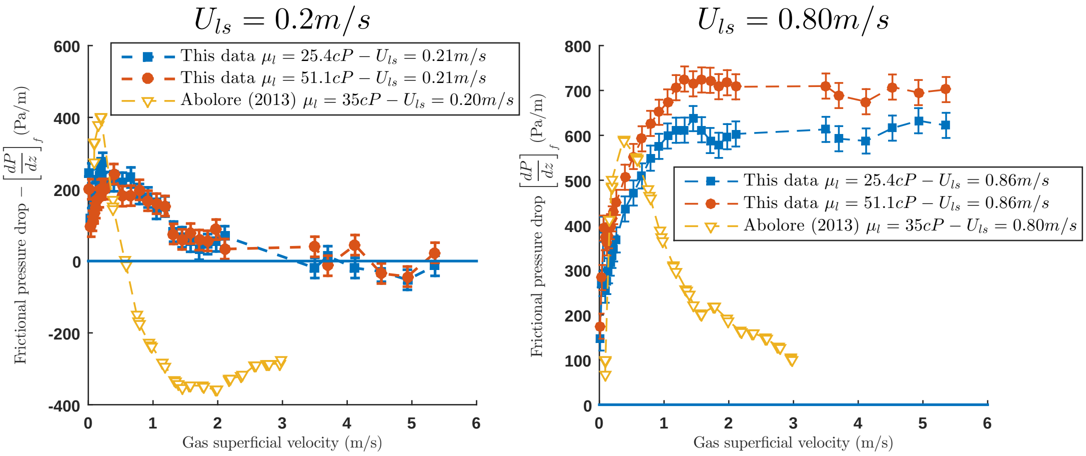

Fig. 5.8 Experimental frictional pressure gradient compared to the data produced by Abolore (2013) [2]. The experiments produced by Abolore (2013) were obtained using SF_6 and a 35 cP oil in a pressurised rig (4.5 bar) but similar pipe diameter (127 mm). The figure shows that a similar trend and a positive frictional pressure gradient are obtained at two different liquid superficial velocities that are comparable to this data.

Figure 5.9 shows a comparison of the current data set with that produced in a 189 mm vertical pipe by Omebere (2006) [138]. Omebere's (2006) data is obtained using Nitrogen-Naphtha fluids at a very high pressure (90 bar), the Naphtha viscosity was measured as 0.325 cP. Expectedly a much lower frictional pressure gradient is obtained in the larger diameter. However, the frictional pressure gradient is always negative in the case of larger diameter throughout all the liquid superficial velocities. This divergence can be attributed to a combined effect of the pipe diameter, liquid viscosity, and the density of the gas phase. Clearly with increasing pipe diameter, it is expected that the churning of flow and backward falling of the film becomes more pronounced at equal gas and liquid superficial velocities. On the other hand, as reflected by the data presented in Figure 5.8 it is indicated that higher gas density seems to enhance backward falling of the film generated by the heavier rising pockets of dense gas phase. In the case of Omebere's (2006) data, the gas density was measured as 102.5 kg/m^3. It is evident from the results presented in Figure 5.7 that viscosity increase results in a higher frictional pressure gradient, it is reasonable to infer that the lower viscosity of the high pressure data contributed to the much lower frictional pressure gradient obtained in Figure 5.9.

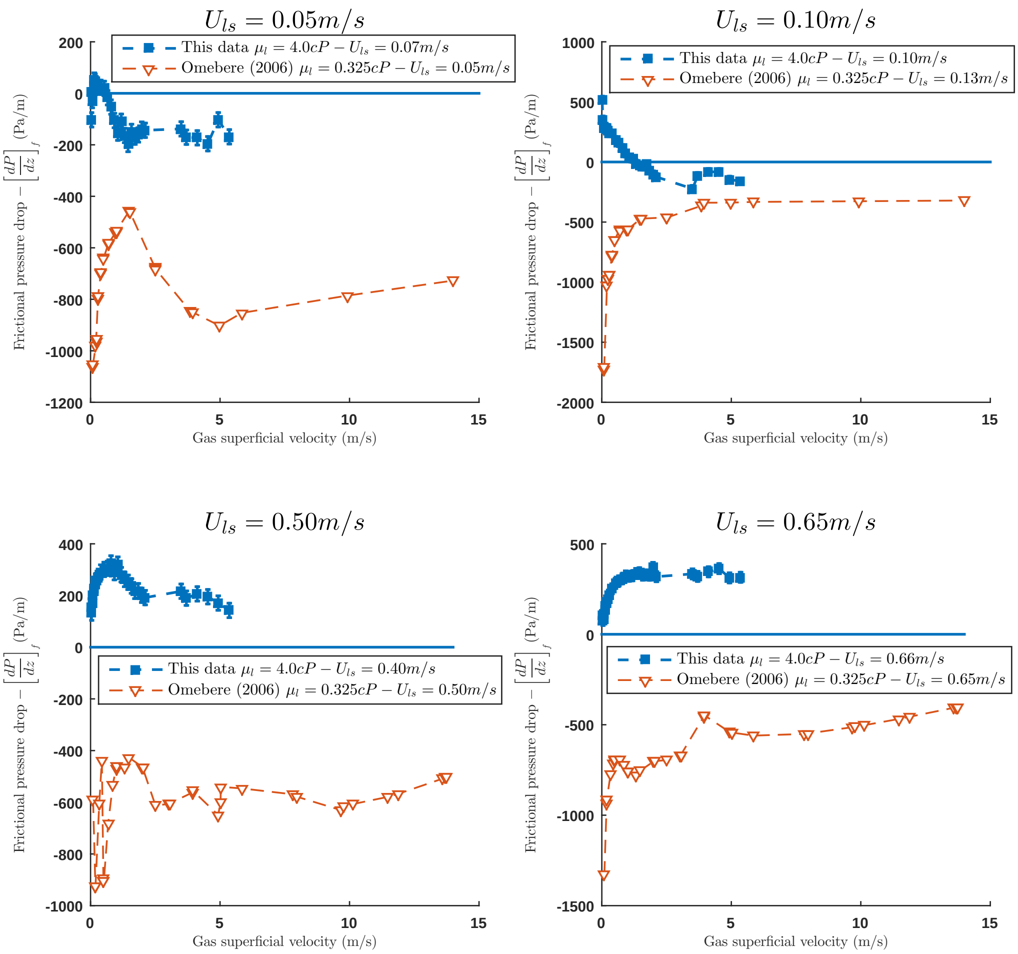

Fig. 5.9 Experimental frictional pressure gradient compared to the data produced by Omebere (2006) [138]. The experiments by Omebere (2006) were obtained using Nitrogen and Naphtha of 0.325 cP viscosity in a highly pressurised rig (90 bar) but a bigger pipe diameter (189 mm). The figure reflects similarity in the trend and the positive frictional pressure gradient.

Assessment of the performance of pressure gradient models against experimental data

Many models have been proposed in the literature to predict two-phase pressure gradient. A brief description of the different modelling approaches is provided in section 2.5 of Chapter 2. The performance of these models differ according to the range and type of data used to derive the individual closure models employed in the evaluation of the different attributes of two-phase flows. Indeed some of these models are theoretical and their performance is expected to differ according to the departure from the underlying assumptions made in their formulation.

Numerous studies have been published to investigate the performance of these models against either laboratory or field data. Some of these studies are found within the papers presenting new models themselves when making the case of the suitability of the new models, where the most likely conclusion is the superiority of the proposed model over the others. Other evaluation investigations have also been published against field and laboratory data. One of the recent studies is the one by Ruiz et al (2014) [155] where they evaluated the performance of 8 popular models against 108 field data from viscous wells of diameters 25 mm and 38 mm. The field viscosities fall in the range of 108 cP to 310 cP. They concluded that the correlation of Hagedorn and Brown (1965) performed the best followed by that of Beggs and Brill (1973). Chibuike (2014) [40] studied the performance of several models against air-water data generated in a 127 mm vertical pipe at elevated pressures. Their study found that the correlation of Hagedorn and Brown (1965) produced the closest prediction while the largest deviation was produced by the correlation of Chisolm (1967). Mekisso (2013) [123] studied the performance of over 42 frictional pressure correlations in horizontal pipes. The best fit to their data was produced by the correlation of Dukler et al (1964) [54]. Biria (2013) [33] compared the performance of several correlations against air-water data in a 52 mm vertical pipe. The correlation of Kabir and Hasan (1990) was found to produce the closest prediction. Ghajar and Bhagwat (2013) [64] investigated several frictional pressure correlations, they proposed the correlation of Awad and Muzycka (2008) [19] for pipe diameter above 40 mm.

Akhiyarov et al (2010) [8] investigated the performance of 4 pressure gradient models including the one by Hagedorn and Brown (1965) against viscous vertical flow data in a 52.5 mm vertical pipe. They concluded that the unified model of Tulsa, published in [192] produced the closest prediction against their data and some other data collected from the literature for high viscosity vertical flows. A very refined evaluation of pressure drop models was published by Shoham (2006) [167]. Where several models performance was evaluated against 1,712 data point gathered from different sources for flows at different diameters and inclinations. They found that overall, the correlation of Hagedorn and Brown (1965) performed the best. Spedding et al (1998) [170] investigated several frictional pressure gradient theories performance, which they found hugely departed from the experimental data, no correlation was recommended.

In this section the performance of several selected models is evaluated against the unique data presented in Chapter 4 (720 runs). These models are; Lockhart and Martinelli (1949) [116] using Chisolm's (1967) correlation [41], Hagedorn and Brown (1965) [73], Aziz et al (1972) [21], Beggs and Brill (1973) [31],Friedel (1979) [61], Mukherjee and Brill (1985) [129], Kabir and Hasan (1990) [102], and Ansari et al (1994) [18]. The performance of these models is presented in terms of prediction of the pressure gradient profile and the deviation from the experimental data. The deviation from experimental data will be presented in terms of Average Percentage Error (APE) and Absolute Average Percentage Error (AbAPE). The formula for both measures is expressed as

$$APE_{i,j} = \frac{1}{N}\sum \frac{\left(\frac{dP}{dz}\right)_P - \left(\frac{dP}{dz}\right)_m}{\left(\frac{dP}{dz}\right)_m} \times 100 \tag{5.9}$$

$$AbAPE_{i,j} = \frac{1}{N}\sum \left| \frac{\left(\frac{dP}{dz}\right)_P - \left(\frac{dP}{dz}\right)_m}{\left(\frac{dP}{dz}\right)_m} \right| \times 100. \tag{5.10}$$

The models of Lockhart and Martinelli and Friedel (1979) only predict frictional pressure gradient, to estimate the overall pressure gradient a void fraction predicting method needs to be used in combination, most often it is used with a drift flux model or the CISE correlation published in [148]. In this section only the frictional pressure component is calculated for both models and compared against the data. Figure 5.10 and Figure 5.11 show the frictional pressure gradient profiles predicted by the Lockhart-Martinelli (1949) and Friedel (1979) respectively plotted together with the experimental values. It can be clearly seen that both model depart grossly from the experimental values, while at low gas superficial velocity, where bubbly flow is expected the models often grossly under-predict the frictional losses, while the models seem to increase almost linearly with increasing gas superficial velocity, frictional losses are often over-predicted; especially by the model of Friedel (1979).

These results are not surprising because other researchers have reported gross departure from experimental values by most if not all of the published models for frictional pressure gradient [170]. It should also be noted that none of the two models predicted the positive frictional pressure gradient discussed earlier. That can be attributed to the dependence on single phase pressure drop by the model of Lockhart-Martinelli (1949), where no back-flow occurs. In the case of the empirical correlation of Friedel (1979) the deviation might have been due to the lack of large diameter data employed in the formulation of the correlation.

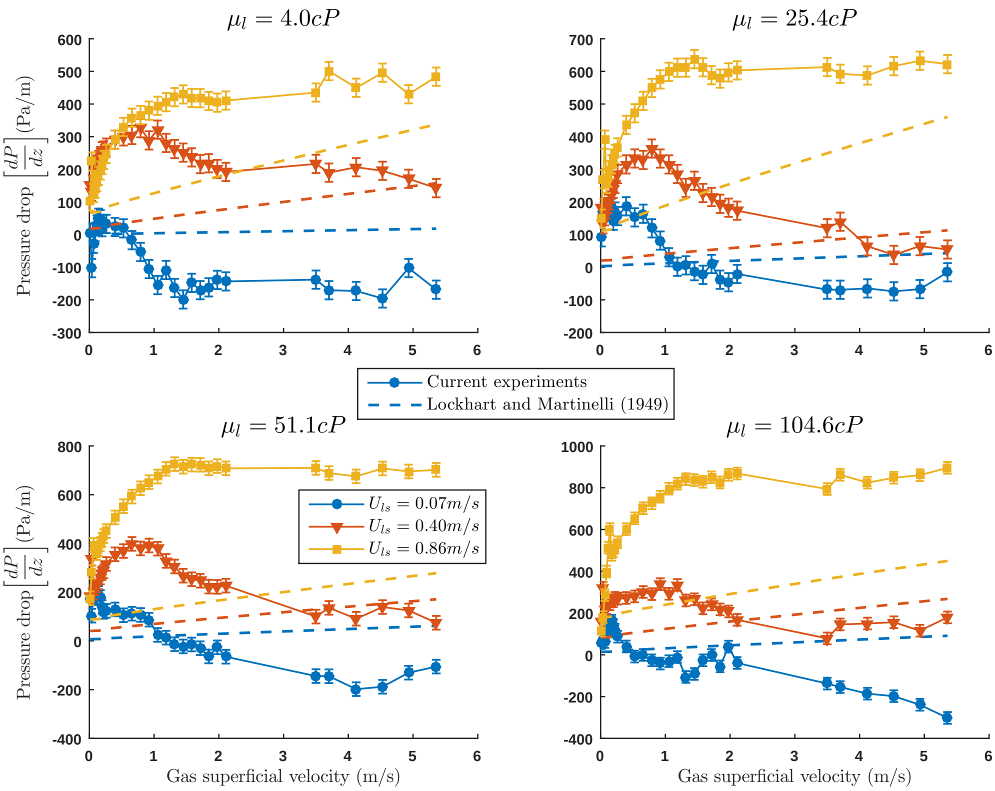

Fig. 5.10 Experimental frictional pressure gradient profile at different viscosities and the predictions of Lockhart and Martinelli (1949) model [116].

Figure 5.12 and Figure 5.13 show the deviation of the predicted frictional pressure gradient by Lockhart-Martinelli (1949) and Friedel (1979) correlations respectively plotted against the experimental data. Both Figures demonstrate that with increasing liquid viscosity the divergence from the experimental data becomes more significant. It is also notable that both models dramatically underestimate the measured frictional pressure gradient except at very low frictional pressure gradient values where negative

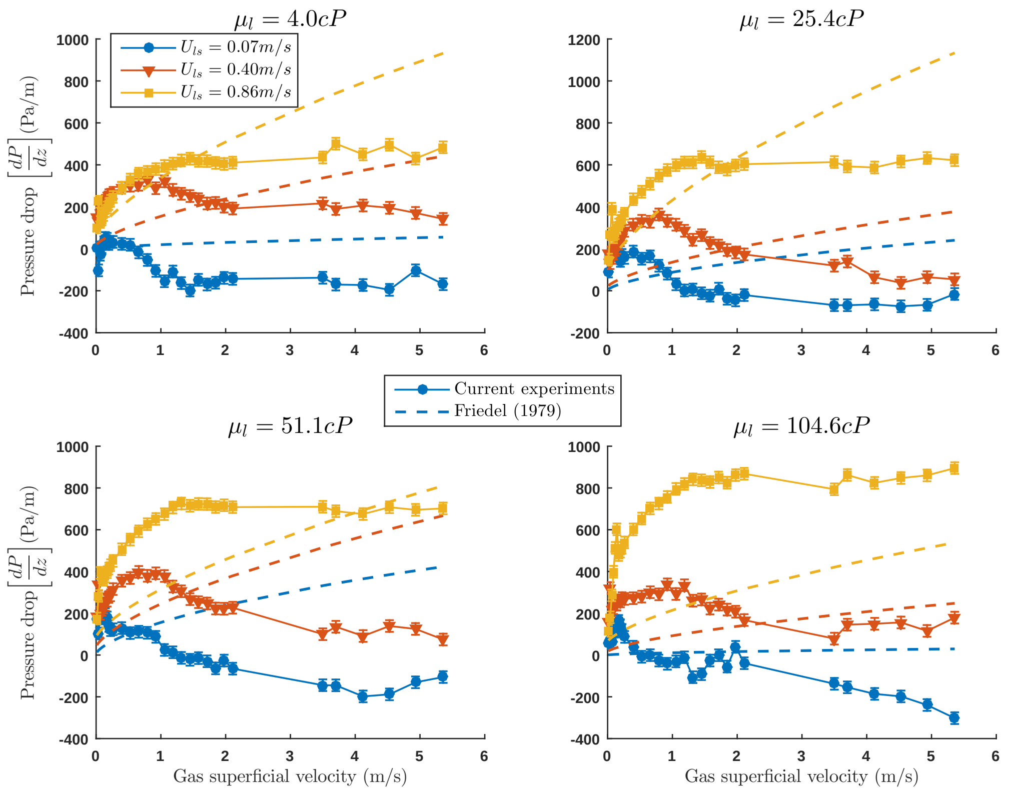

Fig. 5.11 Experimental frictional pressure gradient profiles at different viscosities and the predictions of Friedel (1979) model [61].

experimental frictional pressure gradient is detected the models are found to over-predict the frictional losses. It can also be noted that the prediction of both models seem to improve slightly with increasing liquid superficial velocity where the slip ratio becomes smaller and the behaviour grows more resemblant to the homogeneous flow.

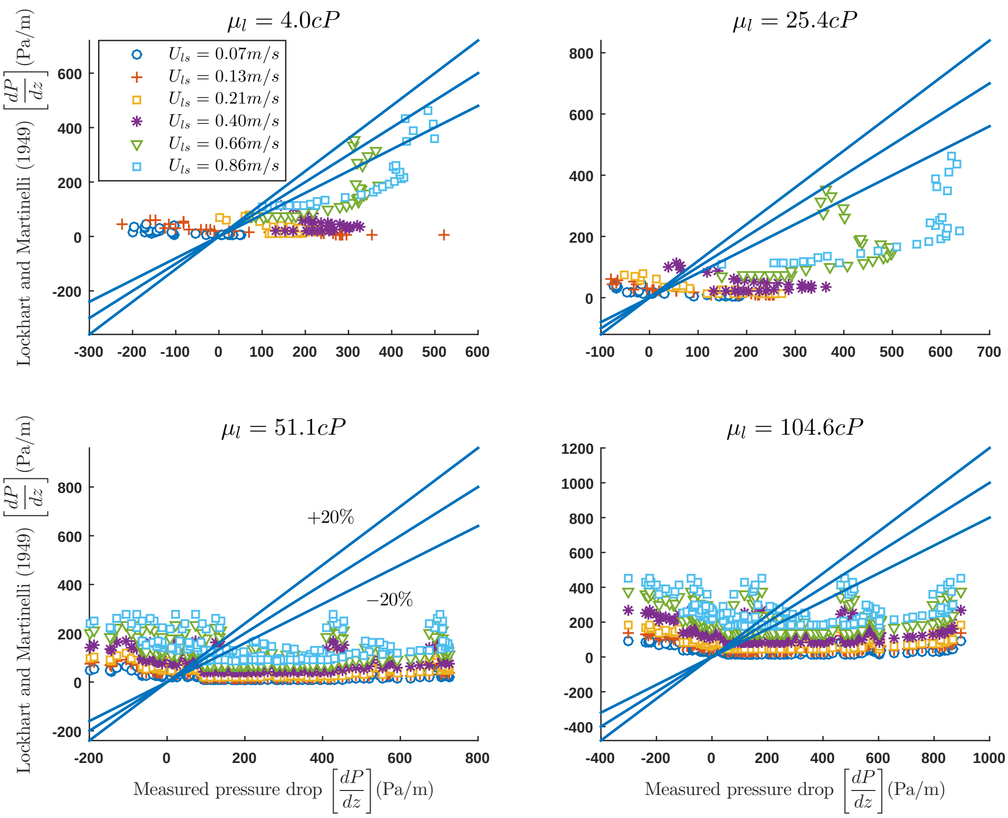

Fig. 5.12 Deviations of the predictions of Lockhart and Martinelli (1949) correlation [116] from the experimental values at different viscosities.

Figure 5.14 shows the overall pressure gradient profiles of Hagdorn and Brown (1965) [73] correlation together with the experimental values. The correlation was derived using experimental data-bank generated from an industrial size experimental well of three different pipe diameters and employing air and liquids covering viscosities from 0.85-110 cP. As can be seen in Figure 5.14 the prediction improves dramatically with increasing liquid viscosity, liquid superficial velocity, and the gas superficial velocity. While very large discrepancies are observed at low gas superficial velocities, the profiles grow closer with increasing liquid superficial velocity. This might be an attribute of the decreased slip or perhaps the closeness of the data to the range of velocities in the data-bank used by Hagedorn and Brown (1965).

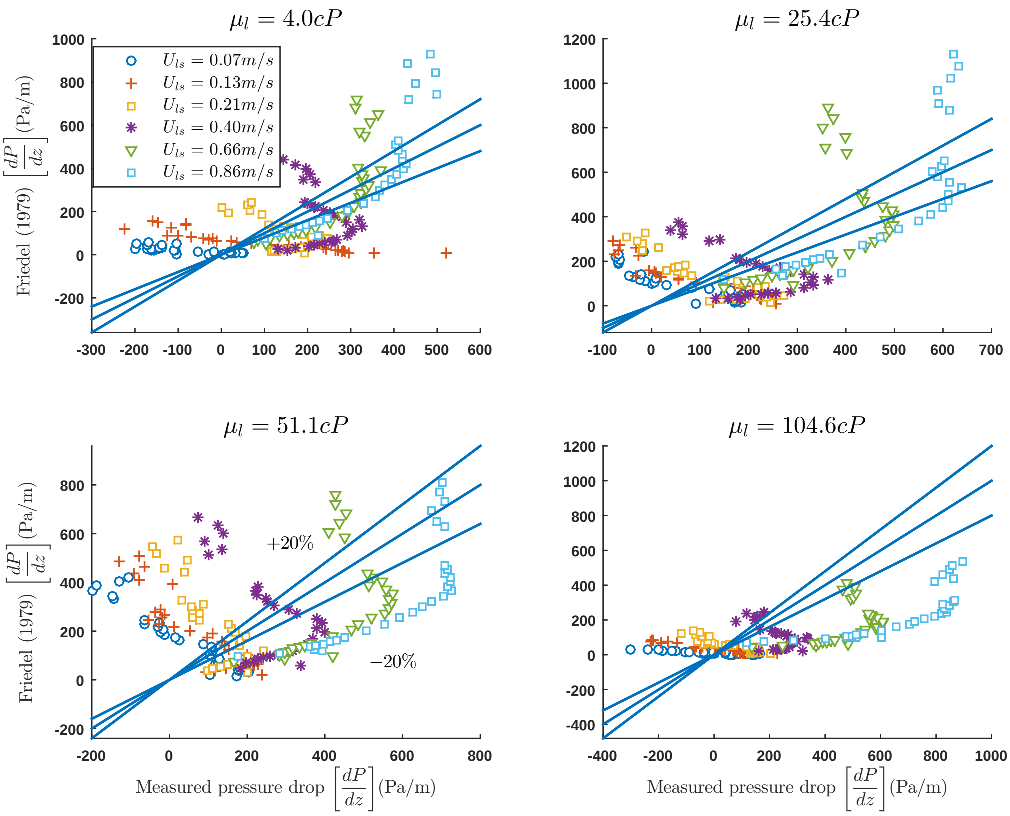

Fig. 5.13 Deviation of predicted frictional pressure gradient by Friedel (1979) [61] from experimental data.

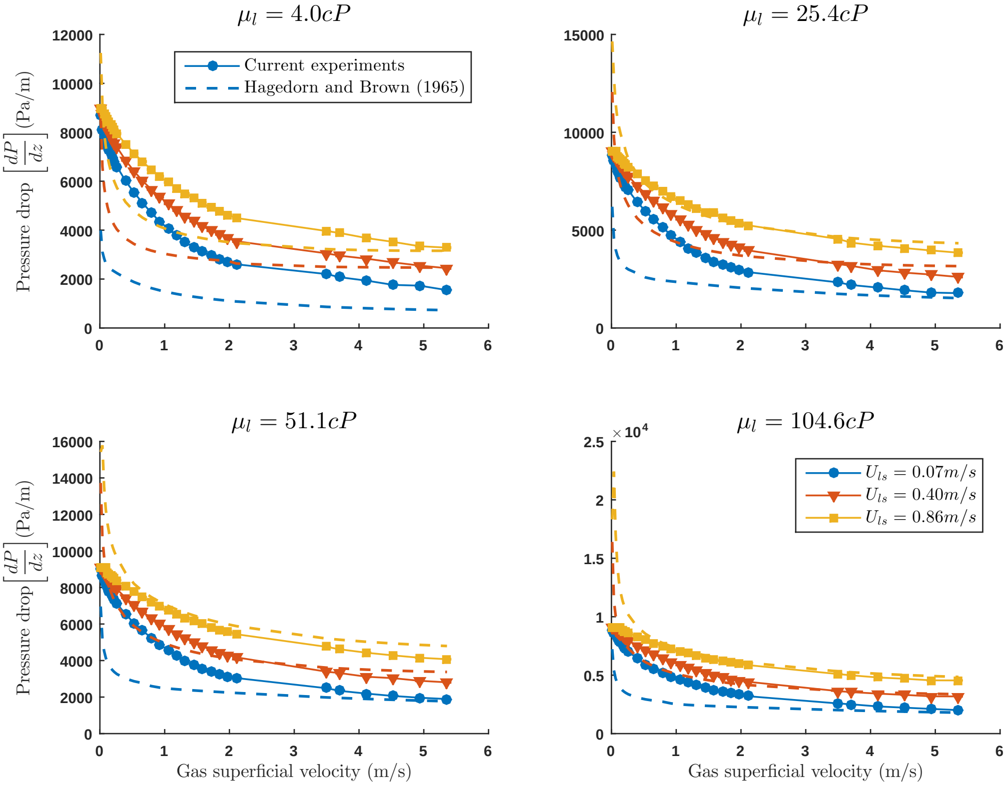

Fig. 5.14 Experimental total pressure gradient profile at different viscosities and the predictions of Hagedorn and Brown (1965) model [73].

Figure5.15 shows the deviation of the predicted values by Hagedorn and Brown (1965) model from the experimental values. In concordance with what was observed earlier for both the models of Friedel (1979) and the one by Lockhart-Martinelli (1949), the closeness of predictions seems to improve with increasing liquid superficial velocity as consistently exhibited by the profiles in Figure5.15. It can also be observed that although the model generally under-predicts pressure gradient, it over-predicts pressure gradient at low gas superficial velocities (in the bubbly flow region). The departure from experimental data in that region becomes more significant with increasing liquid viscosity, while it reduces for all other data-points.

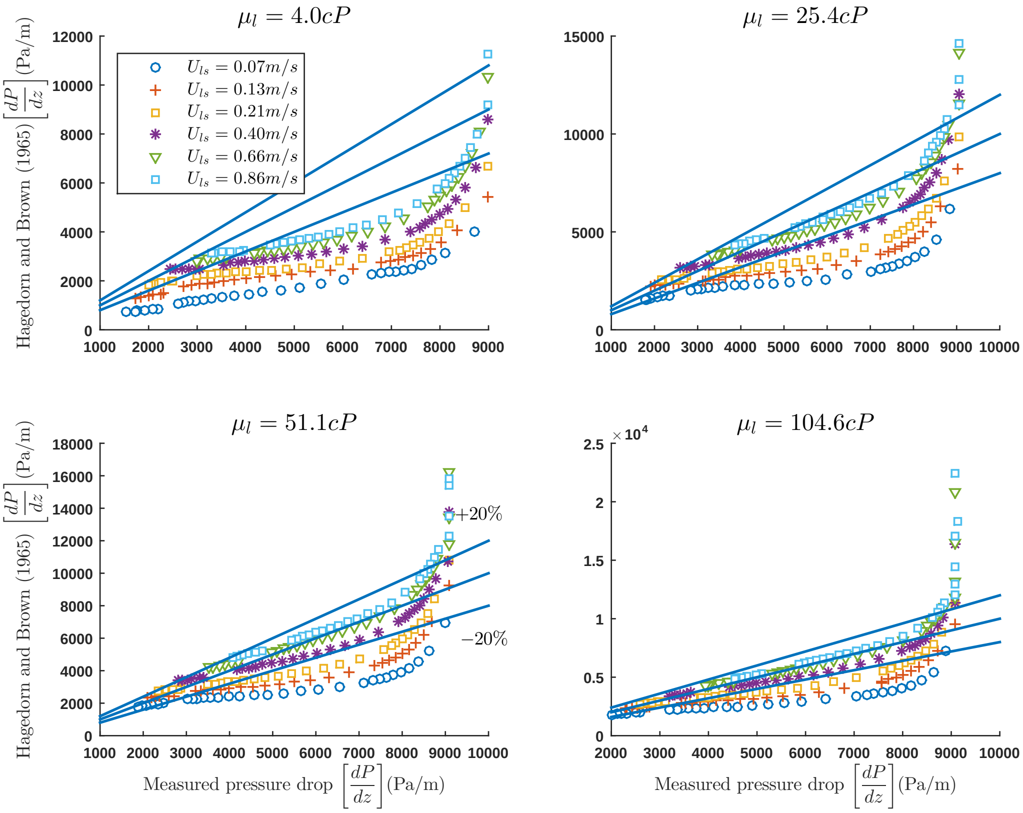

Fig. 5.15 Deviation of predicted total pressure gradient by Hagedorn and Brown (1965) [73] from the experimental data.

Figure 5.16 shows the predicted overall pressure gradient profiles by the model of Aziz et al (1972) [21] plotted with the experimental data against gas superficial velocity for the four viscosities studied. The mechanistic model of Aziz et al (1972) was developed based on the flow pattern map of Govier et al (1957), then using a drift flux model to predict void fraction for only bubbly and slug flow. No model was proposed for churn or annular flow, therefore the model does not extend over all the experimental range as depicted in Figure 5.16. The sharp bubbly-slug regime transition boundary can be clearly seen especially in the profiles at lower liquid superficial velocity where the phase slippage is more significant. The deviation from experimental data seem to increase with increasing liquid viscosity and decrease with increasing liquid superficial velocity. Although the drift velocity and distribution coefficient in the slug flow region is dependent on the non-dimensional viscosity number, yet the drift velocity in the bubbly flow region is considered independent of the viscosity. Also employing a viscosity independent flow regime map contributes towards the poorer performance of the model at higher viscosities.

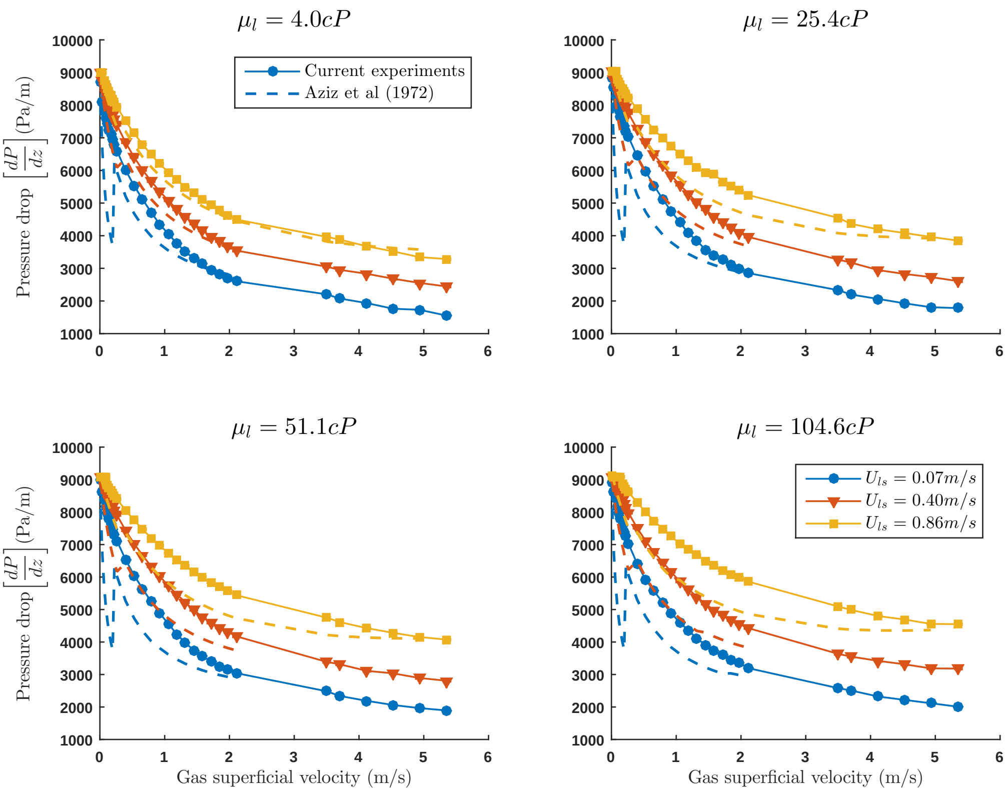

Fig. 5.16 Experimental total pressure gradient profile at different viscosities and the predictions of Aziz et al (1972) model [21].

Figure 5.17 show the deviation of the overall pressure gradient predicted by the model of Aziz et al (1972) against the experimental data at different velocities. It can be seen that the performance is mostly satisfactory and falls within the 20% deviation lines in all the viscosities, despite the large divergence observed at low gas and liquid superficial velocities. This divergence is attributed to the supposition of a constant drift velocity, while at low slip ratio the employed drift velocity might be satisfactory, at low liquid superficial velocities the predicted drift velocity seems to be much higher, resulting in a gross over-estimation of the void fraction.

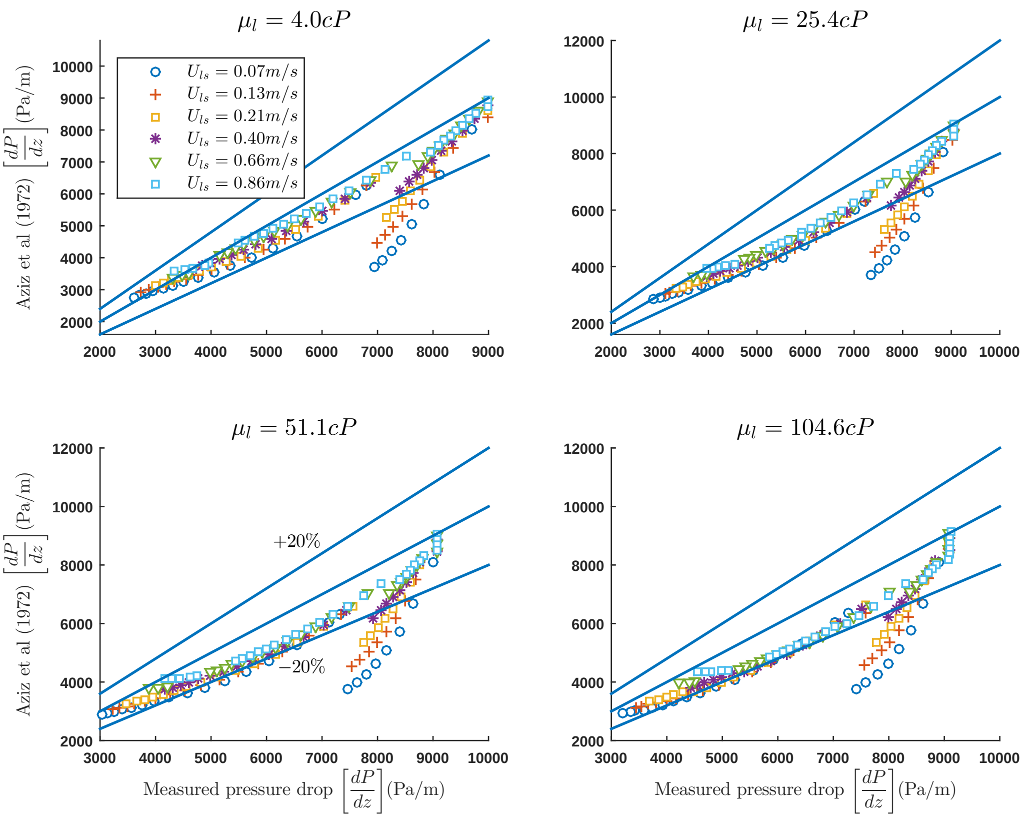

Fig. 5.17 Deviation of predicted total pressure gradient by Aziz et al (1972) [21] from the experimental data.

Figure 5.18 shows the total pressure gradient profiles predicted by Beggs and Brill (1973) [31] homogeneous flow model and the experimental data. It can be seen that the model predicts pressure gradient quite well at low viscosities, a marked deviation from the experimental values is observed with increasing liquid viscosity. It can also be observed that considerable deviation is observed at very low gas superficial velocities, and is more significant at lower liquid superficial velocities.

Figure 5.19 shows the deviation of the predicted pressure gradient of Beggs and Brill (1973) from the experimental data. It can be seen that a much better prediction is obtained at higher liquid superficial velocities. This can be attributed to the closeness to the homogeneous behaviour at higher liquid superficial velocities due to increased

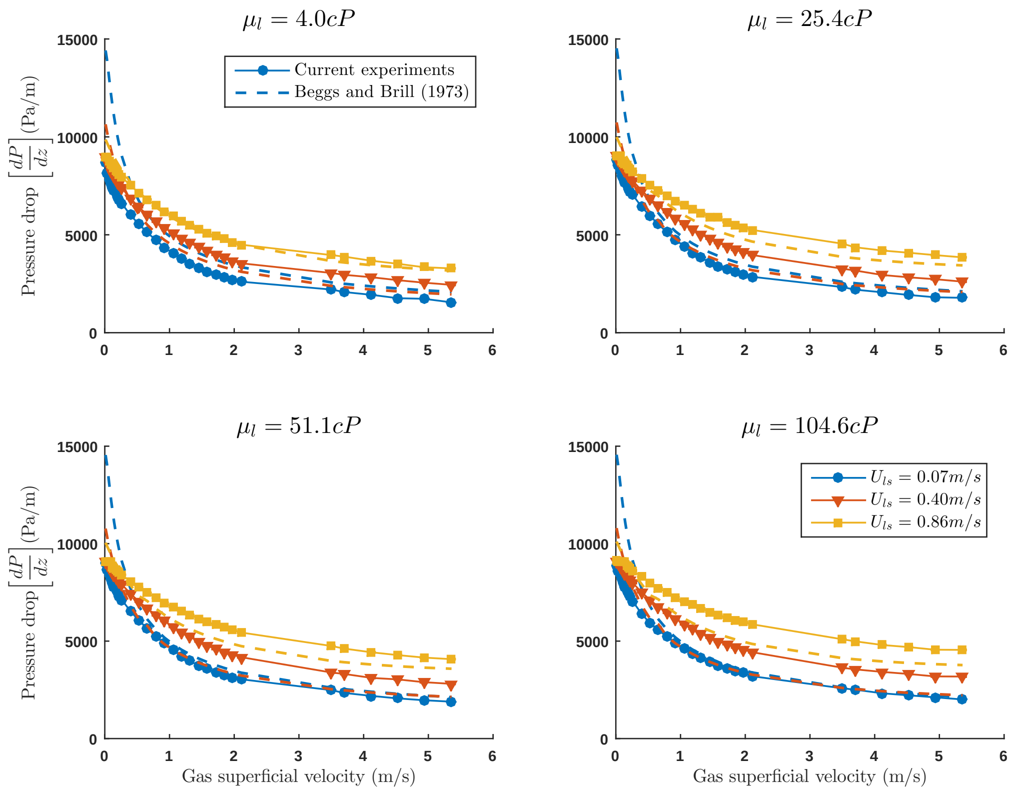

Fig. 5.18 Experimental total pressure gradient profile at different viscosities and the predictions of the homogeneous model by Beggs and Brill (1973) [31].

liquid turbulence and decreased slippage between the phases. The divergence from the experimental and predicted values seem to increase with increasing viscosity. This can be attributed to the correlations used in the prediction of void fraction been developed for air-water systems in pipes of diameters below 38 mm.

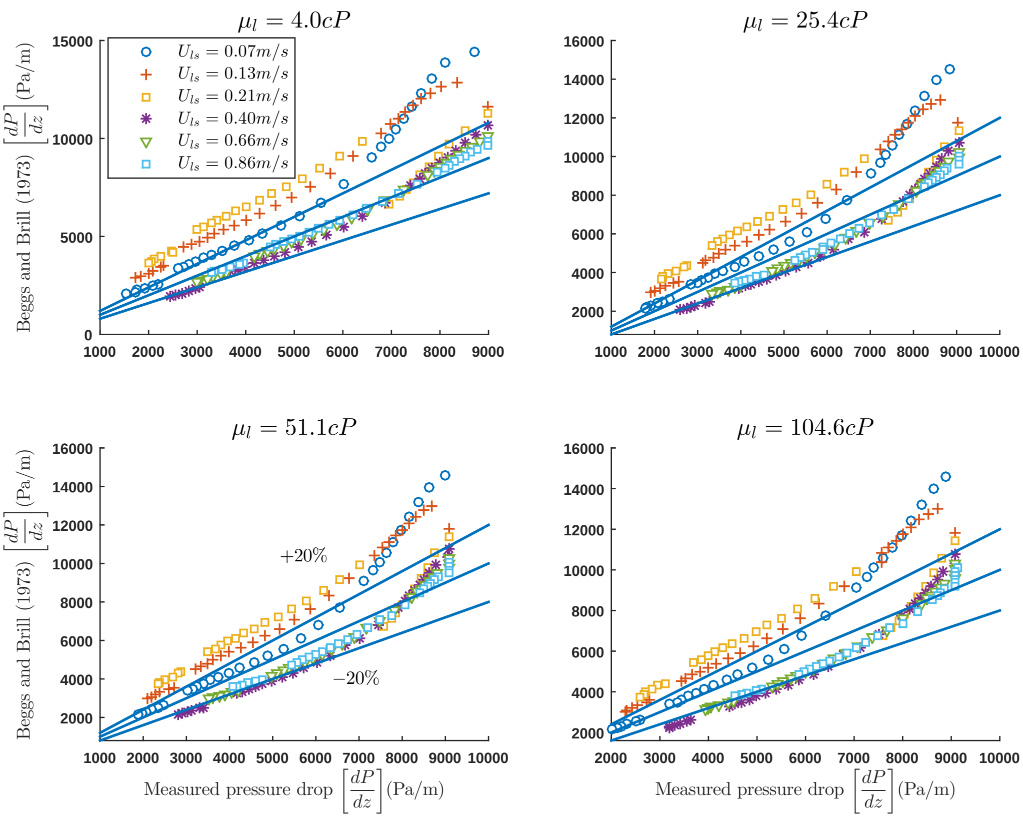

Fig. 5.19 Deviation of predicted frictional pressure gradient by Beggs and Brill (1973) [31] from the experimental data.

Figure 5.20 shows the predictions of the model of Mukherjee and Brill (1985) plotted together with the experimental profiles at various viscosities. Mukherjee and Brill (1985) model was developed for flow in inclined pipes, where a no-slip frictional pressure gradient is estimated in the bubbly and the slug flow regimes. As can be seen in Figure 5.20 the model provides good prediction at the lower viscosities (<51.4 cP), the profiles deviate substantially at 51.1 cP while it becomes completely unrealistic at the 104.6 cP. The erroneous profile obtained for the 104.6 cP is referred to the liquid hold-up correlation that is dependent on the non-dimensional liquid viscosity number, where above a viscosity of 65 cP, the correlation produces hold-up higher than 1. Therefore, the model applicability is only limited to lower viscosities.

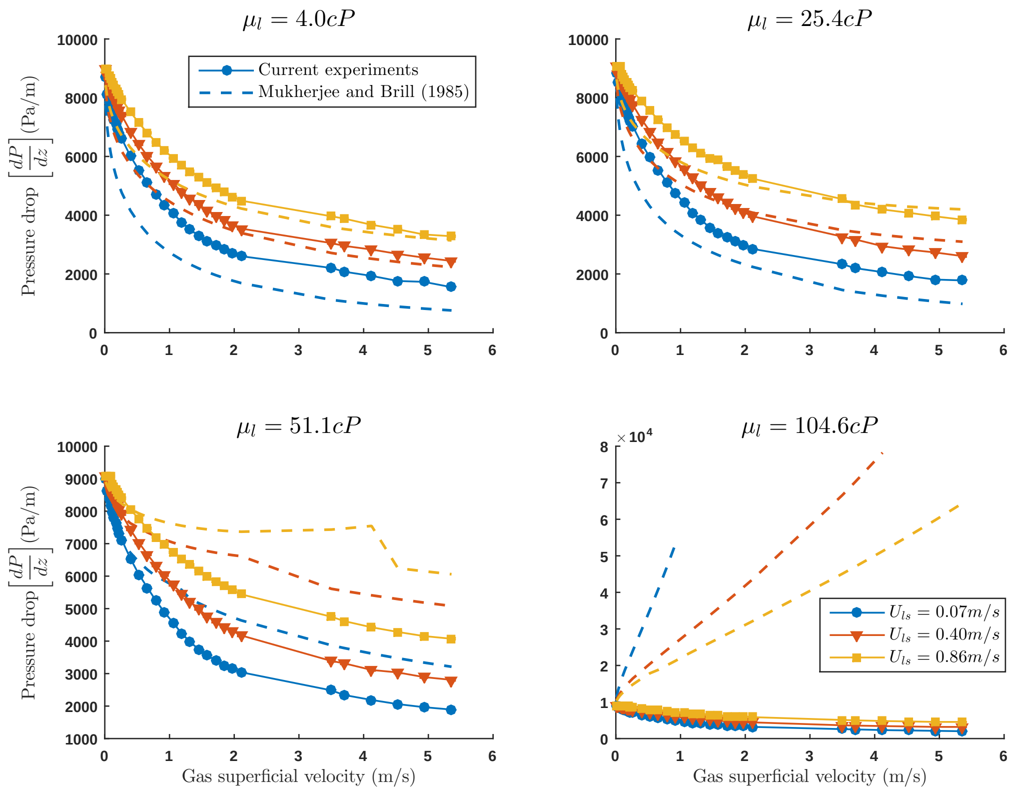

Fig. 5.20 Predicted total pressure gradient by Mukherjee and Brill (1985) [129] together with the experimental pressure gradient profile against gas superficial velocity at various viscosities.

Figure 5.21 shows the measured pressure gradient data plotted against the predicted values of Mukherjee and Brill (1985). It can be seen in agreement with the performance of the models discussed earlier, the a better prediction is produced with increasing liquid superficial velocity.

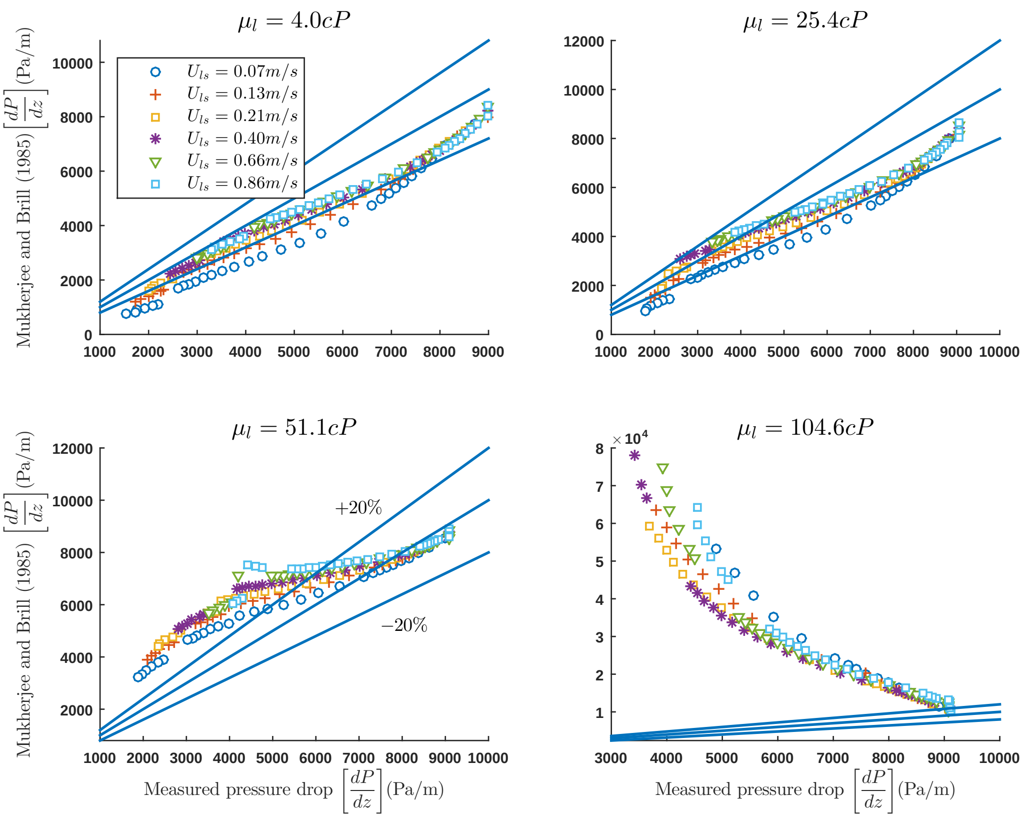

Fig. 5.21 Deviation of the predicted total pressure gradient by Mukhaerjee and Brill (1985) [129] from the experimental data.

Figure 5.22 shows the predictions of Kabir and Hasan (1990) [102] total pressure gradient plotted with the experimental data against the gas superficial velocity. This model is formulated of a flow regime transition criterion and two drift-flux models for both bubbly and slug flow regimes, and a flow pattern dependent model for predicting frictional pressure gradient. It can be seen in Figure 5.22 that the model predicts the trend and produces close values to the experimental data. The performance deteriorates dramatically with increasing viscosity departing away from the measured data. With regard to the effect of liquid superficial velocity on performance, contrary to what was observed in the models discussed earlier,the performance seems to be negatively influenced by the increase in liquid superficial velocity.

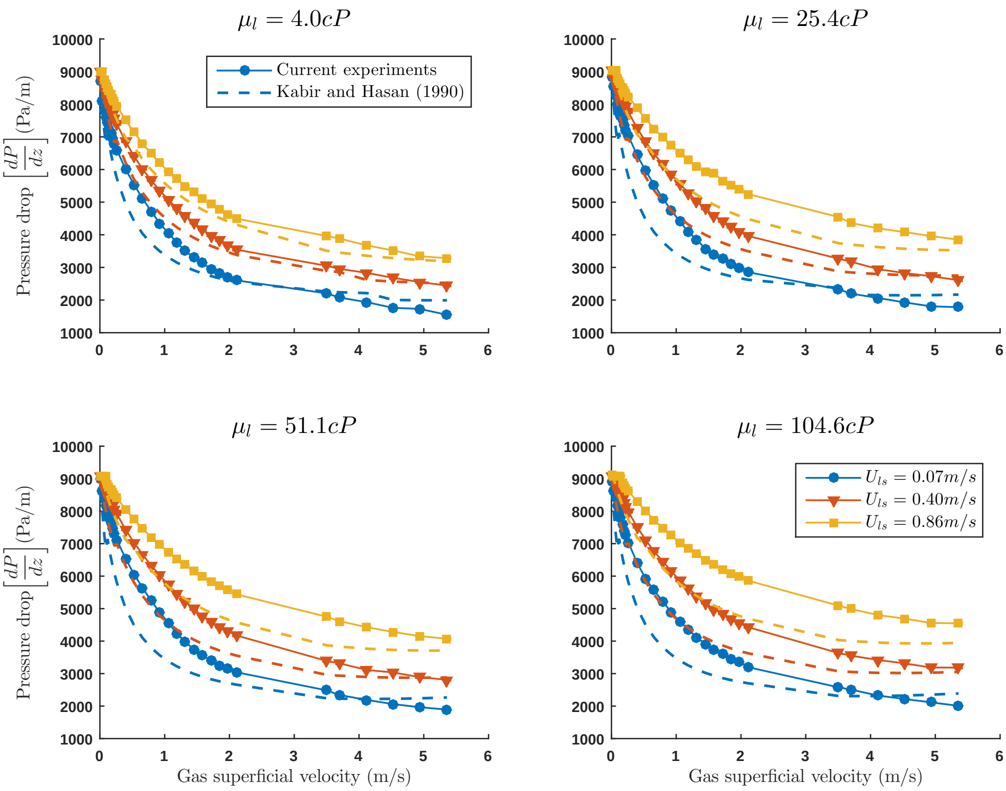

Fig. 5.22 Predicted total pressure gradient by Kabir and Hasan (1990) [102] together with the experimental pressure gradient profile against gas superficial velocity at various viscosities.

Figure 5.22 shows the deviation of the predicted profiles shown in Figure 5.21 from the experimental data. It can be seen that better performance is produced at lower viscosity, it departs systematically with increasing viscosity from the equality line. Larger divergence is observed at intermediate pressure values, while at lower and higher pressure gradient values the performance appears to be much better. This suggests that the correlation of slug and churn flow is more likely to be performing poorly in comparison to the bubbly and annular flow correlations.

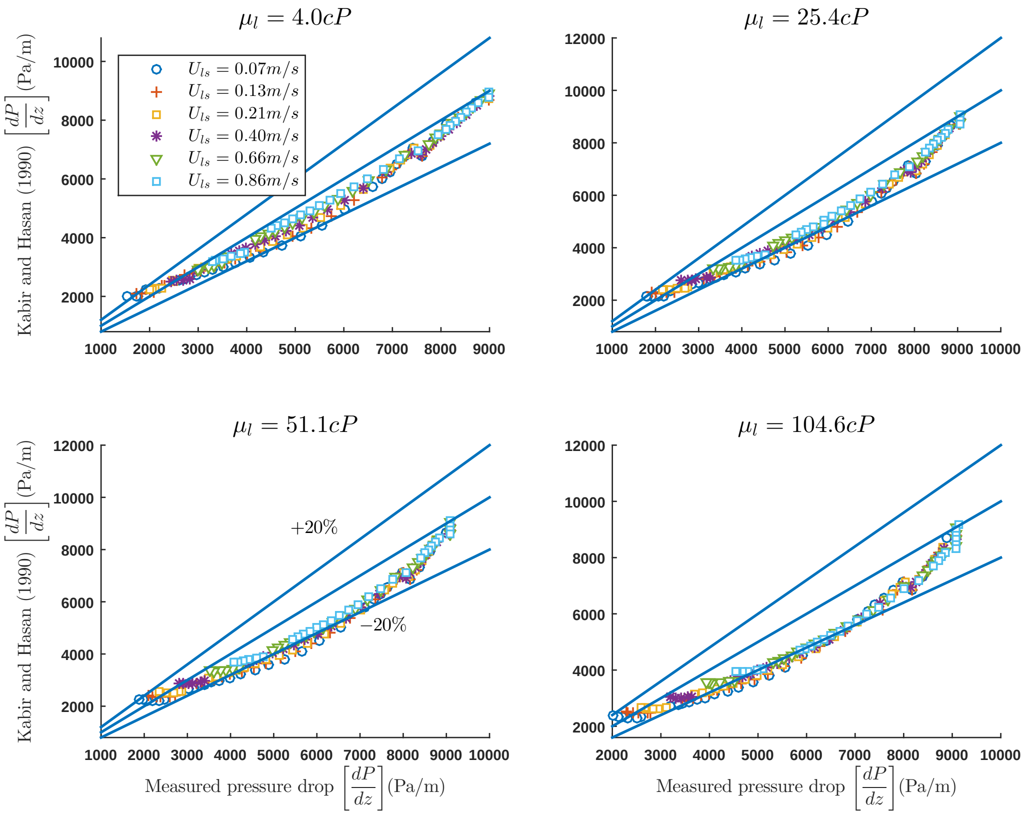

Fig. 5.23 Deviation of the predicted total pressure gradient by Kabir and Hasan (1990) [102] from the experimental data.

Figure 5.23 shows the total pressure gradient produced by Anasri et al (1994) [18] mechanistic model together with the experimental profiles. It can be seen the model overall performs poorly throughout. The divergence increases with increasing liquid viscosity and decreasing liquid superficial velocity. This large divergence can be attributed to the disregarding of the churn flow regime, providing only models for bubbly, slug and annular flow. It should be noted that it was not possible to implement the developing slug flow model they proposed due to the difficulty to evaluate the cap length from the Nusselt's film thickness as proposed in the paper, because it would yield a third order polynomial that needs more relations to evaluate.

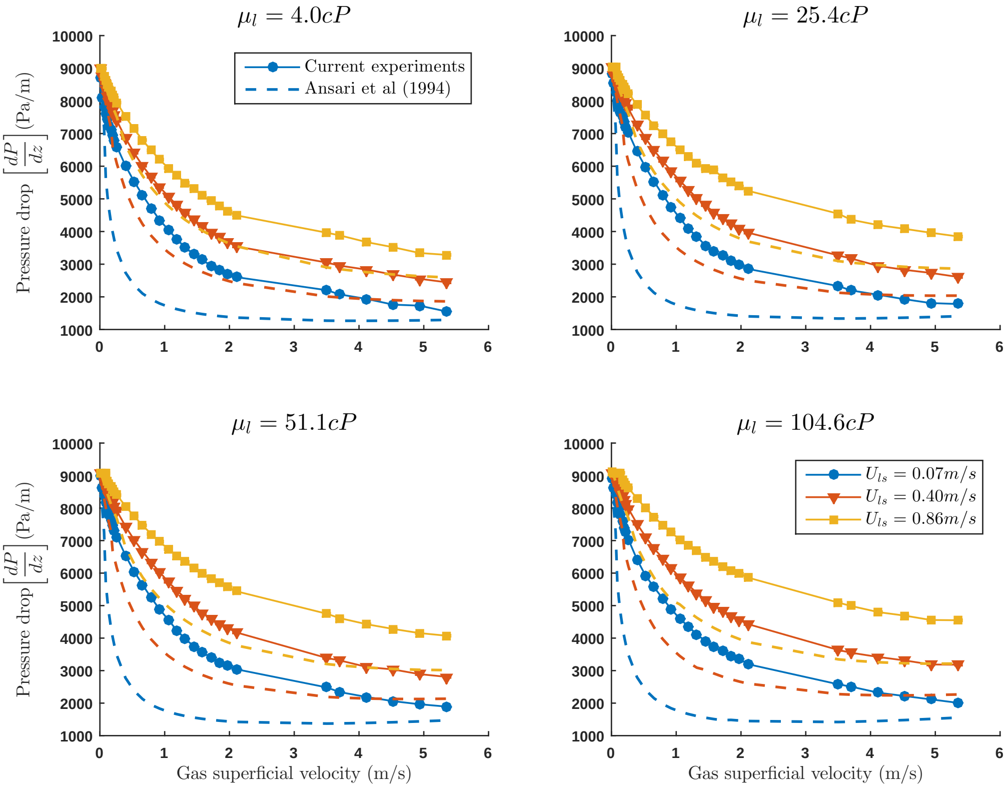

Fig. 5.24 Predicted total pressure gradient by Ansari et al (1994) [18] together with the experimental pressure gradient profile against gas superficial velocity at various viscosities.

Figure 5.24 shows the deviation of the Ansari et al (1994) model from the experimental data. It can be seen that most of the data points fall outside the 20% deviation line. However, very close predictions are produced at high pressure gradient values, in the bubbly flow region, which suggests that the bubble flow void fraction correlation proposed by Ansari et al (1994) performs well.

The overall performance of the models is assessed using Average Percentage Error(APE) and the Absolute Percentage Error (AbPE) as given by equation 5.9 and 5.10. The average percentage error allows to show if the respective model either over-predict or under-predict the pressure gradient. The absolute percentage error quantifies the magnitude of the overall deviation from experimental data. The error is first calculated for only the frictional pressure gradient including the models of Friedel (1979) and

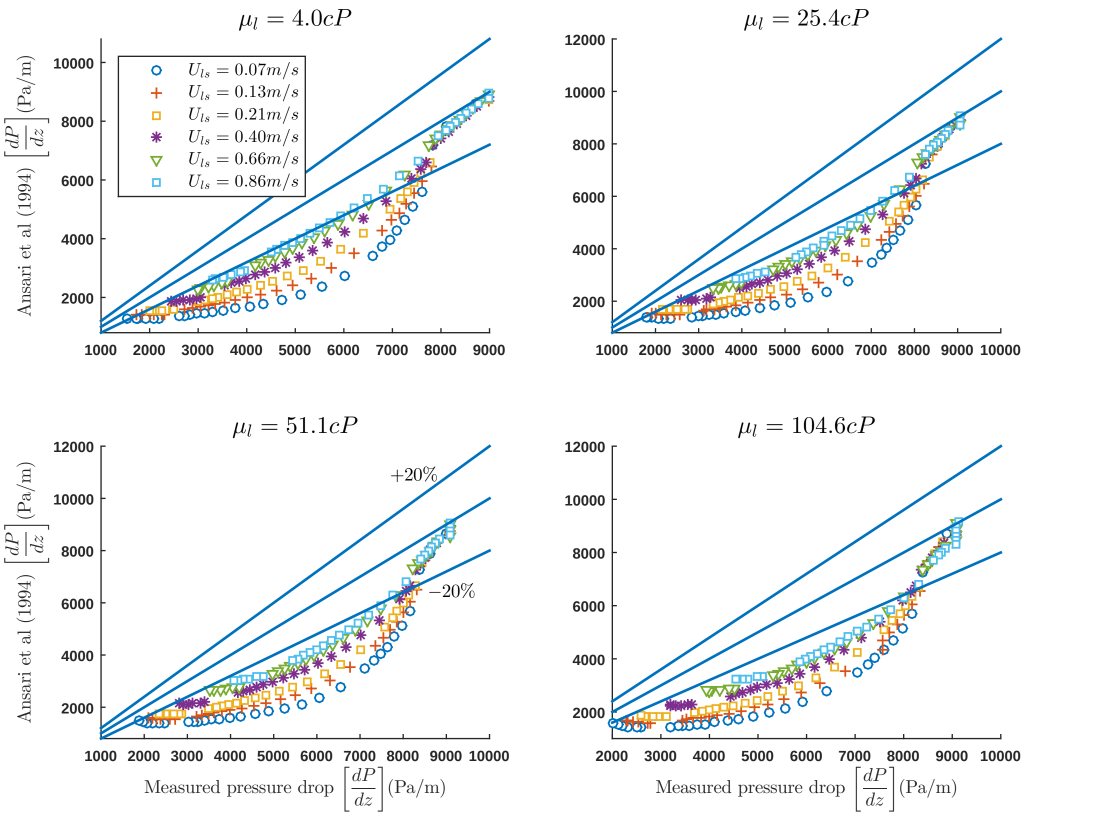

Fig. 5.25 Deviation of the predicted total pressure gradient by Ansari et al (1994) [18] from the experimental data.

Lockhart and Martinelli (1949) as presented in Figure 5.26. It should be noted that the error of Lockhart and martintelli (1949) was not included in the Figure due to its substantial under-prediction compared to the other models as presented earlier in Figure 5.11 and 5.12. It can be seen that most models under-predict frictional pressure gradient quite grossly. The deviation becomes more significant with increasing viscosity. It is hard to judge which model performed the best as all of them has deviated by the order of 100% at one of the viscosities. It can be said that none of the models studied, including that of Lockhart and Martinelli (1949) [116] produces satisfactory prediction of the frictional pressure gradient measured in this experimental study.

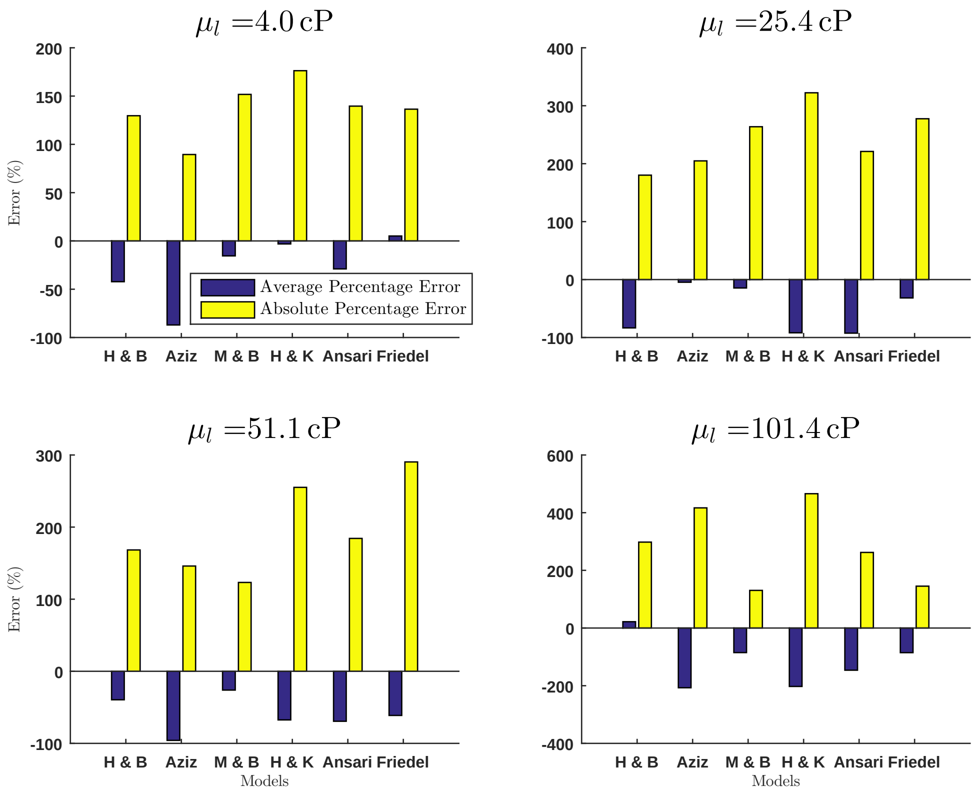

Fig. 5.26 Error of the predicted frictional pressure gradient by models of Hagedorn and Brown (1965) [73] denoted as (H & B), Aziz et al (1972) [21], Mukherjee and Brill (1973) (M & B), Kabir and Hasan (1990) [102] (H & K), Ansari et al (1994) [18],Friedel (1979) [61].

The predictability of the overall pressure gradient is compared for the rest of the models excluding Lockhart and Martinelli (1949) and Friedel (1979). The error is presented for each viscosity in Figure 5.27. It can be seen that the predictability improves dramatically as most models predict the overall pressure gradient within 30% accuracy. It can also be seen that most models under-predict the overall pressure-gradient aside from Beggs and Brill (1973) [31]. It is also observable that with increasing liquid viscosity the error produced by most of the models increase. However, the performance of Beggs and Brill (1973), and Hagedorn and Brown (1965) seems to improve with increasing liquid viscosity.

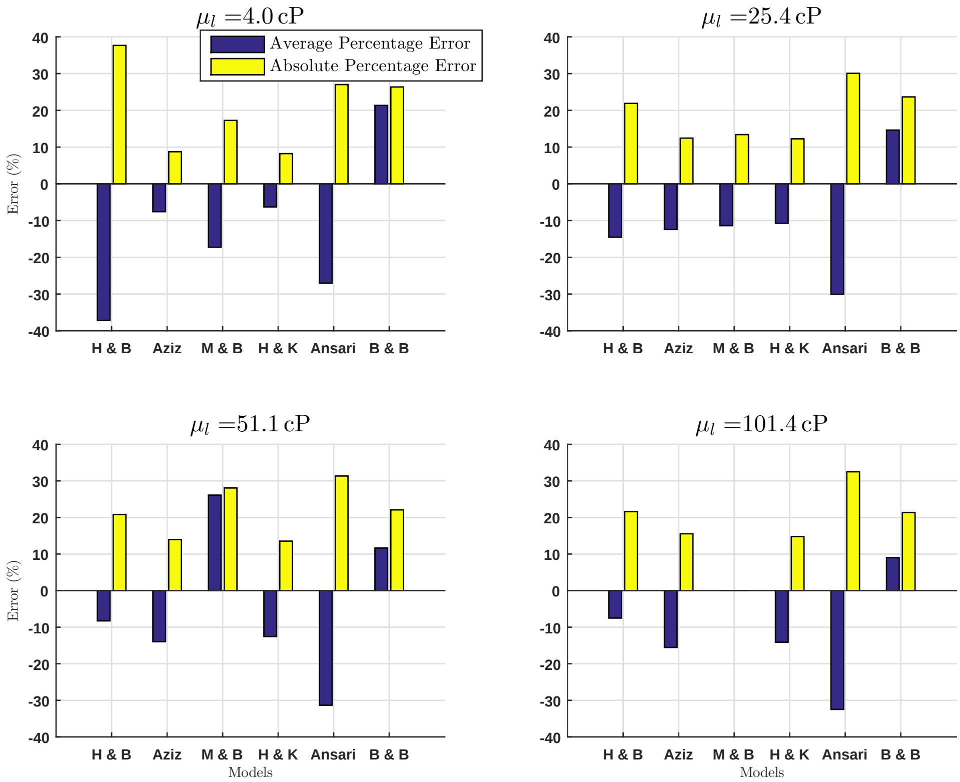

Fig. 5.27 Error of the predicted overall pressure gradient by models of Hagedorn and Brown (1965) [73] denoted as (H & B), Aziz et al (1972) [21], Mukherjee and Brill (1973) (M & B), Kabir and Hasan (1990) [102] (H & K), Ansari et al (1994) [18],and Beggs and Brill (1973) [31] (B & B). Error of (M & B) is not plotted at the 101.4 cP to maintain comparability because it is colossal compared to the other models.

To judge the overall performance of the models across all viscosities, the average error and average absolute error presented in Figure 5.27 are averaged and plotted in Figure 5.28. It is notable that both the models of Aziz et al (1972) [21] and Kabir and Hasan (1990) [102] produce comparable small error from the experimental data.

However the model of Kabir and Hasan (1990) [102] performs the best amongst the studied models in this section.

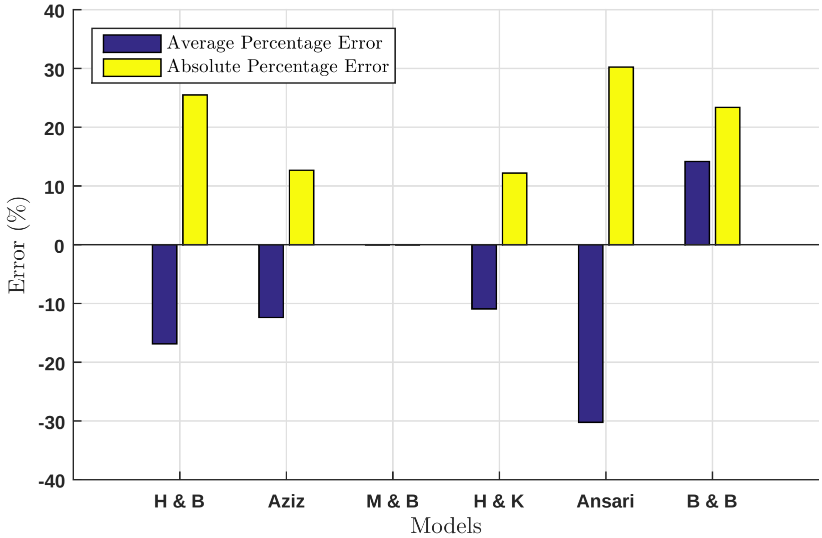

Fig. 5.28 Overall performance at all viscosities by the models of Hagedorn and Brown (1965) [73] denoted as (H & B), Aziz et al (1972) [21], Mukherjee and Brill (1973) (M & B), Kabir and Hasan (1990) [102] (H & K), Ansari et al (1994) [18],and Beggs and Brill (1973) [31] (B & B).

5.2.3 Prediction of structure frequency at high viscosities

Structure frequency of vertical flows has recieved very little attention, while many correlations have been proposed for frequency in horizonatl and slightly deviated pipes. The reader is referred to the article by Baba et al (2017) [29] for a recent review of these models. A few attempts have been made to model frequency in vertical and near vertical pipes [14, 76, 104, 11]. This lack of models can be partly attributed to the fact that in statistical terms, flow in vertical pipes is far too common, especially in the field of oil and gas transport compared to vertical and near vertical flows. One contributing factor is the rarity of frequency data for flows in vertical pipes, only a limited number of reports are available [11, 76, 172, 25, 56, 4, 182, 143, 14, 28, 3, 184, 105, 104]. Which presents the case for the significance of the frequency data presented in chapter 4, making it the only available frequency information on viscous flows in large diameter vertical pipes. It is therefore necessary to try to investigate the performance of these available models against the data and perhaps suggest a new correlation if the need arises. The proposed models for frequency in vertical flow are published in [76, 104, 14, 11] and summarised in Table 5.1.

Table 5.1 Models for structure frequency in vertical pipes

Reference	Proposed Correlation
Zabaras (1999) [190]	$f_s = 0.0226\left(\frac{U_{ls}}{gD}\right)^{1.2}\left[\frac{212.6}{U_{ms}}+U_{ms}\right]^{1.2}\left(0.836+2.75\sin^{0.25}\theta\right)$
Kaji et al (2009) [104]	$\frac{fD}{U_{ms}} = U_{gs}^{-0.75}\left(0.74U_{ls}+0.53\right)\left(\frac{z}{D}\right)^{-0.6}$
Hernandez et al (2010) [76]	$f^v = 0.8428\left[\frac{U_{ls}}{gD}\left(\frac{19.75}{U_{ms}}+U_{ms}\right)\right]^{0.25}$ $f^h = 0.0226\left[\frac{U_{ls}}{gD}\left(\frac{212.6}{U_{ms}}+U_{ms}\right)\right]^{1.2}$ $f = f^h\cos\theta + f^v\sin\theta$
Alruhaimani (2015) [14]	$f_s = \ln\left[3.216+0.794N_{Fr_l}N_{\mu}^{-0.5}\frac{U_{ls}}{D}\right]$ $N_{Fr_l} = \frac{U_{ls}}{(gd)^{0.5}}\sqrt{\frac{\rho_l}{\rho_l-\rho_g}}$ $N_{\mu} = \frac{U_{ms}\mu_l}{gD^2(\rho_l-\rho_g)}$

It is a common recourse to try to predict frequency using an empiricism approach. One of the common approaches is the correlation of gas/mixture-based Strouhal number against the Lockhart and Martinelli parameter as proposed by Azzopardi (1997) [24]. It was therefore decided to calculate the mixture-based Strouhal number (St_m) given by equation 5.11, and plot it against the mixture superficial velocity (U_{ls}) as in Figure 5.29. As can be seen, the trends can be reasonably fitted to a power-law relationship, with R^2 above 93% in most of the cases except at the highest viscosity where quite a considerable scatter is observed. It has been found that the Strouhal number evolution with the mixture superficial velocity follows a relationship in the form of equation 5.12. The coefficients A and B vary with liquid viscosity as can be noted from the formula displayed in Figure 5.29.

$$St_m = \frac{fD}{U_m} \tag{5.11}$$

$$St_m = A \times \left(\frac{U_m}{\sqrt{gD}}\right)^B \tag{5.12}$$

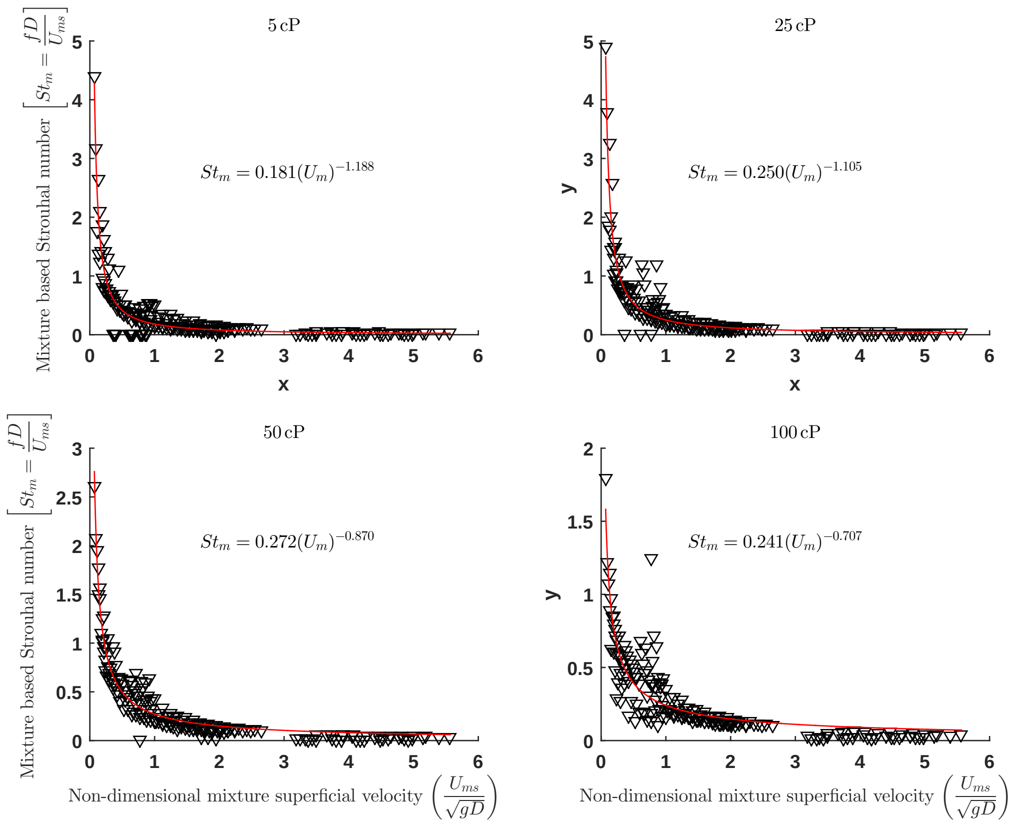

Fig. 5.29 Mixture-based Strouhal number (St_m) plotted against non-dimensional mixture superficial velocity $\left(\frac{U_m}{\sqrt{gD}}\right)$ for each viscosity separately. The trends are fitted to a power-law equation displayed on the figures.

In an attempt to observe the change of the coefficients with the fluids' physical properties it has been decided to carry out a similar exercise to that presented in the void fraction section of this chapter. The product of Morton number (equation 5.3) and the viscosity number (equation 5.2) will produce a correlation that is inclusive of most of the geometrical and physical properties of the flow, and may provide a more comprehensive and universal applicability of the correlation. Consequently a correlation of the coefficients A and B is produced and displayed in Figure 5.30. The relationship for both coefficients is presented in equation 5.13 and 5.14. Finally, an implicit expression for the frequency as Strouhal number can be presented as the correlation in equation 5.15.

$$A = 0.225\left(N_{\mu_l} N_{Mo}\right)^{0.031} \tag{5.13}$$

$$B = -1.012\left(N_{\mu_l} N_{Mo}\right)^{-0.045} \tag{5.14}$$

$$St_m = 0.225\left(N_{\mu_l} N_{Mo}\right)^{0.031} \times \left[\frac{U_m}{\sqrt{gD}}\right]^{-1.012\left(N_{\mu_l} N_{Mo}\right)^{-0.045}} \tag{5.15}$$

The performance of the correlation against the experimental data can be viewed in Figure 5.31. It can be seen that most of the experimental frequencies are predicted with a reasonable accuracy. It should be noted that the behaviour of frequency differ dramatically with the gas and liquid superficial velocity as well as the flow regime, especially near bubbly flow where intermittency might not be easily detectable as exhaustively explained in Chapter 4. Therefore, although the performance of the model might not seem accurate enough, however it is universal and applicable across a wider range of regimes and fluid properties in comparison with other models.

In an attempt to observe the correlation of the frequency, embedded in the gas-based Strouhal number against the Lockhart and Martinelli parameter as proposed by Azzopardi (1997) [24] Figure 5.32 is produced. The figure shows that the trend in the frequency could be correlated in that manner, however a quite considerable scatter is observed in the data. Further data is needed, especially at higher liquid superficial velocities to try and observe in the correlation still holds. The scatter is believed to be mostly caused by the difference in liquid superficial velocity.

The performance of other models proposed in literature against the experimental frequency data can be seen in Figure 5.33. It is observable that most of the models

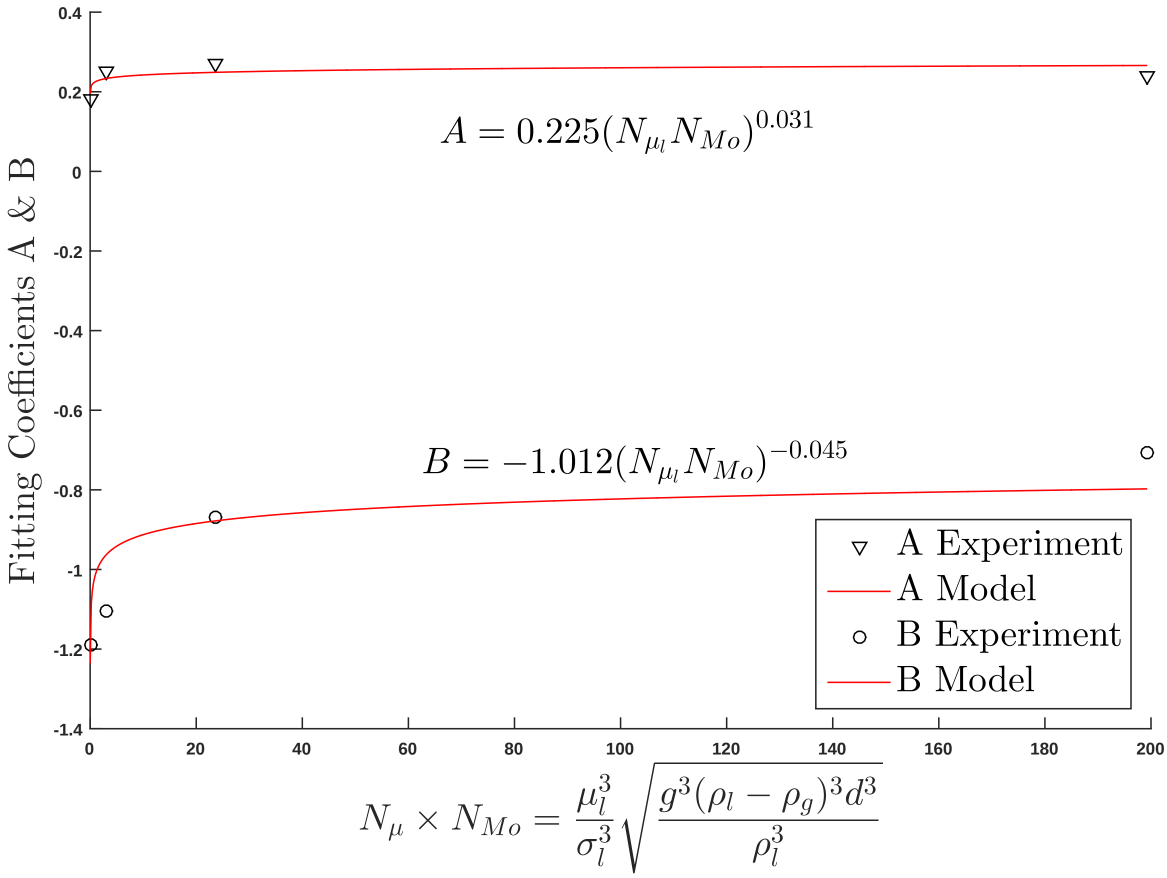

Fig. 5.30 Power-law coefficients correlation to the product of Morton number (N_{Mo}) and Viscosity number (N_{μ_l}).

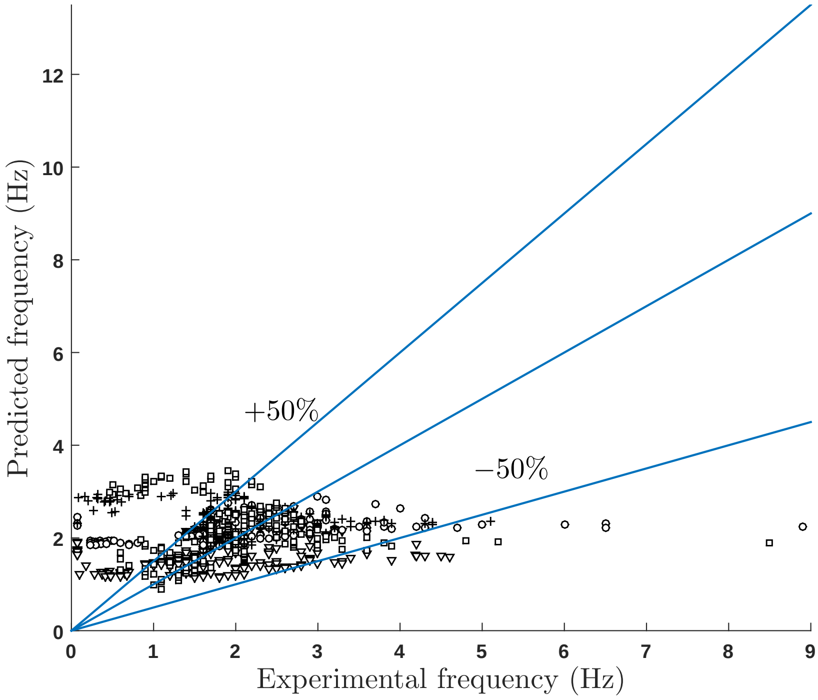

Fig. 5.31 Performance of the frequency correlation against experimental data.

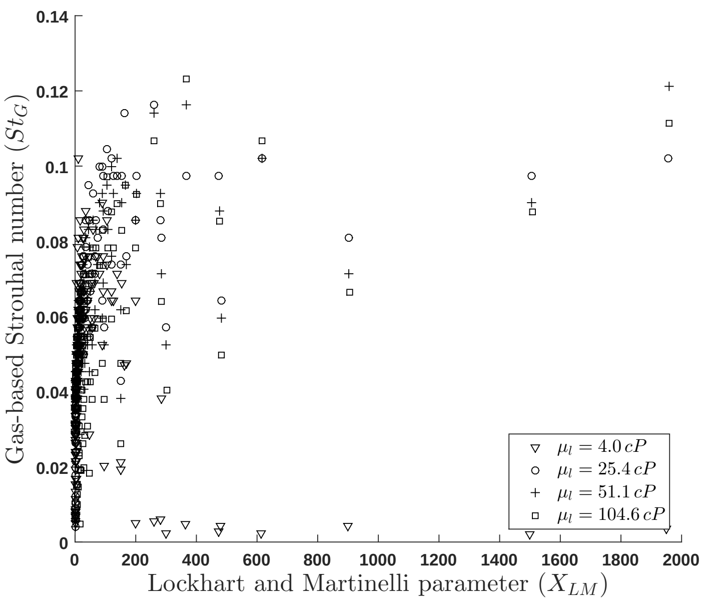

Fig. 5.32 Gas-based Strouhal number plotted against Lockhart and Martinelli parameter $\left(X_{LM} = \sqrt{\frac{\rho_l U_{ls}^2}{\rho_g U_{gs}^2}}\right)$.

included (refer to Table 5.1 for the formula) grossly diverge from the experimental data, yet the model of Kaji et al (2009) seems to perform the best amongst the quadruplet. If the performance is compared to that of this model as per Figure 5.31, it can be judged to perform better than all considered here.

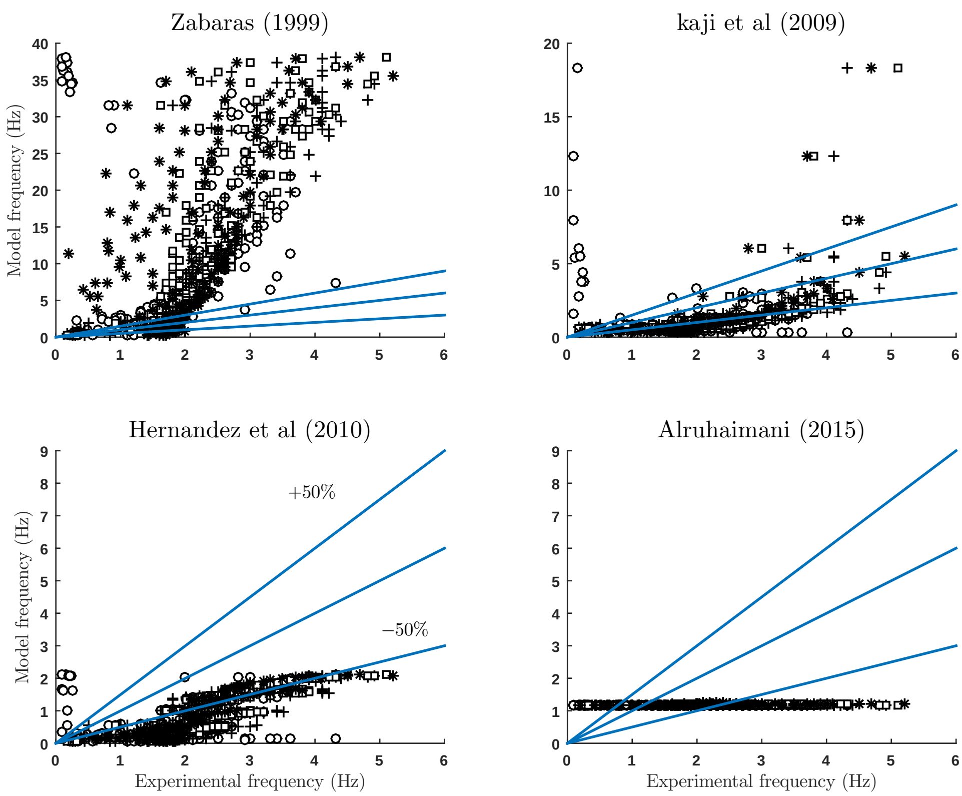

Fig. 5.33 Performance of other models proposed for frequency in vertical pipes against experimental values. The results presented are for the models of Zabaras (1999) [190], Kaj et al (2009) [104], Hernandez et al (2010) [76], and Alruhaimani (2015) [14].

5.3 Conclusions

In this chapter the published state of the art models have been tested against the unique, high resolution data collected for viscous flows in vertical large diameter pipes. One of the most important two phase flow parameters is the void fraction. Several popular models have been employed to reproduce the experimental results. It was found that most models largely deviate, with the divergence becoming more significant with increasing liquid viscosity. A drift-flux correlation has been proposed, a function of the product of Viscosity number (N_{μ_l}) and Morton number (N_{Mo}). The proposed correlation (equations 5.1, 5.4, 5.5) performs better than other models investigated in this study. The performance of the new correlation has also been examined against other published data collected for viscous flows in vertical pipes,the correlation was found to predict the void fraction with a reasonable accuracy.

The pressure gradient has also been dissected in terms of its three components. This chapter provides a strong evidence of existence of positive frictional pressure gradient in the intermittent flow region. To further consolidate the findings, other frictional pressure gradient data has been calculated from literature with focus on viscous flows in vertical large diameter pipes. Positive frictional pressure gradient was also found in the literature data. The positive frictional pressure gradient issue was referred to the average instantaneous wall shear-stress which governs the direction of film flow, when the liquid film predominantly falls back in comparison to the up-ward movement then positive frictional pressure gradient occurs. Early evidence of negative wall-shear stress data was published by Whalley and McQuillan (1985) [186]. It was found that the phenomenon becomes more pronounced with increasing pipe diameter and decreasing liquid viscosity and liquid/gas density ratio.

The performance of most of the popular pressure drop models has been investigated against the experimental data. It was found that the models of Aziz et al (1972) [21] and Kabir and Hasan (1990) [102] produce comparably small error from the experimental data. However, the model of Kabir and Hasan (1990) [102] performs the best amongst the studied models.

The last section of this chapter assesses the performance of the few published structure frequency models for vertical flows. A new empirical correlation has been proposed that is again a function of the product of viscosity and Morton number. The correlation was found to predict experimental frequency with a reasonable accuracy for most of the data. The performance of the correlation was found to be superior to other models, followed by the model of Kaji et al (2009) [104].

Chapter 6

Effect of injector geometry on two-phase flows in a vertical large diameter pipe at elevated viscosities

6.1 Introduction

Effect of injector geometry on two phase flow characteristics is of profound importance to oil and gas industry. If the injection method is found to vary the two phase flow characteristics dramatically, it can be employed to obtain desirable two phase flow regimes/characteristics and avoid rather unsought conditions. This approach could potentially save a lot of costs in the extraction and transportation of oils. Moreover, the issue of flow development and dependency on injection conditions is essential when it comes to modelling two phase flows. A lot of experimental data and numerical models have been published based on systems that are not fully developed. Therefore, inaccurate modelling of the physical interactions of the flow gets adopted and hence large divergence between the models and experimental data produced by other investigators often transpires.

Two approaches are generally adopted to investigate flow development problems. One is through obtaining two phase flow measurements at different axial locations from the injection point, the flow is considered developed when the characteristics remain virtually similar at different axial locations. The other approach is by using different injector geometries and examining the flow attributes at a constant axial location downstream the test section.

6.1.1 Background and review

As mentioned in earlier chapters two-phase flow data in large diameter pipes is scarce. Even less is available on the effect of injector geometry in large diameter pipes. Herringe and Davis (1976) studied entrance effect using three different injector geometries in a 0.051 m pipe, measuring void fraction at three axial positions (8D, 36D, and 108D). Flow development was observed in terms of radial velocity and void fraction profiles, and bubble size distribution. In most of the cases examined the flow was reported to have converged by 108D axial distance [78].

Sekoguchi et al (1980) invegated influence of gas injector in a 0.0169 m pipe using three different injector geometries (two porous tubes and a capillary nozzle). Void fraction was measured at 29.6D and 117.8D axial locations. Radial void fraction profiles exhbited wall peaking for the porous wall injector, while concentric capillary injector produced a distinct core peaking profile at both axial locations at similar gas and liquid input rates [160].

In their pioneering study Ohnuki and Akimoto (1996) investigated the injector geometry effect in a 0.48 m in diameter and 2.016 m length vertical pipe [134]. They employed two different injectors, namely a porous wall tube injector and a nozzle injector using air-water fluids. They varied gas superficial velocity in the range of 0.02-0.87 m/s and the liquid superficial velocity between 0.01-0.2 m/s. They found considerable difference in flow characteristics produced by different injectors in the lower half of the test section. No appreciable effect of the injector was observed in the upper half of the test section. However, a slightly lower void fraction was produced by the nozzle injector, evident from the radial distribution profile published in addition to the higher structure velocity profile produced by the nozzle injector [134].

Guet and Ooms (2003) used three different injectors in a 0.072 m pipe and reported bubble size and void fraction measurements at 70D axial distance from inlet. They observed that introducing finer bubbles near the wall produces wall peaking radial void fraction profiles and much smaller bubbles as far as 70D from the inlet. The introduction of smaller bubbles resulted in shifting bubbly-slug transition to a higher gas superficial velocity [71].

Prasser et al (2007) studied the two phase flow characteristics in a large diameter (0.195 m ID) vertical pipe while varying the distance between injection and measurement point using both water-air and water-steam in a pressurised rig. Axial distance was varied from 1.1D to 40.0D. A small decrease in bubble size was observed as the distance between the injection point and measurement station is increased. With increasing axial distance from the injection point, radial profile of void fraction exhibited lateral shifting from wall-peaking towards core peaking. Same applies to the radial velocity measured using two wire mesh sensors. They also found that small bubbles ($D_{Bub} < 5.8\,mm$) always rise near the wall regardless of the injection location. with increasing gas superficial velocity, flow was reported to develop faster, with slight growth of bubbles observed. Interestingly wall peaking of smaller bubbles was still observed under churn-froth flow conditions. Pressurised steam-water experiments were found to develop much faster, as close as 7D distance from the injection point in addition to having much smaller bubble sizes compared to the air-water system. That in addition to featuring a less significant wall peaking compared to the air-water system, which was attributed to the lower surface tension [145].

Omebere et al (2008) studied flow development in a 0.194 m large diameter pipe using steam-water at elevated pressure. Void fraction information was collected at several axial locations varying from 1.4D to 39.7D. Axial and radial void fraction in addition to bubble size distribution data established that flow develops fully above 7.7D axial distance [139]. However in their study on naphtha-Nitrogen system in a 0.189 m pipe, Omebere (2006) reported that flow needs as long as 157D axial distance to develop [138].

Ali (2009) investigated the effect of injector geometry in a 0.254 m vertical pipe using two different injection methods; horizontal flowline injector and near riser base tee injector. They varied gas and liquid superficial velocities in the range of 0.18-2.2 m/s and 0.25-0.55 m/s respectively. Experiments were conducted under gas-lift condition recording differential pressure measurements, similar flow characteristics were obtained when using both injectors, although the tee injector was recommended [12].

Kaji et al (2009) studied slug flow development in a 0.051 m vertical pipe obtaining measurements at several axial positions in the range of (0.59D and 151.2D) in two rigs of different heights. Their study revealed that void fraction and flow regime vary with axial location. Difference in void fraction between the Taylor bubble and the liquid slug was found to increase with increasing axial distance. Both Taylor bubble's and liquid slug's length was found to stabilise at about 100D axial distance. However, a slight decrease in the slug frequency was detected even past 151D axial distance [104].

Smith et al (2012) studied flow development in two large diameter pipes (0.102 and 0.152 m ID), observing radial void fraction profile at several axial stations. The study reported that flow converges above 4-5D axial distance, although a slight increase in void fraction was detected further downstream the test section [169].

Ibrahim et al (2016) studied the inlet effect in a 0.127 m vertical pipe using a 5 cP nominal viscosity silicone oil in an gas-lift pump using three different injectors. The study revealed that the flow almost converges around 63D downstream the pipe, yet a slight difference in two-phase characteristics was detected [92].

6.1.2 Objectives

As highlighted in the earlier sections, only a few reports are available on the effect of inlet geometry on the flow characteristics in large diameter pipes. All of the published studied were conducted in air-water or steam-water systems because of their relevance to boilers and heat transfer units in nuclear industry except the one by [138] who studied Nitrogen-Naphtha. It is evident that two-phase flow characteristics are dramatically distinct in oil based systems compared to water-based fluids due to the huge difference in surface tension. Although [138] studied Naphtha, the viscosity covered was very low ($\mu_l = 0.35cP$) compared to typical crude oil viscosities (1-100 cP). In addition,the recommended development length appear to vary significantly with the pipe diameter and the physical properties of the fluids employed. This is evidenced by the substantial difference in development lengths reportd by [138] and [139] where flow was reported to develop only after 7.7D axial distance for steam-water system whilst 157D axial distance was needed for the Naphtha-N_2 system. Chapter 4 revealed that the increase in liquid viscosity has a profound impact on two phase flow characteristics.

This chapter will present a novel work on the effect of injector geometry on two phase flow in a large diameter vertical pipe (0.127 m ID), while varying the liquid viscosity. The study will not only bridge the gap about two-phase flow development in large diameter pipes using fluids of low surface tension, but will also be the first of its kind to report how the entrance effect is influenced by the change of viscosity.

The inlet effect will be reported for four oils with different viscosities, namely (4.04, 25.35, 51.10, and 104.58 cP). The oils are all PDMS resin based silicone oils, with different viscosities but virtually identical density and surface tension. The full physical properties of the fluids can be found in Chapter 3. The entrance effect will be investigated by employing three different injector geometries, namely a perforated cylinder injector with 640 holes each is 1 mm in diameter. The other geometry is

an inverted cap nozzle designed to introduced the gas in an annulus closer to the wall. The third geometry is a concentric nozzle with with 25.4 mm in diameter. More details of the geometry of the nozzles can be found in Chapter 3 or [92]. Void fraction information will be collected at 5 axial stations.
The influence of injector geometry will be reported in terms of:

- Transient effect cross-sectionally averaged void fraction
- Time-averaged effect on radial and axial void fraction evolution
- Influence on pressure drop
- Effect on structures, their shapes,and incurring flow regimes
- Effect on velocity of structures
- Bubble size distribution

6.2 Results and discussion

6.2.1 Experimental matrix

180 runs were obtained for each viscosity in the range of gas superficial velocity (U_{gs}) of 0.01-5.40 m/s, and liquid superficial velocity (U_{ls}) in the range of 0.07-0.86 m/s. The experimental matrix is shown in Figure 6.1 plotted on the flow regime map of Taitel et al (1980) [173]. The same experimental matrix was generated for each injector geometry making the total number of runs reported in this chapter (180 x 3 (injectors) x 4 (viscosities)) equals 2160 runs.

6.2.2 Entrance effect on the dynamic behaviour of void fraction

cross-sectionally averaged time series of void fraction gives very clear indication of the incurring flow regime in the pipe. It also gives very insightful information about the dynamic behaviour of the structures and how they evolve with the change of the injector geometry, liquid viscosity, and gas and liquid turbulence levels.

It will also be used later in calculating the frequency and length of the flow structures. In this section the shape of time series upstream (15D) and downstream (62 and 63D)

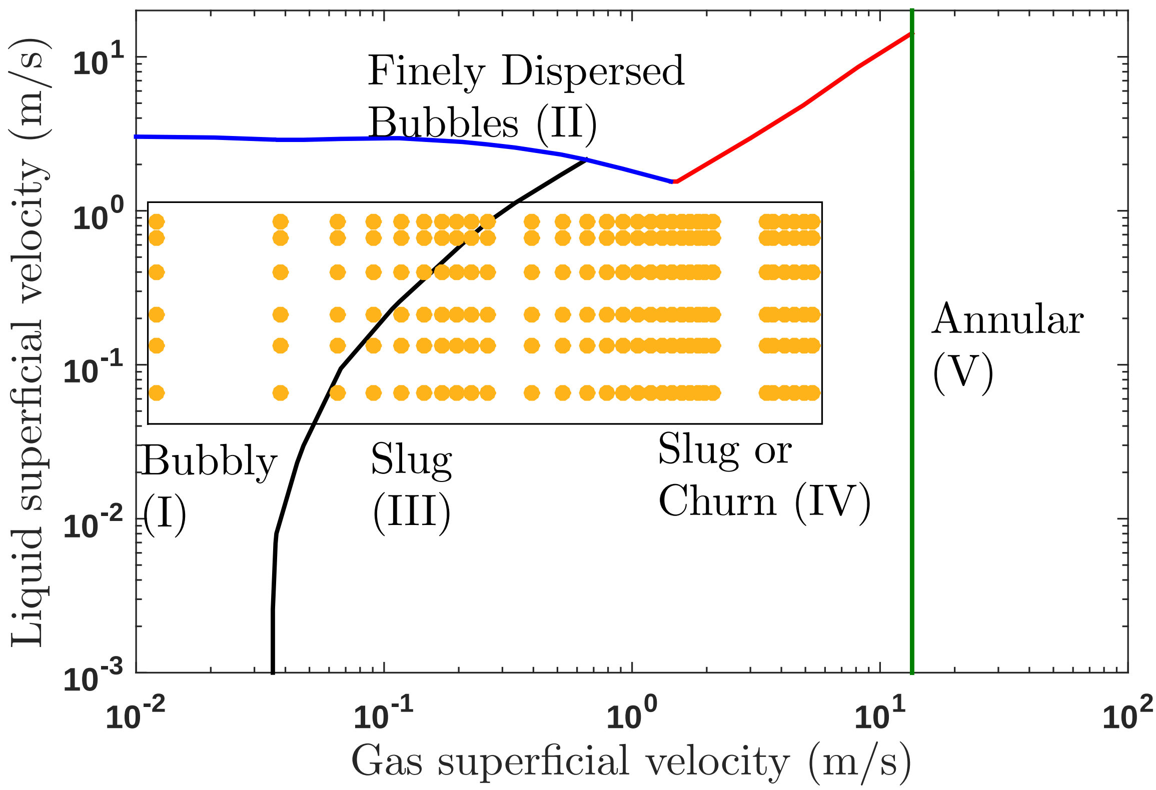

Fig. 6.1 Experimental matrix plotted in the flow regime map of Taitel et al. (1980) [173].

of the test section will be discussed comparing the profiles generated by the three injectors.

Figure 6.2 shows the cross-sectionally averaged void fraction time series produced by the different inlet geometries for the lowest liquid superficial velocity studied ($U_{ls} = 0.07\,m/s$) for the 4.0 cP viscosity oil. The Figure also shows the corresponding probability density function corresponding to the time series displayed on the left. First observation is that the general shape and the void fraction time series and the corresponding flow regime stemmed from the shape of the PDFs produced by the different injectors show great resemblance in agreement with [92]. Nevertheless, a small variation in the shape of the PDFs is observable, resulting in a slight shift in the peak of the PDF, especially in the bubbly flow region. These discrepancies seem to lessen with increasing gas superficial velocity. Suggesting that the flow develops faster with increasing gas input. It can also be observed that in the bubbly flow region the perforated injector (denoted as perf-inj in Figure 6.2) produces higher void fraction, indicating that introducing smaller bubbles to the test section produces smaller bubbles as far as 63D downstream the test section registering higher average void fraction. This observation comes in agreement with the works of [71] and [134]. The PDF of void fraction peak expectedly migrates towards higher void fraction with increasing gas superficial velocity as evidently exhibited by the three injector geometries in Figure 6.2.

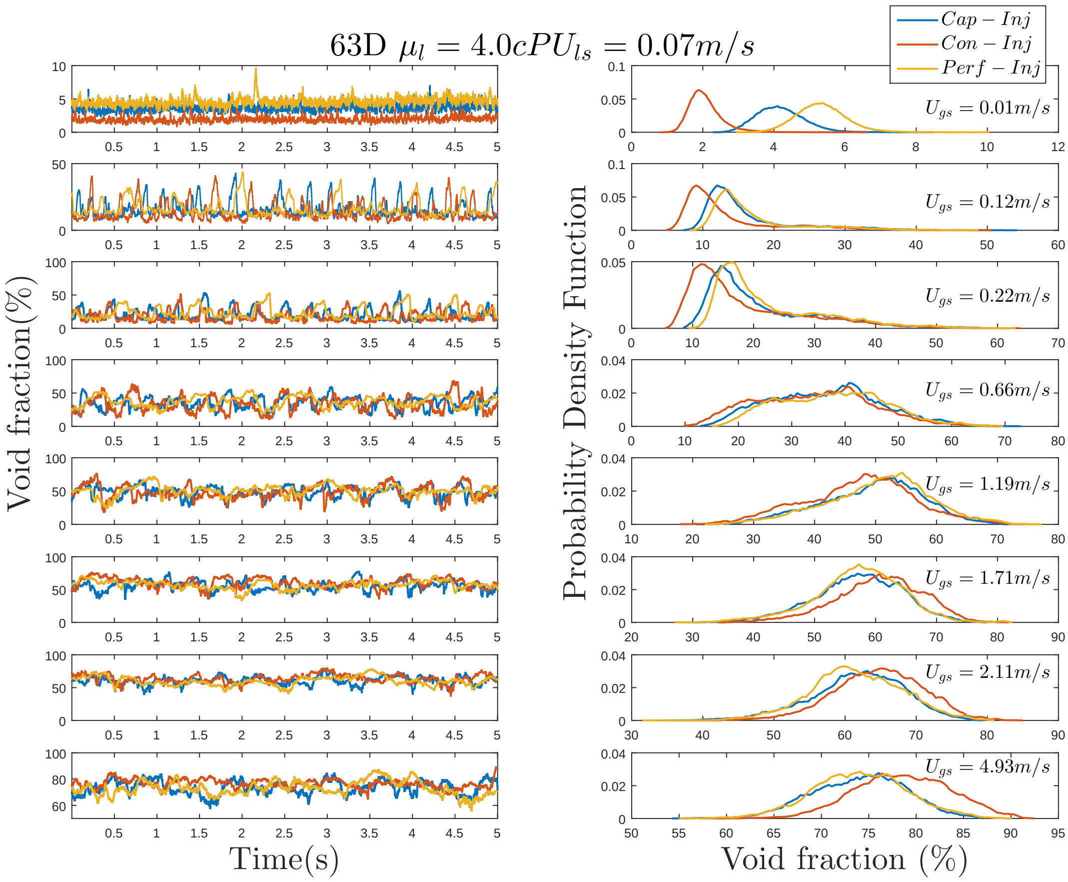

Fig. 6.2 On the left: Cross-sectionally averaged void fraction evolution with increasing gas superficial velocity at 4.0 cP viscosity produced by the different three inlet geometries at 63 D axial position. On the right: the corresponding probability density function of the void fraction time series for the three injectors displayed on the left.

Increasing the viscosity six folds to 25.4 cP at the same liquid and gas superficial velocities results in nearly identical profiles by the three injector geometries as can be noted from Figure 6.3. It is observable that both the shape of the cross-sectionally averaged void fraction time series and PDF show almost identical behaviour throughout the range of gas superficial velocities. This implies that the inlet effect becomes less significant with increasing viscosity, therefore the flow is expected to converge at a shorter axial distance. It is also notable the presence of slug flow regime with two peaks featured at $U_{gs} = 0.66\,m/s$ which was not observed at 4.0 cP viscosity.

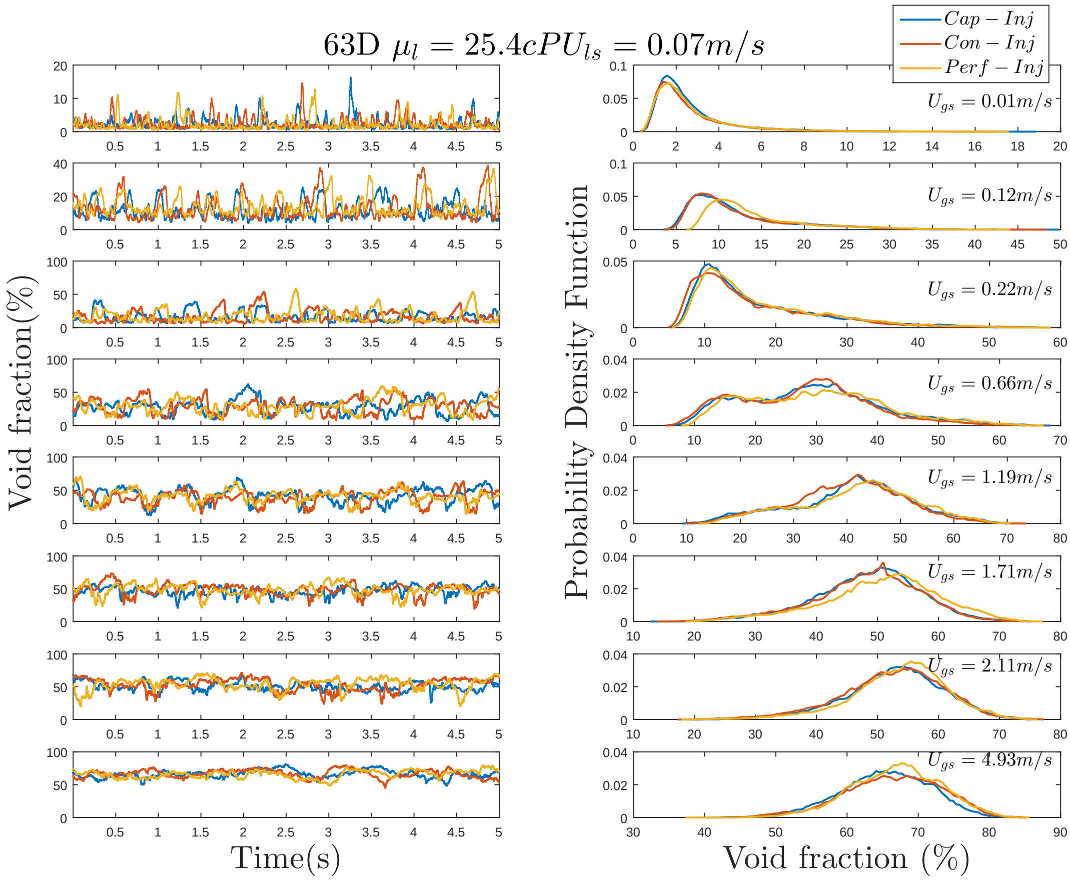

Fig. 6.3 On the left: Cross-sectionally averaged void fraction evolution with increasing gas superficial velocity at 25.4 cP viscosity produced by the different three inlet geometries at 63 D axial distance. On the right: the corresponding probability density function of the void fraction time series for the three injectors displayed on the left.

Doubling the viscosity to 51.1 cP at the same liquid superficial velocity ($U_{ls} = 0.07\,m/s$) effect can be viewed in Figure 6.4. Divergence in void fraction again appears, however still less significant than that observed at 4.0 cP. It can be noted that the capped injector (denoted cap-inj in Figure 6.4) consistently produces a slightly lower void fraction throughout, the discrepancy as observed at lower viscosities is more pronounced at lower gas superficial velocity. No clear explanation for this behaviour can be drawn from the shape of the void fraction time series. The ultimate effect of the injector is mostly on the bubble size and their coalescence-break-up equilibrium, a characteristic that is affected by the injector geometry and essentially the liquid viscosity. Further analysis on the bubble size distribution is needed to see how the bubble size varies by the inlet injector. The perforated injector continues to feature a slightly higher void fraction compared to the other two injectors in concordance with the observations at lower viscosities.

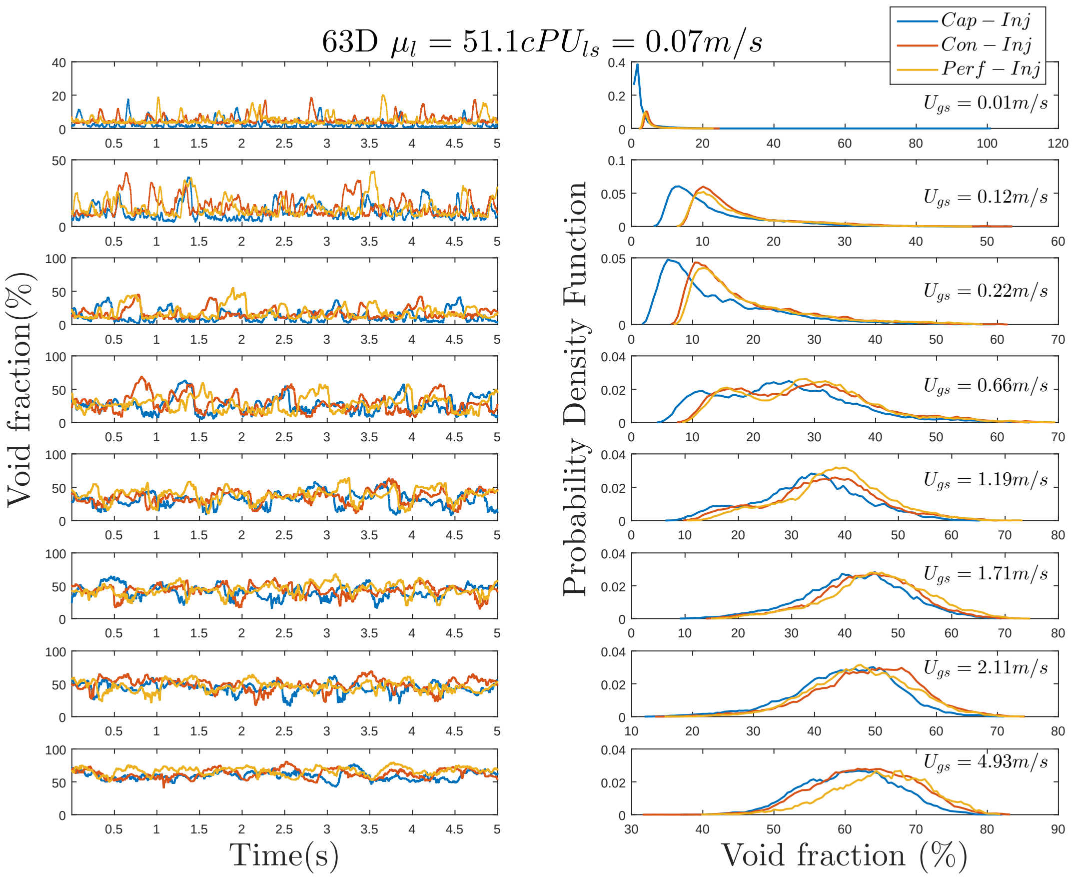

Fig. 6.4 On the left: Cross-sectionally averaged void fraction evolution with increasing gas superficial velocity at 51.1 cP viscosity produced by the different three inlet geometries at 63 D axial station. On the right: the corresponding probability density function of the void fraction time series for the three injectors displayed on the left.

Doubling the viscosity further to 104.6 cP while maintaining the same liquid superficial velocity effect can be observed in Figure 6.5. A small variation can be seen at lower gas superficial velocity, whereas at higher gas superficial velocities, almost identical profiles are produced. Contrary to what was observed at lower viscosities, the perforated injector seems to produce a smaller void fraction compared to the other two inlet geometries. This is evident by the smaller frequency/amplitude of bigger bubbles in the time series and the also the lower average void fraction in the liquid bulk as reflected by the bubbly flow time series. Seemingly introducing the gas near the pipe wall, as achieved by the cap-injector, appear to result in a slightly higher void fraction.

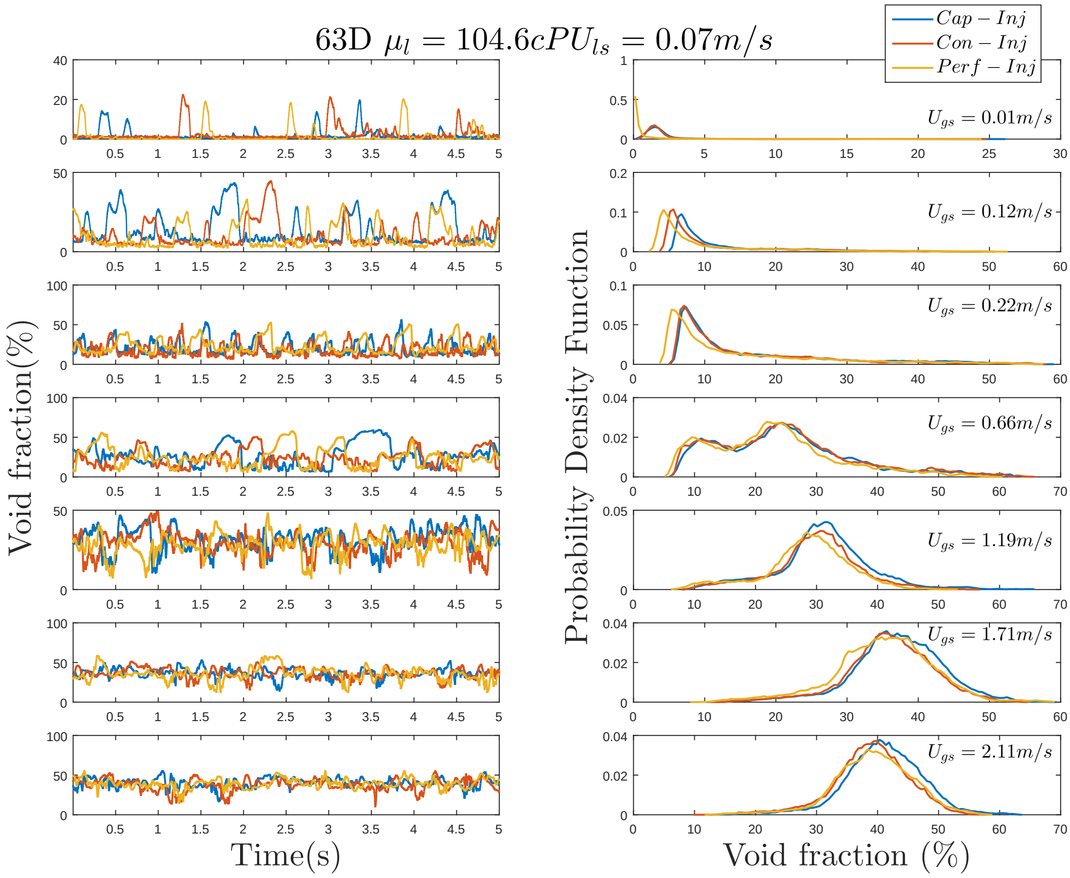

Fig. 6.5 On the left: Cross-sectionally averaged void fraction evolution with increasing gas superficial velocity at 104.6 cP viscosity produced by the different three inlet geometries at 63 D axial distance from injection. On the right: the corresponding probability density function of the void fraction time series for the three injectors displayed on the left.

To look at the influence of liquid superficial velocity on the effect of inlet geometry Figure 6.6 is produced. The Figure shows the profiles for the higher viscosity fluid at equal gas superficial velocities to the ones shown in Figure 6.5, but at the highest liquid superficial velocity studied ($U_{ls} = 0.86\,m/s$). It is observable that the variation in void fraction becomes more pronounced at higher liquid superficial velocity. As observed earlier the discrepancies lessen with increasing gas superficial velocity, whereas more notable effect is observed in the bubbly flow region. At higher gas superficial velocity, where the PDF features a slug flow shape (bimodal distribution), the inlet effect appears more pronounced in the slug peak. This suggests that at higher viscosity, the inlet geometry has more effect on the void fraction in the liquid slug compared to that of the Taylor bubble.

A similar effect of the liquid superficial velocity is observed for the other viscosities, where the effect was found to lessen with increasing liquid viscosity. The more pronounced effect on the liquid slug void fraction was also observed in other viscosities at elevated liquid superficial velocity where slug flow is detected. The figures are not included here for brevity.

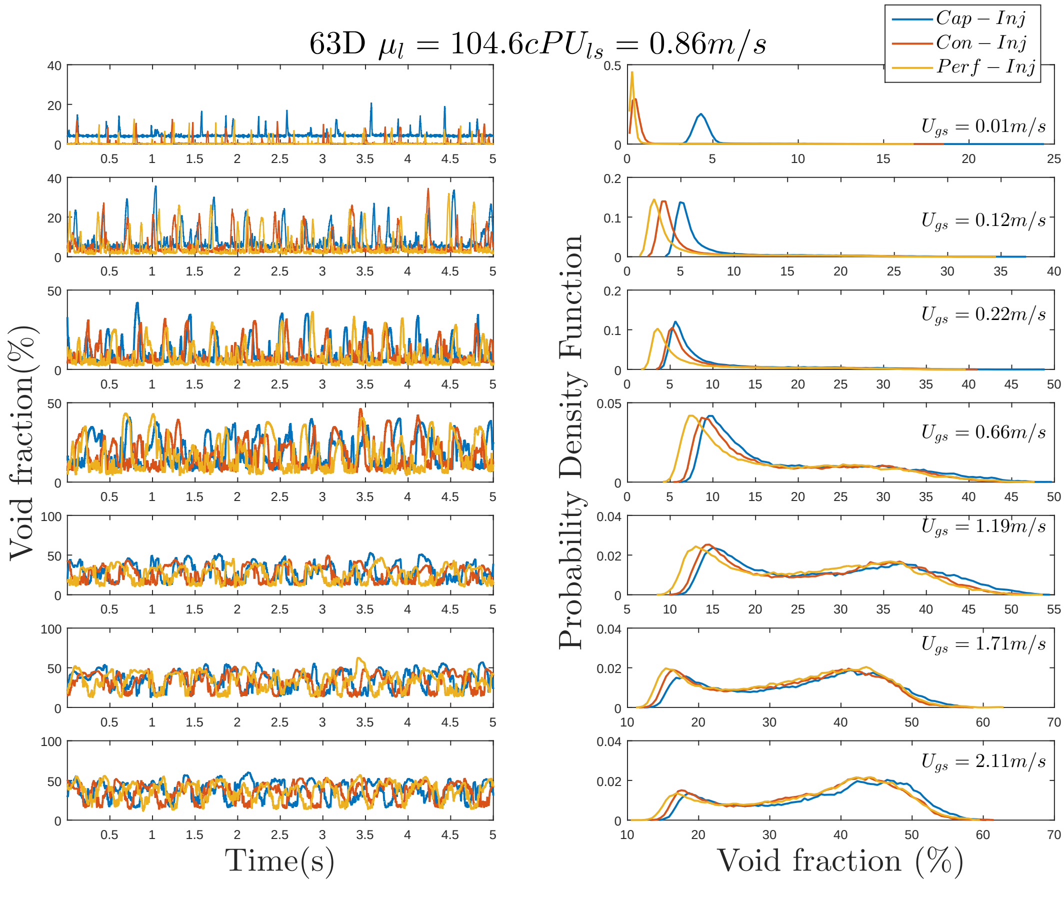

Fig. 6.6 On the left: Cross-sectionally averaged void fraction evolution with increasing gas superficial velocity at 104.6 cP viscosity produced by the different three inlet geometries at $U_{ls} = 0.86\,m/s$, measured at 63 D axial position. On the right: the corresponding probability density function of the void fraction time series for the three injectors displayed on the left. The figure shows the effect of increased liquid superficial velocity on flow development.

6.2.3 Entrance effect on averaged axial void fraction

The influence of injector geometry on axial void fraction downstream the test section at 63D axial distance can be seen in Figure 6.7. The figure shows averaged void fraction against gas superficial velocity for the three injector geometries with increasing viscosity as noted on each individual graph. The graphs are colour-coded to their corresponding liquid superficial velocity. It is notable that all the graphs follow the same trend regardless of the injector geometry. It is also observable that the disparity between different injector profiles decreases with increasing viscosity, affirming what has been indicated earlier by the void fraction time series and the probability density function. The Figure also shows how increasing viscosity systematically limits the effect of liquid superficial velocity on void fraction, making the curves produced at varying liquid superficial velocities nearly collapse onto one. The figure also shows the change in trend at lower liquid and gas superficial velocities that becomes more significant with increasing viscosity. As discussed in chapter 4 this corresponds to the effect of increased drag force on the bubbles, where initially drag effect is more significant on the bubbles due to the high ratio of surface area to volume, with increasing gas superficial velocity and accordingly increasing average bubble size, the drag effect on the bubbles lessens and void fraction eventually falls. The decrease on drag effect can be adhered to two different attributes; first is the decreased average bubble surface area ratio to volume and therefore more dominant buoyancy force. The second attribute is the decreased effective viscosity of the liquid bulk due to the entrapment of fine bubbles into it producing a cloudy milkish medium.

To better visualise the variability of average void fraction due to the change of injector geometry, Figure 6.8 is shown. The figure shows how the average void fraction measured by the various injectors converge with one another. The hologram shows the 5% deviation from the (x=y=z) line. Whilst it is clear that most of the data points fall within the 5% deviation area, yet limited scatter is observed. On the effect of viscosity on flow development Figure 6.8 shows that disparity becomes rather limited with increasing viscosity. While larger deviations are observed at lower viscosity, the dispersion is only limited to lower void fraction values at higher viscosity. Which suggests that the influence of injector geometry is more pronounced at lower gas superficial velocity, where bubbly flow is mostly expected. This might be referred to bubble dynamics in the bubbly flow, especially the homogeneous bubbly flow region. Whereas in the homogeneous bubbly flow, bubble size is mostly governed by the initial bubble size controlled by the injector geometry, while at higher gas superficial

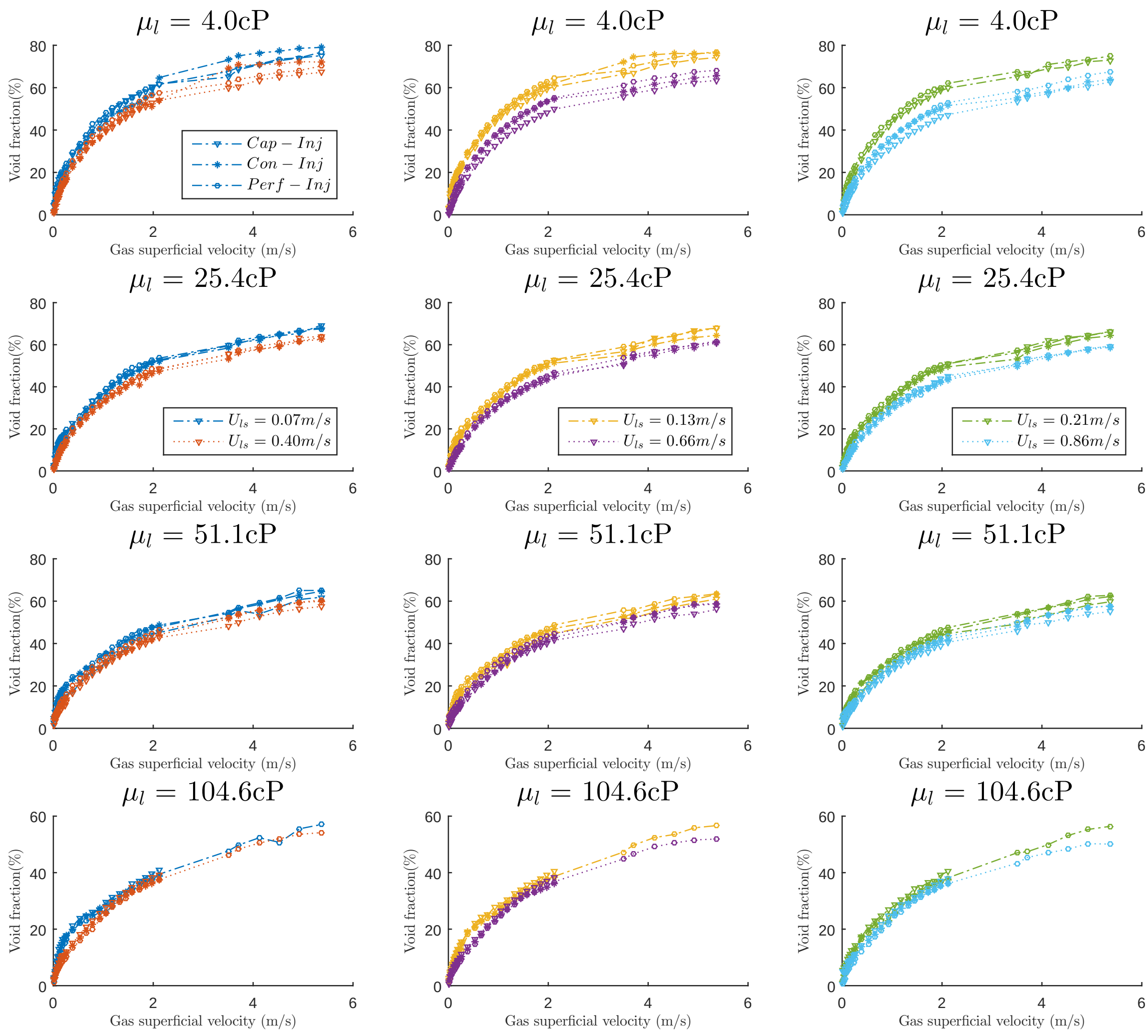

Fig. 6.7 Time averaged void fraction evolution with gas superficial velocity produced by three inlet different geometries for all the gas and liquid superficial velocities studied using four different viscosity fluids. The void fraction presented here is measured at 63 D axial position downstream the test section. The graphs are color-coded to the corresponding liquid superficial velocity denoted in the legends. The three different marker shapes correspond to the injector geometries employed.

velocities, bigger (hence faster) zigzag and swirling bubbles are formed that produce a lot of turbulence in their wakes, enhancing bubbles break-up. This effect is of more profound importance in large diameter pipes as reported by Ohnuki and Akimoto (2000) who suggested that the bubble size in large diameter pipes is greatly influenced by bubble-induced turbulence compared to its small diameter pipes counterpart [135].

It can be established now with greater confidence that the entrance effect becomes less pronounced with increasing viscosity, as suggested by the aforementioned results. This behaviour can be attributed to the enhancing effect of viscosity on bubbles coalescence. It has been argued that the entrance effect is all about the axial distance needed to reach the equilibrium bubble size. As it was evident from the information presented in Chapter 4 that viscosity shifts the break-up/coalescence equilibrium more towards the coalescence side, it is expected that the equilibrium is reached sooner (either in distance or time terms) at a higher viscosity.

To summarise, the decrement of injector effect with increasing viscosity can be referred to two synergetic attributes of viscosity. Firstly, viscosity dramatically increases bubble coalescence as observed by many works in the literature on bubble dynamics in viscous continuum [49, 141, 188]. Secondly, due to enhancing coalescence caused by viscosity, larger bubbles are formed, these bubbles are faster and rise in zig-zag or swirling trajectories creating more turbulence in their wakes allowing for reaching bubble size equilibrium much quicker. Bigger bubble size increase with viscosity is reviewed in [112].

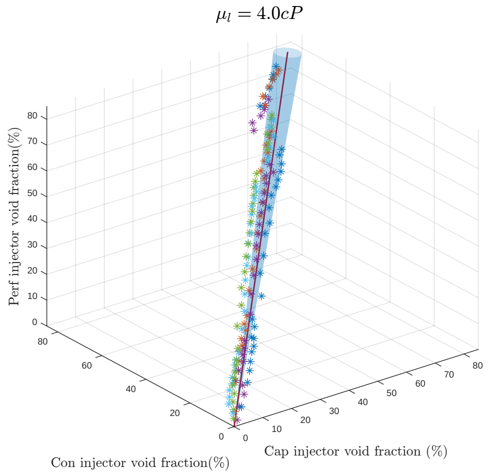

(a) Dispersion of void fraction by injector geometry at 4.0cP viscosity.

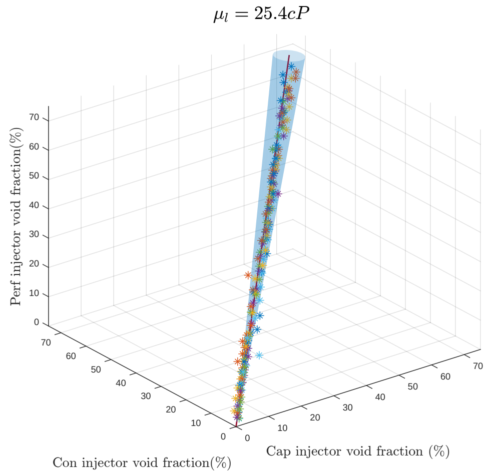

(b) Dispersion of void fraction by injector geometry at 25.4cP viscosity.

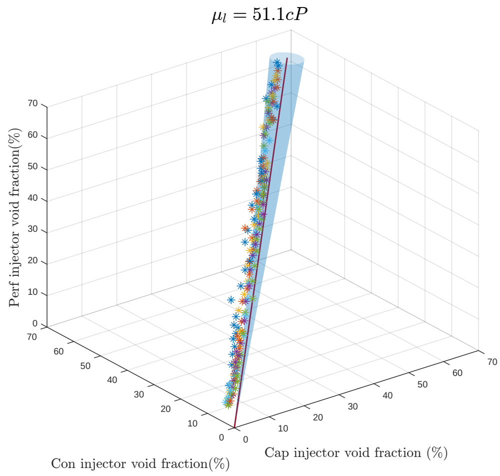

(c) Dispersion of void fraction by injector geometry at 51.1cP viscosity.

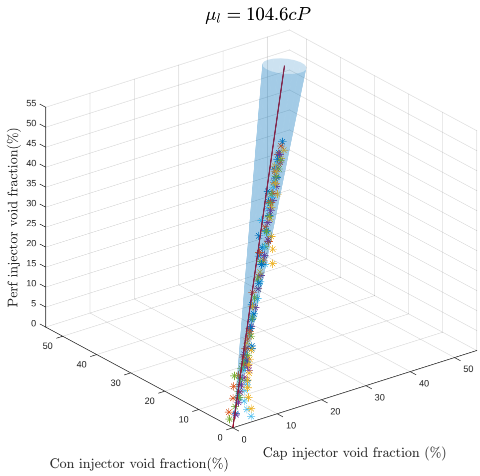

(d) Dispersion of void fraction by injector geometry at 104.6cP viscosity.

Fig. 6.8 Dispersion of time averaged void fraction at various viscosities produced by the three injector geometries employed at 63 D axial distance. The blue hologram represents the 5% deviation cone revolved around the (x=y=z) line where the three injectors produce identical values.

6.2.4 Entrance effect on axial void fraction development

To investigate how the void fraction varies along the axial distance of the test section with the change of injector geometry at different viscosities, void fraction measurements were obtained downstream the test section at 15D and 62D axial distance downstream. The evolution of the shape of the PDF with the change of viscosity and the injector geometry will be discussed in this section together with the average axial void fraction.

Figure 6.9 shows the PDF of void fraction time series produced by the three different injectors for the four viscosities studied obtained at the lowest gas and liquid superficial velocities investigated. As revealed in the earlier section, the figure features a great resemblance in the shape of the PDFs of the same viscosity. In agreement with what was explained earlier the discrepancies between profiles produced by different injectors appears to be more profound at lower viscosities as evident by the 4.0 cP sub-Figure. The discrepancies seem smaller near the injection (15 D), and appear to increase with increasing axial distance. However, the increment might still be proportional to the overall increase in void fraction with increasing axial distance due to gas expansion induced by the decreased static head with axial distance.

With increasing viscosity, Figure 6.9 shows that the PDFs peaks expectedly move towards lower void fraction but featuring a tail extending to higher void fraction due to increased divergence in the size of the produced bubbles. It is interesting to see for the 104.6 cP that the peak shifts towards even lower void fraction with increasing axial distance while the tail extends registering instances of much higher void fraction. This suggests that bigger bubbles can potentially grow to much bigger sizes as they rise in the test section registering values of void fraction as high as 40% in the bubbly flow regime. It can also be noted that the PDF shapes become more comparable between profiles produced by different injectors with increasing viscosity. It can also be drawn that the PDF shapes do not indicate a change in the flow regime with axial distance whereby bubbly flow regime is maintained throughout, yet the long tail is observed downstream marking the appearance of cap-bubbles in the high viscosity fluids.

Figure 6.10 shows void fraction PDFs at a higher gas superficial velocity ($U_{gs} = 0.09\, m/s$)and equal liquid superficial velocity ($U_{ls} = 0.07\, m/s$) to that in Figure 6.9. Again the PDFs produced by different injectors seem almost identical, however some dissimilarities can be spotted for the lower viscosity fluids. Unlike what was observed in Figure 6.9 the flow regime indicated upstream appears to be different than that registered downstream in all the viscosities. While the upstream PDF features a single peak indicating bubbly flow, the downstream produces a prominent tail or even a

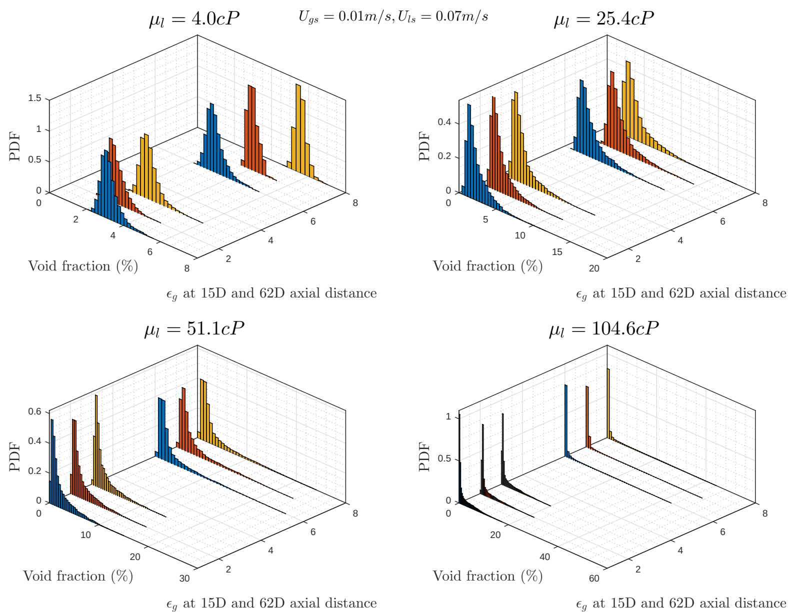

Fig. 6.9 PDF of void fraction time series upstream and downstream the test section. Colour represents the corresponding injector geometry, blue for capped injector, red for concentric injector and the yellow for perforated injector. $U_{ls} = 0.07\,m/s, U_{gs} = 0.01\,m/s$.

second peak in the case of higher viscosities, indicating bubbly flow for the former or slug flow for the latter.

Figure 6.11 shows void fraction PDF at an even higher gas superficial velocity ($U_{gs} = 0.93\,m/s$) while maintaining the liquid superficial velocity ($U_{ls} = 0.07\,m/s$). In concordance with what observed earlier some differences can still be spotted between different injector PDFs at 4.0 cP viscosity. Otherwise the PDFs appear almost identical. At lower viscosity, a single peak near 50% void fraction denoting churn flow both upstream and downstream the test rig is observed. Whereas, at higher viscosity single peak is registered upstream indicating churn-turbulent flow regime whilst two distinct peaks are formed downstream the pipe revealing the formation of slug flow regime. It is notable that the peaks become more sharp with increasing viscosity. Figure 6.12 shows the PDFs for a much higher gas superficial velocity ($U_{gs} = 2.10\,m/s$) at the same liquid superficial velocity where the flow regime appears to be approaching annular flow. A much greater resemblance can be observed between the shape of the PDFs upstream and downstream the pipe regardless of viscosity. This comes in agreement with what has been observed in the earlier section that flow develops faster at higher

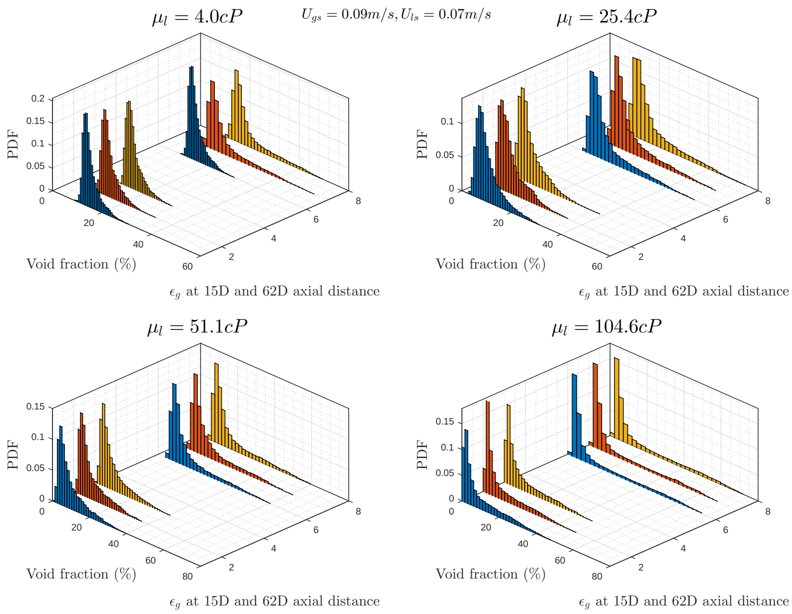

Fig. 6.10 PDF of void fraction time series upstream and downstream the test section. Colour represents the corresponding injector geometry, blue for capped injector, red for concentric injector and the yellow for perforated injector. $U_{ls} = 0.07\,m/s, U_{gs} = 0.09\,m/s$.

gas superficial velocity, owing to the increased gas-induced turbulence. The sameness of PDF shapes upstream and downstream the pipe can also be owed to the decreasing difference in static pressure and therefore gas density upstream and downstream the test section.

To get a hint of the effect of liquid superficial velocity on entrance effect, Figure 6.13 is shown. The figure illustrates PDFs at equal gas superficial velocity to that of Figure 6.12 ($U_{gs} = 2.10\,m/s$) but at a much higher liquid superficial velocity ($U_{ls} = 0.86\,m/s$). No appreciable difference can be spotted on the effect of increased liquid superficial velocity on the injector effect regardless of viscosity. Nevertheless, it worth noting the appearance of slug flow shape at higher viscosity downstream the test section.

Figure 6.14 shows the average axial void fraction upstream plotted against that downstream the test section. It features a similar behaviour across the different viscosities studied, where void fraction initially shows no much discrepancy between upstream and downstream of the test section despite the larger difference in gas density. Unexpectedly, the difference incrementally grows with increasing void fraction until

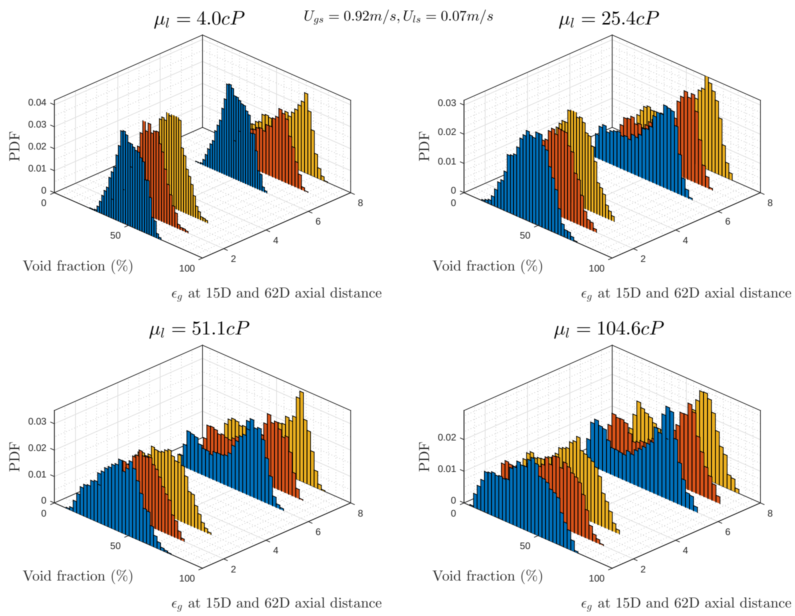

Fig. 6.11 PDF of void fraction time series upstream and downstream the test section. Colour represents the corresponding injector geometry, blue for capped injector, red for concentric injector and the yellow for perforated injector. $U_{ls} = 0.07\,m/s, U_{gs} = 0.93\,m/s$.

it eventually falls again at much higher void fractions above 50%. The increasing difference in average void fraction is undoubtedly a flow development attribute as it counteracts the natural decrease in gas density difference with increasing void fraction as illustrated in Figure 6.15. Only above about 50% void fraction values the axial development difference starts to decrease with increasing void fraction in concordance with the gas expansion relationship. This behaviour can only happen if most of the population of bubbles experience a decrease in size with increasing axial distance from the injection point.

The decrement in bubble size may be partly referred to the bubble-induced turbulence that is very dominant in large diameter pipes as confirmed by Ohnuki and Akimoto (2000) [135]. The decrease of bubble size was reported before by Prasser et al (2007) where they observed that in bubbly flow regime, bubbles mostly exhibit a decrease in size, whilst in slug flow the behaviour reverses for the Taylor bubbles where they grow with axial distance whilst entrained bubbles in the liquid slugs exhibit a slight decrease in size [145]. No appreciable difference in the average values produced by different injectors can be seen in Figure 6.15, most runs collapse into one line

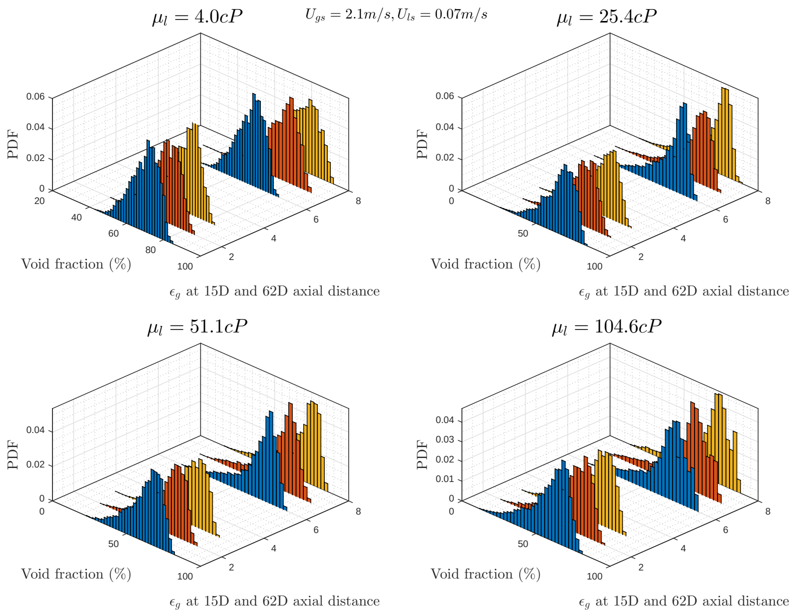

Fig. 6.12 PDF of void fraction time series upstream and downstream the test section. Colour represents the corresponding injector geometry, blue for capped injector, red for concentric injector and the yellow for perforated injector. $U_{ls} = 0.07\,m/s, U_{gs} = 2.1\,m/s$.

despite the limited disparity observed at 4.0 cP viscosity. Looking at the effect of viscosity on axial development of flows, it can be seen that the deviation maxima between the upstream and downstream void fraction increases slightly with increasing viscosity. This might be attributed to the increased drag force with increasing viscosity resulting in an improved break-up of smaller bubbles or a reduced coalescence rate as evident by the work of Orvalho et al (2015). Who found that increasing viscosity in pairwise-interaction of bubbles dramatically reduces coalescence rate and increases the contact time of bubbles needed for coalescence [140].

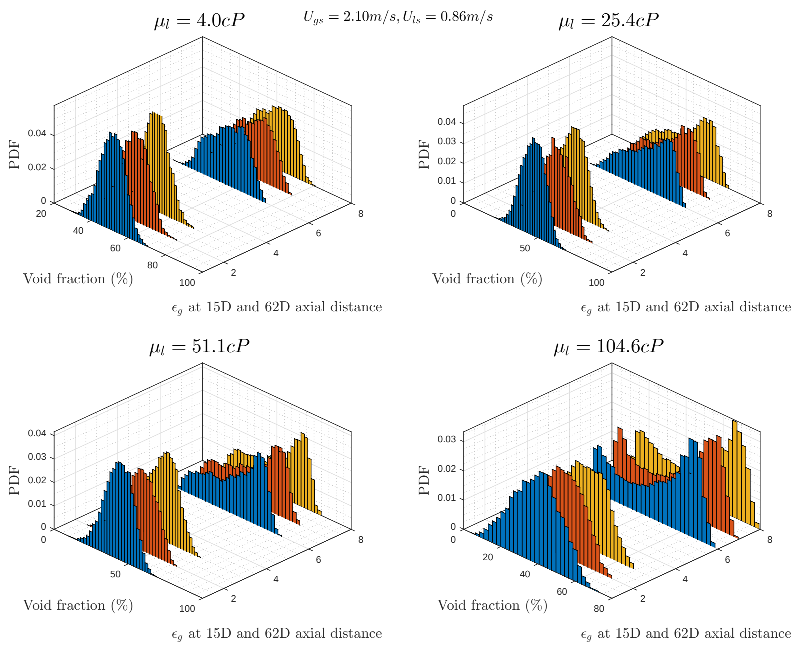

Fig. 6.13 PDF of void fraction time series upstream and downstream the test section. Colour represents the corresponding injector geometry, blue for capped injector, red for concentric injector and the yellow for perforated injector. $U_{ls} = 0.86\,m/s, U_{gs} = 2.1\,m/s$.

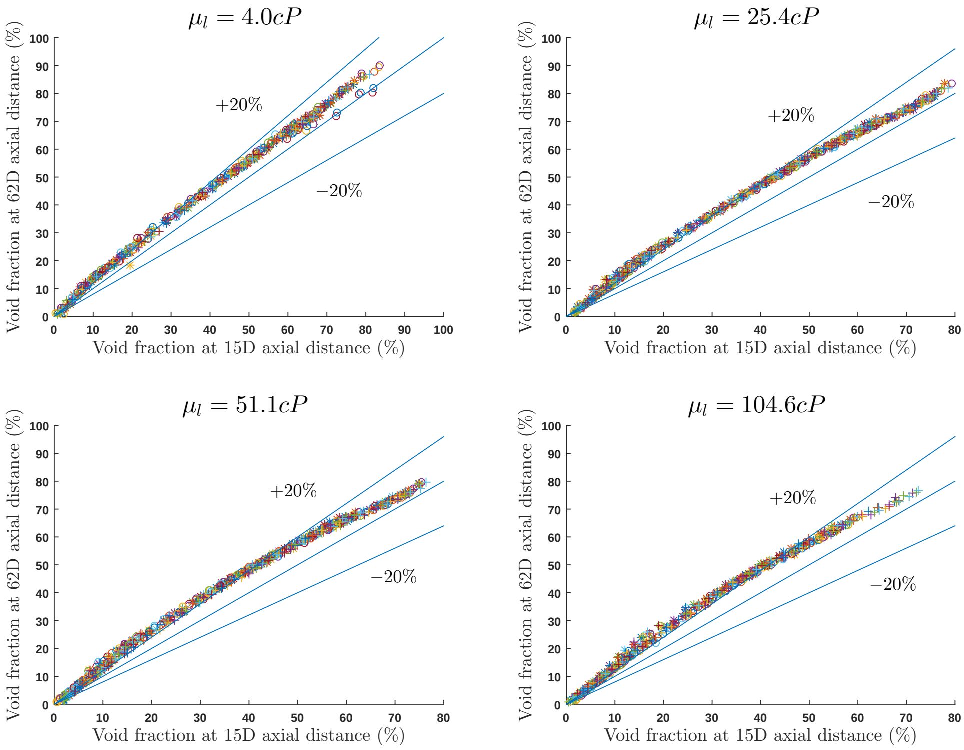

Fig. 6.14 Average axial void fraction upstream the test section (15D) plotted against the average void fraction downstream (62D). The figure illustrates how at higher gas superficial velocity causing essentially resulting in a very low two-phase density, average void fraction upstream becomes almost equal to that downstream.

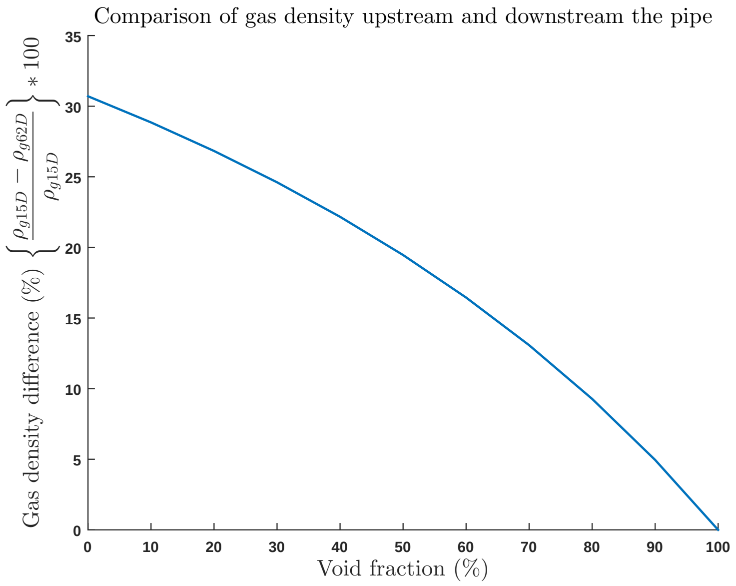

Fig. 6.15 Difference in gas density upstream and downstream the test section with void fraction relationship.

6.2.5 Entrance effect on radial distribution of void fraction

The effect of injector geometry on radial distribution of void fraction has not been studied extensively in the literature. Some researchers studied evolution of radial void fraction with axial distance and injector geometry. Most of them observed transition from wall-peaking to core peaking with increasing axial distance [145, 139, 160]. Qi et al (2012) reported core peaking downstream the pipe in most of the cases except at low gas and liquid superficial velocity where persistent wall peaking was detected as far as 39.9D axial distance from injection [150]. Harringe and Davis (1976) observed significant wall peaking in a 50.6 mm ID pipe as far as 108D axial distance from the injection point with detectable difference in profiles produced by different injectors [78]. In a 70 mm ID rig Guet et al (2003) reported that introducing smaller bubbles from porous injectors produces wall-peaking void fraction profiles whilst large nozzle injector generates a core-peaking profile at 110D axial distance from injection [71]. As mentioned earlier most of these observations are made in air-water or steam-water systems where surface tension is significantly higher than the oil discussed in this study in addition to the significant difference in viscosity.

Figure 6.16 shows the radial void fraction profiles measured at the lowest liquid superficial velocity ($U_{ls} = 0.07\,m/s$) featuring the profiles generated by the different injector geometries for the 4.0 cP and the 25.4 cP viscosity oils. The figure shows appreciable difference in the shape of profiles generated by different injectors at the lower viscosity. This difference seems to diminish with increasing both viscosity and gas superficial velocity. At the lowest gas superficial velocity and lowest viscosity, the radial profile produced by the perforated cylinder injector (nozzles of 1 mm ID) seems to generate a higher void fraction on average and peaks at the wall. However, the profiles generated by the other two injectors are concave in shape and core-peaking. On the other hand, at the higher viscosity, the profiles are almost identical. This behaviour comes in agreement with the observation of Guet et al (2003), however the wall peaking is less pronounced in the current instant [71]. To investigate whether the wall peaking observed in this instant is a singled occurrence amongst the runs, Figure 6.17 is added. The figure shows the radial distribution profiles for the 4.0 cP using the three injectors at the lowest bound of gas superficial velocities, where wall-peaking is more-likely to be observed. It can be seen that while wall peaking is not observed at higher gas velocities yet a slight increase in radial void fraction can be observed near the wall. The void fraction at the wall decreases gradually with increasing gas superficial velocity whilst other injectors profiles remain core-peaking throughout.

The results from Figures 6.16 and 6.17 ratify what has been deduced in earlier sections of this chapter that flow develops faster with increasing viscosity. It can be noted that even when gas velocity is increased further the different injector profiles show more resemblance, yet the resemblance reflected by the higher viscosity fluid is much greater. It should be also noted that profiles of the two higher viscosities (51.1 cP and 104.6 cP) follow a similar trend, for brevity they are not included here.

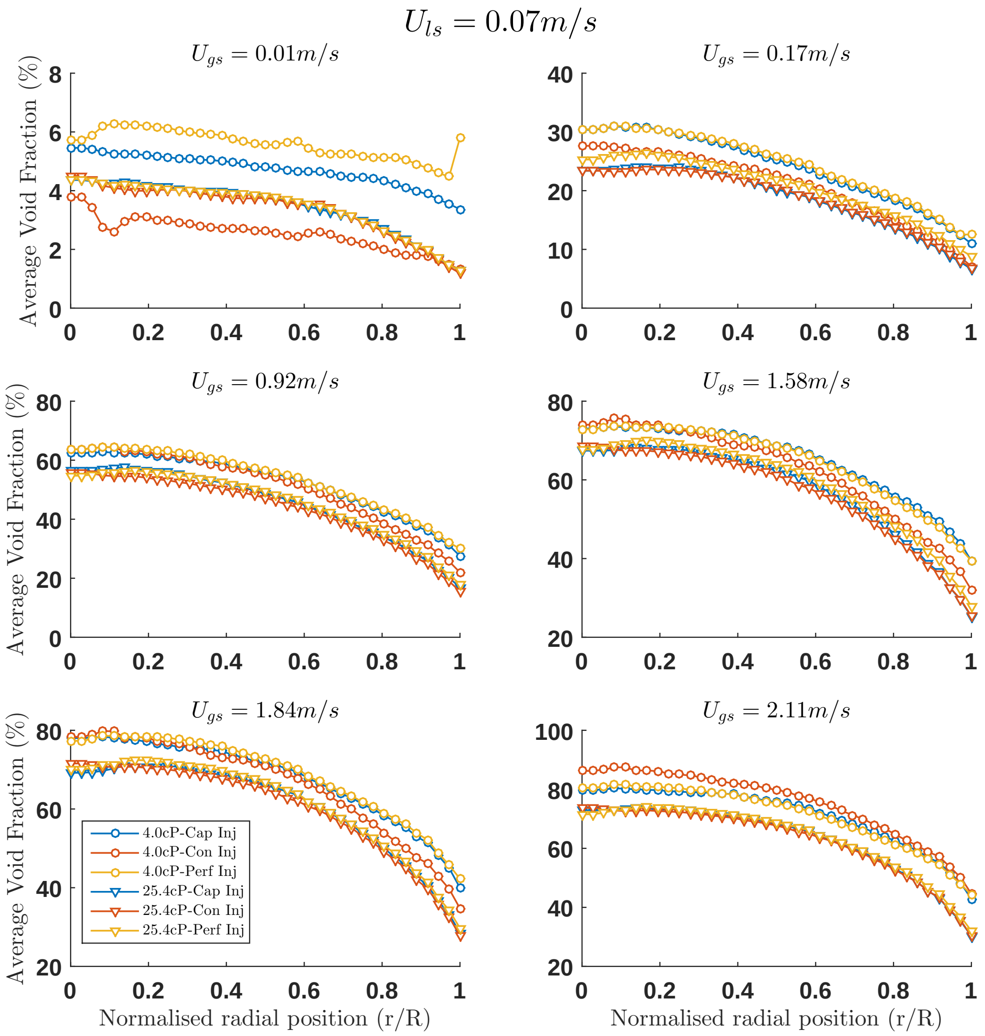

Fig. 6.16 Radial void fraction comparing the 4.0 cP and 25.4 cP viscosity oils using three different inlet injectors. Void fraction measured at 63 D axial distance from the injection.

To investigate the effect of increasing liquid superficial velocity on entrance effect Figure 6.18 is shown. The figure illustrates the radial profiles at constant gas superficial

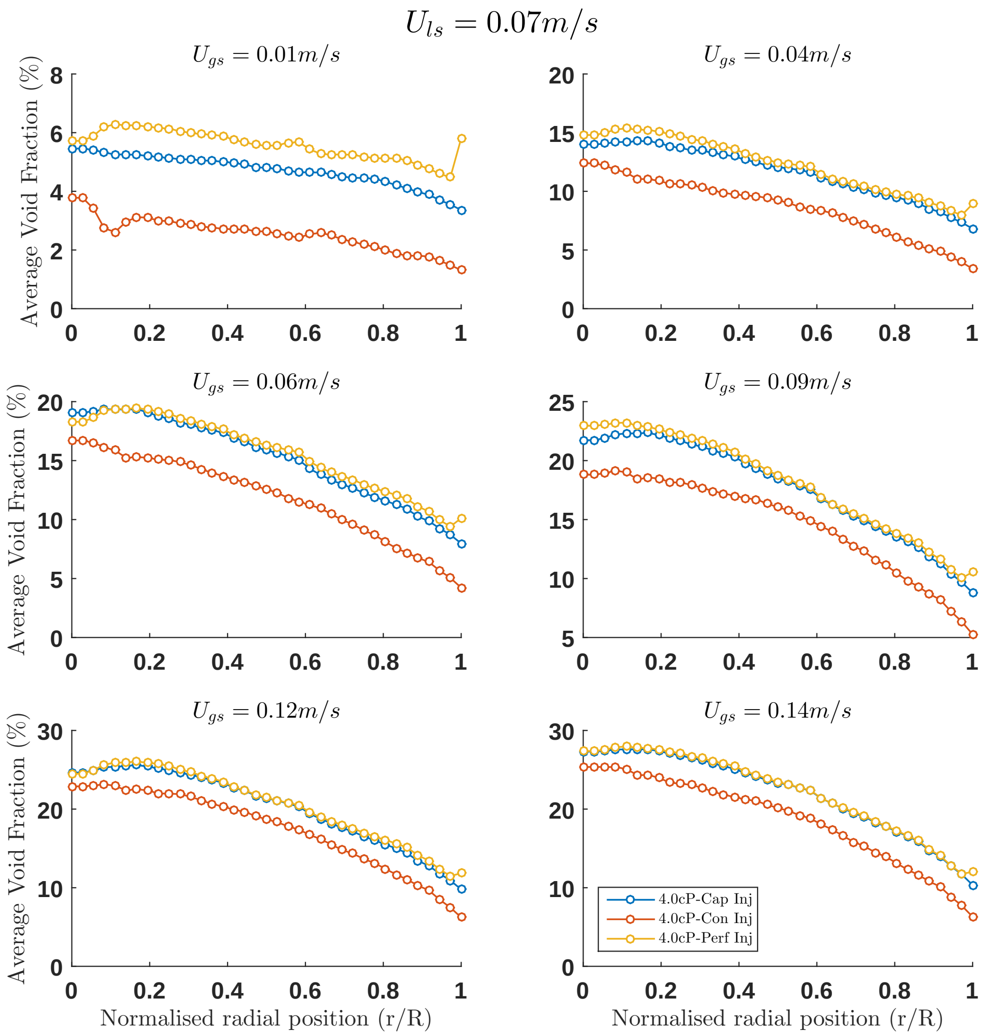

Fig. 6.17 Radial void fraction comparing the 4.0 cP depicting the diminishing wall peaking with increasing gas superficial velocity. Measurements are obtained at 63 D axial position.

velocity ($U_{gs} = 0.92\,m/s$) and three different liquid superficial velocities for 4.0 cP and 25.4c P viscosities. It shows that with increasing liquid superficial velocity the gap between profiles of different viscosities becomes smaller. Concurrently, the disparity between profiles produced by different injectors becomes more pronounced especially for the lower viscosity fluid. A similar trend is also observed when comparing the other viscosities as well. This behaviour suggests that the flow develops slower at higher liquid superficial velocity. This might be attributed to the limiting effect increasing liquid flow has on gas-induced turbulence and therefore impacting bubbles coalescence-breakup equilibrium.

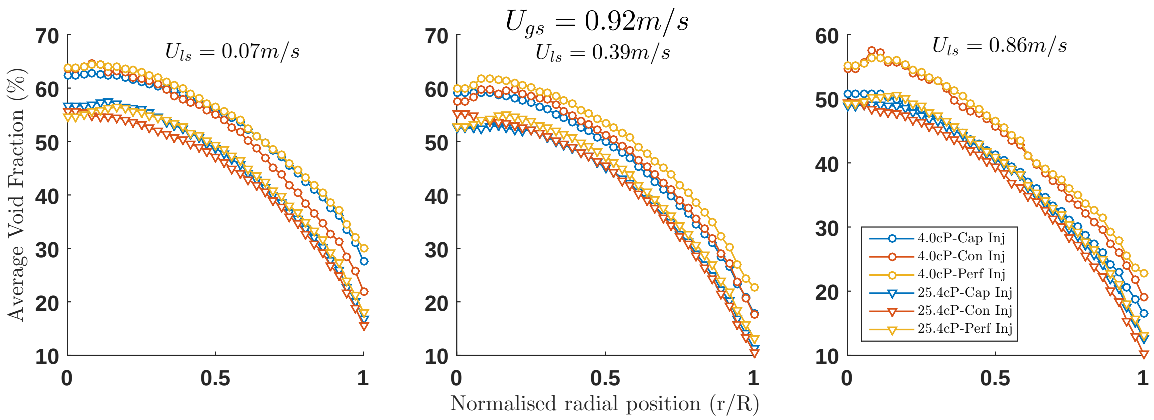

Fig. 6.18 Inlet effect investigated at different liquid superficial velocities at constant gas flow ($U_{gs} = 0.92\,m/s$). The figure features profiles for 4.0 cP and the 25.4 cP oil obtained at 63 D axial position.

6.2.6 Effect of viscosity on the velocity of structures

Structure velocity provides a clear indication of the bubble distribution which is the main attribute the injection method impacts in two phase flows. Indeed smaller bubbles have lower terminal velocity and therefore any difference in bubble population distribution generated by the injector is expected to reflect on the measured structure velocity. Figure 6.19 shows the evolution of structure velocity with gas superficial velocity plotted for the four viscosities studied. Each sub-figure correspond to a constant viscosity, depicting profiles generated by three different injectors at the minimum and maximum liquid superficial velocity studied as denoted in the legend. In agreement with the observations drawn in earlier sections Figure 6.19 shows that variation in the resultant structure velocity generated by different injectors diminishes with increasing viscosity of the liquid. It can be noted that profiles generated by different injectors at equal gas and liquid superficial velocity follow a similar trend. At the lowest viscosity the profiles show the greatest disparity amongst the studied range. It is notable that the profiles generated at $U_{ls} = 0.07\,m/s$ show a different trend compared to the rest of the data, where structure velocity gradually increases with increasing gas superficial velocity, then the profile exhibits a sharp increase. The same trend is followed by the three different injectors around the transition boundary to churn-annular flow regime. This, as explained in Chapter 4 might be a reflection of the velocity on the huge waves travelling on the liquid film that are much faster that the liquid slugs that preceded them at lower gas superficial velocities. This might explain why the same trend was not detected neither at higher liquid superficial velocity at the same viscosity nor at higher viscosities. Unlike other attributes of two phase flow discussed here, structure velocity shows no appreciable sensitivity to liquid superficial velocity in relation to the entrance effect. It has been noted before that flow develops slower with increasing liquid superficial velocity. However, no such evidence can be drawn from the structure velocity data.

To better visualise the disparity of structure velocity with changing the injector method for all the experimental data Figure 6.20 is presented. It shows the structure velocity generated by each injector plotted against the other two. The hologram in blue shows the 5% deviation from the equality line. As can be clearly seen very large disparity can be observed at the lower viscosity. The difference becomes greater with increasing structure velocity. With increasing viscosity the resemblance between different injector values grows with limited divergence at higher structure velocity. At the highest viscosity the profiles almost collapse into a single line within the 5% deviation area.

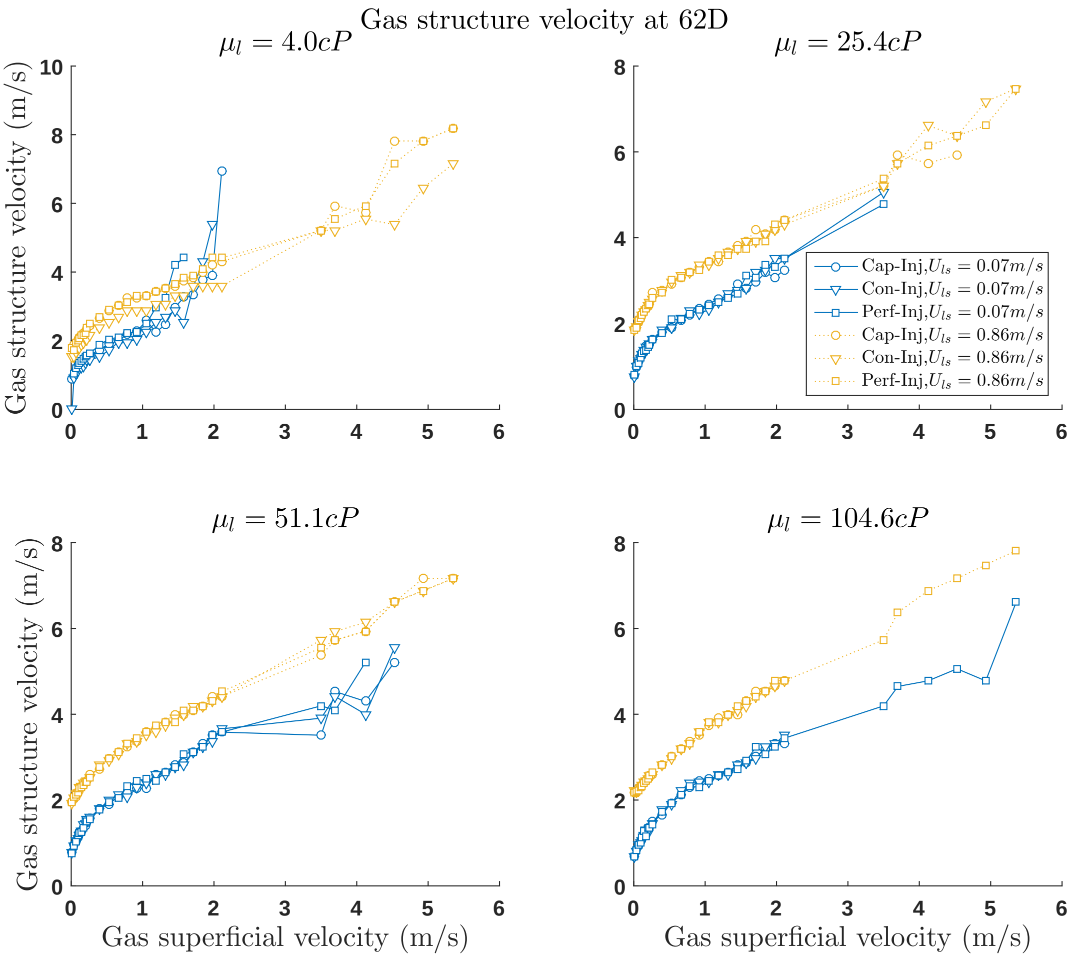

Fig. 6.19 Illustration of gas structure velocity calculated at 62D axial distance variation with the injection method. The graphs are plotted at equal liquid superficial velocities ($U_{ls} = 0.07\,m/s$ and $U_{ls} = 0.86\,m/s$).

This provides further consolidation from one more independent measurement that the flow develops faster at higher viscosity.

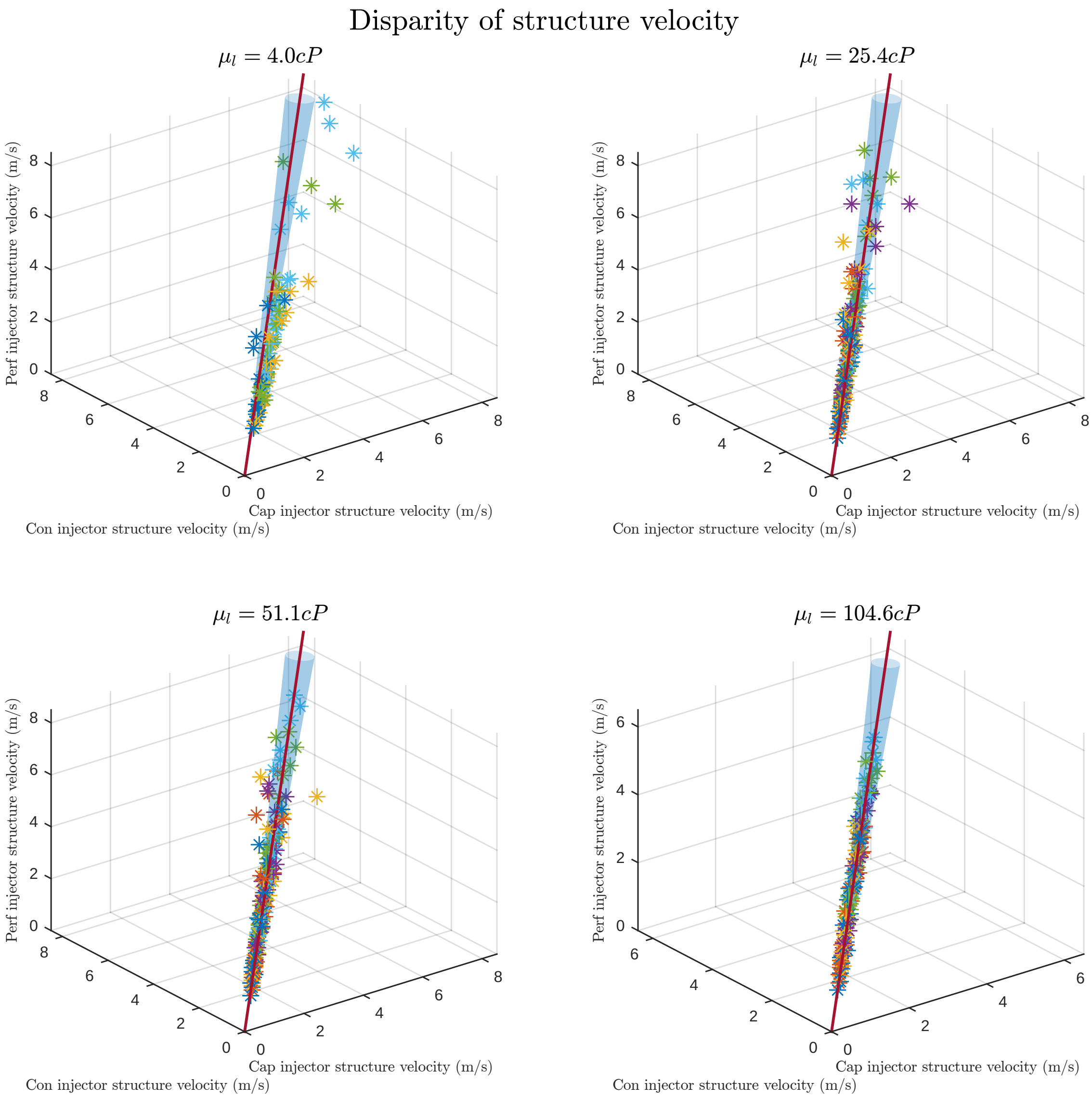

Fig. 6.20 Disparity of structure velocity with injection method for the four viscosities studied at 62 D axial distance. The hologram represents the 5% deviation surface revolved around (x=y=z) line.

Figure 6.21 shows the structure velocities calculated upstream the test section at 15D axial distance from the injection point for the same runs presented in Figure 6.20. It is expected to observe a larger divergence in the structure velocity due to the closeness from the injection point where a larger deviation in bubble size is anticipated.

However, Figure 6.20 shows no appreciable increase in the discrepancy between the profiles generated by different injectors, although the decrement in disparity with increasing viscosity can be clearly seen at this axial distance. This might be attributed to the increased gas density upstream and therefore limiting the variation in bubble sizes. Comparing the profiles upstream and downstream the test section, it can be noted that the slope becomes steeper as gas structures rise in the test section. It is also observable that the increase in structure velocity becomes remarkably larger at high gas superficial velocities. This might be an effect of bubbles coalescence where if two larger bubbles coalesce, the resultant bubble size will have a much greater terminal velocity.

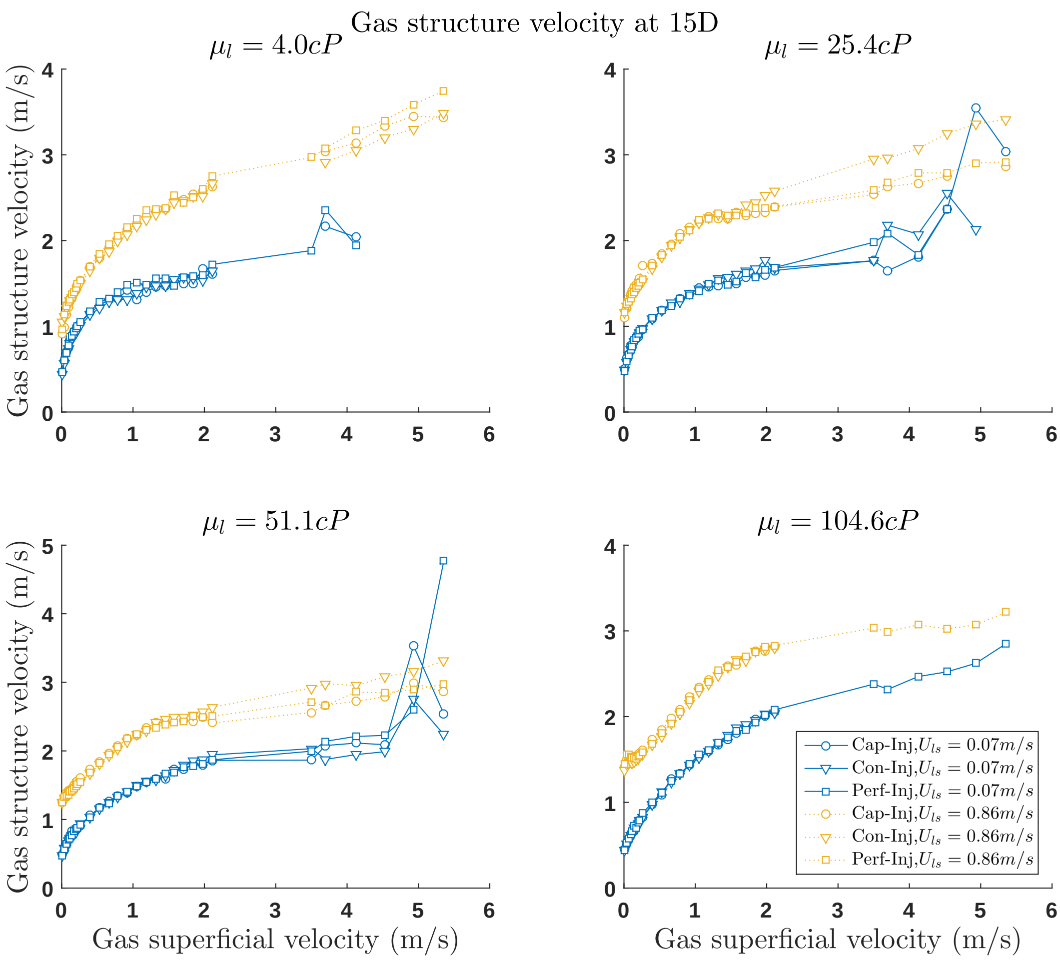

Fig. 6.21 Illustration of gas structure velocity calculated at 15 D axial distance variation with the injection method. The graphs are plotted at equal liquid superficial velocities ($U_{ls} = 0.07\,m/s$ and $U_{ls} = 0.86\,m/s$).

As discussed in Chapter 4, it was found that structures velocity behaves in two distinct regimes when they rise in the test section from 15D to 62D; at lower gas superficial velocity it it was observed that the velocity increases by about 60% regardless of the liquid viscosity or the superficial velocities of the gas and the liquid. At higher gas superficial velocities, it was observed that the structures become much faster where the velocity increases dramatically downstream. Figure 6.22 is presented here showing the structure velocities calculated upstream at 15 D plotted against that measured at 62 D downstream the test section for all the viscosities featuring all the injectors employed. It can be seen that the structure velocity fits nicely to the linear relationship of $U_{g,62D} = 1.60 U_{g,15D}$ up to a certain gas velocity. Above that value the appreciable discrepancy can be observed. It can be clearly seen that this transition value increases with increasing both liquid superficial velocity and the liquid viscosity. As suggested earlier, this transition velocity might correspond to the regime transition to churn-annular flow where it was found to shift towards higher liquid superficial velocity with increasing both liquid superficial velocity and the liquid viscosity. The behaviour of the different injector profiles is coherent with the observations drawn earlier in this section.

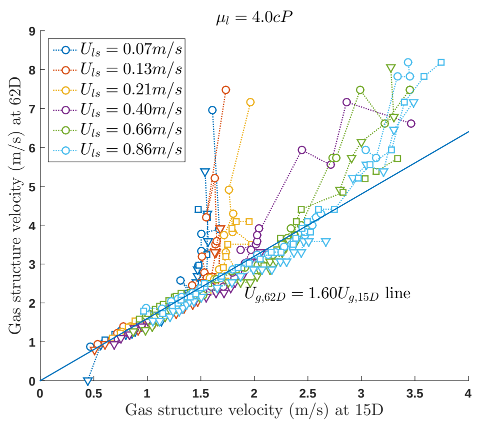

Axial development at 4.0cP

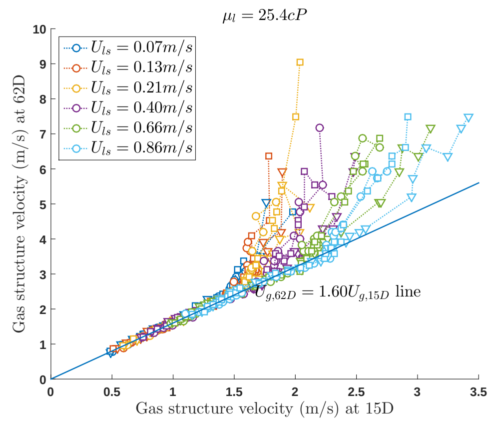

(a) Axial development at 25.0cP

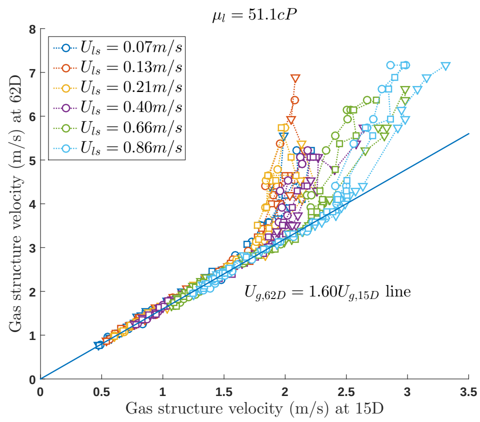

Axial development at 51.1cP

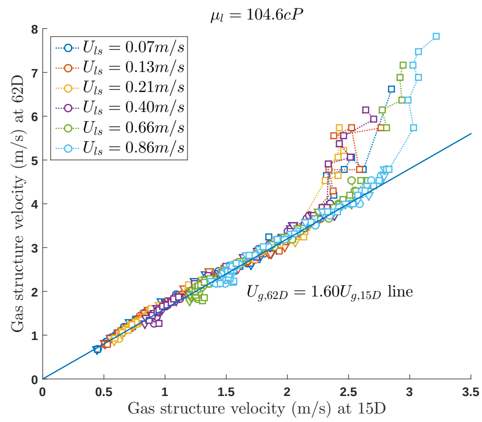

Axial development at 104.6cP

Fig. 6.22 Axial development of gas structure velocities for all the experimental runs featuring the three different injectors profiles. The graphs are colour coded, each corresponding to the liquid superficial velocity on the legend. The circular marker represents values from the capped-injector, the triangle for concentric injector and the square for the perforated injector.

6.2.7 Effect of viscosity on bubble size distribution

Bubble size distribution can be obtained from the void fraction measurements of the WMS using a filling algorithm proposed by [147]. The distribution is defined as contribution of a class of bubbles of a given equivalent diameter to the integral volumetric void fraction (%/mm). The distribution can be expressed in equation 6.1 below.

$$BSD(D_{Bub}) = \frac{d\epsilon}{dD_{Bub}} \tag{6.1}$$

Bubble size distribution has been reported on air-water based systems in conjunction with flow development by Herringe and Davis (1976), Guet et al (2003), Prasser et al (2007), Qui et al (2012), and Rabha et al (2014) [78, 71, 145, 150, 151]. Guet et al (2003) observed large variation in bubbles' chordal length when comparing bubbles generated by porous injectors to a large nozzle injector as far as 70D downstream a pipe of 70 mm ID. They reported a considerable improvement in gas-lift efficiency when smaller bubbles are introduced [71]. Prasser et al (2007) studied flow development in a 195 mm vertical pipe at elevated pressures comparing flow development in air-water and steam-water systems by varying the injector orifice size and axial location. They reported that in bubbly flow region bubbles exhibit a slight decrease in size with increasing axial distance from injection, a similar observation was reported by [78] when comparing distribution at 8D to that at 108D axial distance. They also observed that steam-water systems at higher pressures when compared to air-water systems has less tendency to exhibit bimodality distribution. Their paper mentioned existence of significant difference in bubble size evolution when the injector orifice is changed from 1 mm to 4 mm, however no much detail was given on these differences [145]. Qui et al (2012) studied bubble size evolution in the same facility (195 mm ID) by dividing bubbles into two classes; spherical bubbles and cap-bubbles according to the max stable spherical bubble diameter suggested by [97]. They observed that with increasing gas superficial velocity the presence of larger bubbles contribute mainly to increasing the population of smaller bubbles but not their size regardless of the axial location from the injection. They also reported persitent wall peaking of bubbles at low gas superficial velocities, however wall peaking completely diminished with increasing gas superficial velocity for both classes of bubbles [150].

Figure 6.23 shows the bubble size distribution for a selection of gas superficial velocities at a constant liquid superficial velocity of $U_{ls} = 0.39\, m/s$ downstream the test section at 63D axial distance. Each sub-figure constitute the distribution generated by each of the three different injectors employed. It is observable that the distribution appears very similar in most of the cases despite the relatively larger divergence observed at lower gas superficial velocity. This comes in concordance with the observations drawn earlier that generally the flow converges by 63D downstream the test section however at lower liquid superficial velocity longer axial distance is required as evidently clear from the shape bubble size distribution depicted in Figure 6.23. It is also observable that the average bubble size increases with increasing viscosity. At higher gas superficial velocities it the profiles almost overlap regardless of the liquid viscosity. No clear distinction can be made between the distributions obtained at different viscosities. At the higher bound of gas superficial velocities while the smaller peaks are identical for the profiles generated by different injectors yet some divergence is observed at the higher peak. This might be a lack of sampling problem, where the experimental run might need to be run for a longer period of time to obtain enough population of larger bubbles to create a smooth distribution. A problem that is not valid for smaller and populous bubbles.

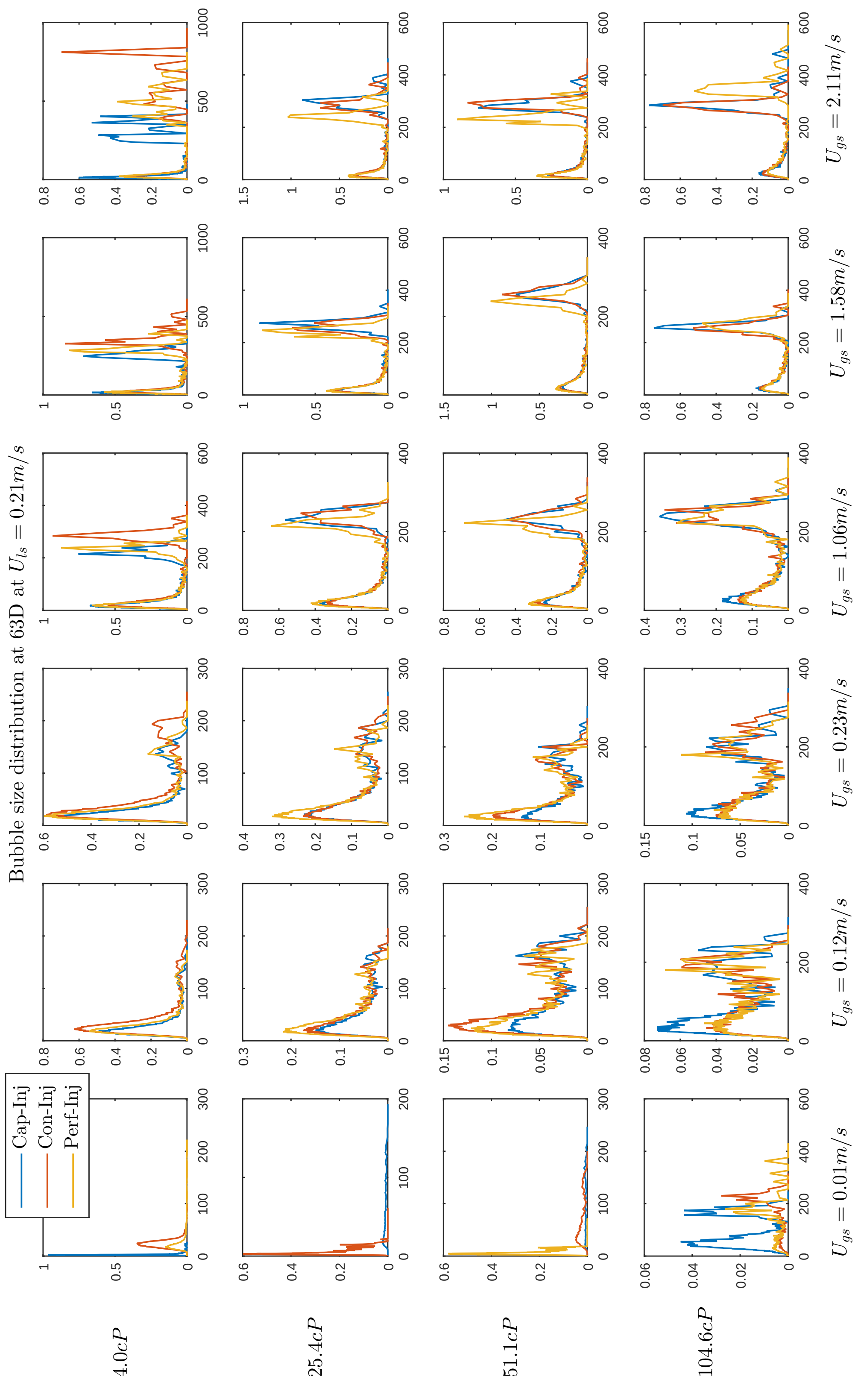

Fig. 6.23 Bubble size distribution computed using Prasser's algorithm for the studied matrix of gas and liquid superficial velocities expressed as % contribution to the volumetric void fraction by each class of bubbles $[\frac{\Delta\epsilon}{\Delta d_B}](\%/mm)$ (Y-axis) plotted against volume equivalent diameter in the x-axis in (mm). The figure features the variation in bubble sizes generated by different injection methods measured at 63 D axial distance from injection point.

To further investigate the effect of injector on the evolution of bubble size, profiles of average equivalent bubble diameter are obtained at two liquid superficial velocities ($U_{ls} = 0.07\,m/s$ and $U_{ls} = 0.39\,m/s$) for the four viscosities studied in Figure 6.24. The average bubble size is calculated using the formula mentioned in equation 4.5. The figure reflects the increase in average bubble diameter with increasing gas superficial velocity almost in a linear fashion. The rate of increase of average bubble size (gradient of the graphs) can be seen to decrease with increasing liquid superficial velocity owing to the increased turbulence level generated by the liquid and its counteraction against coalescence of the bubbles (refer to Figure 4.37). It is also evident that the deviation between the different injectors profiles decreased with increasing viscosity reconfirming what has been deduced in various parts of this chapter that the flow seems to converge faster with increasing liquid viscosity.

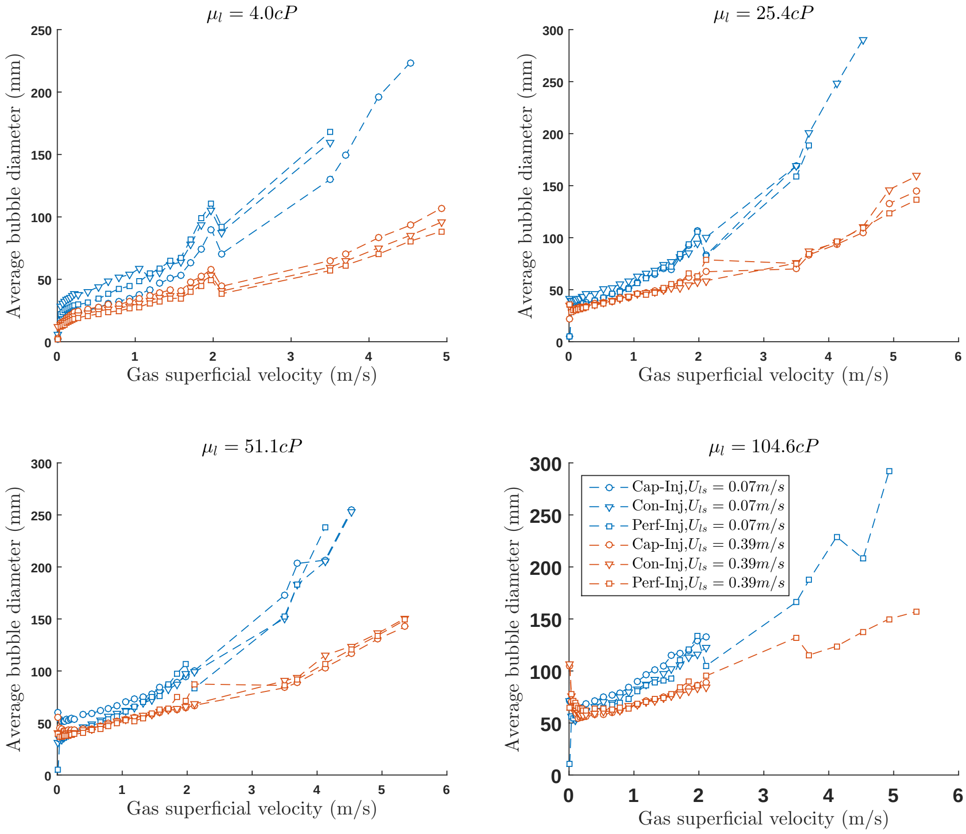

Fig. 6.24 Average bubble size against gas superficial velocity comparing the different injector methods employed for all the viscosities studied. The graphs are obtained at two liquid superficial velocities $U_{ls} = 0.07\,m/s$ and $U_{ls} = 0.39\,m/s$ at 63 D axial distance from the injection point.

6.2.8 Entrance effect on pressure drop

Another independent measurement obtained in this campaign is the differential pressure gradient. From the results catered in earlier sections of this chapter, it is demonstrable that the injector geometry affects flow development and therefore void fraction. This influence is expected to be reflected on the differential pressure profile. This is evident from the results reported by Guet et al (2003), where lower pressure gradient was registered when smaller bubbles are introduced to the test section in the bubbly flow region [71]. In this section the differential pressure gradient measured between 18 D and 60 D axial distance will be reported for the three different injectors and the variation of the injector influence with viscosity will be discussed.

Figure 6.25 shows the pressure gradient per unit length measured using the three different injectors at the four viscosities studied. The profiles presented in the figure are measured at three different liquid superficial velocities, namely 0.07, 0.40 and 0.86 m/s. In agreement with the previous sections of this chapter the figure reflects great resemblance between the profiles generated by different injection methods. Looking at the effect of liquid superficial velocity at constant viscosity; it can be observed that with increasing liquid superficial velocity the disparity between different injector profiles increases slightly, in concordance with other two phase flow attributes discussed in this chapter. It is also observable that some divergence in the profiles is observed at 4.0 cP, it diminishes with increasing liquid viscosity.

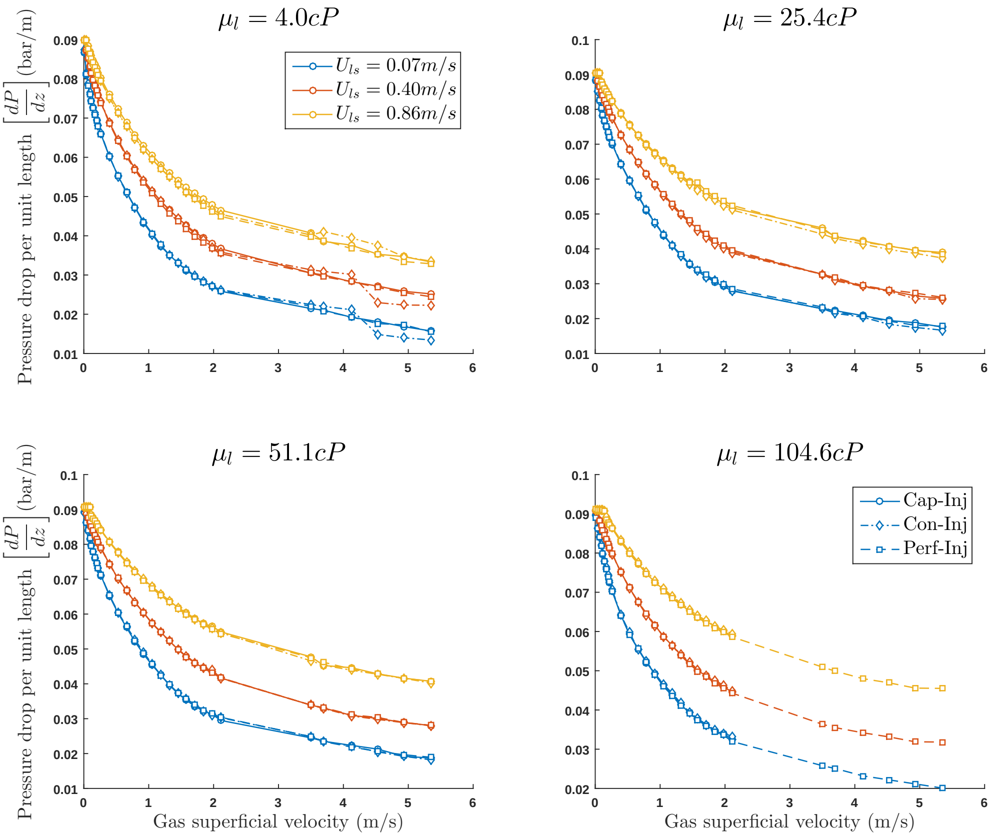

Fig. 6.25 Overall pressure gradient for the four viscosities studied against gas superficial velocity, the figure shows profiles generated by different injectors, circular markers correspond to cap-injector, the diamond for the concentric and the square for the perforated injector. The lines are colour-coded for the corresponding liquid superficial velocities as denoted in the legend. Each sub-figure presents the profiles obtained at constant viscosity.

6.3 Conclusions

The problem of flow development has been studied in this chapter. The development has been investigated by a combination of methods; obtaining measurements at various axial locations and using different injector geometries at the gas input point. The entrance effect on various attributes of two phase flows was measured and discussed with particular emphasis on the change of injector influence with liquid viscosity. From the results and discussions presented in this chapter the following conclusions can be drawn:

- In most of the studied experimental matrix, void fraction seems to converge at 63D axial distance from the injection point with exception of low gas superficial velocities;
- The flow is observed to develop faster at higher gas superficial velocity as evidenced by the various characteristics of two phase flow presented in this chapter. This is foreseen to be caused by the effect of bubble-induced turbulence that has been reported to be more significant in large diameter pipes by [135];
- The results presented in this chapter suggest that the flow develops faster with increasing liquid viscosity. This is referred to two synergetic attributes of viscosity. Firstly, the enhancement of bubble coalescence rate that increases dramatically with viscosity. Secondly, having bigger bubbles generates enhanced bubble-induced turbulence on the flow allowing reaching equilibrium bubble size happen sooner (either in distance or space terms);
- Introducing smaller bubbles at the injection is suggested to produce a slightly higher void fraction and smaller bubbles as far as 63D axial distance. However, the effect is limited at higher viscosities;
- In concordance with single phase flows the results suggest that increasing liquid superficial velocity inversely affects flow development. Longer entrance distance is needed when liquid superficial velocity is increased;
- Void fraction PDFs suggest that at higher viscosities when slug flow is present, the injection method has a more significant effect on the void fraction in the liquid slug rather than the Taylor bubble;

- In the bubbly flow regime, it was observed that at higher viscosities considerably larger bubbles form downstream the pipe due to bubble coalescence while remain undetectable upstream;

- At higher viscosities, it was observed that void fraction PDF featured churn flow shape registering a wide broad peak averaging around or above 50% void fraction upstream. Whilst a bimodal slug flow PDF is registered downstream. This indicates the appearance of churn flow as a developing flow regime for slug flow;

- Comparing average void fraction upstream and downstream the test section reveals that at lower gas superficial velocity the disparity in void fraction increases with increasing void fraction. This indicates the significance of bubble induced turbulence in enhancing bubbles break-up resulting in a higher void fraction upstream. The figures presented also suggest that the increasing drag at higher viscosities either improves the break-up of bubbles or hinders their coalescence resulting in a higher void fraction;

- Bubble size distribution, pressure gradient gas structure velocity, and radial distribution of void fraction all provided further evidence to the decrement of the entrance effect with increasing liquid viscosity and gas superficial velocity.

Chapter 7

Effect of viscosity on gas-lift performance in a vertical large diameter pipe

7.1 Introduction

In the previous chapters it has been demonstrated how greatly viscosity influences the two-phase flow characteristics. It has also been extensively explained how the state of the art models often depart significantly from the experimental data for viscous flows, especially in large diameter pipes where a clear lack of experimental data is faced.

7.1.1 Background and review

Nicklin (1963) [132] proposed a model to predict gas-lift performance based on the slug flow theory. Nicklin carried out momentum balance around the pump by estimating two-phase pressure gradient while neglecting the accelerational component. The hydrostatic pressure was predicted by evaluating void fraction along the axial length of the tube using a drift flux approach. In the energy balance models Darcy equation was used to estimate the frictional losses. Nicklin assumed a constant gas superficial velocity which is valid only for short pumps or highly pressurised rigs due to the gas expansion.

Stenning and Martin (1968) [171] derived a theoretical model for the gas lift pumps by performing momentum balance incorporating the effect of the slip between the fluids and a suitable model for the pressure losses.

Husain and Spedding (1976) [91] proposed a model based on performing energy balance around the lift pump considering the system as a closed thermodynamic loop with deficient energy (potential energy) that need to be compensated by energy input from the gas injection. The injector was considered an emitting source of energy contained in the isothermal expansion of bubbles as they rise in the test column. Jeelani et al (1979) reported that the model showed good predictions for small diameter pipes and high fluids input rate [100].

Clark and Dabolt (1986) [47] presented a theoretical model for gas-lift pumps using a drift flux correlation expression for the evaluation of gas velocity and Lockhart and Martinelli (1949) correlation for pressure drop. Chisti et al (1988) [43] suggested a model based on an energy balance approach around the gas-lift system while evaluating the energy losses around the rig. The model was proposed for bioreactors where void fraction of gas is considered in the downcomer column as well.

Reinemann et al (1990) [153] studied experimentally the effect of diameter on the performance of airlift pumps 3-25 mm. Extending Nicklin's theory to incorporate the effect of surface tension in terms of inverse Eötvos number. François et al (1996) [60] proposed a theoretical model based on solving the overall pressure drop equation in Bernoulli's terms considering the expansion of gas in the riser column. The produced model is mostly a modification of Clark and Dabolt's (1986) model [47].

Kassab et al (2009) [106] proposed a theoretical model for airlift taking into account the flow regime near high efficiency range. They concluded that the best lift is achieved under slug and slug-churn flow patterns. A model was proposed for the operation at slug flow condition using momentum balance around the system. The model is a modification of Clark and Dabolt's (1986) model by presenting the pressure drop in terms of Bernoulli's equation.

Many investigators have studied the effect of injector geometry on the performance of gas-lift. These include [176, 90, 71, 20, 110, 7]. Significant differences are often reported in the efficiency with the change of injector geometry all revolving around the line of the smaller the bubbles are in the injection point, the better the performance. However, many investigators fail to put the energy losses incurred by the pressure drop happening across the injector into consideration in the definition of efficiency, and therefore fall in the trap of reporting improved pumping performance whilst in energy terms, it could be a deteriorated performance.

Ahmed (2014) [6] studied gas-lifting in a three phase system utilising air, oil and water in a 10.5 m, 52 mm vertical riser. The studied gas superficial velocities range from 0.1 to 6.30 m/s. Pump assisted gas lift was used with varying liquid superficial velocities from 0.25 to 2 m/s. The three phases study concluded that the gas injection rate does not have a large effect on the liquid inversion point. However, a small shift was reported in the very high region of gas superficial velocities that incur churn to annular regimes in the riser. It was also reported that the injection method does not have an appreciable influence on flow characteristics when they measured void fraction around 182 diameter distance downstream the test section.

Abueidda et al (2014) [5] evaluated the performance of analytical models against the large eddy simulation (LES) numerical modelling. They acknowledged the good performance of the models of [153] and [171] while highlighting the advantage of identifying the flow pattern when LES models are employed.

Kim et al (2014) [111] studied the effect of submergence ratio and pipe diameter on the efficiency and operation of gas-lift pumps. They found that the efficiency increases with increasing the submergence ratio and decrease of the pipe diameter. Awari et al (2004) [20] reached an opposite conclusion with regard to the pipe diameter effect. In an attempt to correlate the effect of physical properties of the fluids they employed the correlation of Reinmann et al (1990) [153] where the drift velocity is expressed as a function of Bolton number. Yet the model suffered a large divergence from the experimental data which the authors attributed to the exclusion of the effect of pipe diameter in the model.

Ahmed et al (2016) [7] studied the effect of injector geometry on gas lift performance in a 31.75 mm pipe. They reported a significant increase in efficiency when gas is introduced using a combination of methods, perforated cylinder orifices and introducing air near the wall concurrently to the direction of flow. They also reported a significant increase in efficiency when gas injection is pulsated.

7.1.2 Objectives

It can be seen from the review presented here that there is an absence of gas-lift data in large diameter pipes (D>100 mm). In addition no trace was found for a parametric study that characterises the effect of viscosity on the performance of gas-lift. Building on the previous papers published on the effect of injector geometry on gas-lift performance in a passive lift system and a pump-assisted lift published in [92, 93], this chapter will report the effect of viscosity on the performance of gas-lift in a large diameter (127 mm) vertical pipe for both passive and pump-assisted gas-lift. The liquid used was Polydimethylsiloxane (PDMS) silicone oil of varying viscosities and air. Four different viscosities were studied, namely 4.04, 25.35, 51.10, and 104.58cP. The effect on gas lift performance will be reported in terms of

- Effect on void fraction evolution
- Effect on efficiency
- Effect on transient behaviour and flow regimes
- Effect on pressure drop

7.2 Results and discussions

7.2.1 Effect on gas-lift performance curve

Gas-lift performance curve is often expressed as the profile of the pumped liquid flow rate plotted against gas input in a passive lift system. Figure 7.1 below shows the performance curve for all the four viscosities studied here. It can be seen that the performance differs dramatically with the change of liquid viscosity. As depicted by the figure it can be seen that the pumped liquid flow rate becomes considerably lower with increasing liquid viscosity. This is potentially directly attributed to the effect of viscosity on void fraction, where - as discussed in chapter 4- increase in viscosity results in a lower void fraction and therefore higher pressure to overcome for the gas-lift upstream pressure.

It is also observable that the rate decrease in pumped liquid flowrate with viscosity is analogous to the change of void fraction with viscosity. It has been shown in chapter 4 that the decrease in void fraction is more dramatic when viscosity is increased from 4.04 to 25.4 cP. However, when the viscosity is doubled to 51.1 cP and further increased to 104.6 cP the resultant decrease in void fraction is much lower. This might explain why much better performance is exhibited by the lowest viscosity fluid in Figure 7.1, whilst at the higher viscosities liquid flow profiles almost overlap. At higher gas superficial velocity, the difference seems visibly bigger which is potentially an impact of higher variation in void fraction produced by different viscosities as well as the effect of increased liquid flow on void fraction.

It should also be noted that the higher viscosities profiles presented in Figure 7.1 exhibit crossing around $U_{ls} = 0.1\, m/s$ where profiles flip. Prior to that point highest viscosity produces higher liquid flowrate compared to the other two, above that point the highest viscosity profile becomes lower than the other two lower viscosities. This could be corresponding to the change in void fraction profile observed in chapter 4, where the regime changes from dispersed flow to undistributed flow. This phenomenon is often termed "double effect of viscosity" by bubble-column and bioreactors researchers [32].

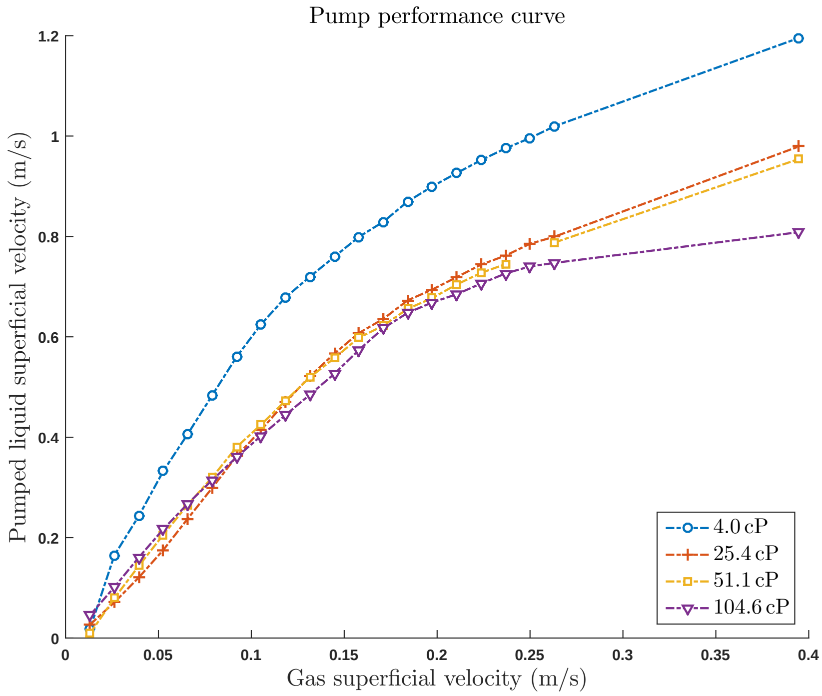

Fig. 7.1 Gas-lift pump performance curve at the four different studied viscosities. The figure features much lower produced liquid flow with increasing liquid viscosity.

7.2.2 Effect on gas-lift efficiency

Richardson and Higson (1962) proposed a definition of gas lift efficiency based on the net work done to lift the liquid relative to the work done for the isothermal expansion of gas as in the equation below [154]

$$\eta = \frac{Q_l h \rho_l g}{Q_g P ln\left(\frac{BHP}{P_{atm}}\right)} \tag{7.1}$$

Where η is the efficiency h is the tube height, Q_l and Q_g are the liquid and gas flowrates respectively and (BHP) is the Bottom Hole Pressure, P_{atm} is the atmospheric pressure [60]. Figure 7.2 shows the gas-lift efficiency for all the four viscosities studied evaluated at four different gas superficial velocities. It can be seen the higher liquid flow produced at the lowest viscosity observed earlier is reflected in its efficiency profile. Where a considerably higher efficiency is featured by the 4.04 cP profile. This is expected due to the improved liquid flow observed earlier and the void fraction behaviour explained in chapter 4.

Figure 7.2 shows that the efficiency profile shape is almost consistent for all the viscosities, where at very low gas input rate the resultant efficiency is low. With increasing gas superficial velocity it increases to a maxima after which it decreases systematically with increasing gas superficial velocity registering low efficiency at the highest gas-flow studied. In concordance with the pump performance curve profiles, it can be seen that the higher viscosity profiles flip cross around $U_{ls} = 0.1\,m/s$. This is potentially an attribute of the void fraction behaviour around that range of gas superficial velocity, which could be a reflection of the change of flow regime from dispersed to undistributed bubbly flow.

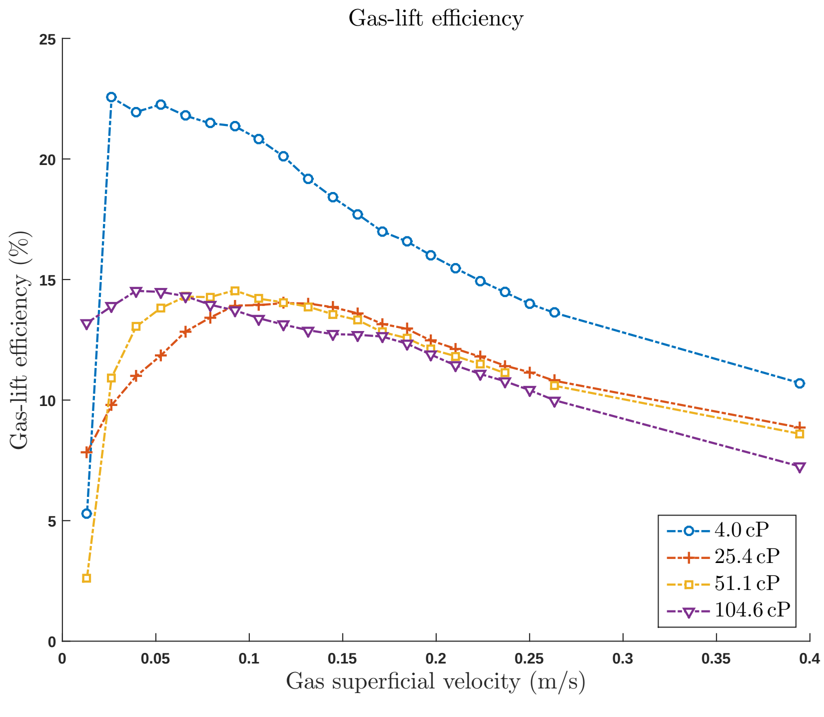

Fig. 7.2 Gas-lift efficiency calculated for the four studied viscosities against gas superficial velocity. It is clearly evident that the efficiency severely degrades with increasing liquid viscosity.

7.2.3 Effect on void fraction and flow regimes

To better explain the results presented earlier about the pump performance and understand the influence of viscosity on the performance of the gas-lift pumps it is of profound importance to study void fraction. Figure 7.3 shows evolution of averaged void fraction with gas superficial velocity measured at 62D axial distance from the injection point. Expectedly, It can be observed that the void fraction increases systematically with increasing gas superficial velocity. Although when gas input is increased to the test section, the pumped liquid flow also increases, however the overall effect features an increase in void fraction. This increase in void fraction is attributable to two synergetic effects. First increased volume of gas input is expected to naturally increases void fraction. In addition, the increase in gas input induces higher liquid flow and therefore higher turbulence level that enhanced bubble break-up and therefore the combined effect results in a higher void fraction.

It is also observable from Figure 7.3 that the average void fraction is higher the lower the viscosity. However, the divergence in void fraction with viscosity is much lower than that observed in the void pump performance curve. Although the quantities compared are of different nature, noting that shows how a small percentage variation in void fraction could result in a much improved performance of the gas-lift system.

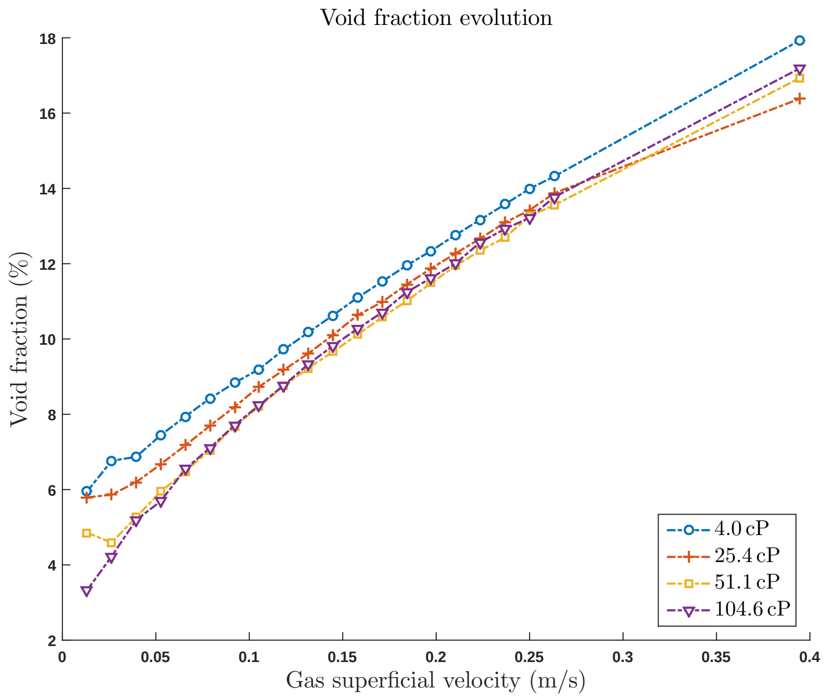

Fig. 7.3 Void fraction evolution with gas superficial velocity for the four studied viscosities. Lower void fraction is produced with increasing liquid viscosity.

PDF of void fraction time series

An established method of characterising the incurring flow regime is often carried out by examining the probability density function (PDF) shape of the void fraction time series. This has been extensively elucidated in the earlier chapters of this thesis. Figure 7.4 shows the PDFs of void fraction time series at four different gas superficial velocities. Each sub-figure presents four PDFs each correspond to one of the four different viscosities studied. Generally it can be seen that consistently in all the graphs the profile produced by the lower viscosity fluid peaks at higher void fraction value, the peak shifts towards lower void fraction with increasing viscosity. Looking at the evolution of the shape of the PDF with increasing liquid viscosity, it appears that at lower viscosities, the PDF features a single peak indicating presence of bubbly flow. With increasing viscosity the PDF features a tail that becomes more pronounced with increasing liquid viscosity, indicating the presence of cap-bubbles in the pump.

Looking at the effect of increasing gas superficial velocity on the incurring flow regime, Figure 7.4 demonstrates a clear shift of the PDF peak towards higher void fraction with increasing gas superficial velocity regardless of the viscosity. However, the PDFs shape does not indicate any change in flow regime whereas bubbly slug flow seems persistent. This suggests the general beleif that gas-lift pumps often operate at the same flow regime and rarely exhibit a regime transition. This is also supported by the observations presented in [92, 93]. It is also notable that increasing gas input has a more pronounced effect on the higher viscosity fluid, making the tail more prominent and at the highest viscosity featuring an obscure bimodal distribution which is the characteristic shape for cap-bubbly flow.

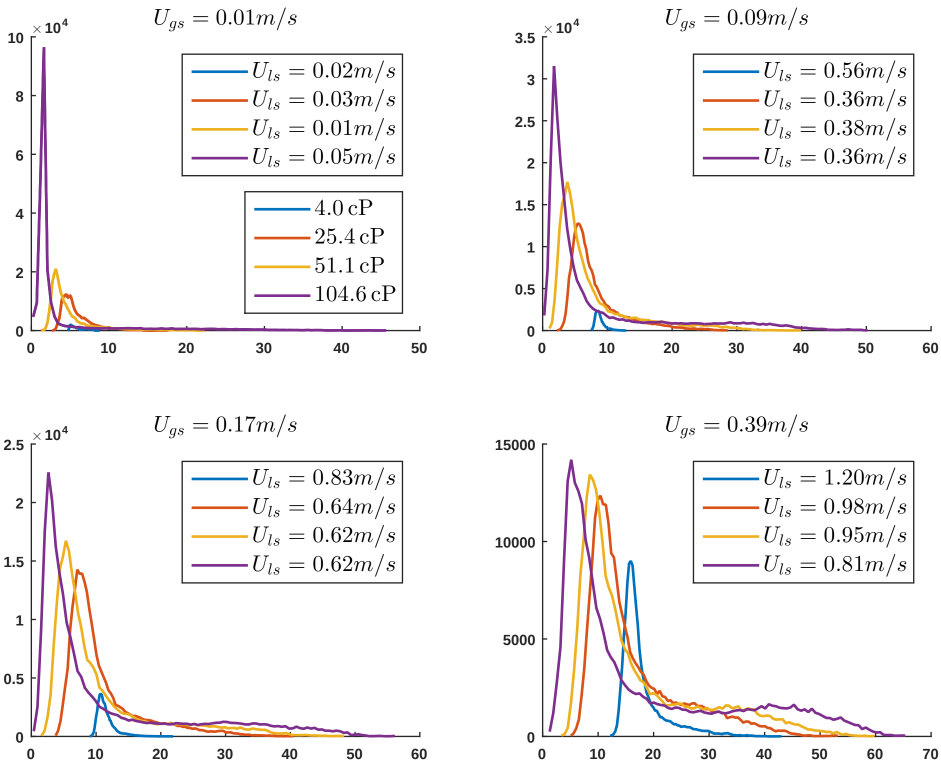

Fig. 7.4 PDF of void fraction time series at four different gas superficial velocities. Each sub-figure features the PDF shape of the four viscosities studied as per the legend in the first sub-figure. Each curve represents profile registered at different liquid superficial velocity depending on the lift efficiency as indicated in the legend.

Spatio-temporal images from the WMS

The WMS enables high resolution visualisation of void fraction distribution in the pipe. There is a common recourse to present WMS phase distribution information as a slice of phase distribution along the core of the pipe resolved in time. With the knowledge of velocity of the gas structures and acquisition frequency, the y-axis (time) could be converted to length which would provide a much realistic representation of the shape of structures in the pipe. This has been exhaustively explained in Chapter 4.

Figure 7.5 shows the aforementioned spatio-temporal phase diametrical distribution of void fraction. Where the x-axis of each small slice represents the pipe diameter, the y-axis is the equivalent pipe length (to scale with the diameter). The blue colour represents oil while the red stands for the gas. the figure shows four rows of images each corresponds to one of the four studied viscosities as indicated in the figure. Each row presents profiles with increasing gas superficial velocity from the left to right. It can be seen that in general the images come in concordance with what has been indicated by the PDF shapes, whereby most of the images depict the presence of bubbly flow. They show that the dispersity of the gas phase decreases dramatically with increasing liquid viscosity. This explains the higher average void fraction obtained for lower viscosity fluid and therefore the higher efficiency featured for the gas-lift. Another relative notable attribute is the increased clustering/coalescence of bubbles with increasing liquid viscosity, as evidently clear in the figure.

In the gas-lift mode as gas velocity is increased, the liquid input increases, however the increase in gas-input results in a net higher increase in gas concentration compared to the liquid. This is evident by the various attributes of void fraction presented earlier in this chapter as well as the images shown in Figure 7.5.

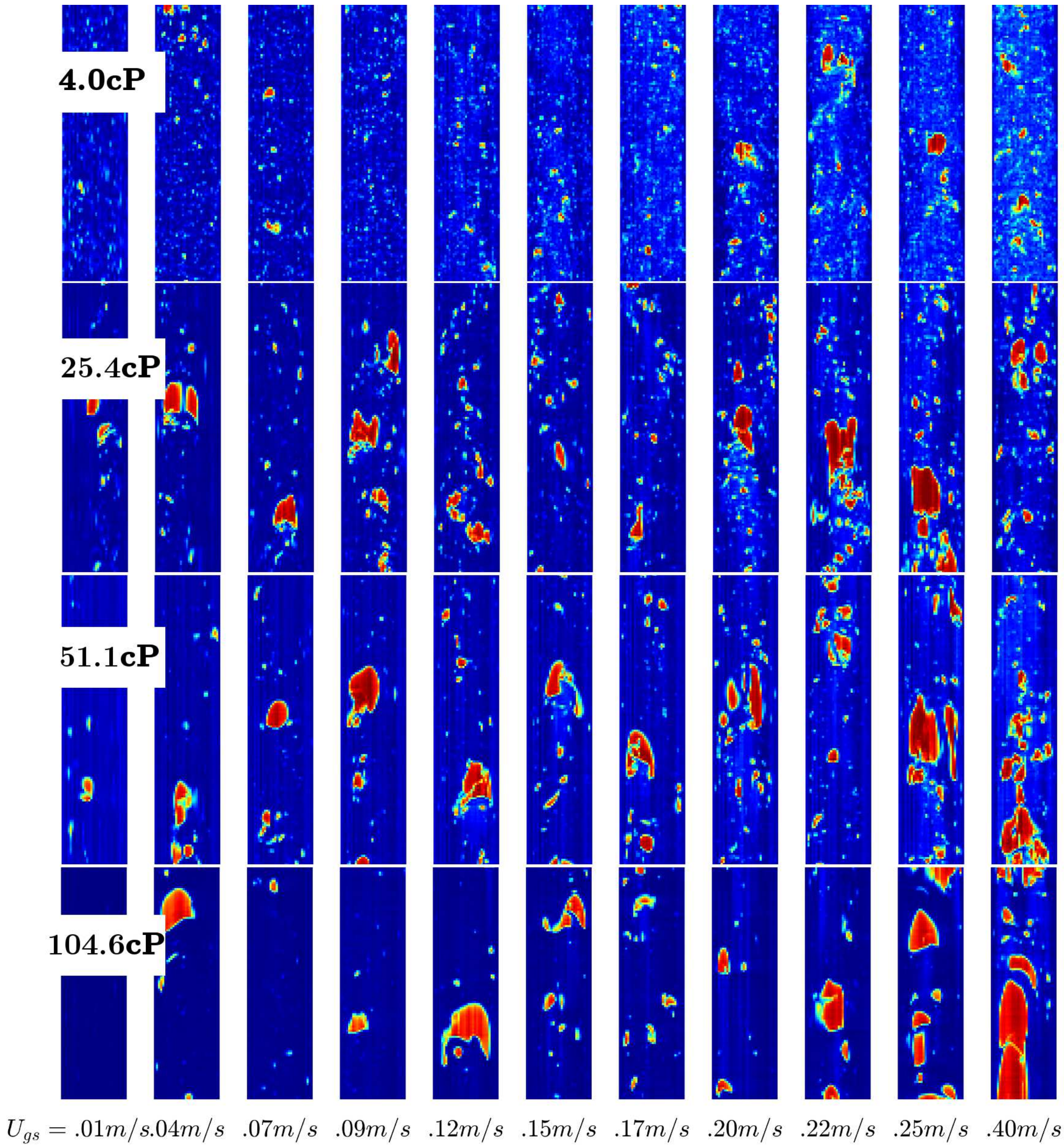

Fig. 7.5 Spatio-temporal phase diametrical distribution of void fraction. X-axis of each small slice represents the pipe diameter, the y-axis is the equivalent pipe length (to scale with the diameter). The blue colour represents oil while the red stands for the gas.

7.2.4 Effect on pressure gradient

Figure 7.6 shows the evolution of pressure gradient with gas superficial velocity for the four viscosities studied. It is notable that much lower pressure gradient is obtained at the lowest viscosity. This could be ascribed to the higher void fraction obtained at the lowest viscosity as manifested in the earlier section. Expectedly, the profiles of different viscosities are arranged where pressure gradient increases with increasing liquid viscosity, in concordance with the other aspects of gas-lift discussed in this chapter. This could be referred to the influence of void fraction on pressure gradient where the gas-lift is mostly operated in bubbly and slug flow regions where gravitational pressure gradient is dominant. It should also be noted that the profile exhibits a change in trend where at the lower side of gas superficial velocities the pressure gradient sharply drops with increasing gas input. At a slightly higher gas superficial velocity the profiles change slope and become almost linearly decreasing with increasing gas input.

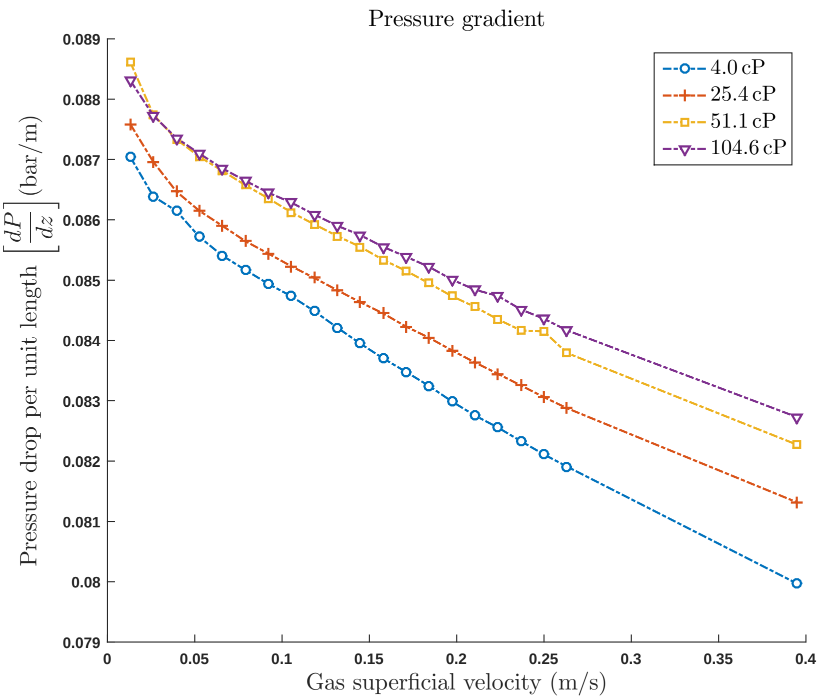

Fig. 7.6 Pressure gradient variation with the change of oil viscosity. Much higher pressure drop is generated when the liquid viscosity is increased.

7.2.5 Effect on gas structure velocity

Structure velocity can be calculated by cross-correlating void fraction time series across two axial measurements obtained not far from each other. The experimental arrangement used in this study enabled the calculation of structure velocity at two axial positions, for brevity only one axial location information will be reported here. This provides another independent indication of the dynamics of the flow and therefore consolidating the understanding of how viscosity actually influences the performance of gas-lift.

Figure 7.7 shows the gas structure velocity plotted against mixture superficial velocity. In this instance it was chosen to plot the gas structure velocity $\left(U_g = \frac{U_{gs}}{\varepsilon_g}\right)$ against mixture superficial velocity instead of gas superficial velocity in order to identify at which velocity structures are faster (i.e. bigger) considering the effect of liquid superficial velocity. It is observable that the smaller structures produced by the lowest viscosity fluid have a considerably much lower rise velocity compared to the higher viscosity fluids. This consolidates the information presented earlier that gas-lift is more efficient at lower viscosity due to the impact of viscosity on increasing bubble size, therefore directly reducing void fraction resulting in a much higher gravitational pressure gradient. The previous statement is only valid however in the regions where gravitational pressure gradient is dominant, which is the most common range of operation for gas-lift pumps. However, in the rare cases where gas-lift is operated in churn flow and near annular flow condition the situation may differ, efficiency (low as it maybe) is expected to be higher for the higher viscosity fluids due to the effect of interfacial friction.

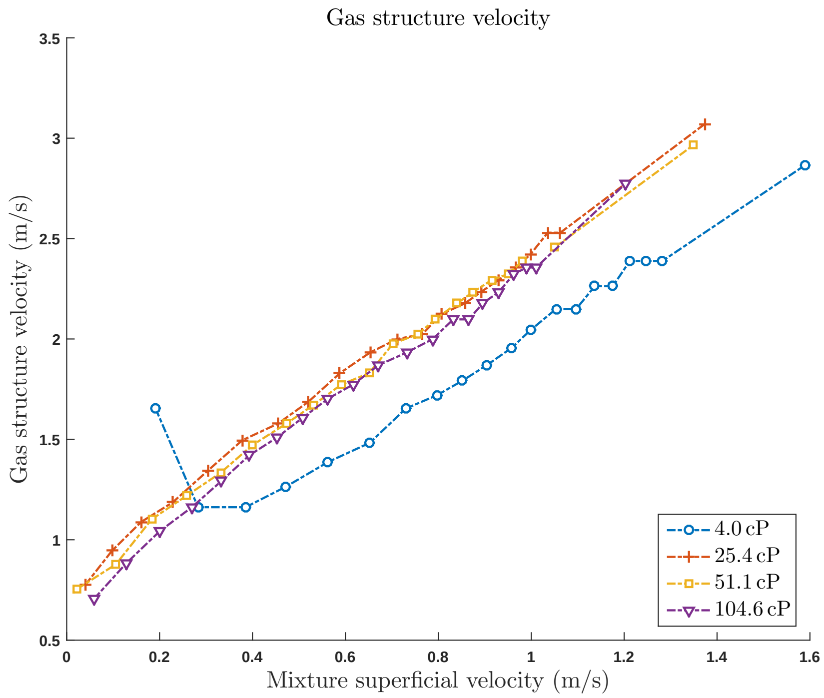

Fig. 7.7 Gas structure velocity against mixture superficial velocity for all the viscosities studied.

7.2.6 Investigation into pump-assisted gas-lift

It has been attempted to study the effect of pumping liquid through a parallel channel using a positive displacement pump. The idea is to introduce extra liquid in the column using the mechanical pump and also allow natural recirculation to take place in a parallel channel and study how that affects the performance of the gas-lift. The pump was operated at two different liquid superficial velocities, namely 0.20 and 0.5 m/s. The performance curves of the gas-lift with only natural recirculation and the pump-assisted lift at the two velocities is shown in Figure 7.8 below. It can be noted that the trend generated in the three cases is very similar. This has also been observed in the paper published in [93], where profiles generated by the three different arrangements eventually collapse into one line. This can be owed to the hindering effect the presence of extra liquid (provided by the pump) induces on the natural lift causing initially a negative liquid flow on the natural recirculation channel. This suggests that the profiles generated by these three arrangements in terms of gas and liquid velocities in the test section are essentially the same. The similarity is plainly evident and presented in Figure 7.8 below.

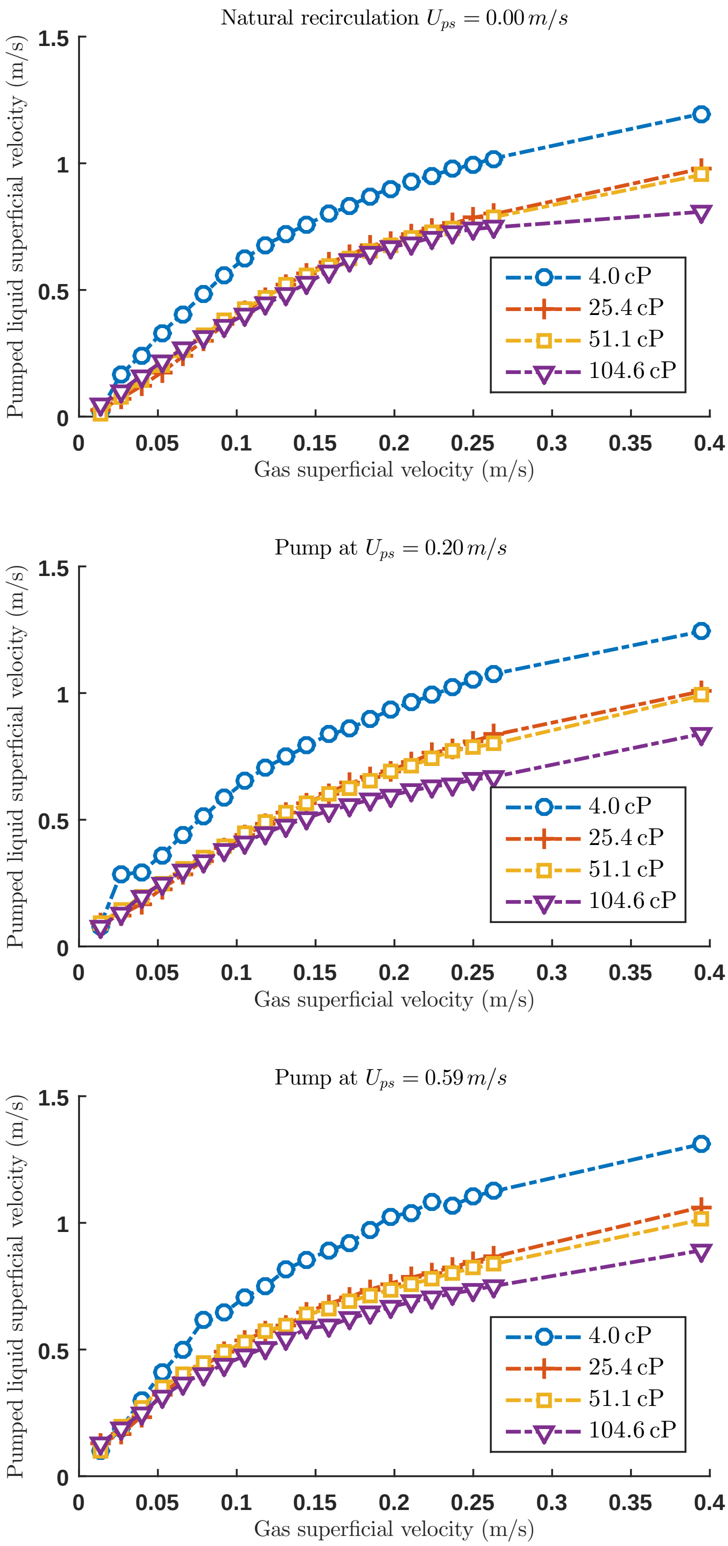

Fig. 7.8 Gas structure velocity against mixture superficial velocity for all the viscosities studied.

7.2.7 Performance of gas-lift models

There are three approaches to predict liquid flowrate corresponding to a specific gas input. One approach is the empirical correlations, developing empirical correlations based on various experimental data performed in pipes with different sizes. The second approach is analytical that involves performing energy balance investigating several conditions around the maximum efficiency. The most commonly used formula of this approach is the Ingersoll-Rand equation. The model of Francois et al (1996) [60] is considered in this section from this category.

The third group of methods is a one dimensional two-phase flow modelling approach. It is based on developing representative mass and momentum balance equations around the system. Development of these models involves incorporating many simplifying approximations which limit the range of applicability of the proposed models. The simplifications include, neglecting the accelerational pressure drop and also the compressibility of the gas phase. Much of the models discussed in this section are from this category.

Figure 7.9 shows the performance of some of the popular models briefly reviewed earlier in the introduction of this chapter in comparison to the experimental data. It can be seen than most models diverge grossly from the experimental data. This can be partly owed to the fact that many of these models, either empirical, energy balance or two-phase models have been derived either for small diameter gas-lift pump or for air-water systems. It has been explained in Chapter 2 how vastly the two-phase characteristics differ in large diameter pipes compared to that in smaller pipes. Chapter 4 has demonstrated exhaustively how viscosity affects two-phase characteristics and specifically its impact on average void fraction. All those factors combined are believed to have caused the dramatic inaccuracy of some of the state of the art gas-lift models available in literature.

Figure 7.9 also shows that the predictability of most of the models appear to improve with increasing liquid viscosity. This might be attributed to the greater resemblance to behaviour in small diameter pipes that is observed at elevated viscosity. One of these aspects is the presence of Taylor bubbles and the characteristic slug flow regime. The improvement in the models performance maybe attributed to adoption of the slug flow theory used in most of the drift-flux based models.

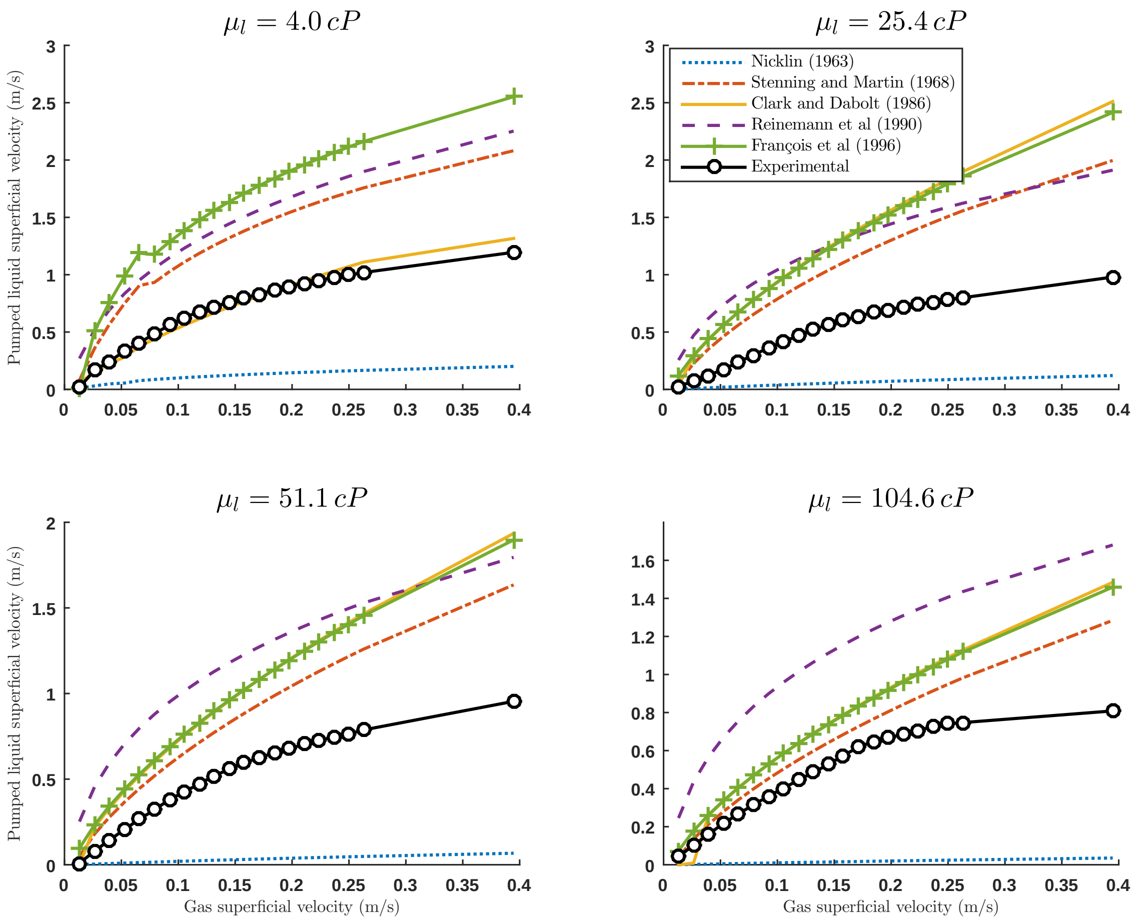

Fig. 7.9 Performance of popular gas-lift models compared to experimental data across the four viscosities studied. It can be seen that most models diverge greatly from the experimental data.

7.2.8 Proposal of an improved model for gas-lift performance prediction

In the previous section it has become evident that there is a genuine need for better performing models for gas-lift prediction. One way of achieving that could be by using improved drift-flux correlations and plug it into already established models and observe the performance. This approach has been exercised with the drift-flux model proposed by Clark and Dabolt (1986) [47]. The model uses a drift-flux approach, based on the slug flow theory to predict void fraction and therefore estimate the gravitational pressure gradient component. An approximation of the other pressure losses are incorporated in the model to predict the overall pressure gradient and therefore the expected liquid flowrate at a specific gas input. The original model incorporates the drift velocity (V_d) first proposed by Dumitrescu (1943) [55] as depicted in equation 7.2. The distribution coefficient of Zuber and Findlay [193] has been used as ($C_o = 1.2$).

As demonstrated in Figure 7.9, the original model of Clark and Dabolt (1986) deviates remarkably from the experimental results. Plugging in a more accurate correlation is expected to considerably improve the performance. This is attributable to the fact that air-lift pumps are most efficient if operated in a gravity dominated flow regime whereby the prediction of void fraction is of paramount significance. Accordingly, the drift-flux model proposed in Chapter 5 has been employed in the integrated formula of the Clark and Dabolt (1986) [47] model. The new formulations for the distribution coefficient and the drift velocity are given in equations 7.3 and 7.4 respectively.

$$V_d = 0.35 \times \sqrt{gD} \tag{7.2}$$

$$C_o = 0.038 \times (N_\mu N_{Mo})^{0.249} + 1.089 \tag{7.3}$$

$$V_d = [0.2061 \times (N_\mu N_{Mo})^{0.127} + 0.172]\sqrt{gD} \tag{7.4}$$

$$N_\mu = \frac{\sqrt{gd^3(\rho_l - \rho_g)\rho_l}}{\mu_l} \tag{7.5}$$

$$N_{Mo} = \frac{g\mu_l^4(\rho_l - \rho_g)}{\rho_l^2\sigma_l^3} \tag{7.6}$$

Figure 7.10 shows that predictions of the modified model in comparison to the original Clark and Dabolt (1986) model and the experimental data. It can be seen that the introduction of the new drift-flux correlation has resulted in a significant improvement of the performance of the model. As can be seen the performance curve produced by the modified model almost overlaps the experimental curve. Against expectations some deviation is observed at the highest viscosity. This is not expected as the accuracy of the drift-flux model is superior as viscosity increases as elucidated in Chapter 5. The deviation can be attributed to the frictional pressure gradient as it becomes more significant with increasing viscosity. The Clark and Dabolt (1986) model uses an approximation formula for the Lockhart and Martinelli (1949) frictional pressure gradient [116]. In the very same Chapter 5 it has been manifested how grossly this model deviates from the experimentally estimated frictional pressure gradient.

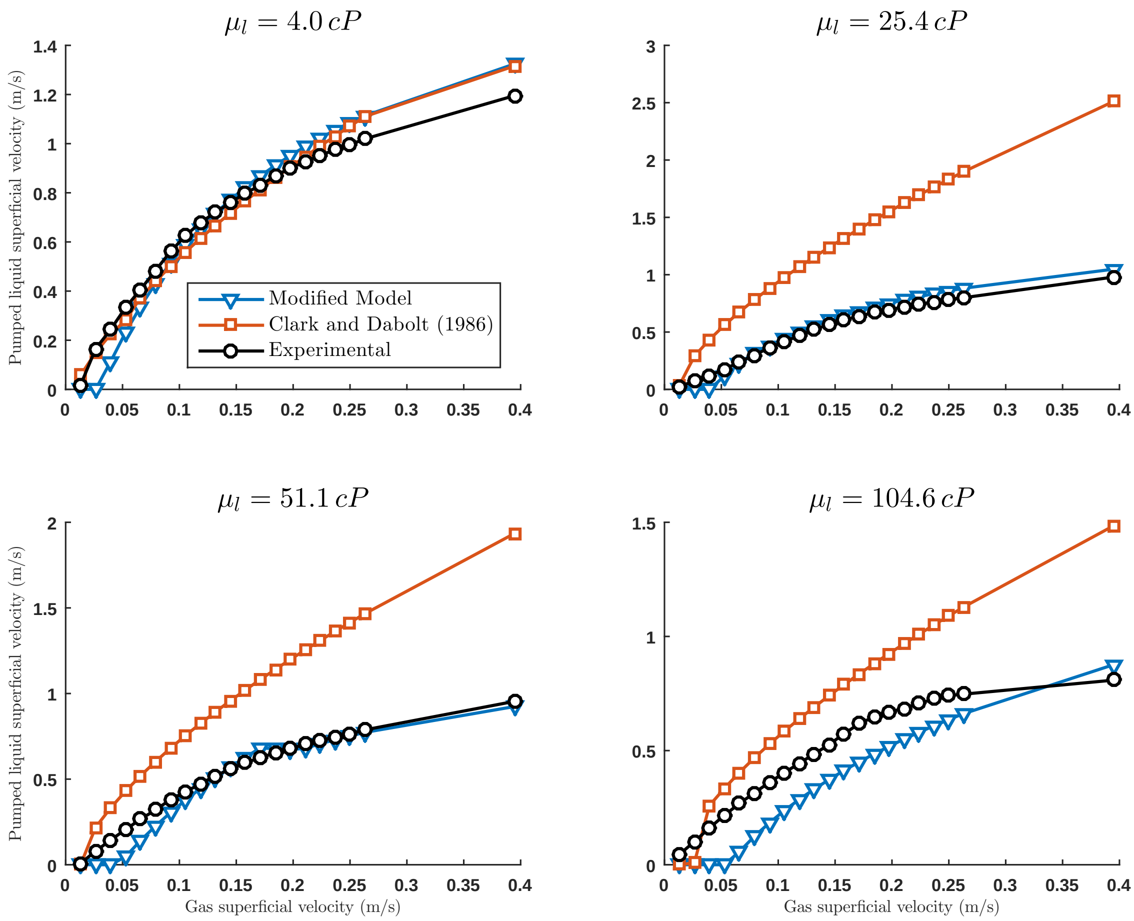

Fig. 7.10 Performance of the modified model together with that of Clark and Dabolt's (1986) and the experimental data.

7.3 Conclusions

In this chapter the effect of viscosity on gas-lift performance has been investigated. The gas-lift performance curves have been presented for four different viscosity oils. High spatial and temporal resolution two-phase flow information was collected and presented. The viscosity effect on various two-phase flow attributes has been presented and discussed. An evaluation of some published gas-lift models against the data has been presented and a proposed modified model is presented with a much superior performance. From the information presented in this chapter the following conclusions can be drawn:

- The gas-lift performance curves and the assessment of gas-lift efficiency shows a significant degradation of the performance of gas-lift as the liquid viscosity is increased. This was attributed to the impact of viscosity on void fraction where increase in liquid viscosity results in a decrease in average void fraction at the same gas input rate;

- Gas-lift efficiency revealed that the efficiency is highest in the bubbly flow region, as gas superficial velocity is further increased the efficiency drops dramatically. The efficiency is not necessarily higher at lower viscosities especially at very low gas superficial velocities;

- In concordance with the data presented in Chapter 4 average void fraction decreases with increasing liquid viscosity throughout the studied range of gas superficial velocities;

- In the range of gas superficial velocities employed the PDFs of void fraction time series and the spatio-temporal images reveal that the incurring void fraction was bubbly flow throughout. In agreement with the conclusions of Chapter 4 there is a tendency of formation of larger gas structures with increasing liquid viscosity. At the highest viscosity the presence of cap-bubbly flow regime was detected by the appearance of obscure bimodal PDF shape;

- The independent measurements of pressure gradient show that pressure increases with increasing liquid viscosity in correspondence to the decrease in average void fraction elucidated earlier;

- The models of Nicklin (1963) [132], Stenning and Martin (1968) [171], Clark and Dabolt (1986) [47], Reinemann et al (1990) [47], François et al (1996) [60] have been evaluated against the experimental data. It was found that all the aforementioned models perform poorly against experimental results;

- A new revised model is proposed and assessed against the experimental data. The proposed model is a modification of the model of Clark and Dabolt (1986) [47] whereby the improved drift-flux correlation presented in Chapter 5 is employed.

Chapter 8

Conclusions and recommendations

This thesis aims to experimentally investigate the gas-lift technique for viscous fluids in vertical large diameter pipes. This inquiry can only be achieved by performing a fundamental study to understand the overarching physical mechanisms that underpin viscous two-phase flows in vertical pipes. The improved understanding of the physics will thereafter be used to improve models and predictive tools that operators and design engineers employ in various industries.

Accordingly, this thesis is structured in a narrative that reflects the aforementioned story. Starting with highlighting the significance of this area of research and the potential impact of the study on both academic and industrial arenas. That is followed by a literature review chapter providing a broad background of multiphase flows and the particular terminologies and approaches in the field as well as surveying the progressive developments in the relevant attributes of two phase flows accomplished by the scientific community. Following that, the methodology by which the experimental campaign will be conducted is detailed featuring the experimental facility (127 mm ID pipe), the measurement techniques, and the fluids employed.

Thereafter, the results are presented in four experimental chapters. The first experimental chapter presents a novel parametric study on the effect of viscosity in large diameter vertical pipes; whereby the results are assessed and analysed both qualitatively and quantitatively using advanced instrumentation techniques. The second experimental chapter examines the performance of the state of the art models against the unique experimental data presented in the earlier chapter and introduces new improved global models for various multiphase flow features. The third experimental chapter discusses the flow development issue and elucidate on how the entrance effect varies with viscosity. Finally, the last experimental chapter investigates the performance of an actual large scale gas-lift pump and describes the results. The chapter extends onto assessing the performance of the models and proposing improved models based on conclusions from the fundamental study presented in the earlier chapters.

This chapter will highlight the chief conclusions drawn from each of the results chapters of this thesis and ends with a note of recommendations for further research.

8.1 Conclusions

8.1.1 Chapter 4: Effect of viscosity on two phase flows in a vertical large diameter pipe

This chapter presents a novel experimental study on the effect of viscosity on two phase flow attributes in a vertical large diameter pipe, namely a 127 mm pipe. The effect of viscosity was investigated using four different viscosities; namely 4.0, 25.4, 51.1, 104.6 cP Silicone oils while varying the liquid superficial velocity from 0.07-0.86 m/s and the gas superficial velocity from 0.01-5.40 m/s, generating a matrix of 720 runs. Void fraction was measured using Electrical Capacitance Tomography (ECT) and the Wire Mesh Sensor (WMS) at 5 different axial stations along the 10.12 m length of the test section. The prime conclusions from the results and analysis can be summarised as follows:

- Generally, time averaged void fraction indicates that void fraction decreases with increasing viscosity at the same as and liquid superficial velocity. This is attributed to the viscosity effect of shifting the coalescence-breakup equilibrium of bubbles towards higher coalescence.

- At low gas superficial velocities, the 'dual effect of viscosity' is observed whereby higher viscosity void fraction exhibits higher void fraction and eventually fall below that of lower viscosities with increasing gas superficial velocity. The phenomenon is more pronounced at low liquid superficial velocities.

- The viscosity impact on void fraction was found to decrease with increasing liquid superficial velocity. On the contrary, at lower liquid superficial velocity, gas superficial velocity has a greater impact on the effect of viscosity on void fraction.

- Radial void fraction profile revealed that liquid film becomes thicker with increasing liquid viscosity. In addition the profile becomes more parabolic with increasing viscosity. While wall peaking is observed at the lowest viscosity 4.0 cP at low gas superficial velocities; higher viscosities only exhibited core peaking suggesting that increased viscosity drives bubbles away from the wall into the pipe core.

- Higher pressure gradient was recorded with increasing liquid viscosity. This is ascribed to the increase in wall shear stress as well as the higher gravitational pressure gradient owing to the lower void fraction.

- Characteristic bullet shaped Taylor bubbles were observed in a large diameter pipe at a slightly elevated viscosities characterised by the spatio-temporal images from the WMS, bimodal Probability Density Function (PDF) shape, and high speed photographs of the flow.

- The slug flow region increases with increasing both liquid viscosity and the liquid superficial velocity. The bubbly-slug transition line moves to lower gas superficial velocities with increasing liquid viscosity. The opposite is exhibited by the slug-churn transition boundary.

- Structure frequency was found to increase slightly with increasing liquid viscosity. Indicating that the structures move faster with increasing viscosity.

- Bubble/structure size distribution revealed that increasing viscosity increases average bubble size, indicating that viscosity stabilises the interface and improves bubbles coalescence.

8.1.2 Chapter 5: Modelling of viscous flows in vertical large diameter pipes

This chapter assesses the performance of predictive state of the art models proposed for global design parameters in two phase flows in vertical pipes. The chapter also introduces improved models for these paramount parameters. The conclusions drawn from this chapter can be summarised as follows:

- Performance of popular void fraction models was assessed whereby most correlations were found to grossly diverge from the experimental data. The models investigated include Premolie et al (1971) also known as ICSE correlation, Aziz et al (1972) [21], Mukherjee and Brill (1973), Kabir and Hasan (1990) [102], and Ansari et al (1994) [18].

- A new drift flux correlation has been proposed as a function of the non-dimensional viscosity number (N_{μ_l}) and Morton number (N_{Mo}) as per equations 5.1, 5.4, and 5.5. The performance of the new correlation has been tested against current experimental data as well as data collected from various sources in the literature. The correlation was found to reproduce experimental values with very good accuracy.

- Observation of positive frictional pressure gradient at low liquid superficial velocities is reported. The phenomenon was ascribed to the average instantaneous wall shear stress competition in the slug/intermittent flow region between the backward falling film in the Taylor bubble region and the forward moving film in the liquid slug region. The phenomenon was found to be more significant with increasing pipe diameter and decreasing liquid viscosity as well as liquid/gas density ratio.

- Popular pressure gradient models' performance was assessed against the experimental data. These include the models of Hagedorn and Brown (1965) [73], Aziz et al (1972) [21], Mukherjee and Brill (1973), Kabir and Hasan (1990) [102], Ansari et al (1994) [18],and Friedel (1979) [61]. Both the models of Aziz et al (1972) and Kabir nad Hasan (1990) were found to produce comparably small errors.

- A new correlation has also been proposed for prediction of structure characteristic frequency as a function of non-dimensional viscosity number and Morton number. The correlation was found to reproduce experimental results with a reasonable accuracy.

8.1.3 Chapter 6: Effect of injector geometry on two-phase flows in a vertical large diameter pipe

This chapter investigates the issue of flow development using two methods; measuring void fraction at several axial stations along the test section, and using different geometries for bubble injection into the base of the pipe. The investigation emphasises on the influence of viscosity on the entrance effect. The study is achieved by contrasting the 180 runs produced using three different injectors, the runs are repeated using 4 different viscosities, marking 2160 experimental run. The conclusions drawn from this chapter can be summarised as follows:

- In most of the studied experimental runs flow seems to develop at 63D axial distance from the injection point.
- Flow was found to develop faster with increasing liquid viscosity. This effect was attributed to the synergy between the enhanced bubble coalescence with increasing viscosity, coupled with the bubble-induced turbulence that allows reaching bubble size equilibrium faster (either in length or time). This is supported by the bubble size distribution analysis, gas structure velocity, pressure gradient, and radial distribution of void fraction results.
- Introducing smaller bubbles to the test section was found to produce a slightly higher void fraction at low viscosities. When viscosity increases the effect becomes minimal.
- Longer development length is needed at higher liquid superficial velocities, in accordance with single phase flows. While the opposite was observed when gas superficial velocity is increased.
- In the slug flow region, the PDFs suggest that the injection method has a more pronounced effect on the void fraction in the liquid slug as opposed to that in the Taylor bubble.
- Looking at the axial development of the flow, it was found that void fraction downstream increases compared to that upstream by a disproportional amount to that caused by gas expansion. This indicates the significance of bubble induced turbulence in enhancing bubbles break-up resulting in a higher void fraction upstream. The figures presented also suggest that the increasing drag at higher viscosities either improves the break-up of bubbles or hinders their coalescence resulting in a higher void fraction.

8.1.4 Chapter 7: Effect of viscosity on gas-lift performance in a vertical large diameter pipe

After the fundamental understanding of the viscosity influence on different two phase flow attributes has been established in the previous chapters both qualitatively and quantitatively. The effect of viscosity on gas-lift performance was investigated in a natural recirculation loop employing the very 4 different viscosities mentioned earlier. From the information presented in the chapter the following conclusions can be drawn:

- The gas-lift performance exhibits a significant decline as the liquid viscosity is increased. This was inferred by the pump performance curve and the analysis of the lift efficiency. This was attributed to the impact of viscosity on void fraction where increase in liquid viscosity results in a decrease in average void fraction at the same gas superficial velocity.

- Gas-lift efficiency appears to be highest in the bubbly flow region, as the gas superficial velocity is further increased the efficiency falls dramatically. The efficiency is not necessarily higher at lower viscosities especially at very low gas superficial velocities.

- In all experimental runs investigated, the PDFs of void fraction time series and the spatio-temporal images revealed that the incurring void fraction was bubbly flow throughout. In agreement with the conclusions of Chapter 4 there is a tendency of formation of larger gas structures with increasing liquid viscosity. At the highest viscosity the presence of cap-bubbly flow regime was registered by the appearance of an obscure bimodal PDF footprint.

- An evaluation of the performance of a selection of popuar gas-lift models was achieved againt the experimental results. The models include the model of Nicklin (1963) [132], Stenning and Martin (1968) [171], Clark and Dabolt (1986) [47], Reinemann et al (1990) [47], François et al (1996) [60]. It was found that all the aforementioned models perform poorly.

- An improved model was proposed and assessed against the experimental results. The proposed model is a modification of the model of Clark and Dabolt (1986) [47] whereby the improved drift-flux correlation presented in Chapter 5 was utilised.

8.2 Recommendations for further work

Undoubtedly, the information presented in this thesis provides a new insight into the paradigm of viscous two-phase flows in vertical large diameter pipes. Unique database has been generated that was used as a benchmark to test the performance of models against as well as employed to propose new models. Yet, a lot of the multiphase flow aspects remain improperly modelled leaving a huge room for improvement. Certainly that requires engaging in further experimental campaigns to investigate conditions at the same viscosities but different pipe geometries or even higher range of viscosities. However, still a great deal of more information can be extracted from the experiments presented in this thesis through further analysis. The following recommendations are therefore presented here for further future development of this research problem.

- The results presented in Chapter 4 included detailed characterisation of the flow regimes encountered at four different viscosities. Although a flow regime map is shown marking the evolution of transition boundaries with increasing viscosity, yet the theoretical and phenomenological models proposed in the literature for these transitions have not been tested. It is crucial to verify and assess the predictability of these models against this unique set of data. This is of profound importance since it allows to identify whether their performance is satisfactory or further development is necessary.

- It has been demonstrated in Chapter 5 that frictional pressure gradient models grossly depart from the experimental values. This was reflected in predicting pressure gradient in both low and high viscosity fluids. This necessitates formulation of new models that first improve predictability, with the capability of modelling the positive frictional pressure gradient observed in large diameter pipes. Moreover, the phenomenon of positive frictional pressure gradient needs further investigation. A simultaneous measurement of void fraction, differential pressure gradient, and wall shear stress will provide a much clearer understanding of the physical mechanisms that govern this phenomenon, the starting point of establishing a comprehensive model.

- The experimental campaign presented in this thesis is cemented by high speed videography of the flow. The videos are collected after matching refractive indices and accounting for the curvature of the pipe making the dimensions in the image true. These are very clear at low gas superficial velocities before the bubble density becomes high enough to limit the penetration depth of the light. These frames can be used to estimate the bubble size distribution in the pipe, and study the bubble movements providing further information to check against the bubble distribution obtained from the WMS at the same conditions. This will help reveal the distribution especially in bubble sizes below the spatial resolution of the WMS. Additionally, the high speed imaging information can also be used to verify the structure frequency results by counting the number of dominant gas structures in for a fixed period of time.

- One of the inherent limitations of the measurement techniques employed in this study, or perhaps the way the data is visualised is the inability to capture backward flow. For instance if a huge wave is falling down the liquid film, or through the core it will be registered by either the ECT or the WMS as a longer wave. Whilst from the shape of the structure its flow direction can be speculated, yet its length will be over-predicted. Therefore, synchronous videographs and tomographic measurements can be conducted to investigate this problem and perhaps propose algorithms to improve representation or at least accommodate for its existence in the visualisation of the WMS results.

- A lot of the significance of the results presented in this thesis comes from the critical choice of the simulant oils used. The Silicone oils employed allowed for varying viscosity a number of magnitudes higher while maintaining other physical properties of the oil virtually constant. It is very intriguing to find out how the behaviour would change if the viscosity is further increased to higher values covering up to 500 cP. This research will be of profound interest to the oil and gas industry as well as food and beverages industry where highly viscous fluids are often being handled. An even more interesting study would be varying only surface tension while maintaining other physical properties constant.

- In order to establish a more profound characterisation of the effect of physical properties of the fluids on two phase flows to ultimately improve modelling; further parametric studies are needed on both single and dual bubble interaction level as well as large scale experimentation level. This involves characterising the effect of density ratio, surface tension, and viscosity ratio of the fluids on both levels mentioned. That should be assessed in conjunction with studying the impact of geometrical parameters, such as the conduit hydraulic diameter as well as the injection method.

Bibliography

[1] Aamo, O. M., Eikrem, G., Siahaan, H., and Foss, B. A. (2005). Observer design for multiphase flow in vertical pipes with gas-lift- theory and experiments. *Journal of process control*, 15(3):247–257.

[2] Abdulahi, A. (2013). *Investigating the effect of liquid viscosity on two-phase gas-liquid flows*. PhD thesis.

[3] Abdulkadir, M., Hernandez-Perez, V., Lowndes, I., Azzopardi, B. J., and Dzomeku, S. (2014). Experimental study of the hydrodynamic behaviour of slug flow in a vertical riser. *Chemical Engineering Science*, 106:60–75.

[4] Abdulkadir, M., Hernandez-Perez, V., Lowndes, I. S., Azzopardi, B. J., and Sam-Mbomah, E. (2016). Experimental study of the hydrodynamic behaviour of slug flow in a horizontal pipe. *Chemical Engineering Science*, 156:147–161.

[5] Abueidda, D., Dalaq, A., Hafiz, H., and Elawadi, K. (2014). On the performance of air-lift pumps: From analytical models to large eddy simulation.

[6] Ahmed, S. (2014). *A study of gas lift on oil/water flow in vertical risers*. PhD thesis.

[7] Ahmed, W. H., Aman, A. M., Badr, H. M., and Al-Qutub, A. M. (2016). Air injection methods: The key to a better performance of airlift pumps. *Experimental Thermal and Fluid Science*, 70:354–365.

[8] Akhiyarov, D. T., Zhang, H.-Q., and Sarica, C. (2010). High-viscosity oil-gas flow in vertical pipe.

[9] Al-Ruhaimani, F., Pereyra, E., Sarica, C., Al-Safran, E. M., and Torres, C. F. (2016). Experimental analysis and model evaluation of high-liquid-viscosity two-phase upward vertical pipe flow. *SPE Journal*.

[10] Al-Sarkhi, A., Pereyra, E., Sarica, C., and Alruhaimani, F. (2016). Positive frictional pressure gradient in vertical gas-high viscosity oil slug flow. *International Journal of Heat and Fluid Flow*, 59:50–61.

[11] Alamu, M. B. (2010). *Investigation of periodic structures in gas-liquid flow*. PhD thesis.

[12] Ali, S. F. (2009). *Two phase flow in large diameter vertical riser*. PhD thesis.

[13] Alimonti, C. and Galardini, D. (1992). The modeling of an air-lift pump for the design of its control system. *European journal of mechanical engineering*, 37:191–197.

[14] Alruhaimani, F. A. S. (2015a). *Experimental Analysis and theoretical modeling of high liquid viscosity two-phase upward vertical pipe flow*. PhD thesis.

[15] Alruhaimani, F. A. S. (2015b). *Experimental Analysis and theoretical modeling of high liquid viscosity two-phase upward vertical pipe flow*. PhD thesis.

[16] Ambrosini, W., Andreussi, P., and Azzopardi, B. J. (1991). A physically based correlation for drop size in annular flow. *International Journal of Multiphase Flow*, 17(4):497–507.

[17] Andritsos, N., Williams, L., and Hanratty, T. (1989). Effect of liquid viscosity on the stratified-slug transition in horizontal pipe flow. *International Journal of Multiphase Flow*, 15(6):877–892.

[18] Ansari, A., Sylvester, N., Shoham, O., and Brill, J. (1994). A comprehensive mechanistic model for upward two-phase flow in wellbores.

[19] Awad, M. and Muzychka, Y. (2008). Effective property models for homogeneous two-phase flows. *Experimental Thermal and Fluid Science*, 33(1):106–113.

[20] Awari, G., Ardhapurkar, P., Wakde, D., and Bhuyar, L. (2004). Performance analysis of air-lift pump design. *Proceedings of the Institution of Mechanical Engineers, Part C: Journal of Mechanical Engineering Science*, 218(10):1155–1161.

[21] Aziz, K. and Govier, G. W. (1972). Pressure drop in wells producing oil and gas. *Journal of Canadian Petroleum Technology*, 11(03).

[22] Azzopardi, B. (2006). *Gas-liquid Flows*. Begell House.

[23] Azzopardi, B. (2010). Multiphase flow. *Chemical Engineering and Chemical Process Technology-Volume I: Fundamentals of Chemical Engineering*, page 97.

[24] Azzopardi, B. J. (1997). Drops in annular two-phase flow. *International Journal of Multiphase Flow*, 23, Supplement(0):1–53.

[25] Azzopardi, B. J. (2017). The frequency of periodic structures in vertical pneumatic conveying of large particles. *Chemical Engineering Science*.

[26] Azzopardi, B. J., Abdulkareem, L. A., Zhao, D., Thiele, S., da Silva, M. J., Beyer, M., and Hunt, A. (2010). Comparison between electrical capacitance tomography and wire mesh sensor output for air/silicone oil flow in a vertical pipe. *Industrial and Engineering Chemistry Research*, 49(18):8805–8811.

[27] Azzopardi, B. J., Do, H. K., Azzi, A., and Hernandez Perez, V. (2015). Characteristics of air/water slug flow in an intermediate diameter pipe. *Experimental Thermal and Fluid Science*, 60:1–8.

[28] Azzopardi, B. J., Ijioma, A., Yang, S., Abdulkareem, L. A., Azzi, A., and Abdulkadir, M. (2014). Persistence of frequency in gas–liquid flows across a change in pipe diameter or orientation. *International Journal of Multiphase Flow*.

[29] Baba, Y. D., Archibong, A. E., Aliyu, A. M., and Ameen, A. I. (2017). Slug frequency in high viscosity oil-gas two-phase flow: Experiment and prediction. *Flow Measurement and Instrumentation*, 54:109–123.

[30] Baker, R. (2005). *Flow Measurement Handbook: Industrial Designs, Operating Principles, Performance, and Applications*. Cambridge University Press.

[31] Beggs, D. H. and Brill, J. P. (1973). A study of two-phase flow in inclined pipes. *Journal of Petroleum technology*, 25(05):607–617.

[32] Besagni, G., Inzoli, F., De Guido, G., and Pellegrini, L. A. (2017). The dual effect of viscosity on bubble column hydrodynamics. *Chemical Engineering Science*, 158:509–538.

[33] Biria, S. (2013). *Prediction of pressure drop in vertical air/water flow in the presence/absence of sodium dodecyl sulfate as a surfactant*. PhD thesis.

[34] Brauner, N. and Barnea, D. (1986). Slug/churn transition in upward gas-liquid flow. *Chemical Engineering Science*, 41(1):159–163.

[35] Brennen, C. E. (2005). *Fundamentals of multiphase flow*. Cambridge university press.

[36] Brodkey, R. S. (1967). *The phenomena of fluid motions*. Courier Corporation.

[37] Brooks, C. S., Paranjape, S. S., Ozar, B., Hibiki, T., and Ishii, M. (2012). Two-group drift-flux model for closure of the modified two-fluid model. *International Journal of Heat and Fluid Flow*, 37(0):196–208.

[38] Chen, X. T., Cai, X. D., and Brill, J. P. (1997). A general model for transition to dispersed bubble flow. *Chemical Engineering Science*, 52(23):4373–4380.

[39] Cheng, H., Hills, J. H., and Azzorpardi, B. J. (1998). A study of the bubble-to-slug transition in vertical gas-liquid flow in columns of different diameter. *International Journal of Multiphase Flow*, 24(3):431–452.

[40] Chibuike, N. K. (2014). Detailed analysis of pressure drop in a large diameter vertical pipe. Master's thesis.

[41] Chisholm, D. (1967). A theoretical basis for the lockhart-martinelli correlation for two-phase flow. *International Journal of Heat and Mass Transfer*, 10(12):1767–1778.

[42] Chisholm, D. (1973). Pressure gradients due to friction during the flow of evaporating two-phase mixtures in smooth tubes and channels. *International Journal of Heat and Mass Transfer*, 16(2):347–358.

[43] Chisti, Y. (1989). *Airlift bioreactors*. Elsevier Applied Science.

[44] Cholet, H. (2008). *Well Production Practical Handbook*. Editions Technip.

[45] Clark, N. and Flemmer, R. (1985). Predicting the holdup in two-phase bubble upflow and downflow using the zuber and findlay drift-flux model. *AIChE journal*, 31(3):500–503.

[46] Clark, N. and Flemmer, R. (1986). The effect of varying gas voidage distributions on average holdup in vertical bubble flow. *International Journal of Multiphase Flow*, 12(2):299–302.

[47] Clark, N. N. and Dabolt, R. J. (1986). A general design equation for air lift pumps operating in slug flow. *American Institute of Chemical Engineering Journal*, 32:56–64.

[48] Costigan, G. and Whalley, P. B. (1997). Slug flow regime identification from dynamic void fraction measurements in vertical air-water flows. *International Journal of Multiphase Flow*, 23(2):263–282.

[49] Crabtree, J. R. and Bridgwater, J. (1971). Bubble coalescence in viscous liquids. *Chemical Engineering Science*, 26(6):839–851.

[50] Da Hlaing, N., Sirivat, A., Siemanond, K., and Wilkes, J. O. (2007). Vertical two-phase flow regimes and pressure gradients: Effect of viscosity. *Experimental Thermal and Fluid Science*, 31(6):567–577.

[51] Da Silva, M., Schleicher, E., and Hampel, U. (2007). Capacitance wire-mesh sensor for fast measurement of phase fraction distributions. *Measurement Science and Technology*, 18(7):2245.

[52] Da Silva, M. J., Thiele, S., Schleicher, E., and Hampel, U. (2009). Wire-mesh-sensors for high resolution gas-liquid multiphase flow visualisation.

[53] Davies, R. and Taylor, G. (1950). The mechanics of large bubbles rising through extended liquids and through liquids in tubes. In *Proceedings of the Royal Society of London A: Mathematical, Physical and Engineering Sciences*, volume 200, pages 375–390. The Royal Society.

[54] Dukler, A. E., Wicks, M., and Cleveland, R. G. (1964). Frictional pressure drop in two-phase flow: A. a comparison of existing correlations for pressure loss and holdup. *AIChE Journal*, 10(1):38–43.

[55] Dumitrescu, D. T. (1943). Strömung an einer luftblase im senkrechten rohr. *ZAMM-Journal of Applied Mathematics and Mechanics/Zeitschrift für Angewandte Mathematik und Mechanik*, 23(3):139–149.

[56] Escrig, J. E., Hewakandamby, B., Dimitrakis, G., and Azzopardi, B. (2016). Influence of inclination angle on intermittent two phase flows.

[57] Fabre, J. and Line, A. (2010). Slug flow.

[58] Farsetti, S., Farisè, S., and Poesio, P. (2014a). Experimental investigation of high viscosity oil-air intermittent flow. *Experimental Thermal and Fluid Science*, 57:285–292.

[59] Farsetti, S., Farisè, S., and Poesio, P. (2014b). Experimental investigation of high viscosity oil-air intermittent flow. *Experimental Thermal and Fluid Science*, 57:285–292.

[60] Fran¸cois, O., Gilmore, T., Pinto, M., and Gorelick, S. (1996). A physically based model for air-lift pumping. *Water resources research*, 32:2383–2399.

[61] Friedel, L. (1979). Improved friction pressure drop correlations for horizontal and vertical two phase pipe flow. *ROHRE - ROHRELEITUNGSBAU - ROHRELEITUNGSTRANSPORT*, 18 , July 1979:485–491.

[62] Fukano, T. and Furukawa, T. (1998). Prediction of the effects of liquid viscosity on interfacial shear stress and frictional pressure drop in vertical upward gas–liquid annular flow. *International journal of multiphase flow*, 24(4):587–603.

[63] Furukawa, T. and Fukano, T. (2001). Effects of liquid viscosity on flow patterns in vertical upward gas–liquid two-phase flow. *International Journal of Multiphase Flow*, 27(6):1109–1126.

[64] Ghajar, A. J. and Bhagwat, S. M. (2013). Effect of void fraction and two-phase dynamic viscosity models on prediction of hydrostatic and frictional pressure drop in vertical upward gas–liquid two-phase flow. *Heat Transfer Engineering*, 34(13):1044–1059.

[65] Gokcal, B., Al-Sarkhi, A., Sarica, C., and Alsafran, E. M. (2009). Prediction of slug frequency for high viscosity oils in horizontal pipes.

[66] Gokcal, B., Wang, Q., Zhang, H.-Q., and Sarica, C. (2008). Effects of high oil viscosity on oil/gas flow behavior in horizontal pipes. *SPE Projects, Facilities & Construction*, 3(02):1–11.

[67] Govan, A. H., Hewitt, G. F., Richter, H. J., and Scott, A. (1991). Flooding and churn flow in vertical pipes. *International Journal of Multiphase Flow*, 17(1):27–44.

[68] Grandjean, B. P. A., Ajersch, F., Carreau, P. J., and Patterson, I. (1987). Study of an air-lift system, part ii: Heat transfer in co-current, vertical two-phase, non-boiling flows. *The Canadian Journal of Chemical Engineering*, 65:437–442.

[69] Guet, S. (2004). *Bubble size effect on the gas-lift technique*. PhD thesis, Technische Universiteit Delft.

[70] Guet, S. and Ooms, G. (2006). Fluid mechanical aspects of the gas-lift technique. *Annu. Rev. Fluid Mech.*, 38:225–249.

[71] Guet, S., Ooms, G., Oliemans, R., and Mudde, R. (2003). Bubble injector effect on the gaslift efficiency. *AIChE journal*, 49(9):2242–2252.

[72] Haberman, W. and Morton, R. (1953). An experimental investigation of the drag and shape of air bubbles rising in various liquids. Technical report, DTIC Document.

[73] Hagedorn, A. R. and Brown, K. E. (1965). Experimental study of pressure gradients occurring during continuous two-phase flow in small-diameter vertical conduits. *Journal of Petroleum Technology*, 17(04):475–484.

[74] Harmathy, T. Z. (1960). Velocity of large drops and bubbles in media of infinite or restricted extent. *AIChE Journal*, 6(2):281–288.

[75] Heritage, J. E. (1989). The performance of transit time ultrasonic flowmeters under good and disturbed flow conditions. *Flow Measurement and Instrumentation*, 1(1):24–30.

[76] Hernandez-Perez, V., Abdulkadir, M., and Azzopardi, B. (2010). Slugging frequency correlation for inclined gas–liquid flow. *World Acad. Sci., Eng. Technol*, 6:44–51.

[77] Hernandez Perez, V., Zangana, M., Kaji, R., and Azzopardi, B. (2010). Effect of pipe diameter on pressure drop in vertical two-phase flow. University of Florida Digital Collections.

[78] Herringe, R. t. and Davis, M. (1976). Structural development of gas-liquid mixture flows. *Journal of Fluid Mechanics*, 73(01):97–123.

[79] Hewakandamby, B., Kanu, A., Azzopardi, B., and Kouba, G. (2014). Parametric study of churn flow in large diameter pipes. volume 1D.

[80] Hewitt, G. F. (2010). *Two Phase Flows*. Begell House, THERMOPEDIA A-to-Z Guide to Thermodynamics, Heat & Mass Transfer, and Fluids Engineering. (Accessed on 11/05/2015).

[81] Hewitt, G. F. and Hall-Taylor, N. (1970). *Annular two-phase flow*. Pergamon.

[82] Hewitt, G. F., Lacey, P., and Nicholls, B. (1964). *Transitions in film flow in a vertical tube*. UK Atomic Energy Authority Research Group.

[83] Hewitt, G. F. and Wallis, G. B. (1963). Flooding and associated phenomena in falling film flow in a tube. Technical report, United Kingdom Atomic Energy Authority. Research Group. Atomic Energy Research Establishment, Harwell Berks, England.

[84] Hibiki, T. and Ishii, M. (2001). Effect of inlet geometry on hot-leg u-bend two-phase natural circulation in a loop with a large diameter pipe. *Nuclear Engineering and Design*, 203(2–3):209–228.

[85] Hibiki, T. and Ishii, M. (2003a). One-demensional drift-flux model for two-phase flow in a large diameter pipe. *International Journal of Heat and Mass Transfer*, 46(10):1773–1790.

[86] Hibiki, T. and Ishii, M. (2003b). One-dimensional drift-flux model and constitutive equations for relative motion between phases in various two-phase flow regimes. *International Journal of Heat and Mass Transfer*, 46(25):4935–4948.

[87] Hills, J. H. (1976). The operation of a bubble column at high throughputs: I. gas holdup measurements. *The Chemical Engineering Journal*, 12(2):89–99.

[88] Hinze, J. (1955). Fundamentals of the hydrodynamic mechanism of splitting in dispersion processes. *AIChE Journal*, 1(3):289–295.

[89] Hirao, Y., Kawanishi, K., Tsuge, A., and Kohriyama, T. (1986). Experimental study on drift flux correlation formulas for two-phase flow in large diameter tubes. In *Proceedings of second international topical meeting on nuclear power plant thermal hydraulics and operations*.

[90] Hu, D., Tang, C.-L., Cai, S.-P., and Zhang, F.-H. (2012). The effect of air injection method on the airlift pump performance. *Journal of Fluids Engineering*, 134(11):111–302.

[91] Hussain, L. A. and Spedding, P. L. (1976). Explore the potential of air-lift pumps and multiphase. *International Journal of Multiphase Flow*, 3:83–87.

[92] Ibrahim, A., Hewakandamby, B., and Azzopardi, B. (2016a). Experimental investigation of gas lift performance in a large diameter pipe. In *Proceedings of the 10th North American Conference on Multiphase Technology*. BHR group.

[93] Ibrahim, A., Hewakandamby, B. N., and Azzopardi, B. J. (2016b). Comparison of three injector geometries in gas lift performance of a large diameter pipe. In *Proceedings of the 9th International Conference on Multiphase Flow*.

[94] IEA (2017). Oil information 2017: Overview. Technical report.

[95] Institute, A. P. (1994). *API Gas Lift Manual*. American Petroleum Institute (API).

[96] Ishii, M. (1977). One-dimensional drift-flux model and constitutive equations for relative motion between phases in various two-phase flow regimes. Technical report, Argonne National Lab., Ill.(USA).

[97] Ishii, M. and Zuber, N. (1979). Drag coefficient and relative velocity in bubbly, droplet or particulate flows. *AIChE Journal*, 25(5):843–855.

[98] Jayanti, S. (2010). *Churn Flow*. Begell House, THERMOPEDIA A-to-Z Guide to Thermodynamics, Heat & Mass Transfer, and Fluids Engineering. (Accessed on 25/04/2014).

[99] Jayanti, S. and Hewitt, G. F. (1992). Prediction of the slug-to-churn flow transition in vertical two-phase flow. *International Journal of Multiphase Flow*, 18(6):847–860.

[100] Jeelani, S. A. K., Kapsipati Rao, K. V., and Balasubramananian, G. R. (1979). The theory of the gas-lift pump: a rejoinder. *International Journal of Multiphase Flow*, 5:225–228.

[101] Jones Jr, O. C. and Zuber, N. (1975). The interrelation between void fraction fluctuations and flow patterns in two-phase flow. *International Journal of Multiphase Flow*, 2(3):273–306.

[102] Kabir, C. S. and Hasan, A. R. (1990). Performance of a two-phase gas/liquid flow model in vertical wells. *Journal of Petroleum Science and Engineering*, 4(3):273–289.

[103] Kajero, O. T., Azzopardi, B. J., and Abdulkareem, L. (2012). Experimental investigation of the effect of liquid viscosity on slug flow in small diameter bubble column. *EPJ Web of Conferences*, 25:01037.

[104] Kaji, R., Azzopardi, B. J., and Lucas, D. (2009). Investigation of flow development of co-current gas-liquid vertical slug flow. *International Journal of Multiphase Flow*, 35(4):335–348.

[105] Kanu, A. U. (2013). *Characterisation of churn flow coalescers (CFC) in vertical pipes*. PhD thesis.

[106] Kassab, S. Z., Kandil, H. A., Warda, H. A., and Ahmed, W. H. (2009). Air-lift pumps characteristics under two-phase flow conditions. *International Journal of Heat and Fluid Flow*, 30(1):88–98.

[107] Kataoka, I. and Ishii, M. (1987). Drift flux model for large diameter pipe and new correlation for pool void fraction. *International Journal of Heat and Mass Transfer*, 30(9):1927–1939.

[108] Kataoka, I. and Serizawa, A. (2010). Bubble flow.

[109] Khaledi, H. A., Smith, I. E., Unander, T. E., and Nossen, J. (2014). Investigation of two-phase flow pattern, liquid holdup and pressure drop in viscous oil–gas flow. *International Journal of Multiphase Flow*, 67:37–51.

[110] Khalil, M. F., Elshorbagy, K. A., Kassab, S. Z., and Fahmy, R. I. (1999). Effect of air injection method on the performance of an air lift pump. *International Journal of Heat and Fluid Flow*, 20(6):598–604.

[111] Kim, S. H., Sohn, C. H., and Hwang, J. Y. (2014). Effects of tube diameter and submergence ratio on bubble pattern and performance of air-lift pump. *International Journal of Multiphase Flow*, 58:195–204.

[112] Kulkarni, A. A. and Joshi, J. B. (2005). Bubble formation and bubble rise velocity in gas-liquid systems: a review. *Industrial and Engineering Chemistry Research*, 44(16):5873–5931.

[113] Levy, S. (1999). *Two-phase flow in complex systems*. John Wiley & Sons.

[114] Liu, H., Vandu, C. O., and Krishna, R. (2005). Hydrodynamics of taylor flow in vertical capillaries: flow regimes, bubble rise velocity, liquid slug length, and pressure drop. *Industrial and engineering chemistry research*, 44(14):4884–4897.

[115] Liu, L. (2014). The phenomenon of negative frictional pressure drop in vertical two-phase flow. *International Journal of Heat and Fluid Flow*, 45:72–80.

[116] Lockhart, R. and Martinelli, R. (1949). Proposed correlation of data for isothermal two-phase, two-component flow in pipes. *Chem. Eng. Prog*, 45(1):39–48.

[117] Lucas, D., Krepper, E., and Prasser, H.-M. (2005). Development of co-current air–water flow in a vertical pipe. *International Journal of Multiphase Flow*, 31(12):1304–1328.

[118] Magnaudet, J., Takagi, S., and Legendre, D. (2003). Drag, deformation and lateral migration of a buoyant drop moving near a wall. *Journal of Fluid Mechanics*, 476:115–157.

[119] Mandhane, J., Gregory, G., and Aziz, K. (1974). A flow pattern map for gas—liquid flow in horizontal pipes. *International Journal of Multiphase Flow*, 1(4):537–553.

[120] Matsubara, H. and Naito, K. (2011). Effect of liquid viscosity on flow patterns of gas–liquid two-phase flow in a horizontal pipe. *International Journal of Multiphase Flow*, 37(10):1277–1281.

[121] McNeil, D. A. and Stuart, A. D. (2003). The effects of a highly viscous liquid phase on vertically upward two-phase flow in a pipe. *International Journal of Multiphase Flow*, 29(9):1523–1549.

[122] McQuillan, K. W. and Whalley, P. B. (1985). Flow patterns in vertical two-phase flow. *International Journal of Multiphase Flow*, 11(2):161–175.

[123] Mekisso, H. M. (2013). *Comparison of Frictional Pressure Drop Correlations for Isothermal Two-Phase Horizontal Flow*. PhD thesis.

[124] Mendelson, H. D. (1967). The prediction of bubble terminal velocities from wave theory. *AIChE Journal*, 13(2):250–253.

[125] Mir-Yusif, M.-B. (2011). The role of azerbaijan in the world's oil industry. *Oil-Industry History*, 12(1):109–123.

[126] Mishima, K. and Ishii, M. (1984). Flow regime transition criteria for upward two-phase flow in vertical tubes. *International Journal of Heat and Mass Transfer*, 27(5):723–737.

[127] Morris, A. and Langari, R. (2012). *Measurement and Instrumentation: Theory and Application*. Academic Press.

[128] Morrison, G. L., Zeineddine, T. I., and Henriksen, M. G. B. T. (1987). Experimental analysis of the mechanics of reverse circulation air lift pump. *Industrial and engineering chemistry research*, 26:387–391.

[129] Mukherjee, H. and Brill, J. (1985). Pressure drop correlations for inclined two-phase flow. *Journal of energy resources technology*, 107(4):549–554.

[130] Murase, M., Suzuki, H., Matsumoto, T., and Naitoh, M. (1986). Countercurrent gas-liquid flow in boiling channels. *Journal of Nuclear Science and Technology*, 23(6):487–502.

[131] Nädler, M. and Mewes, D. (1995). Effects of the liquid viscosity on the phase distributions in horizontal gas-liquid slug flow. *International Journal of Multiphase Flow*, 21(2):253–266.

[132] Nicklin, D. (1963). The air lift pump theory and optimization. *Trans. Inst. Chem. Eng*, 41:29–39.

[133] Nicklin, D. J. (1962). Two-phase bubble flow. *Chemical Engineering Science*, 17(9):693–702.

[134] Ohnuki, A. and Akimoto, H. (1996). An experimental study on developing air-water two-phase flow along a large vertical pipe: effect of air injection method. *International Journal of Multiphase Flow*, 22(6):1143–1154.

[135] Ohnuki, A. and Akimoto, H. (2000). Experimental study on transition of flow pattern and phase distribution in upward air-water two-phase flow along a large vertical pipe. *International Journal of Multiphase Flow*, 26(3):367–386.

[136] Oliemans, R. and Pots, B. (2006). Gas–liquid transport in ducts. *Multiphase Flow Handbook, CRC Press, Boca Raton*, pages 37–81.

[137] Olivieri, G., Russo, M. E., Simeone, M., Marzocchella, A., and Salatino, P. (2011). Effects of viscosity and relaxation time on the hydrodynamics of gas–liquid systems. *Chemical engineering science*, 66(14):3392–3399.

[138] Omebere-Iyari, N. K. (2006). *The effect of pipe diameter and pressure in vertical two-phase flow*. PhD thesis.

[139] Omebere-Iyari, N. K., Azzopardi, B. J., Lucas, D., Beyer, M., and Prasser, H. M. (2008). The characteristics of gas/liquid flow in large risers at high pressures. *International Journal of Multiphase Flow*, 34(5):461–476.

[140] Orvalho, S., Ruzicka, M. C., Olivieri, G., and Marzocchella, A. (2015). Bubble coalescence: Effect of bubble approach velocity and liquid viscosity. *Chemical Engineering Science*, 134:205–216.

[141] Otake, T., Tone, S., Nakao, K., and Mitsuhashi, Y. (1977). Coalescence and breakup of bubbles in liquids. *Chemical Engineering Science*, 32(4):377–383.

[142] Owen, D. G. (1986). *An experimental and theoretical analysis of equilibrium annular flows*. PhD thesis. Dimensionless pressure drop against gas superficial velocity.

[143] Parsi, M., Vieira, R. E., Torres, C. F., Kesana, N. R., McLaury, B. S., Shirazi, S. A., Schleicher, E., and Hampel, U. (2015). On the effect of liquid viscosity on interfacial structures within churn flow: Experimental study using wire mesh sensor. *Chemical Engineering Science*, 130(0):221–238.

[144] PetroWiki (2017). Wellbore flow performance @ONLINE. (Accessed on 18/10/2017).

[145] Prasser, H.-M., Beyer, M., Carl, H., Gregor, S., Lucas, D., Pietruske, H., Schütz, P., and Weiss, F.-P. (2007). Evolution of the structure of a gas–liquid two-phase flow in a large vertical pipe. *Nuclear Engineering and Design*, 237(15–17):1848–1861.

[146] Prasser, H. M., Böttger, A., and Zschau, J. (1998). A new electrode-mesh tomograph for gas–liquid flows. *Flow Measurement and Instrumentation*, 9(2):111–119.

[147] Prasser, H.-M., Scholz, D., and Zippe, C. (2001). Bubble size measurement using wire-mesh sensors. *Flow Measurement and Instrumentation*, 12(4):299–312.

[148] Premoli, A., DiFrancesco, D., and Prina, A. (1971). A dimensionless correlation for the determination of the density of two-phase mixtures. *Termotecnica,(Milan)*, 25(1):17–26.

[149] Pringle, C. C. T., Ambrose, S., Azzopardi, B. J., and Rust, A. C. (2014). The existence and behaviour of large diameter taylor bubbles. *International Journal of Multiphase Flow*.

[150] Qi, F. S., Yeoh, G. H., Cheung, S. C. P., Tu, J. Y., Krepper, E., and Lucas, D. (2012). Classification of bubbles in vertical gas–liquid flow: Part 1 – an analysis of experimental data. *International Journal of Multiphase Flow*, 39:121–134.

[151] Rabha, S., Schubert, M., and Hampel, U. (2014). Regime transition in viscous and pseudo viscous systems: A comparative study. *AIChE Journal*, 60(8):3079–3090.

[152] Radovcich, N. A. and Moissis, R. (1962). The transition from two phase bubble flow to slug flow. Technical report, Cambridge, Mass.: MIT Division of Sponsored Research,[1962].

[153] Reinemann, D. J., Parlange, J. Y., and Timmons, M. B. (1990). Theory of small-diameter airlift pumps. *International Journal of Multiphase Flow*, 16:113–122.

[154] Richardson, J. F. and Higson, D. J. (1962). A study of the energy losses associated with the operation of an air-lift pump. *Trans. Inst. Chem. Eng*, 40:169–182.

[155] Ruiz, R., Brito, A., and Marquez, J. G. (2014). Evaluation of multiphase flow models to predict pressure gradient in vertical pipes with highly viscous liquids.

[156] Ruzicka, M. C., Drahoš, J., Mena, P. C., and Teixeira, J. A. (2003). Effect of viscosity on homogeneous–heterogeneous flow regime transition in bubble columns. *Chemical Engineering Journal*, 96(1–3):15–22.

[157] Schlegel, J. P. and Hibiki, T. (2015). A correlation for interfacial area concentration in high void fraction flows in large diameter channels. *Chemical Engineering Science*, 131(0):172–186.

[158] Schlegel, J. P., Hibiki, T., and Ishii, M. (2016). Characteristics of two-phase flows in large diameter channels. *Nuclear Engineering and Design*, 310:544–551.

[159] Schmidt, J., Giesbrecht, H., and van der Geld, C. W. M. (2008). Phase and velocity distributions in vertically upward high-viscosity two-phase flow. *International Journal of Multiphase Flow*, 34(4):363–374.

[160] Sekoguchi, K., Nakazatomi, M., and Tanaka, O. (1980). Forced convective heat transfer in vertical air-water bubble flow. *Bulletin of JSME*, 23(184):1625–1631.

[161] Serizawa, A., Kataoka, I., and Michiyoshi, I. (1975). Turbulence structure of air-water bubbly flow—ii. local properties. *International Journal of Multiphase Flow*, 2(3):235–246.

[162] Sharaf, S. (2011). *Testing and Application of Wire Mesh Sensor in Vertical Gas Liquid Two-Phase Flow*. PhD thesis.

[163] Sharaf, S., van der Meulen, G. P., Agunlejika, E. O., and Azzopardi, B. J. (2016). Structures in gas–liquid churn flow in a large diameter vertical pipe. *International Journal of Multiphase Flow*, 78:88–103.

[164] Shen, X., Hibiki, T., and Nakamura, H. (2015). Bubbly to cap bubbly flow transition in a long 26m vertical large diameter pipe at low liquid flow rate. *International Journal of Heat and Fluid Flow*, 52(0):140–155.

[165] Shen, X., Schlegel, J. P., Chen, S., Rassame, S., Griffiths, M. J., Hibiki, T., and Ishii, M. (2014). *Flow Characteristics and Void Fraction Prediction in Large Diameter Pipes*. Springer.

[166] Shipley, D. G. (1984). Two phase flow in large diameter pipes. *Chemical Engineering Science*, 39(1):163–165.

[167] Shoham, O. (2006). *Mechanistic modeling of gas-liquid two-phase flow in pipes*. Richardson, TX: Society of Petroleum Engineers.

[168] Silva, M. J. d. (2008). *Impedance Sensors for Fast Multiphase Flow Measurement and Imaging*. PhD thesis.

[169] Smith, T. R., Schlegel, J. P., Hibiki, T., and Ishii, M. (2012). Two-phase flow structure in large diameter pipes. *International Journal of Heat and Fluid Flow*, 33(1):156–167.

[170] Spedding, P. L., Woods, G. S., Raghunathan, R. S., and Watterson, J. K. (1998). Vertical two-phase flow. *Chemical Engineering Research and Design*, 76(5):628–634.

[171] Stenning, A. H. and Martin, C. B. (1968). An analytical and experimental study of air-lift pump performance. *Journal of Engineering for Gas Turbines and Power*, 90:106–110.

[172] Szalinski, L., Abdulkareem, L., Da Silva, M., Thiele, S., Beyer, M., Lucas, D., Hernandez Perez, V., Hampel, U., and Azzopardi, B. (2010). Comparative study of gas–oil and gas–water two-phase flow in a vertical pipe. *Chemical Engineering Science*, 65(12):3836–3848.

[173] Taitel, Y., Bornea, D., and Dukler, A. E. (1980). Modelling flow pattern transitions for steady upward gas-liquid flow in vertical tubes. *AICHE. J.*, 26(3 , May 1980):345–354.

[174] Taitel, Y. and Dukler, A. E. (1987). Effect of pipe length on the transition boundaries for high-viscosity liquids. *International Journal of Multiphase Flow*, 13(4):577–581.

[175] Takacs, G. (2005). *Gas Lift Manual*. PennWell.

[176] Tang, C., Hu, D., and Zhang, F. (2013a). Effect of air injector on the airlift performance in air-water-solid three-phase flow. *Journal of Energy Engineering*, 140(1):04013006.

[177] Tang, C. C., Tiwari, S., and Ghajar, A. J. (2013b). Effect of void fraction on pressure drop in upward vertical two-phase gas-liquid pipe flow. *Journal of Engineering for Gas Turbines and Power*, 135(2):022901.

[178] Thurston, R. and Pierce, A. (2012). *Ultrasonic Measurement Methods*. Elsevier Science.

[179] Todoroki, I., Sato, Y., and Honda, T. (1973). Performance of air-lift pump. *Bulletin of JSME*, 16:733–741.

[180] Tomiyama, A., Tamai, H., Zun, I., and Hosokawa, S. (2002). Transverse migration of single bubbles in simple shear flows. *Chemical Engineering Science*, 57(11):1849–1858.

[181] Van Geest, S. (2000). *Comparison of different air injection methods to improve gas-lift performance*. PhD thesis, Technische Universiteit Delft.

[182] Vieira, R. E., Parsi, M., Torres, C. F., McLaury, B. S., Shirazi, S. A., Schleicher, E., and Hampel, U. (2015). Experimental characterization of vertical gas–liquid pipe flow for annular and liquid loading conditions using dual wire-mesh sensor. *Experimental Thermal and Fluid Science*, 64(0):81–93.

[183] Wallis, G. B. (1969). One-dimensional two-phase flow.

[184] Waltrich, P. J., Falcone, G., and Barbosa Jr, J. R. (2013). Axial development of annular, churn and slug flows in a long vertical tube. *International Journal of Multiphase Flow*, 57(0):38–48. Hazuku structures detection method.

[185] Weisman, J., Duncan, D., Gibson, J., and Crawford, T. (1979). Effects of fluid properties and pipe diameter on two-phase flow patterns in horizontal lines. *International Journal of Multiphase Flow*, 5(6):437–462.

[186] Whalley, P. and McQuillan, K. (1985). The development and use of a directional wall shear stress probe.

[187] Wilkinson, P. M., Spek, A. P., and van Dierendonck, L. L. (1992). Design parameters estimation for scale-up of high-pressure bubble columns. *AIChE Journal*, 38(4):544–554.

[188] Wilkinson, P. M., Van Schayk, A., Spronken, J. P. M., and Van Dierendonck, L. (1993). The influence of gas density and liquid properties on bubble breakup. *Chemical Engineering Science*, 48(7):1213–1226.

[189] Yang, W. and Peng, L. (2003). Image reconstruction algorithms for electrical capacitance tomography. *Measurement Science and Technology*, 14(1):R1.

[190] Zabaras, G. (1999). Prediction of slug frequency for gas-liquid flows.

[191] Zangana, M. H. S. (2011). *Film behaviour of vertical gas-liquid flow in a large diameter pipe*. PhD thesis.

[192] Zhang, H.-Q., Wang, Q., Sarica, C., and Brill, J. P. (2003). Unified model for gas-liquid pipe flow via slug dynamics—part 1: model development. *Journal of energy resources technology*, 125(4):266–273.

[193] Zuber, N. and Findlay, J. (1965). Average volumetric concentration in two-phase flow systems. *Journal of Heat Transfer*, 87(4):453–468.

Appendix A

Instruments calibration

A.1 Flowmeters

A.1.1 Ultrasonic liquid flowmeter

The flowmeter measures the liquid flowrate up to an accuracy of up to 5%. It gives a current output signal of (4-20 mA) which is converted into a voltage output to comply with the data acquisition module by using a 250Ω resistor. The calibration equation is pretty much linear as shown in the curve in Figure A.1 below. The calibration equation is implemented into the LabVIEW program and direct flowrate measurements are obtained and logged in .tdms format. Figure below shows the calibration curve of the flowmeter.

Transit time ultrasonic principle is based on measuring time delay of ultrasonic waves propagating through a fluid in a path of a known distance. The sound wave will travel in the direction of a flowing fluid at a speed equal to the speed of sound in the fluid + fluid velocity ($C_s + V_f$) in a time period (t_d). Also if the wave is propagating opposite to the flow direction it will travel at a speed ($C_s - V_f$) in a time period (t_u). The fluid speed can then be calculated from the equation below:

$$V_f = \frac{L^2 \Delta t}{2X t_u t_d} \tag{A.1}$$

Where X is the axial distance between the transducers, L is the sound path length,Δt is the time difference between t_u and t_d[30]. Accuracies of transit time flowmeters with two paths range from 1-1.5% for liquids [75].

There are two principles to measure the ultrasonic time delay:

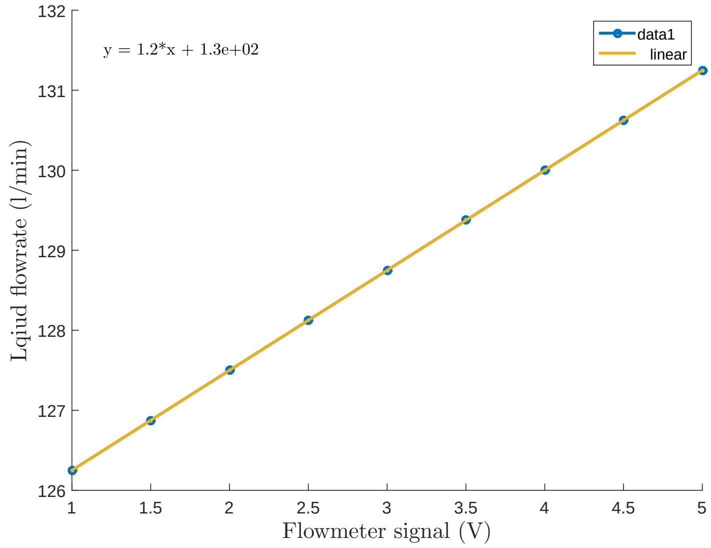

Fig. A.1 Ultrasonic liquid flowmeter calibration curve.

1. Pulse Echo Overlap method (PEO) This method measures the time delay by overlapping two ultrasonic waves; the start and the end wave over a specific distance. This overlap can be captured by an oscilloscope to set the period of sweeping frequency of the overlapping waves to be equal to the time delay [178].

2. Measurement of ultrasonic attenuation Attenuation signifies the rate of decay of ultrasonic mechanical vibrations as it propagates through the material; which is represented by the equation below:

$$A = A_o e^{-\alpha z} e^{i(\omega t - kz)} \tag{A.2}$$

Where α is the wave attenuation (nepers/length), k is the propagation constant $= \frac{2\pi}{\lambda}$, A is the amplitude (wave is considered infinite extend and a uniform amplitude) , and ω is the Angular frequency.

A.1.2 Oval gear liquid flowmeter

Oval gear flowmeter is used to measure liquid flow in the forced flow loop setting of the Statoil gas-lift rig. It is fitted about 15D on the discharge line of the Netzsch positive displacement pump. The flowmeter is a positive displacement type that comprises of two oval gears that rotate whenever a known quantity of liquid passes through the chamber. It was particularly chosen for its suitability to measure high viscosity liquid flowrates. High resolution pulses are generated by magnets planted in the oval gears and therefore the flowrate is linked to the number of pulses generated by unit time. It produces a (4-20mA) output current signal that is converted to (1-5V) signal by a 250Ω resistor. It is connected to the NI9205 data acquisition module. Figure A.7 below shows the calibration curve. Equipment is supplied with a 5 point calibration certificate issued by the manufacturer.

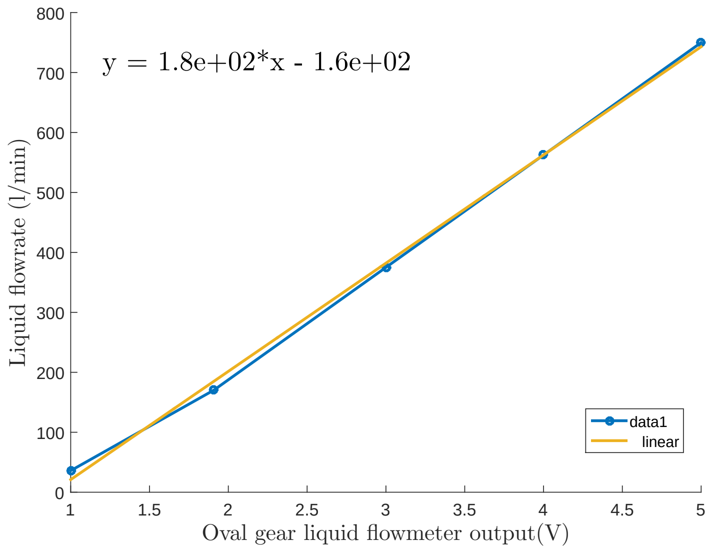

Fig. A.2 Oval gear flowmeter calibration curve.

A.1.3 Thermal mass flowmeter and controller

The gas flowrate is measured and controlled automatically using a thermal mass flowmeter and controller from Bronkhorst (F-203AV-1M0-ABD-99-V). The flowmeter measures in the range of (33.4-1670 l/min) of air. The flowmeter has been calibrated at the lab conditions (6.89 bar upstream pressure and 20^oC temperature) and it was found to produce a maximum error of 10.02 l/min at full scale. The flowmeter produces a voltage output signal of (0-10 Vdc) which is acquired instantaneously using the NI9205 data acquisition module. The controller however is a PID (Proportional Integral Derivative) controller. It allows the modification of the individual control parameters to achieve the required flowrate based on the balance between system stability, recovery time and error elimination. It is connected to the computer using an RS232 connection protocol and a designated user interface to adjust the controller parameters and set points with online plotting of the actual rates. The calibration certificate of the flowmeter is shown in Figure A.3 below.

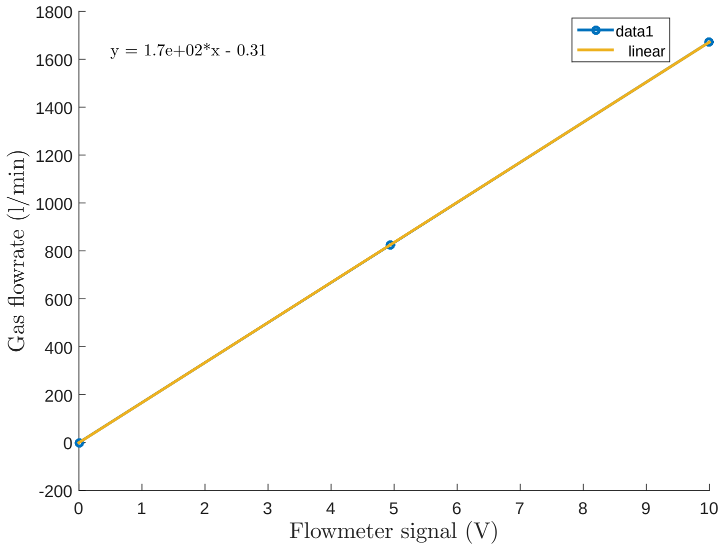

Fig. A.3 Thermal mass flowmeter calibration curve.

A.2 Pressure measurement

A.2.1 Differential pressure transmitter

The transmitter measures the differential pressure between two points in the column. 4 pressure fittings are attached to the wall of the testing column distributed every 2 meters. It measured the pressure difference up to 1 bar. It gives an output signal of 0-10 volts. It was calibrated and the readings are shown in Figure A.4 below.

Gas injection pressure transducer

The air injection line pressure is measured with a pressure transducer that measures in the range from 0-10 bars to an accuracy of 0.25%. The device gives a current output of (4-20 mA) which is similarly converted into voltage signal using a 250 Ω resistor. The relationship is almost linear as shown in Figure A.5 below.

Test section base pressure is measured by a similar transducer. The calibration curve is shown in Figure A.6 below.

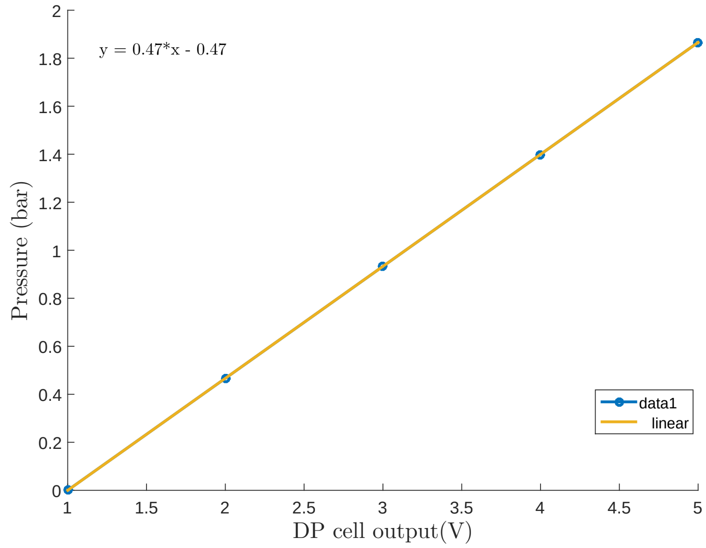

Fig. A.4 Differential pressure sensor calibration curve.

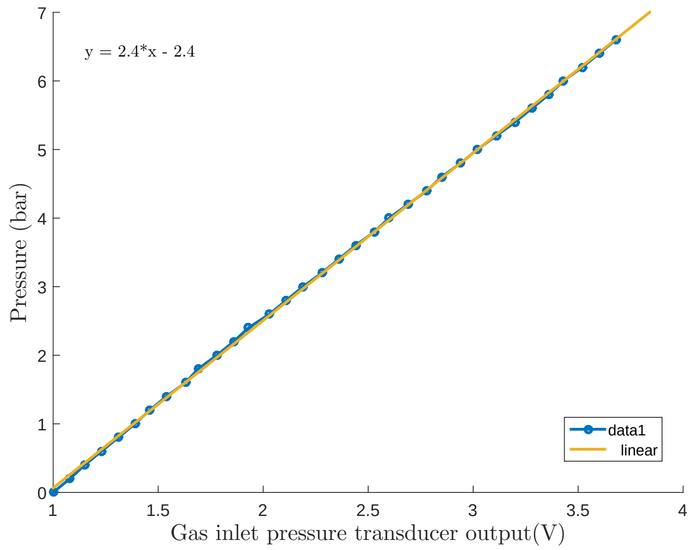

Fig. A.5 Gas inlet pressure transducer calibration curve.

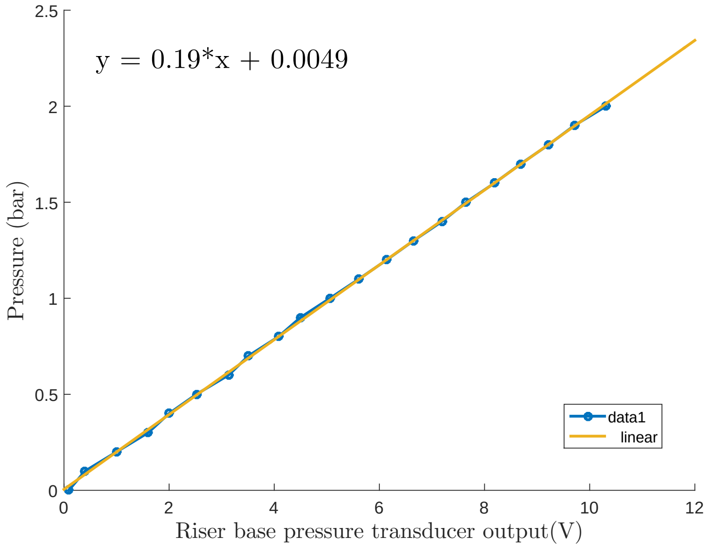

Fig. A.6 Riser base pressure transducer calibration curve.

A.3 Temperature measurement

The gas injection temperature is sensed using type K thermocouple that is adjusted to accurately measure the temperatures in the range from $0 - 100^oC$. The data is acquired using a special data acquisition module (NI-9211) from national instruments which directly translates the voltage output of the thermocouple into temperatures. The thermocouple was tested with boiling water and icy water to double check the validity of the results and it was in agreement with the $0 - 100^oC$ values.

A.4 Data acquisition program

As explained in the methodology chapter, National Instruments (NI) data logging hardware has been employed in this work interfaced and programmed using LabVIEW. The serial number of modules and the compactDAQ chassis were presented in the methodology chapter. The data acquisition is triggered by a voltage signal produced by the WMS electronic box to be received by the ECT electronics box and the NI chassis. The data is acquired at a frequency of 1 kHz for a period of 60 seconds, generating 60,000 readings per run.

An overview of the LabVIEW block diagram is presented in Figure A.7. the program is formed of DAQ Assistant sub-vi that log data from respective physical channels from different modules. The acquisition frequency is can be set by this sub-vi. In addition calibration equations are implemented within. Write to measurement file sub-vi is added to log the data into binary .tdms files that can be treated later via Matlab. Elapsed time sub-vi is added to stop the acquisition once the 60 seconds period had elapsed.

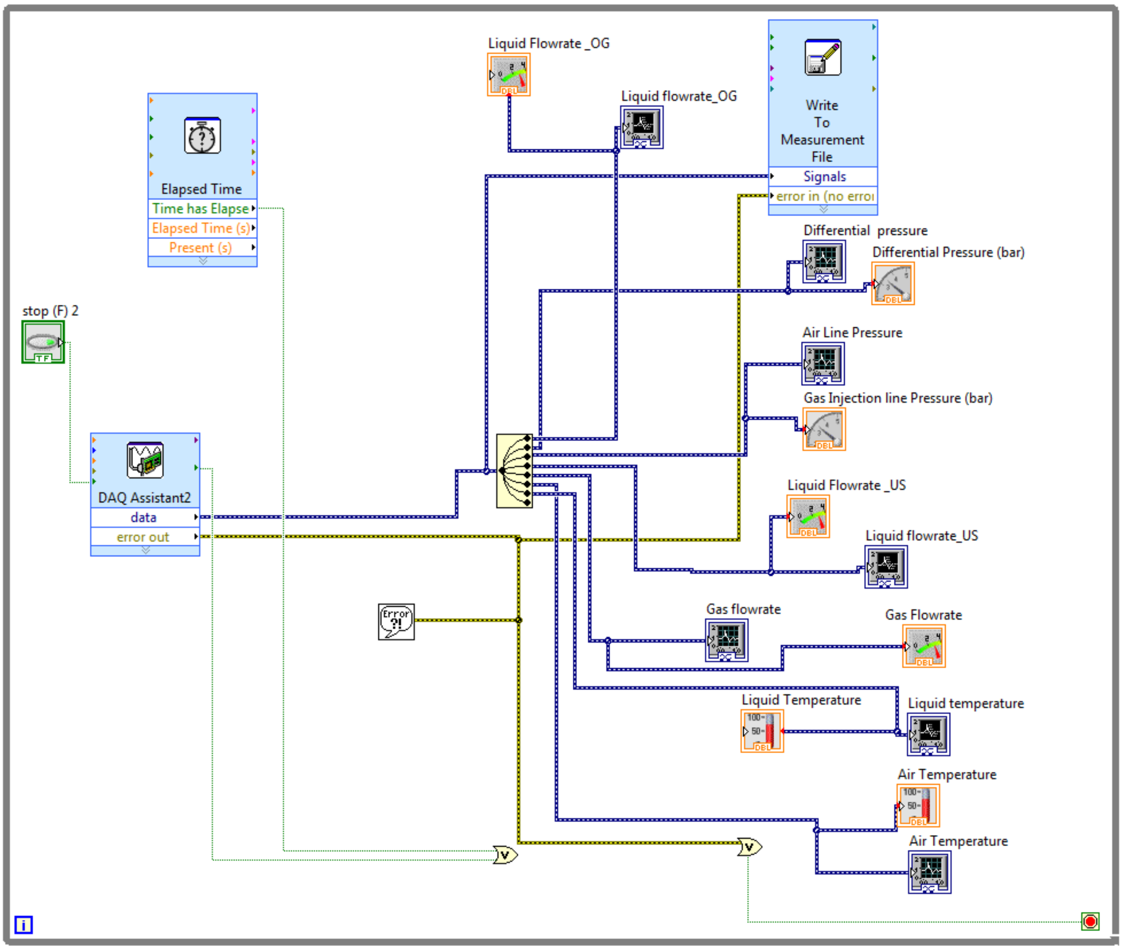

Fig. A.7 Overview of the block diagram of the data acquisition program.